Novel Self-Expanding Stent Retractors for Neuroendoscopy

Yang Xia

St Cross College

University of Oxford

A thesis submitted for the degree of

Doctor of Philosophy

Trinity 2017

To my family

Abstract

Novel Self-Expanding Stent for Neuroendoscopy

Yang Xia
St Cross College

A thesis submitted for the degree of Doctor of Philosophy
in Department of Engineering Science, University of Oxford, Trinity Term 2017

This thesis reports on the development of a novel self-expanding stent retractor (SESR), one that could replace the rigid tubular retractors in common use for minimally invasive neuroendoscopy. The thesis begins with a comprehensive literature review, focusing on existing neuroendoscopy techniques and devices that treat deep brain lesions. The motivation behind this project, including its potential scientific and practical value, is set out clearly. The main body of the thesis describes three different activities.

The first part presents preliminary studies on brain tissue that have been conducted to set up an appropriate medium for SESR deployment. A finite element model of brain tissue phantom was built in Abaqus/Explicit and several surgical scenarios were simulated. The finite element model was validated through comparisons with existing simulation results, data from the literature review and experimental measurements. It is found that the pressure required to create a 16mm diameter corridor in the brain tissue phantom through radial expansion is 2.089 kPa.

The second part of the thesis explains the process of designing and analysing the SESR. Conceptual designs identify the dimensions, materials, and functions of SESR, along with its accessory components. Theoretical analysis found a range for geometric design based on z shape stent radial pressure. Finite element analysis was applied to thoroughly study single z shape stents and SESRs, identifying 5-crown stent SESR (wire diameter 0.31mm to 0.33mm) and 10-crown stent SESR (wire diameter 0.34mm to 0.36mm) to be suitable designs for neuroendoscopy deployment. Finally, prototypes were manufactured and experiments conducted to validate these results of finite element analysis.

The third part of the thesis explores the SESRs' deployment in brain tissue. In both finite element analysis and *in vitro* experiments, SESRs created access corridors in the brain tissue phantom similar in efficacy to those by rigid tubular retractors, while reducing the pressure on surrounding tissue. By changing SESR's radial pressure along its longitudinal direction, alternative deployment shapes were also attainable, which suggested suitability for varying surgical needs.

In summary this thesis demonstrates that the proposed novel self-expanding stent retractor is a viable design with potential to reduce tissue damage during surgical use.

Keywords: self-expanding stent, nitinol, finite element analysis, neuroendoscopy, minimally invasive, tubular retractor.

CONTENT

List of Figures

List of Tables

Nomenclature

α	Material coefficient constant
A_f	Austenite finishing temperature
C	Z shape stent circumference
COF	Chronic outward force
D	Z shape stent outer diameter
$D_{bending}$	Shell element bending rigidity
d	Z shape stent wire diameter
Δ	Deflection of planar z shape stent
E	Young's elastic modulus
E_A	Austenite elasticity
E_M	Martensite elasticity
El_r	Residual elongation
El_u	Uniform elongation
ε^L	Transformation strain
ε_V^L	Volumetric transformation strain
F_θ	Total radial force
f_θ	Radial force per unit length
g_k	Relaxation coefficient
H	Z shape stent height
I	Moment of inertia

k_θ	Radial pressure/stiffness
k_{pinch}	Pinch stiffness
L	Z shape stent strut length
λ	Principal stretch
LPS	Lower plateau strength
M	Bending moment
μ	Shear modulus
μ_0	Instantaneous shear modulus
n	Z shape stent number of crowns
v	Poisson's ration
v_A	Austenite Poisson's ratio
v_M	Martensite Poisson's ratio
p	Pressure
ρ	Density
RRF	Radial resistive force
σ	Stress
σ_L^S	Stress at start of transformation loading
σ_L^E	Stress at end of transformation loading
σ_U^S	Stress at start of transformation unloading
σ_U^E	Stress at end of transformation unloading
σ_{CL}^S	Stress at start of transform stress compression
T	Horizontal force applied at planar z shape stent
T_0	Reference temperature

t	Z shape stent strut thickness
τ_k	Characteristic time
θ	Half of the angle between z shape stent struts
U	Strain energy
UPS	Lower plateau strength
W	Ogden strain energy function
w	Z shape stent strut width

1. Introduction

1.1 Background of neurosurgery and stent

Minimally invasive neuroendoscopy has become a well-accepted neurosurgery technique owing to developments in endoscopic tools and neuronavigation in recent decades. To treat deep-seated brain lesions such as intraparenchymal tumours, minimally invasive neuroendoscopy is preferable to craniotomy, because it causes less damage to the healthy part of patient's brain. Instead of temporarily removing a large section of the skull, as is done in craniotomy surgeries, neuroendoscopy only drills a small hole into the skull, through which neurosurgeons use ultrasonic knives and endoscopes to access and remove tumours. This surgical technique is often assisted by a tubular retractor device (sometimes also called a sheath, a cannula, or simply a tube), that is inserted through the hole to reach the lesion site. Once a hole is drilled into the skull, a retractor and a dilator, which tightly fits inside the retractor, are used in pairs to create a corridor into lesion site (Fig. 1.1 A). After a corridor is created, the dilator is removed, leaving the retractor inside the brain to maintain the corridor for operation (Fig. 1.1 B). The retractor not only provides surgeons with a convenient access portal to the lesion site for the whole duration of surgery but also protects surrounding healthy tissue from surgical trauma (Fig. 1.1 C). In the past few decades, the tubular retractors have undergone modifications to enhance the efficiency of this neurosurgical technique. It has also been commercialised and widely adopted by neurosurgeons, as evidenced by products such as METRx tubular retraction system, BrainPath Endoport system, and ViewSite Brain Access System. However, despite most

literature reporting positive results from using the tubular retractor systems, such devices still have two major drawbacks. Firstly, because of the rigidity and relatively large size of such retractors, they still pose potential damage to surrounding healthy brain tissue, especially when the surgery lasts as long as six hours. Secondly, the long and narrow cylindrical corridor which the rigid retractor creates hinders free movements of surgical instruments. This could make the surgeries more difficult to perform and lead to subtotal resection of tumours in some cases.

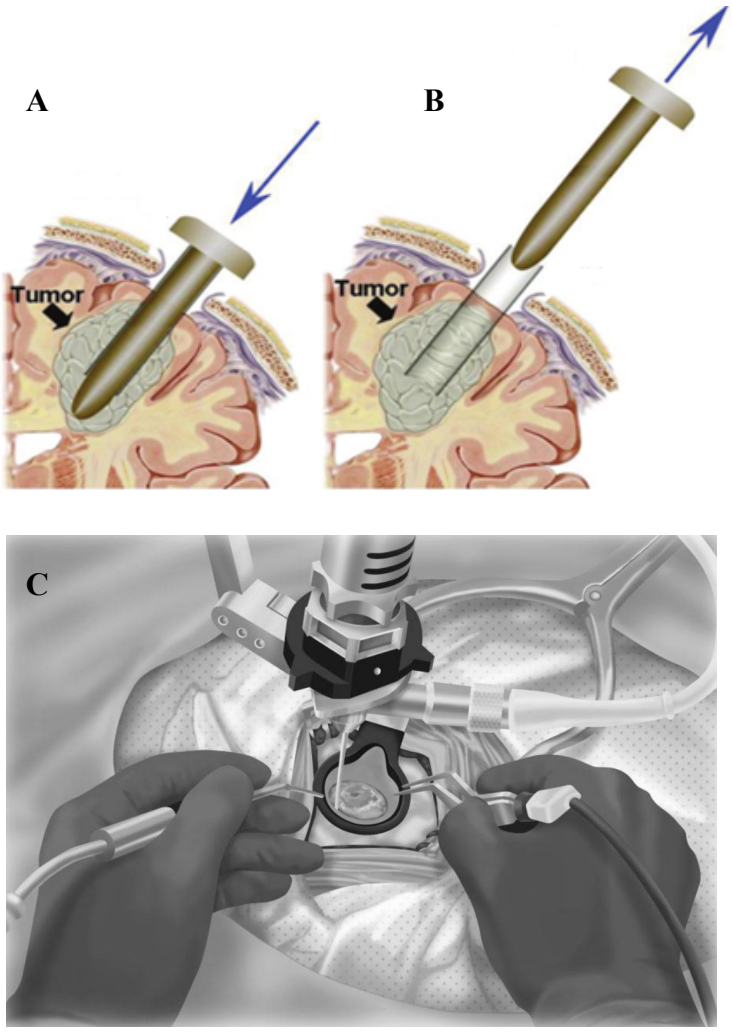

Figure 1.1– (A) Insertion of a retractor paired with a dilator to gain access to a tumour and (B) after withdrawing the dilator, the retractor is left in place to provide a corridor for surgical operation (reproduced from Kassam et al. 2009). (C) A surgeon treating brain lesion through the tubular retractor (reproduced from Akiyama et al. 2015).

Stents, on the other hand, are small, expandable and flexible tubes commonly to be inserted into vessels or passageways to keep them open. For their special ability to bridge gaps in biological tissue, the concept of stents can be borrowed and applied to designing a novel tubular retractor that improves neuroendoscopy. Stents nowadays are classified into two main groups: balloon-expanding stents and self-expanding stents, depending on how they are expanded during deployment. A balloon-expanding stent, mainly made of stainless steel, is manufactured in the crimped state size and expanded by inflating a balloon to plastically deform the stent. A self-expanding stent (Fig. 1.2) is manufactured most often using superelastic nitinol and radially crimped in a sheath of smaller diameter before deployment; once the intended delivery site is reached, the restraining sheath is removed, thus allowing the stent to expand back to its original size. This thesis focuses on self-expanding stent because the superelasticity of nitinol makes it possible to crimp the stent into a much smaller profile before insertion. Moreover, nitinol is less stiff than traditional metal such as stainless steel, thus enables a more flexible design that exerts less pressure on brain tissue.

Figure 1.2 – A self-expanding stent is deployed from its catheter. The left-hand side of the stent is deployed and self-expands back to its original diameter while the right-hand side of the stent is still crimped inside the catheter (reproduced from Blockwise Engineering).

1.2 Aim and scope

In light of inadequacies in current neuroendoscopy techniques and inspired by self-expanding stents, this thesis applies deployable structure principles and proposes a novel self-expanding stent retractor (SESR) system to access lesions located deep inside patient's brain. The aim is to develop a retractor that not only provides an access corridor but also reduces injury to surrounding tissue. As illustrated in the schematic drawings in Fig. 1.3, the self-expanding stent retractor would first be compressed and confined in a thin outer sheath and then inserted into the brain as the dilator penetrates. When inside the brain, the outer sheath would be extracted to deploy the retractor and allowing it to expand. Once the retractor fully self-expands to a desirable diameter, the dilator is also extracted, eventually creating a clear corridor to the lesion site.

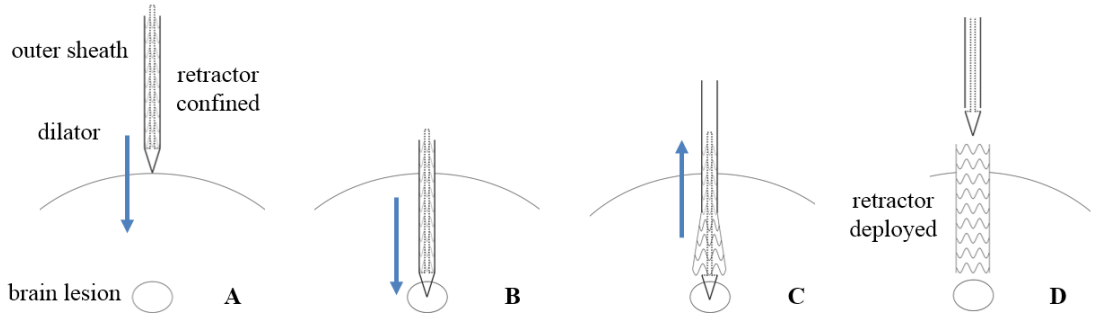

Figure 1.3 – (A) The retractor is confined inside the outer sheath, about to be inserted into patient's brain. (B) The dilator penetrates and the retractor is delivered to the desired location. (C) The outer sheath is slowly removed, deploying the retractor. (D) The retractor is fully deployed, creating a flexible corridor to the lesion site.

The self-expanding stent retractor would have the following advantages over existing rigid retractors. First, the retractor would be of a smaller size so that damage is minimised during insertion, while sufficient surgical space is still ensured as the retractor expands to a desirable diameter once inside the brain. This strategy of inserting a thinner

retractor and then expanding it inside the brain tissue is also more sensible when considering the orientation of brain fibre tracts (Fig. 1.4). The thinner retractor could be inserted into the gaps between fibre tracts without causing significant damage to axons. Secondly, the retractor would have an optimal radial pressure to minimise pressure exerted on brain tissue. It would be designed in such way that the stents will be strong enough to guarantee expansion to a required diameter, while the covering layer would be very soft to minimise the chance of secondary retraction injury during surgery and only act as an insulator that protects healthy tissue from surgical instruments. Thirdly, the deployed shape of retractor would be programmable and flexible, catering to the needs of specific surgery and promising a larger range of movements for the surgical instruments operating within the access corridor.

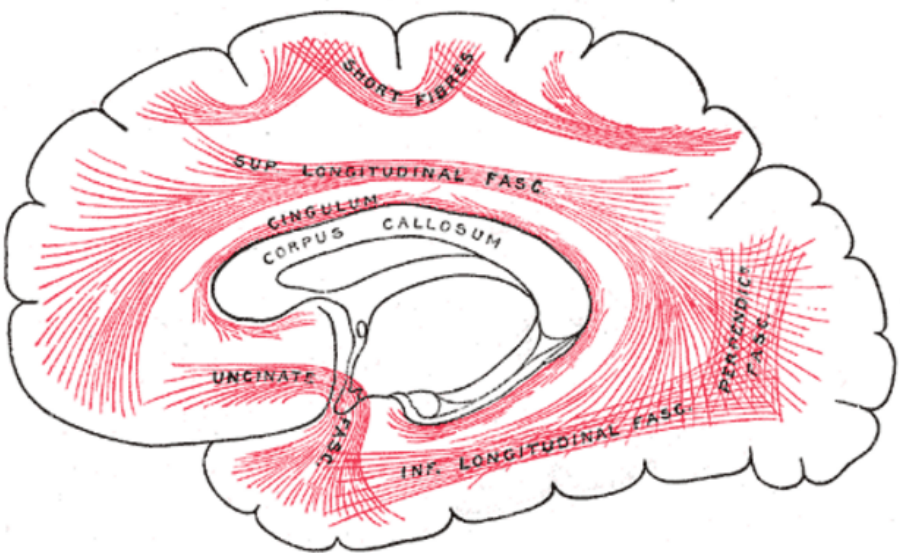

Figure 1.4 – Diagram showing principal white fibres tracts in the cerebrum (reproduced from Standring 2005).

1.3 Layout

This thesis consists of four main chapters. Chapter 2 reviews previous work that is relevant to this study. Firstly, the evolution of neuroendoscopy techniques and devices for treating deep brain lesions is briefly reviewed to explain the motivation of this project and demonstrate the need for developing a better access device. Next, brain tissue properties, special characteristics of human brains, injury criteria of brain tissue, and finite element methods and experimental methods are thoroughly reviewed to better understand the medium in which the retractor will be used. Finally, development and application of stents, self-expanding stents and stent grafts, the superelastic material property of nitinol and finite element and experimental modelling approaches are reviewed.

Chapter 3 describes the preliminary studies on brain tissue we have done that are essential to developing the self-expanding stent retractor. First, a finite element model of brain tissue phantom is built and validated based on data from the literature. Then two surgical scenarios are analysed using this finite element model. Finally, two experiments are conducted to not only validate the finite element analysis but also demonstrate the capability of experimental methods in terms of evaluating brain tissue injury.

Chapter 4 focuses on the design and analysis of the self-expanding stent retractor. First, the conceptual design of the SESR system is described. A theoretical approach is then taken to find out the range of geometric design of the SESR. Next, finite element models are built to analyse a single z shape stent as well as a SESR; a functional design that can expand to desirable diameter in brain tissue is reached. At the end, prototypes are made and experiments are conducted to validate finite element analysis results and prepare for deployment studies.

Chapter 5 studies the deployment of SESR in brain tissue. Finite element method is used to evaluate, analyse and compare several SESR designs. *In vitro* experiments using agarose gel and the porcine brain is also conducted to validate the finite element model and further prove the design concept. Finally, Chapter 6 concludes the main findings of this study and proposes work to be done in the future.

2. Literature Review

2.1 Current neuroendoscopy techniques and devices

Neurosurgery has come a long way since Mr Rickman J. Godlee performed the first successful resection of a primary brain tumour in 1884. Although his first patient died on the 28th postoperative day, this event had kick-started innovations in the neurosurgical field that were to follow (Kirkpatrick 1984). In early 20th century, Harvey Cushing made early strides toward brain tumour removal by adopting new anaesthetic methods and using the motor-driven suction technique, while Fedor Krause promoted using x-rays routinely for assistance in localising intracranial tumours (Preul 2005). Fast forward a hundred years, advancements in endoscopes, frame-based stereotaxy, and neuronavigation technologies have greatly improved neurosurgeons' ability to remove tumours and at the same time reduce operative risk (Grunert 2013; Di Ieva et al. 2014).

This thesis focuses on endoscope-assisted neurosurgery, sometimes called neuroendoscopy, to treat intracerebral hematomas, putaminal haemorrhage, intraparenchymal tumours, intraventricular tumours, and other lesions located deep inside the brain. Deep-seated brain lesions can be as deep as 5cm underneath the patient's skull, therefore, it is imperative to have a working corridor that not only gives complete access to the lesion site but also protects surrounding healthy tissue. Currently, a typical neuroendoscopy procedure is described in the following. Firstly, planning is done using neuronavigation software packages with images acquired from MRI scans, during which the lesion is located, and an ideal entry point and a safe trajectory are identified. Usually,

a most direct path to the tumour is chosen (or preferred) in the interest of avoiding the eloquent area of cortex and minimising the extent of white matter tract resection. Secondly, the patient undergoes routine neuro-anaesthesia and his or her skull is immobilised with a fixation device. After removing patient's hair and sterilising surrounding area, the neurosurgeon drills a small hole with a diameter of 1cm to 1.5cm at the previously identified ideal entry point and temporarily removes this piece of skull. Then, a specially designed tubular retractor with an internal obturator is progressively inserted into the brain. Once in position, the obturator is removed and the retractor is left inside to maintain the corridor for operation. The endoscope is then introduced through the retractor to inspect and confirm the correct position. Endoscopes used for this kind of surgery have outer diameters of less than 4mm and angles of views ranging from 0 to 70 degrees to enable vision on any corner of the surgical field and avoid unnecessary interference with other surgical instruments (Sgouros 2014). Finally, ultrasonic knives, suction catheters, and other surgical devices are introduced through the retractor, in parallel to the endoscope, to operate and remove the tumour. Once the intended resection is completed, the retractor is gradually removed with constant endoscopic visualisation so that eventual bleeding at the pathway walls can be observed and controlled.

Neuroendoscopy techniques emerged in the late 1980s. Kelly et al. (1988) used a cylindrical retractor that is attached to a standard stereotaxic frame to help remove intracranial lesions. After drilling a small hole into the skull, they used a retractor with a diameter range of 20mm to 30mm, paired with a dilator that tightly fits inside the retractor, to progressively penetrate through brain tissue and create a corridor into lesion site. Once a target area is reached, the dilator is removed, leaving the retractor inside the brain to maintain the corridor for operation (Fig. 2.1). Although they used microscopes instead of

endoscopes in their operation, their technique in terms of accessing the tumour was indeed innovative and inspired many new techniques and devices to follow (Fig. 2.2). Nishihara et al. (2000) used a 10cm long transparent sheath made of acrylic plastic, paired with a metal stylet to access intracerebral hematomas. Their retractor has an outer diameter of 8mm and an inner diameter of 6mm, which is significantly smaller than the one Kelly used. Moreover, the transparent sheath, together with a 2.7mm non-angled endoscope inserted within it, greatly improved visualisation of the surgical field. Chen et al. (2005) used similar access technique to evacuate putaminal haemorrhage. A 11cm long stainless steel tube with outer and inner diameters of 10mm and 8mm was used to create the corridor, while a 4mm endoscope and a 2.5mm suction tube were inserted through the tube to treat haemorrhage. Kassam et al. (2009) also reported complete resection of intraparenchymal brain tumours using similar access technique. Ogura et al. (2006) introduced a trans-cylinder approach which used a 0.1mm thick transparent polyester film to create the cylindrical surgical route. The polyester film was rolled around a holding needle about 8mm in diameter and 5-7cm in length. After being introduced to target lesion area, the holding needle was removed and the polyester film expanded to 2cm in diameter. The author claimed that surgical route can be changed by tilting the film retractor, while the pressure around the cylinder was always less than 10mmHg during surgical manoeuvres. Waran et al. (2009) introduced an oval-shaped expandable cannula system, which was able to open up using a screw mechanism. The retractor has a 2 × 5mm leading end before being inserted into the brain and can be expanded to yield a viewing window of 16 × 5mm.

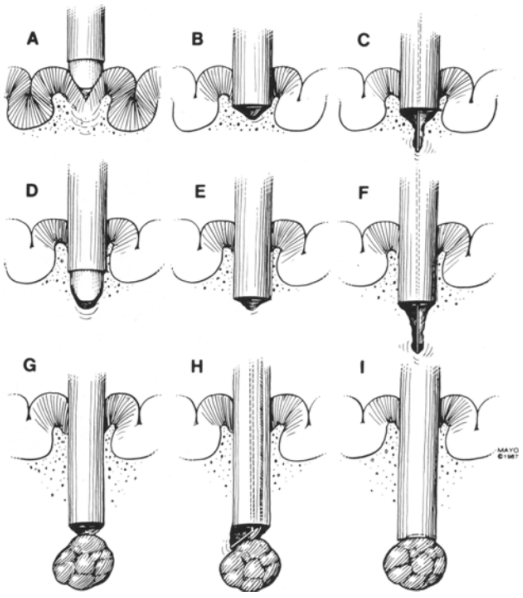

Figure 2.1 – Schematic drawings of a tubular retractor being gradually inserted into the patient's brain to gain access to a tumour (reproduced from Kelly et al. 1988).

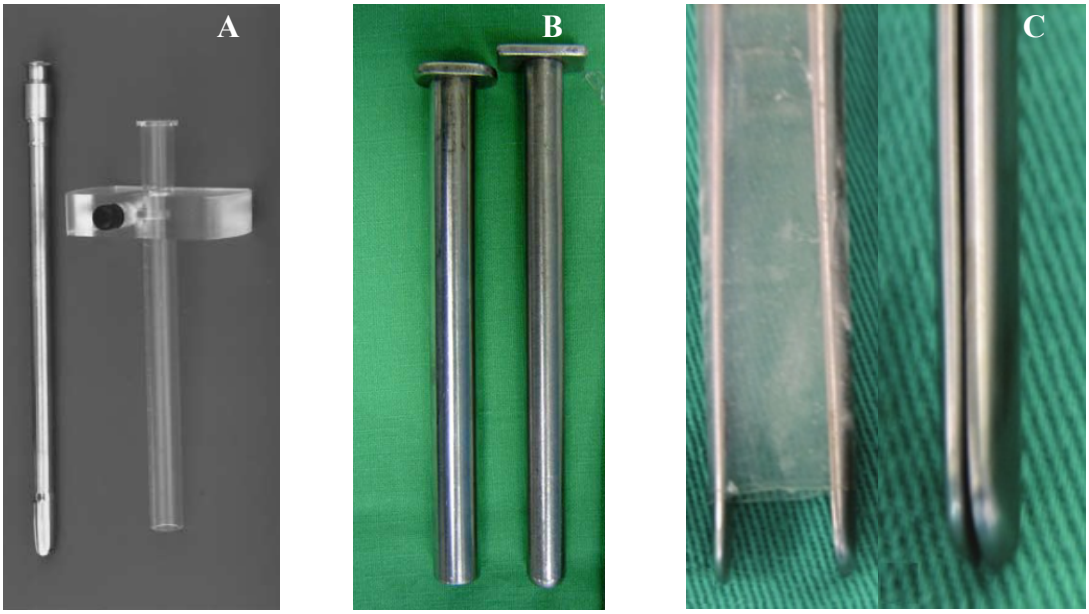

Figure 2.2 – (A) A metal stylet and a transparent acrylic plastic sheath with handle (reproduced from Nishihara et al. 2000). (B) A stainless steel sheath and stylet (reproduced from Chen et al. 2005). (C) An expandable cannula in its open and closed position (reproduced from Waran et al. 2009).

In addition to the specially made devices mentioned above, as reported in literature, commercial products have also emerged in recent years and yield positive

results for treating deep-seated brain lesions (Herrera et al. 2010; Akiyama et al. 2015; Bernardo et al. 2015; Ding et al. 2015; Shoakazemi et al. 2015; Rymarczuk et al. 2015). For example, the NICO BrainPath® (NICO Corporation, Indianapolis, IN, USA) is a set of tubular sheath and obturator devices that provide atraumatic access to the subcortical space (Fig. 2.3). The set consists of a metal obturators and transparent acrylic sheath of various length from 50mm to 75mm. The obturators are designed with atraumatic tips, which minimise tissue damage by displacing brain tissue during advancement to targeted abnormality. There are also hook and holding devices that can be used to keep the sheath in position.

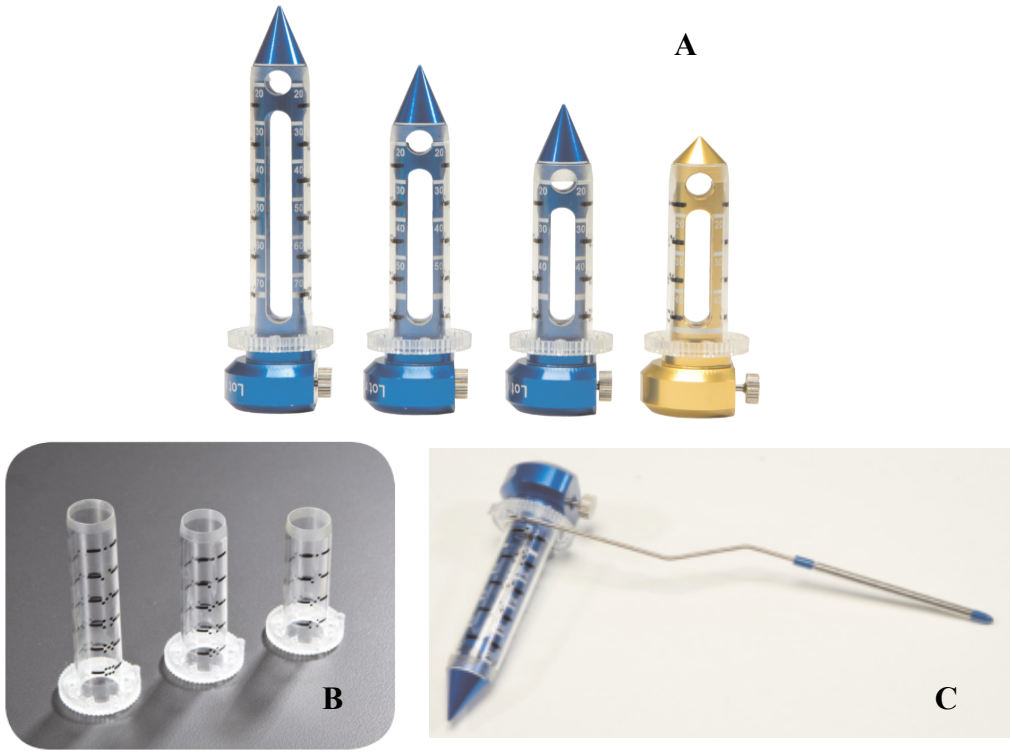

Figure 2.3 – (A) A set of BrainPath® tubular retractors of various length from 50mm to 75mm paired with metal obturator. (B) Tubular retractors are transparent with depth marks. (C) A pair of retractor and obturator attached to NICO Shepherds Hook for better handling during operation (reproduced from NICO Corporation 2014).

ViewSite™ Brain Access System (Vycor Medical, Boca Raton, FL, USA) is another set of such devices (Fig 2.4). Different from BrainPath® products, the

ViewSite™ sheaths have oval-shaped cross-sections. They are also more cone shaped, featuring a little narrower opening at the distal end. They come in four widths of 12mm, 17mm, 21mm and 28mm, as well as three lengths of 3cm, 5cm and 7cm.

Figure 2.4 – (A) A set of ViewSite Brain Access System (VBAS) featuring width from 12mm to 28mm and length from 3cm to 7cm. (B) A closer look shows its modified bevelled tip at the distal end of retractor as well as the introducer. There is also a clip/hook at the other end for better handling during operation (reproduced from Bernardo et al. 2015).

Despite the developments in techniques and positive results reported in the literature, there remains much room for improvement for this deep brain access system because current devices still have two major drawbacks as shown in Fig. 2.5. Firstly, the long and thin cylindrical corridor that the rigid retractor created hinders free movements of endoscopes and other surgical instruments. The transparent and stainless steel retractors may also create glare in the endoscope and distract the surgeon (Singh & Agrawal 2010). Although tilting and moving the retractor is always an option, and sometimes a necessity to reach lesions that extend beyond the scope of the retractor opening, surgeons have to take extra care doing so because excess movements of the retractor will cause even more damage to surrounding tissue. Therefore, using such

retractor techniques not only makes the surgery difficult to perform but also risks subtotal resection of lesions in some cases. Secondly, because of the rigidity and relatively large size of such retractors, they continue to be potentially damaging to surrounding healthy brain tissue. Especially for surgeries that last as long as 6 hours, brain region exposed to retraction is prone to haemorrhagic infarction. White matter damage along the surgical trajectory has been reported (Raza et al. 2011; Recinos et al. 2011), while cytotoxic oedema and cellular damage still happen even when surrounding tissue damage is minimised (Bander et al. 2015). Plaha et al. (2014) argued that brain is a pulsatile organ confined in skull, which is a tight space, therefore although a rigid tubular retractor maintains the access corridor, it exerts constant circumferential pressure on adjacent, already swollen white matter fascicles, which contributes to ischemic injury and retraction injury to surrounding brain. They further pointed out the need of new retractor devices that can not only maintain the access corridor but also ensure that surrounding brain tissue can continue to pulsate freely and maintain adequate perfusion.

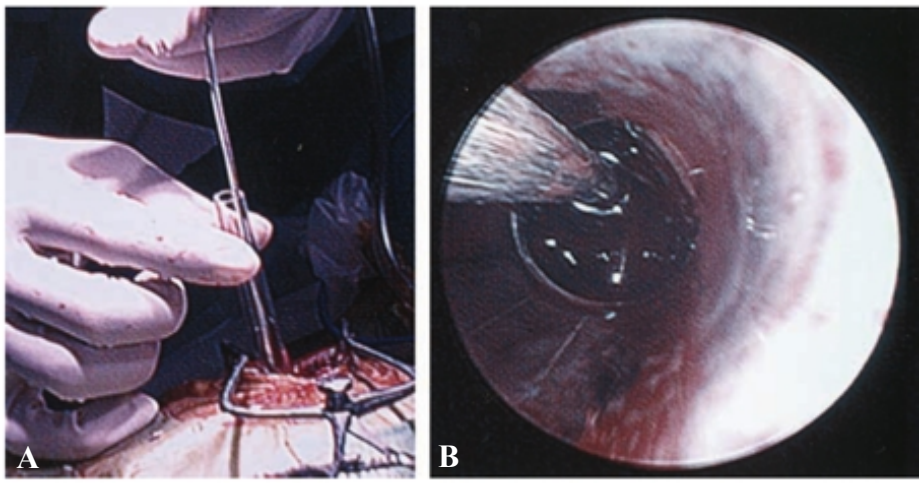

Figure 2.5 – (A) An endoscope being inserted into a patient's brain through the tubular retractor. Movement of the endoscope is obviously limited and it is inevitable to tilt and move around the rigid retractor during operation. (B) Visualisation of the lesion through the retractor. Illumination of the surgical field deep into the brain is poor and there is some glare on the right-hand side of the retractor wall (reproduced from Nishihara et al. 2000).

2.2 The human brain

A thorough understanding of the human brain is required for this study. This section reviews five aspects of the brain that are highly relevant to developing the proposed new self-expanding stent retractor. Section 2.2.1 reviews basic mechanical properties of brain tissue and identifies results from the literature that are applicable to neurosurgery. Section 2.2.2 reviews the interaction between brain tissue and needle. Specifically, the force required to insert a needle into brain tissue and the pressure at the tissue-needle interface are studied to better understand how brain tissue responds to surgical instruments. Section 2.2.3 reviews some special characteristics of the human brain. Brain pulsation and retraction of brain tissue are studied and tissue injury criteria are selected from the literature. Section 2.2.4 reviews previous methods of finite element modelling of brain tissue. Section 2.2.5 reviews histology analysis technique, an experimental method that would be explored to evaluate brain tissue injury.

2.2.1 Mechanical properties of brain tissue

The human brain tissue is a porous, fluid-saturated, almost incompressible, anisotropic nonlinear solid, a multi-component material with viscous contribution to its solid phase deformation (Goriely et al. 2015). The mechanical properties of brain tissue have been rigorously studied in the past fifty years, mostly with the intent of better understanding traumatic brain injury, which is caused by direct or indirect high loading rate impact experienced by skull and brain. Brain tissue response under low loading rate has also been studied to develop computational models for surgical simulations. However, it is a very challenging task to comprehensively characterise human brain tissue because of its

multiphasic nature and regional variation of mechanical responses. To date, there is yet a widely accepted constitutive model for brain tissue that is able to match the full spectrum of the strongly strain rate sensitive, non-linearly viscoelastic behaviour of brain tissue. Thus, different models may be required for different studies depending on the particular topic of interest.

The computational models most suitable for surgical simulations model brain tissue as an isotropic, incompressible, nonlinear viscoelastic and strain rate sensitive solid, with higher stiffness corresponding to higher strain rate. The most popular constitutive model is based on quasilinear viscoelastic theory, which typically uses a hyperelastic model to describe the nonlinear elasticity, combined with a linear viscoelastic relaxation modulus to describe the time-dependent behaviour (Bilston 2011). Although most literature successfully captures the strongly strain-rate sensitive, nonlinear viscoelastic behaviour of brain tissue, it is impossible to integrate all of these data since they are collected from different species, used different experimental setups, subjected to different loading regimes, and tested at different postmortem times. Studies have shown that loading region, age, post-mortem times and sample preparation methods could all affect the mechanical response of brain tissue (van Dommelen et al. 2009). Even at slow loading rates, experimental data still differ due to aforementioned factors. Figure 2.6 A, B, and C shows compilations of mechanical responses of brain tissue under shear, compressive and tension loading, respectively; different loading condition and strain rates produce very different stress vs. strain plots. Figure 2.6 D shows that different loading conditions also result in very different relaxation moduli (Miller et al. 2000; Miller & Chinzei 2002; Hrapko et al. 2006; van Dommelen et al. 2009; Bilston 2011). Nonetheless, data does show consistency in that brain tissue are most stiff in compression, moderately stiff in

tension and least stiff in shear. It also suggests that tissue failure would occur at 100% ~ 200% strain for shear loading, 30% ~ 50% strain for compressive loading, and 20% ~ 60% strain for tensile loading, depending on the loading speed. Although some studies have tested brain tissue to failure, to the author's knowledge, there has not been any research dedicated to studying mechanical failure criteria for brain tissue.

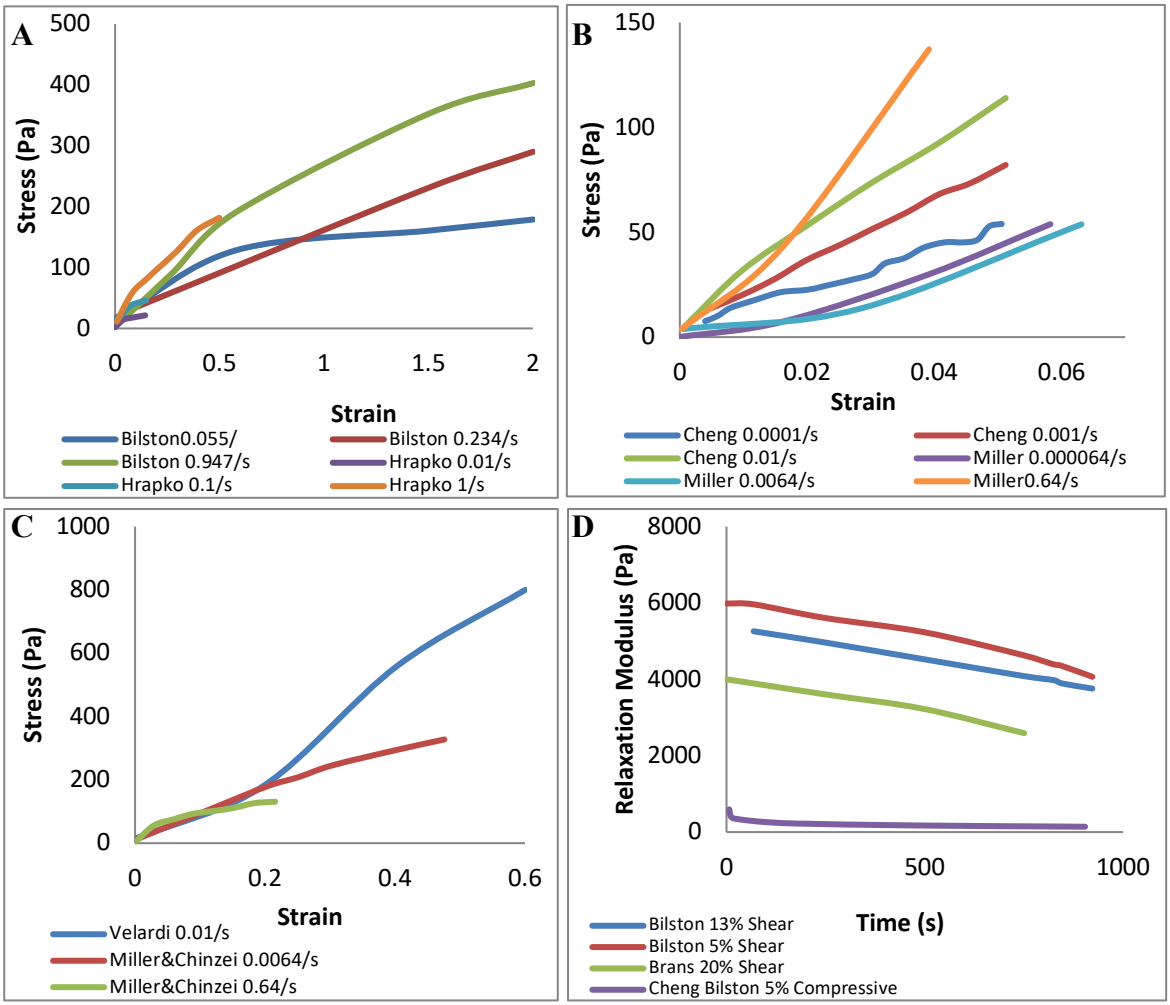

Figure 2.6 – Compilations of loading responses of brain tissue under (A) shear strain, (B) compressive strain, (C) tension strain, and (D) relaxation moduli under different loading conditions.

Miller et al. (1999; 2002) proposed an Ogden-based hyper-viscoelastic model specifically built for surgical procedures based on experimental results of in vitro uniaxial tension and compress tests of porcine brain tissue. It accounts well for brain tissue

responses in both tension and compression, true strain between -30% to 20%, for strain rates ranging over five orders of magnitude. This model has been adopted by other researchers to model human brain deformation in surgical simulations (Gao et al. 2005; Wittek et al. 2008; Ma et al. 2010). The model assumes homogeneity, isotropy and incompressibility for the entire brain. Since the movements of medical instruments during surgery are relatively slow, this model also assumes that the whole process is quasi-static and neglects dynamic components. This model's hyperelastic parameters describe the nonlinear elasticity and its linear viscoelastic relaxation modulus describes the strain rate dependent behaviour. Ogden-type strain energy function, which is suitable for very soft biological tissue, is represented as a convolution integral that describes the relaxation of the shear modulus of brain tissue

$$W = \frac{2}{a^2}\int_0^t \left[\mu(t-\tau)\frac{d}{d\tau}(\lambda_1^\alpha + \lambda_2^\alpha + \lambda_3^\alpha - 3)\right] d\tau\,, \tag{2.1}$$

where W is the potential function, μ is the shear modulus, λ are principal stretches and α is a material coefficient arbitrarily defined. Then, the viscoelastic behaviour is described by Prony series

$$\mu = \mu_0\left[1 - \sum_{k=1}^{n} g_k\left(1 - e^{-\frac{t}{\tau_k}}\right)\right], \tag{2.2}$$

where μ is the time-dependent shear modulus, μ_0 is the instantaneous shear modulus in undeformed state, τ_k is characteristic time and g_k are relaxation coefficients. A set of parameters has also been found out by nonlinearly fitting the tension and compression experimental results; they are listed in Table 2.1.

Recent studies have revealed more useful information on modelling brain tissue for surgical procedures. Efforts have been made towards modelling the inhomogeneity of brain tissue in order to incorporate more anatomical details of the human brain (Gao 2007). Although it is not this study's objective to develop a complex human brain model, apparent structure difference between white and grey matter should be acknowledged (Fig. 2.7).

Table 2.1 – Hyperelastic and viscoelastic parameters of brain tissue.

Hyperelastic parameters	Viscoelastic parameters	
$n = 2$ $\mu_0 = 842Pa$ $\alpha = -4.7$	$k = 1$	$k = 2$
	$\tau_1 = 0.5s$ $g_1 = 0.450$	$\tau_2 = 50s$ $g_2 = 0.365$

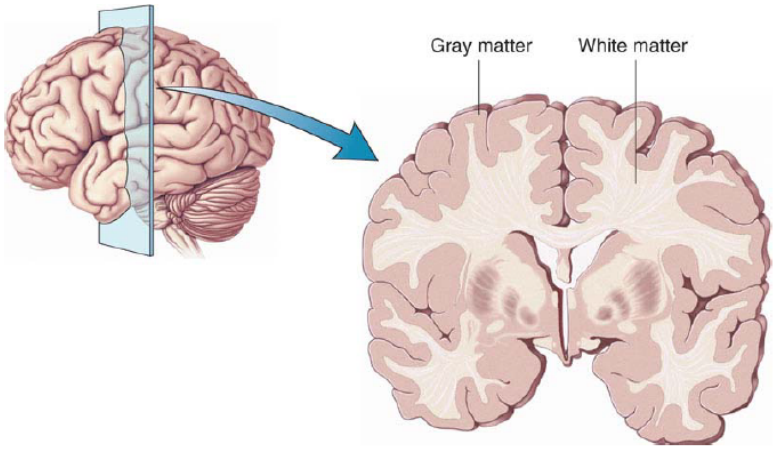

Figure 2.7 – A schematic drawing of a coronal section of human brain showing grey and white matter (reproduced from Gao 2007).

Budday et al. (2015) studied the mechanical properties of grey and white matter through doing in vitro indentation tests on bovine brain tissue and found that white matter, with an average elastic modulus of 1.895 kPa ± 0.592 kPa, was on average 39% stiffer than grey matter, which has an average modulus of 1.389 ± 0.289 kPa. White matter was

also found more viscous than grey matter, responding less rapidly to mechanical loading. Elastic moduli and stress relaxation parameters are shown in Table 2.2. This is an insightful result for developing the self-expanding stent retractor because when accessing lesion as deep as 5cm inside the brain, both white matter and grey matter should be considered.

Table 2.2 – Viscoelastic parameters of white and grey matter brain tissue.

	Elastic modulus	Stress relaxation
White matter	$E = 1.895 \pm 0.592\ kPa$	$\tau_1 = 4.24 \pm 0.59$ s $\tau_2 = 105.74 \pm 50.97$ s
Grey matter	$E = 1.389 \pm 0.289\ kPa$	$\tau_1 = 4.40 \pm 0.22$ s $\tau_2 = 160.74 \pm 18.37$ s

Dommelen et al. (2010) performed indentation tests on porcine brains to study the interregional variations of brain tissue. They used a spherical indenter with a diameter of 2mm to indent for a maximum depth of approximately 0.4mm at different speeds, 0.1mm/s, 0.34mm/s and 1mm/s; the tissue was held for 25 seconds after indentations. They found average moduli for white matter and grey matter during indentation at speed of 0.1mm/s to be 1.01 kPa and 0.752 kPa, which are equivalent to elastic moduli of 3.083 kPa and 2.223 kPa if almost incompressibility of brain tissue is assumed. Their results are 60% stiffer than those reported by Budday et al. However, it is understandable because indentation tests performed by Dommelen et al. were at a much higher loading rates.

While the regional difference is critical in this study, whether to model brain tissue as viscoelastic is debatable. On time scales on the order of milliseconds or seconds, brain tissue is highly sensitive to loading rates, thus the viscoelastic characteristic of brain tissue is critical when modelling traumatic brain injury. However, when modelling a

neurosurgical procedure such as decompressive craniotomy, Weickenmeier et al. (2016) argued that it is reasonable to approximate the brain as purely hyperelastic because surgeries happen on time scale on the order of minutes or hours. By adapting the Mooney-Rivlin hyperelastic parameters reported in literature (Mihai et al. 2015) and assuming cerebral white matter is twice as stiff as cerebral grey matter, they were able to simulate the surgery, identify regions of maximum principal strain and compare different strain based damage criteria.

Mendizabal et al. (2015) tested porcine brain tissue on a rotational rheometer at low strain rates and large strains in an attempt to characterise brain tissue at similar conditions to those during surgical procedures. Using experimental results, their study defined and compared the accuracy and simplicity of three models – linear elastic, hyperelastic and quasi-linear viscoelastic. They found that all three models could be feasible for simulating neurosurgeries, the choice of the model depends on whether strain rate is an influential factor and what the largest strains are during the surgical procedure. If the strain rate is not taken into account and the maximum strains are around 10%, the linear elastic model would be sufficient. If the strains are larger than 10%, the hyperelastic models should be used. On the other hand, if the strain rate is taken into account, quasi-linear viscoelastic model is the best choice. Ideally, if all requirements, i.e., the strain rate, large strain and high accuracy, were to be met, a nonlinear viscoelastic model should be used. However, this would result in increased computational cost. To develop the proposed retractor, we should choose a model that is simple yet accurate enough to describe brain tissue during this specific neuroendoscopy procedure.

2.2.2 Brain tissue – needle interaction

To come up with a set of parameters that best suit the neuroendoscopy procedure in this study, it is important to understand how brain tissue responds to surgical instruments. Due to the lack of information that correlates strain or stress to brain tissue failure, the experimental measurements of the forces needed to insert needles into brain tissue is very valuable information on how to model the step where the proposed retractor is introduced into patient's brain. Moreover, the pressure at tissue-needle interface provides information on how much pressure in the radial direction the retractor would experience once inside patient's brain, which is imperative in designing the proposed retractor.

Jensen et al. (2007) studied the forces required for microelectrodes of 50 μm diameter to penetrate and advance in rabbit's brain. Sharp et al. (2009) studied the cutting force and frictional force of moving a surgical probe, again in micro scale, using rat's brain. For instruments of larger size, Molloy et al. (1990) studied the force required for insertion of a thermoseed, varying from 3mm to 5mm in diameter, into deep brain tissue using dog's brain. Ritter et al. (1998) studied the friction force of moving a 1.9mm diameter straight catheter through both in vitro bovine brain and gelatine. They were able to correlate their data and find out the static and dynamic frictional coefficients. Most relevantly, Howard et al. (1999) measured the force required to move neurosurgical probes through *in vivo* human brain tissue. From a total of 17 measurements, they found that the penetration force required for a 2.5mmmm diameter stainless steel sphere to penetrate into brain tissue is 8±2 grams (0.0784±0.0196 N), while the friction force for a 3mm diameter ventricular catheter to advance in brain tissue is 2.8±0.3 grams/cm (0.0274±0.0029 N/cm). Although past studies have used instruments of different shapes and sizes, different brain samples, and different measurement techniques, the needle force

versus insertion depth plots all follow the same pattern as that of a needle penetrating into soft tissue as shown in Fig. 2.8. The force first increases as the needle tip compresses the soft tissue (region A); once a certain depth is reached, the needle punctures the tissue surface, which results in a sudden drop in the needle force (region B); as the needle keeps advancing, the force continues to increase again (region C). This provides a good guideline of modelling the process of introducing the proposed retractor into the brain.

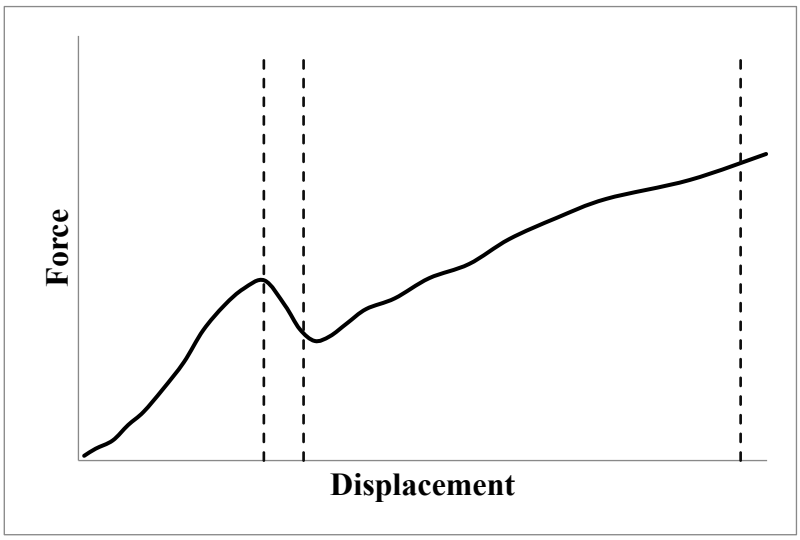

Figure 2.8 – A typical force vs. displacement plot of needle insertion into soft tissue.

Casanova, Carney, and Sarntinoranont (2014a; 2014b) studied effects of needle insertion speed on insertion force, pre-stress, friction stress and tissue injury in rat brains. They used a 32-gauge needle (outer diameter = 0.235mm) to insert into rat brains for 5mm at three different speeds (0.2, 2, and 10mm/s) and used histology analysis to measure the hole left in tissue 10 minutes after the needle is withdrawn. They found that increasing insertion speed results in larger insertion force, large hole size and more tissue damage. Using a hyperelastic model of brain tissue, they were also able to calculate the radial stress at tissue-needle interface from the size of the hole left behind after needle withdrawal, which varies from 0 to 0.485 kPa along the length of needle, with smaller

average values within white matter (0.116 kPa) and larger average values within grey matter (0.301 kPa). Figure 2.9 (A) shows the average radial stress for cortex, external capsule and caudate putamen while Fig. 2.9 (B) shows where these regions are in a rat's brain. This result is very interesting because, despite the fact that white matter is considerably stiffer than grey matter, as reviewed in the previous section, the average radial compressive stress the needle experienced in grey matter region is almost three times greater than that in white matter region. The radial stress at shallower depth is higher than deeper inside brain because in this experiment the brain was well confined inside rat's skull. The boundary conditions on brain tissue play a bigger role than the difference in material property. Therefore, when designing the proposed retractor, care must be taken regarding its radial pressure because once introduced into patient's brain, it would experience varying radial compressive stress along its longitudinal direction.

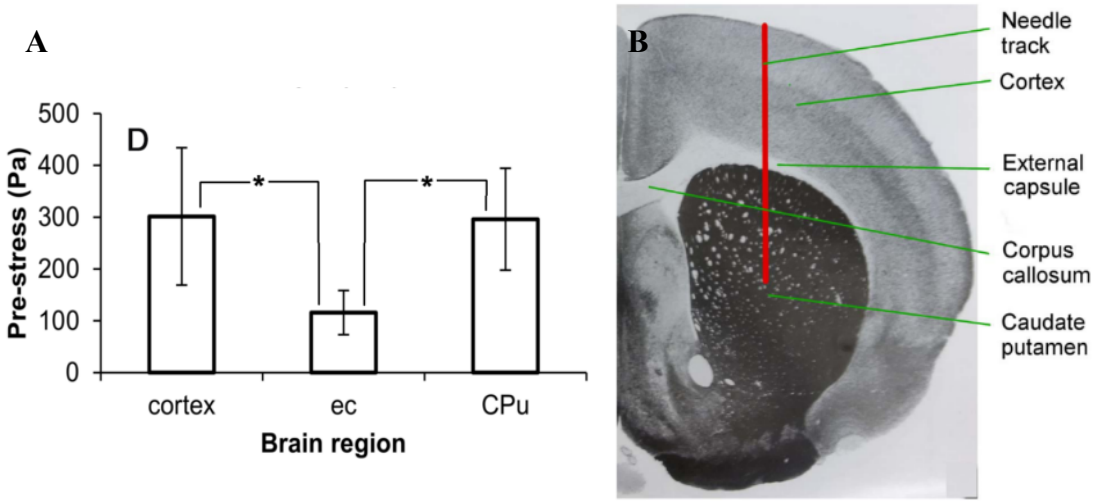

Figure 2.9 – (A) Average radial stress at the tissue-needle interface at different region of the rat's brain. (B) A coronal section of rat's brain showing the cortex, external capsule (ec) and corpus callosum (CPu) region along the needle tract (reproduced from Casanova et al. 2014a).

2.2.3 Pulsation, retraction and injury criteria

Adding to the complexity of mechanical property of brain tissue are some special characteristics of the human brain, which also need to be considered in designing the proposed retractor. First, pulsations of the human brain have been observed since antiquity. The invention of the kymograph transformed the naked eye impressions into records and established the close relationship between the arterial pulse and the waveform of the cerebral movements (Feinsod 2010). Since the brain is enclosed in the fixed skull, any transfer of pulsatility from the arterial walls into the surrounding tissue is felt almost instantaneously everywhere throughout the cranium. Wagshul, Eide, and Madsen (2011) reviewed three primary techniques that have been used to quantify intracranial pulsatility – continuous intracranial pressure (ICP) monitoring, transcranial Doppler ultrasound (TCD), and magnetic resonance imaging (MRI). Among these three techniques, ICP monitoring is the most relevant to our study because it requires placement of a sensor within the skull, either in the brain parenchyma or within a ventricle. Figure 2.10 (A) shows a single intracranial pressure waveform in a time span of 0.5 seconds while Fig 2.10 (B) shows several continuous waves of intracranial pressure; the mean wave amplitude measurements of intracranial pressure, the static pressure is 7.3 mmHg and pulsatile pressure is 6.8 mmHg inside a patient's parenchyma. Therefore, it is clear that during neuroendoscopy procedures, the pressure the retractor experiences is pulsatile instead of static. This statement is also supported by Plaha et al. (2014), who claimed that use of a rigid tubular retractor would hinder pulsatile movements of brain tissue and thus cause damage to surrounding healthy tissue as the operation lasts as long as four hours.

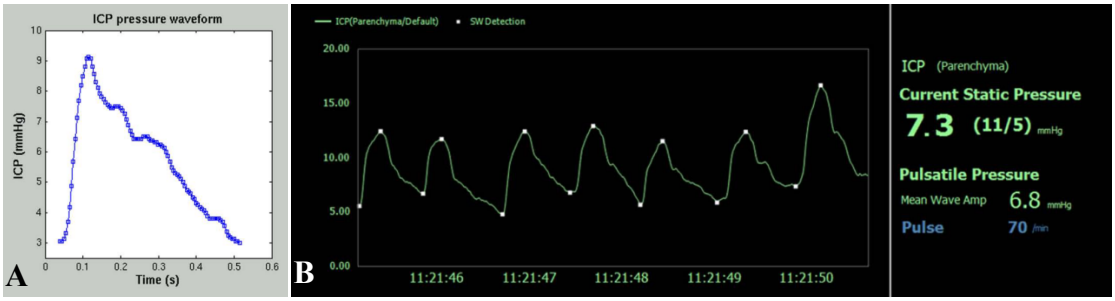

Figure 2.10 – (A) A single pulse wave of brain measured as intracranial pressure. (B) Mean wave amplitude measurements of brain pulsation (reproduced from Wagshul et al. 2011).

Secondly, how brain tissue behaves under retraction and how much retraction is safe should be understood. Back when neuroendoscopy was not yet a well-adopted procedure, craniotomy was performed and brain tissue was held apart by retractor blades, which often causes secondary brain damage during surgery (Zhong et al., 2003). The retractor pressure is transferred to the adjacent brain tissue and subsequently causes deformation and partial or total closure of blood vessels, as well as impaired oxygen delivery to cells. This kind of reduction or cessation of local brain perfusion would result in direct injury to brain tissues and ischemia (Andrews & Bringas, 1993). The severity of this kind of secondary brain damage mainly depends on the brain retraction pressure distribution, retractor blades geometry, vascular pressure and the duration of the retraction. Some animal studies suggest that potential damage occurs when retraction pressure exceed 20mmHg (Albin et al., 1975), while some other studies argue that even with a brain retraction pressure of 20mmHg, there is still a risk of focal ischemic damage if the duration is over 30 minutes (Rosenørn & Diemer, 1982). Although tubular retractors have greatly reduced retraction pressure and Ogura et al. (2006) claimed pressure always less than 10mmHg when using a cylinder retractor, attention still needs to be paid when designing the retractor, with an objective of minimising retraction pressure.

Thirdly, in addition to retraction injury, other brain tissue injury criteria also have to be accounted for. When identifying injury criteria, it is important to distinguish between functional damage and mechanical damage. Functional damage is also considered as injury, such as loss or change of brain tissue cells and breakdown of blood-brain barriers. Whereas mechanical damage affects the mechanical properties of the tissue, such as its ability to support load. It is possible that when the strain in brain tissue is not large enough to cause mechanical damage, functional damage still occurs. Shreiber et al. (1997) conducted *in vivo* experiments on rat's brain and did corresponding finite element studies to find thresholds for mechanical injury to the blood-brain barrier. They found the blood-brain barrier is most sensitive to maximum principle logarithmic strain and breakdown occurs at a strain of 18.8 +/- 3.24%. Bain et al. (2000) conducted experiments on guinea pigs and studied Lagrangian strain based thresholds for morphological damage to white matter. They reported a liberal threshold of 0.34 strain, a conservative threshold of 0.14 strain and an optimal threshold strain criterion of 0.21 strain. Mao et al., (2010) studied neuronal cell loss induced by controlled cortical impact. They reported a linear relationship between the percentage of neuronal loss observed *in vivo* and the maximum principal strain predicted in finite element analysis. As shown in Fig. 2.11, although the maximum principal strain and percentage of neuronal loss have a good linear fit, the regional difference is significant; different regions, cortex, hippocampus, thalamus and cerebellum have different trend lines. Sullivan et al. (2014) conducted experiments on piglet's brain and finite element analysis to study traumatic axonal brain injury taking into account of white matter tract orientation. They reported that the best predictors of traumatic axonal brain injury were tract-oriented strain, strain rate and the product of strain and strain rate.

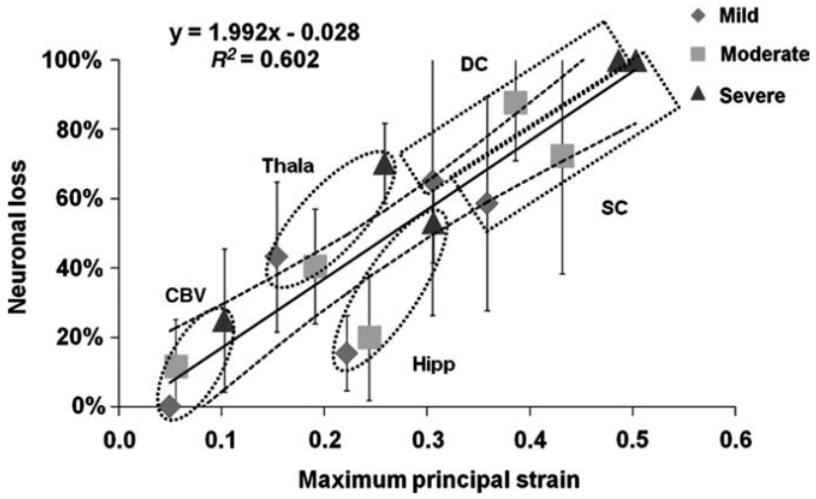

Figure 2.11 – Correlation between neuronal loss and maximum principal strain with standard deviations in different region of rat's brain (reproduced from Mao et al. 2010).

Table 2.3 – Examples of tissue level stress and stain injury criteria from literature.

Study	Injury Type	Injury Criterion	Tolerance Level	Method
Yao et al. (2008)	Severe traumatic brain injury	von Mises stress	14.8+/-4.5 kPa	Finite element model of vehicle accident
Deck et al. (2008)	50% probability of mild diffusive axonal injury	von Mises stress von Mises strain	26 kPa 0.25	Finite element model of vehicle accident
Kleiven (2007)	50% probability of mild diffusive axonal injury	First principle strain	0.26	Finite element model of football collision
Zhang et al. (2004)	50% probability of mild traumatic brain injury	Shear stress	7.8 kPa	Finite element model of football collision
Margulies et al. (1992)	Moderate to severe diffusive axonal injury	Strain	0.05-0.10	Experimental study on baboon and analytical simulation

Wright & Ramesh (2012) reviewed different criteria including pressure, von Mises stress, shear stress, shear strain and maximum principal strain, reported in literature,

as shown in Table. 2.3. To date, the vast majority of brain tissue injury studies are devoted to high impact loadings such as in traumatic brain injury or diffusive axonal injury, while the injury thresholds in surgery scenarios remain unknown. We believe this is because of the difficulties associated with conducting *in vivo* experiments and collecting meaningful data on patients who in the first place need to undergo major surgeries to survive. Priority is always given to treating the lesions and some damage to surrounding healthy tissue is inevitable.

2.2.4 Finite element modelling approaches

Finite element analysis has been widely used by researchers to study the human brain. Different models have been developed for different applications due to the complicated structure and strongly strain rate sensitive nature of brain tissue. For example, when studying traumatic brain injury, detailed brain anatomy structures and viscoelastic material property are often used, whereas for surgical simulations brain is sometimes assumed isotropic and linear elastic material property is used in favour of computing efficiency. In this study, in order to develop and analyse the proposed stent retractor, we first need a simple yet sufficient model of brain tissue. Table 2.4 summarised some representative 3D finite element models of brain tissue for surgical simulations previously reported in literature. Material model choices, mesh elements, purposes of the simulation and validations of model are listed for comparison.

A large amount of existing finite element models is intended for traumatic brain injury when the human head subjects to a sudden external impact and thus the strain rate is extremely large. Though this scenario is very different from surgery, some models of controlled impact could be insightful. Zhang et al. (2001) and Mao et al. (2010) both used a viscoelastic material model of brain tissue and hexahedral mesh in their finite element models to study mild traumatic brain injury and validated their models against either literature or experimental data. The reason for their material model choice is that during controlled cortical impacts, strain rates are usually in range of 100 – 1000 s^{-1}, thus the viscoelasticity of brain tissue has to be accounted for. On the other hand, for neurosurgeries, where strain rate is moderately low at 0.1 – 1 s^{-1}, such as in simulations of tumour growth and gravity induced deformation, the viscoelastic property is sometimes neglected.

Table 2.4 – A summary of finite element models of brain reported in literature.

Study	Material model	Element Type	Purpose of simulation	Validation
Zhang et al. (2001)	Viscoelastic	Hexahedral	Impact: mild traumatic brain injury	Literature
Mao et al. (2010)	Viscoelastic	Hexahedral	Impact: Controlled cortical impact	Experiments
Shreiber et al. (1997)	Hyperelastic	Hexahedral C3D8R	Surgery: Cerebral contusion	Experiments
Castellano-Smith et al. (2001)	Linear elastic	Tetrahedral	Surgery: Gravity induced deformation	MRI images
Clatz et al. (2005)	Linear elastic	Tetrahedral	Surgery: Tumour growth	MRI images
Gao et al. (2005)	Hyper-viscoelastic	Hexahedral and tetrahedral	Surgery: Gravity induced deformation	Literature
Miller et al. (2010)	Hyper-viscoelastic	Hexahedral and tetrahedral	Surgery: Brain shift	MRI images
Weickenmeier et al. (2016)	Hyperelastic	Tetrahedral C3D4H	Surgery: Decompressive craniotomy	MRI images
Wittek et al. (2008)	Hyper-viscoelastic	Tetrahedral	Interaction: Needle insertion force	Experiments
Ma et al. (2010)	Hyperelastic	Tetrahedral C3D10H	Interaction: Indentation of brain tissue	Experiments
Mazumder et al. (2013)	Hyperelastic	Hexahedral	Interaction: Indentation of brain tissue	Experiments
Hamzavi et al. (2013)	Hyperelastic	Hexahedral	Interaction: between neural probe and tissue	N/A
Lehocky et al. (2014)	Hyper-viscoelastic	Tetrahedral C3D10H	Interaction: between needle and tissue	N/A

Castellano-Smith et al. (2001) and Clatz et al. (2005) both defined brain tissue as linear elastic and meshed their brain tissue phantom with tetrahedral elements. Although this simplification sacrifices some accuracy, their models are computationally efficient and validated against literature data or MRI images. Hyperelastic (Shreiber et al. 1997; Weickenmeier et al. 2016) or hyper-viscoelastic (Gao et al. 2005; Miller et al. 2010) definitions of brain tissue are also commonly used in surgical simulations when deformations are large or nonlinear time-dependent behaviour has to be accounted for. In their models, hexahedral, tetrahedral or a combination of hexahedral and tetrahedral elements are used; in general, hexahedral elements would give better results when predicting strain and stress, whereas tetrahedral elements are more computationally efficient and easier to mesh. When complex substructures of the human brain need to be considered, tetrahedral elements are sometimes applied to smooth out the mesh. In addition, finite element models more relevant to this study could be found in simulations of needle insertion force prediction (Wittek et al. 2008), indentations of brain tissue (Ma et al. 2010; Mazumder et al. 2013) and interaction between neural probe and brain tissue (Hamzavi et al. 2013; Lehocky et al. 2014). In these models, either hyperelastic or hyper-viscoelastic material model is used and brain tissue is meshed with hexahedral or tetrahedral elements. They are capable of predicting strain and stress in brain tissue as well as reaction force on surgical tools; some of these finite element models have been validated against experimental data.

It should be noted that all the finite element models reviewed above are based in a Lagrangian framework, where mesh distortion could be a big problem when deformation is large. Furthermore, the lack of existing data on mechanical failure of brain tissue makes it very difficult to model needle insertion, cutting or extreme deformation

of brain tissue. For example, Ma et al. (2010) attempted to study indenter penetration into brain tissue using finite element method. They modelled the brain phantom as hyperelastic and meshed it with 10-node tetrahedron elements and the indenter discrete rigid. Although the indenter force predicted in finite element analysis matches well with experimental measurements, without any yield or failure criteria for brain tissue in the finite element model, the indenter was only able to reach a depth of 9.5mm before elements distortion occurs. Oldfield et al. (2013) overcame the distortion problem and successfully modelled needle insertion into brain phantom by integrating multiple cohesive elements into a finite element mesh in 2D. A crack path is defined before the needle insertion so that cohesive elements could be generated along the crack path. A traction-separation relationship is defined for the cohesive elements to implement damage in the finite element mesh when a needle is inserted. No distortion occurred no matter how deep the needle went; the force vs. displacement plot also closely followed the experimental results. However, this model is not applicable for this study because of two reasons. First, although this finite element model successfully simulates needle insertion into tissue, it is a two-dimensional model which is unable to simulate the three-dimensional expansion of the proposed stent retractor. Secondly, even if it is possible to build a similar 3D model, the predefined crack path implemented with cohesive elements is specifically designed for needle insertion process, which makes it not suitable for expansion. Therefore, another modelling method needs to be sought after.

In recent years, the Coupled-Eulerian-Lagrangian (CEL) method in Abaqus has been used to model extreme deformations, and thus solving the distortion problems happened while using traditional Lagrangian method. The parts that undergo large deformation are modelled as Eulerian while the parts that do not deform significantly are

considered rigid, and thus modelled as Lagrangian. The validity of using this method in solid mechanics is first demonstrated in two of Abaqus Technology Briefs; one modelled a Lagrangian bullet penetrating into Eulerian earth (Dassault Systèmes Simulia Corp. 2009) and another modelled a Lagrangian spud can installing into Eulerian soil (Dassault Systèmes Simulia Corp. 2010), both involving extreme deformations of the Eulerian parts. General contact interaction is used for Eulerian and Lagrangian regions of the model; plastic damage is defined for soil to simulate damage due to complex stress states. The accuracy of the CEL method has also been proved by analysing several benchmark soil mechanics problems (Qiu et al. 2009). Comparing the results of CEL method with those of traditional Lagrangian implicit and explicit analyses, it is claimed that only the CEL method is able to predict the resulting loads at limit state correctly because the Eulerian mesh is not restricted by mesh or element distortion. Although a little accuracy might be sacrificed in the CEL method, this could be made up by using a user subroutine (VUMAT) to better describe the material, hence achieving better accuracy. Gütz et al. (2013) also studied the spud can footing penetration in sand and proved the validity of this method. In terms of soft biological materials like brain tissue, studies have also been done to simulate the needle insertion process. Kataoka et al. (2008) showed that although some degree of accuracy is sacrificed, the CEL method has lots of advantages in simulating soft biological materials because of its versatility and vast potential. Therefore, it is apparent that the brain should be modelled as Eulerian and the retractor as Lagrangian in this project. With all the advantages being discussed, the CEL method does have some limitations (Dassault Systèmes Simulia Corp. 2013). The model is only available in 3D and the only mesh elements available for the Eulerian part are EC3D8R and EC3D8RT. The hyperelastic material property is not recommended because materials flow between

mesh elements. Contact does not support Lagrangian beam, pipe, truss elements, or analytical rigid surfaces. Lagrangian shell elements are supported but often perform poorly due to contact formulations. Hence, solid elements should be used for the Lagrangian part.

After all, the human brain is such a sophisticated biological organ that it would be a simplification to model it as a continuum solid. However, it is beyond the scope of this study to develop a complicated finite element model specifically for neuroendoscopy. Therefore, we decided to borrow data and methods from existing models and use a few different brain tissue phantom models to simulate different surgery scenarios. The finite element results would be metrics of stent retractor performance, instead of conclusive predictions of how brain tissue behave.

2.2.5 Histology analysis

Because of the limited information that finite element method could reveal about biological tissue, experimental methods should also be explored. Histology, which is the study of the microscopic anatomy of tissue, could be very useful in assessing tissue damage due to mechanical stress. Histological analysis is commonly performed by examining tissue by sectioning and staining, followed by examination under microscope and image analysis. De et al. (2007) developed this method to identify stress magnitudes and durations that can be safely applied to different tissue by looking at acute indicators of tissue damage including cellular death and infiltration of inflammatory cells. Using hematoxylin and eosin stain, they were able to visualize the overall changes in morphology and architecture as well as cellular death of liver tissue due to mechanical stress applied by a grasper. More importantly, they made a simple 2D linear elastic finite element model to simulate the grasping and compliment the experimental results. Comparing the finite element analysis results of von Mises stress to a histological section of liver tissue that was vertically compressed by a grasper, they were able to see that the region of stress concentration corresponds to the region of increased vascular damage in liver tissue, indicated by red blood cells.

The capability of this histological technique could even beyond showing the morphology changes and cellular death. Another way of assessing the tissue damage could be through evaluating how well wounds heal. There are two types of scarring tissue forming in the lesion site after traumatic brain injury, the glial scar and fibrotic scar. They are both considered as major impediments for axonal regeneration (Kawano et al. 2012). Wang et al (Wang et al. 2007) used glial scar as an indicator of the healing of a stab wound to the rat's cerebral cortex. By staining the glial fibrillary acidic protein (GFAP)

using immunohistochemistry techniques, they were able to visualize the scar formation and quantify the scar size, and thus find out how the stab wound heals.

Although conducting comprehensive histology analysis is also beyond the scope of this thesis, it is important to show that this experimental method can fill the void that finite element analysis has in terms of evaluating brain tissue injury and further, the performance of proposed stent retractor.

2.3 Stents

This section is a detailed background study of self-expanding stents and stent-grafts as well as how to model them using finite element methods. Section 2.3.1 provides an overview of stent design. Material choices, fabrication methods, geometric patterns and especially geometric variations of z-shape stent rings are reviewed. Section 2.3.2 reviews the superelastic material property of nitinol because it is essential in understanding the behaviour of self-expanding stents. Section 2.3.3 reviews some unique mechanical behaviour of self-expanding stents and explains how they are relevant to designing the proposed stent retractor. Finally, Section 2.3.4 reviews and compares finite element modelling approaches for stents and stent-grafts previously reported in the literature.

2.3.1 A survey of stent designs

The origin of the word "stent" is believed to originate from an English dentist called Charles Thomas Stent, who was a pioneer in denture making back in the 19th century (Roguin 2011). Although today the term "stent" is most often used in cardiology, it began as a term for any kind of non-biological support that gives shape or form to biological tissue (Weldon et al. 1966). In the early 20th century, medical devices like tubes, catheters, retention catheters, internal splints, internal struts, and endoprosthesis were all called stents on many occasions, because they shared the common property of bridging gaps in biological tissue. Today, stents are also widely used in many other medical manoeuvres, including plastic surgery, gastroenterology and urology. As mentioned in the first chapter, stents can be categorised into two groups according to their expansion mechanism, the

balloon-expanding stents and the self-expanding stents. Figure 2.12 shows examples of a balloon-expanding stent and a self-expanding stent.

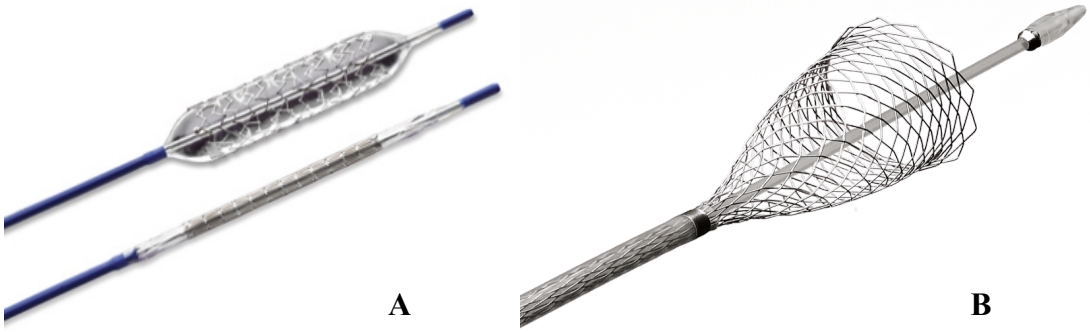

Figure 2.12 – (A) A balloon-expanding stent in its expanded and crimped states (reproduced from Cook Medical 2001). (B) A self-expanding stent is deployed from its catheter (reproduced from Boston Scientific 2014).

A balloon-expanding stent is manufactured in the crimped state size and expanded by inflating a balloon to plastically deform the stent. A self-expanding stent is manufactured, most often using superelastic material such as nitinol, in the deployed state size and then radially crimped into a sheath of smaller diameter; once the intended delivery site is reached, the restraining sheath is removed, thus allowing the stent to expand back to its original size. Figure 2.12 (A) shows a balloon-expanding stent in its crimped and expanded state; the stent is manufactured in the crimped state with smaller diameter and after the inflation of the balloon, the stent is plastically expanded to a much bigger diameter. Figure 2.12 (B) shows a self-expanding stent being deployed from its delivery system, a process very similar to that of the stent graft retractor proposed in this project. After the stent reaches the target site, the outer sheath of the delivery system is slowly extracted. In the bottom left of Fig. 2.12(B), part of the stent is still crimped inside the outer sheath while in the middle of the figure, part of the stent is deployed and allowed to expand. A more detailed classification of stents could be done based on engineering characteristics and design. Based on surveys of stent done by Stoeckel et al. (2002) and

Lally et al. (2006), stents are first categorised by material, raw form of material and fabrication method in Table 2.5. Then categorisation based on common geometric design is summarised in Table 2.6. Finally, stents that consist of individual or sequential rings are categorised based on different connection types in Table 2.7.

Table 2.5 – Categorisations of stents based on material and fabrication.

	Category		Example
Materials	Balloon-expanding stent	Stainless steel (316L)	Majority of balloon-expanding stents
		Tantalum	Medtronic: Wiktor
		Platinum Iridium	AngioDynamics: Angio Stent
		Polymers	Tamai Medical: Igaki-Tamai Stent
	Self-expanding stent	Nitinol	Majority of self-expanding stents
		Cobalt alloy	Boston Scientific: Wallstent
		Full-hard stainless steel	Cook: Z-Stent
Raw material forms	Tube		Majority of stents
	Wire		Boston Scientific: Wallstent
	Sheet		Boston Scientific: NIR
	Ribbon		EndoCare: Horizon Prostatic
Fabrication methods	Laser cutting		Majority of stents
	Photochemical etching		Boston Scientific: NIR
	EDM		Cordis: Palmaz
	Water jet		St. Come: SCS-Z Stent
	Braiding		Boston Scientific: Wallstent
	Knitting		Boston Scientific: Strecker

Table 2.6 – Categorisation based on geometric design (figures from Stoeckel et al. 2002).

Geometry	Example
Coil	InStent EsophaCoil 
Helical spiral	Cordis CrossFlex 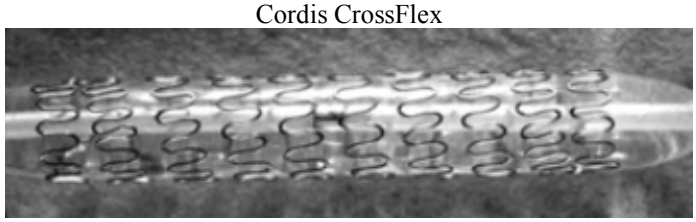
Woven	Boston Scientific Wallstent 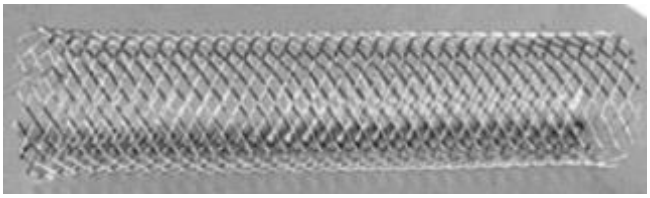
Individual rings	Cook Zenith Stent 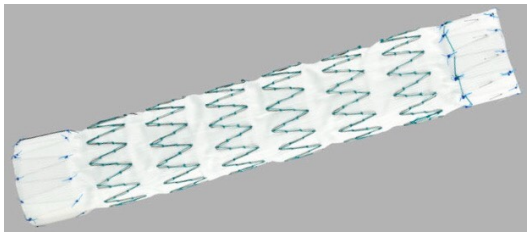
Sequential rings	Medtronic AVE S7 (open cell) 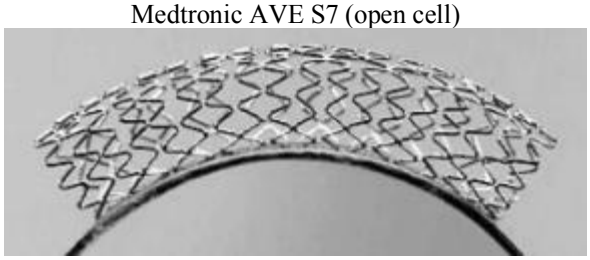
	Boston Scientific NIR (closed cell) 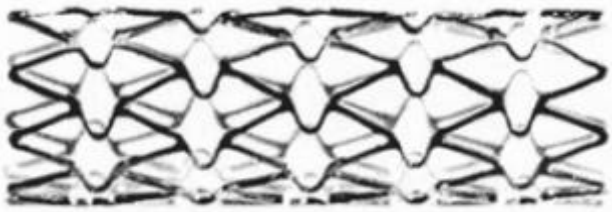

Table 2.7 – Different stent ring connection types (figures from Stoeckel et al. 2002).

Geometry	Connection type	Illustration
Individual rings	Usually sutured or attached to graft	
Sequential rings Open cell	Periodic Peak-Peak Non-flex connections	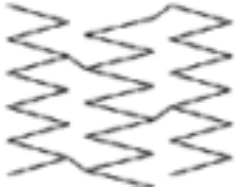
	Periodic Peak-Peak Flex connections	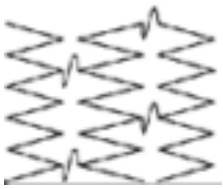
	Peak-Valley connections	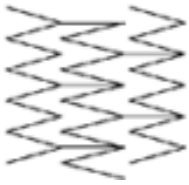
	Midstrut-Midstrut connections	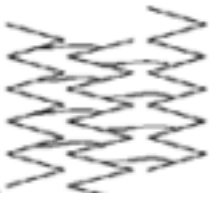
Sequential rings Closed cell	Regular Peak-Peak Non-flex connections	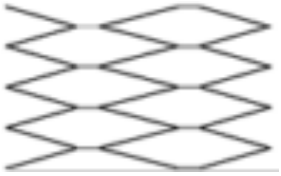
	Regular Peak-Peak Flex connections	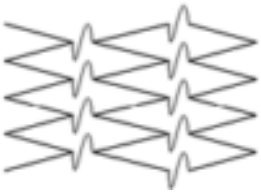
	Regular Peak-Peak Flex/Non-flex connections	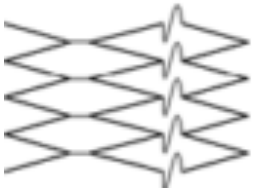

As summarised in Table 2.5, the majority of balloon-expanding stents are made of stainless steel and some alternative materials are tantalum, platinum-iridium and polymers. Balloon-expanding stents undergo plastic deformation through the inflation of a balloon, therefore the ideal material for these stents has low yield stress and high elastic modulus to ensure minimal recoil. On the other hand, the majority of self-expanding stents are made of nitinol and some alternative materials are cobalt alloy and stainless steel. These materials exhibit large elastic strains, which is necessary for the stents to spring back to their original diameter upon deployment. As for raw material forms and fabrication methods, the most common practice is laser cutting of raw material tubes. Other techniques such as braiding of wires and photochemical etching of sheet are also applied in making Boston Scientific's Wallstent and NIR stent, respectively.

Table 2.6 classifies stent geometries into five main categories, coil, helical spiral, woven, individual rings and sequential rings, and gives an example of each geometric design. First, coil stents are extremely flexible and allow retrieval after implantation. However, they usually have a large profile due to low expansion ratio and their radial strength is limited. Secondly, helical spiral stents, similar to coil stents, are generally very flexible but lack longitudinal support. They subject to elongation and compression during delivery and often have irregular shape after deployment. Thirdly, woven stents often provide excellent coverage and their radial strength can vary in a wide range by altering geometric dimensions. While coil and helical spiral stents are usually self-expanding stents, woven stents can be either balloon-expanding or self-expanding. Fourthly, individual rings are z-shaped stents that commonly sutured or attached to grafts to provide radial support. Without any connections between stents, they are rarely used alone with grafts. Fifthly, sequential rings usually consist of a series of z-shaped stents that are

connected by bridging elements. Closed cell means that all internal inflexion points of the stents are connected while open cell means that some but not all internal inflexion points are connected.

A detailed list of connection types for individual and sequential rings are listed in Table 2.7. Open cell design may feature periodic peak-peak, peak-valley or midstrut-midstrut connections, while for closed cell design all adjacent peaks are connected. For both open and closed cell designs, connections can be flex, non-flex or a combination of both. Flex connections improve a stent's bending flexibility but may result in a larger profile when crimped, while non-flex connections make a stent harder to bend but allows for a smaller crimped-state profile. While individual rings are connected by the graft that they are sutured onto, sequential rings can be used with or without grafts. Thus it is also important to understand the graft material used to cover stents. As bare metal stents often cause restenosis and peripheral embolism, graft is added to cover the stents, either to the inside or outside of the stent depending on particular device. The two most commonly used materials for graft are polyethene terephthalate (PET) and polytetrafluoroethylene (PTFE) in vascular applications due to their biocompatibility and durability (Jamshidi et al. 2008). PET is composed of long chains of alternating units of glycol and terephthalic acid, while PTFE is chemically composed of carbon chains saturated with fluorine. Mechanical properties of these two materials will be reviewed in the finite element modelling section 2.3.4.

2.3.2 Nitinol

The unique mechanical characteristics of self-expanding stents cannot be fully understood without first understanding the material property of nitinol. Nitinol (NiTi) is a metal alloy of nickel and titanium that exhibit two unique properties: superelasticity and shape memory effect. Despite the wide range of possibilities shape memory effect enables, the superelasticity of nitinol is the most sought-after property in stent design. Owning to its large recoverable strain of up to 8 – 10%, nitinol allows for designs to be realised which were previously impossible due to the plastic deformation of most alloys, such as stainless steel. Figure 2.13 (A) is an example of the loading-unloading curve illustrating the superelastic behaviour of nitinol.

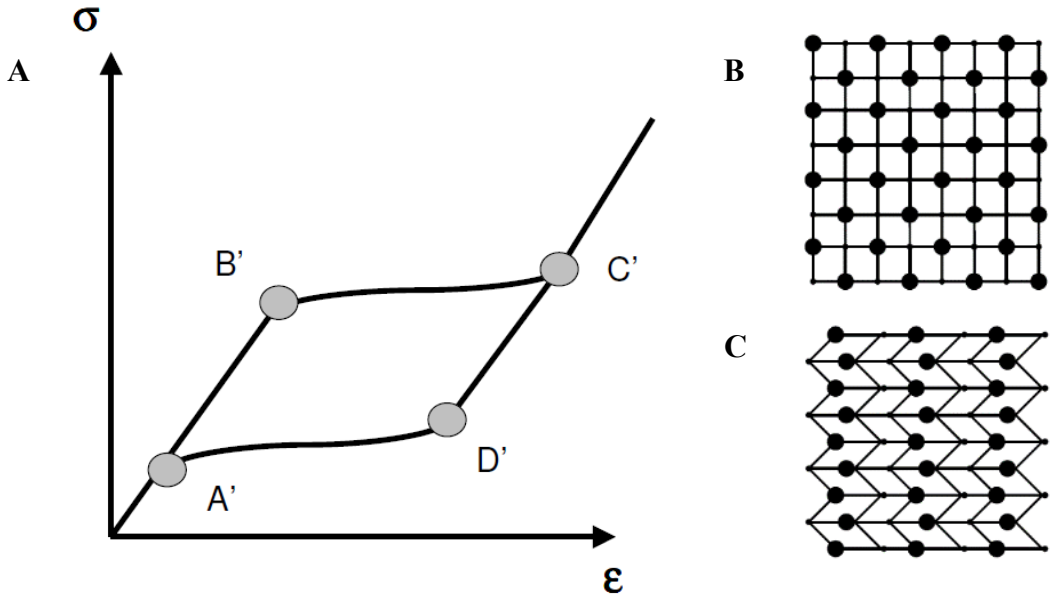

Figure 2.13 – (A) A typical strain-stress plot of nitinol. Crystal structure of nitinol in its (B) austenite phase and (C) martensite phase (reproduced from Conti 2007).

During loading, after an initial linear increase in stress with strain, the superelastic phase of nitinol occurs as the material undergoes stress-induced phase transformation from austenite to martensite (from B' to C'), which leads to a loading plateau with stress

only slightly increasing along with considerable amount of deformation. Once the phase transformation is completed (at point C'), the stress increases more rapidly with increasing strain. During unloading, the stress quickly decreases until the unloading plateau is reached (at point D') and the material starts to transform from martensite back to austenite (from D' to A'). Finally, after the material becomes fully austenitic, the stress decreases linearly again as strain decreases. As shown in Fig 2.13 (B) and (C), in austenite phase microstructure is well defined and has cube shape while in martensite phase the microstructure is defined by a self-accommodating arrangement composed of alternative zig-zag layers.

The exact superelastic behaviour of nitinol, i.e., under how much stress during loading and unloading the phase transformation happens, depends on material composition, which is the percentage of nickel and titanium in the alloy, and austenite finish (A_f) temperature, which is the temperature at which the transformation from martensite to austenite finishes on heating. Within a reasonable range, the alloy producer can control A_f temperature and thus control the material stiffness; the lower the A_f temperature, the more the stress is needed to induce the transformation from austenite to martensite (Stoeckel et al. 2004) For nitinol with a certain A_f temperature, the environment temperature also greatly impacts its mechanical responses. As shown in Fig 2.14, nitinol is tested at different temperatures above its A_f temperature. As the testing temperature increases, the plateau shrinks in width and become less pronounced. If it were to be tested far beyond the A_f temperature, nitinol will have linear elastic material properties (Henderson et al. 2011). Therefore, it is very important to choose and control the A_f temperature during stent design. Since the lower A_f temperature is, the stiffer nitinol would be, an A_f below body temperature should be used to assure that stent will

fully deploy. On the other hand, a very low A_f temperature can lead to a too stiff stent, which exerts unnecessarily high pressure on surrounding tissue. A good practice is choosing nitinol with an A_f close to but below body temperature.

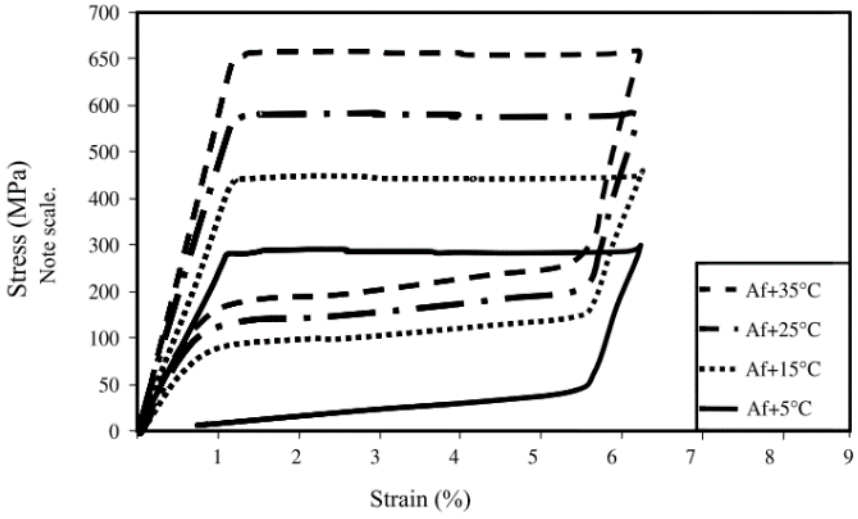

Figure 2.14 – The stress-strain curve of nitinol at different temperature with respect to A_f temperature (reproduced from Henderson et al. 2011).

Although the highly temperature-dependent behaviour of nitinol is a major concern for engineers in designing stents, it could be applied to generate some other innovative solutions. For example, EndoCare Horizon and the D&E Memokath prostatic stents utilise this temperature dependent behaviour for stent retrieval, as prostatic stents are generally temporary and need to be taken out at some point (Fig. 2.15). Cold solution is used to chill the stents so that they become soft and pliable. The radial outward for the stents exert on surrounding tissue decrease and thus can be easily retrieved with a grasping forceps.

Standardised tension test method ASTM F 2516-07 (2006) should be followed when testing nitinol material. Using conventional tensile testing apparatus, nitinol wire or tube should be pulled to 6% strain, then unloaded to less than 7 MPa, then pulled to

failure. As shown in Fig. 2.16, lower plateau strength (LPS), upper plateau strength (UPS), uniform elongation (El_u) and residual elongation (El_r) should be obtained. Tests should be conducted at room temperature 22 ± 2°C; for a certain wire or tube thickness, testing speed should exceed a certain strain rate to prevent significant temperature increase in nitinol. Based on the standard method, Johe (2009) used a fan to improve heat exchange between nitinol specimen and the ambience to allow much higher strain rate. He concluded that with the special setup, strain rate could be two to four times higher than ASTM F 2516-07 suggests without any negative impact on test results.

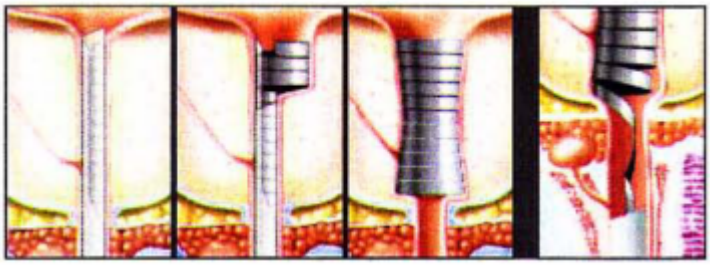

Figure 2.15 – (Left three) EndoCare Horizon stent being deployed in the prostate. (Right) After being chilled by solution, the stent is taken out by forceps (reproduced from Stoeckel et al. 2004).

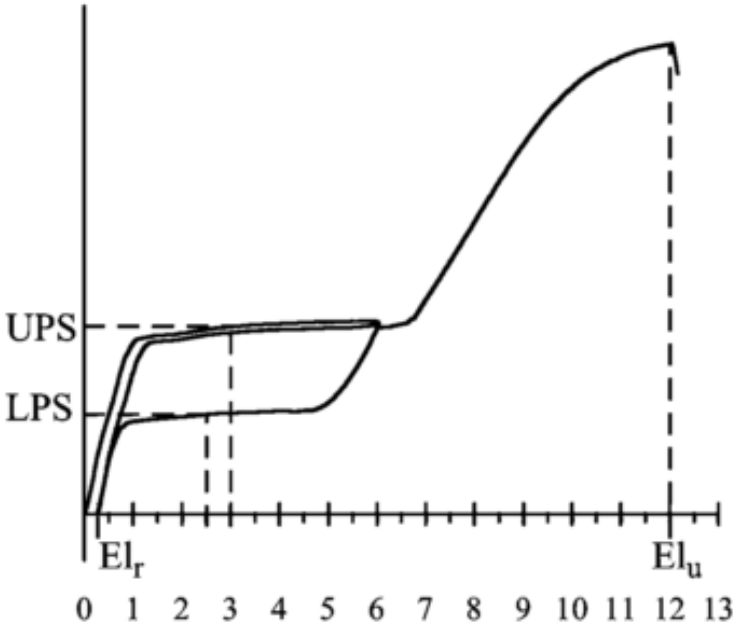

Figure 2.16 – A typical stress-strain plot of nitinol tensile test (reproduced from ASTM 2006).

2.3.3 Self-expanding stents

For a typical self-expanding stent, the most important mechanical design aspects are its ability to expand to the desired size to support artery and its durability, i.e. to withstand pulsatile load of the cardiac cycle and last for years. Thus the fatigue life analysis is imperative for stent design. However, for this study, the proposed stent retractor will be only used for a few hours, rendering the fatigue analysis irrelevant. Therefore, this section only focuses on reviewing self-expanding stents' ability to elastically recover from crimp state and how this property is related to the stents' geometric parameters. Take the stent with open cell sequential z-shape rings in Fig. 2.17 as an example. The stent features 12 crowns and 4 peak-to-peak non-flex connections between units. Zoom into one unit-cell, the strut has length L_s, width w and thickness t.

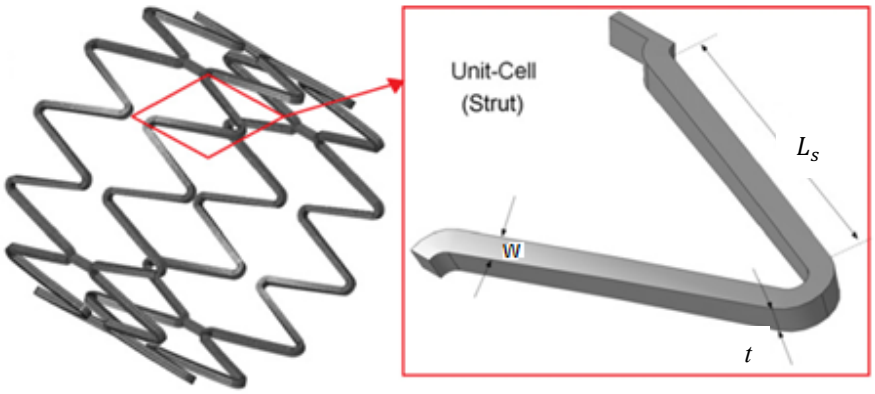

Figure 2.17 – An example of the z-shape stent with open cell sequential rings and a closer look at one unit-cell showing the length (L_s), width (w) and thickness (t) of a strut (reproduced from Azaouzi et al. 2012).

Figure 2.18 shows two common loading modes that stents are subjected to, radial load and pinch load (Duerig et al. 2000). Pressures applied to a thin-walled cylindrical subject, such as a blood vessel or a stent, will result in a circumferential, or radial load of the structure. This pressure and radial stress in the stent is described as

$$\sigma = \frac{p\varphi}{2t}, \tag{2.3}$$

where σ is radial stress, p is pressure, φ is stent outer diameter and t is wall thickness, which is equivalent to stent strut thickness in this case. Then, the radial force per unit length can be described as

$$f_\theta = \frac{F_\theta}{L} = \frac{\sigma t L}{L} = \frac{p\varphi}{2}, \tag{2.4}$$

where L is stent length, F_θ is total radial force and f_θ is radial force per unit length. And finally, the radial stiffness of a stent is defined as the radial force per unit length required to elastically change a stent's diameter and expressed as

$$k_\theta = \frac{f_\theta}{\Delta\varphi}, \tag{2.5}$$

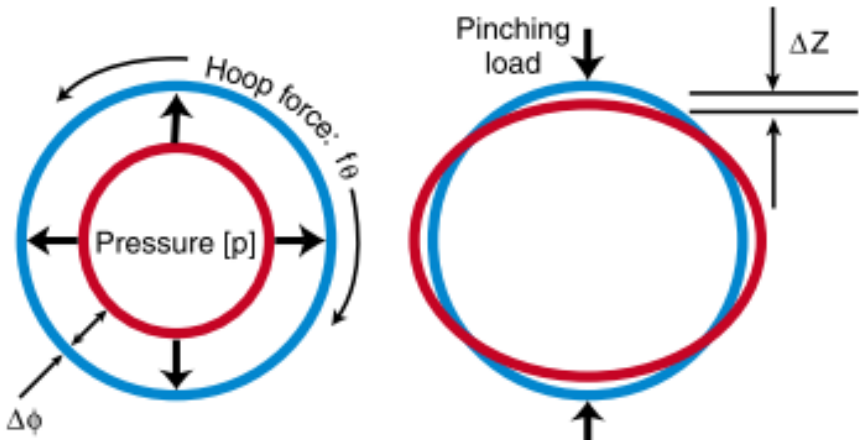

Figure 2.18 – Two most common types of loading for stents are (A) radial and (B) pinch load (reproduced from Duerig et al. 2000).

Using analytical mechanics, we can estimate the radial stiffness of a conventional z-shape stent (Duerig et al. 2000). The change in stent diameter due to an external radial load is related to the stent geometry by

$$\Delta\varphi \propto \frac{p\varphi n L_s^3}{E w^{3t}}, \tag{2.6}$$

where L_s is the length of a strut, w the strut width, t is the thickness of the stent, n is the number of struts around the circumference, and E is the elastic modulus of the material. Following equations 2.3 to 2.6, the radial stiffness per unit length k_θ can be determined and expressed as

$$k_\theta \propto \frac{E w^3 t}{n L_s^3}, \tag{2.7}$$

The relationship between radial stiffness and strut width is cubic while between radial stiffness and strut length is linear. However, if the stent is squeezed by two plates, instead of uniformly radially compressed, it is subjected to a pinching load. The pinch stiffness can be described as

$$k_{pinch} \propto \frac{E w t^3}{n L_s^3}, \tag{2.8}$$

Under pinch loads, stent struts are subjected to out of plane bending and the stent geometry deflection depends on tension, torsion and bending components. Note that the strut width and thickness contribution to pinch stiffness are precisely the opposite of those for radial stiffness. It worth pointing out that if the stent strut has a circular cross-section, for example when the stent is made of nitinol wires instead of being laser cut from nitinol tube, the strut width and thickness are the same and thus the stent geometry contribution to radial stiffness and pinch stiffness will be the same.

It is important to understand that the radial and pinch stiffness estimated by Eq. 2.7 and 2.8 are only good approximations for small deflections within the linear elastic range of the material. Similar estimation has been reported by (P B Snowhill et al. 2001),

who used Castigliano's theorem and the law of Laplace to calculate the theoretical radial force of a typical z-shape stent from its geometric parameters. These estimations are good for summarising trends between stent geometry and its mechanical properties. However, if larger deformations and more complicated geometries are involved, it is necessary to use more advanced techniques such as finite element analysis.

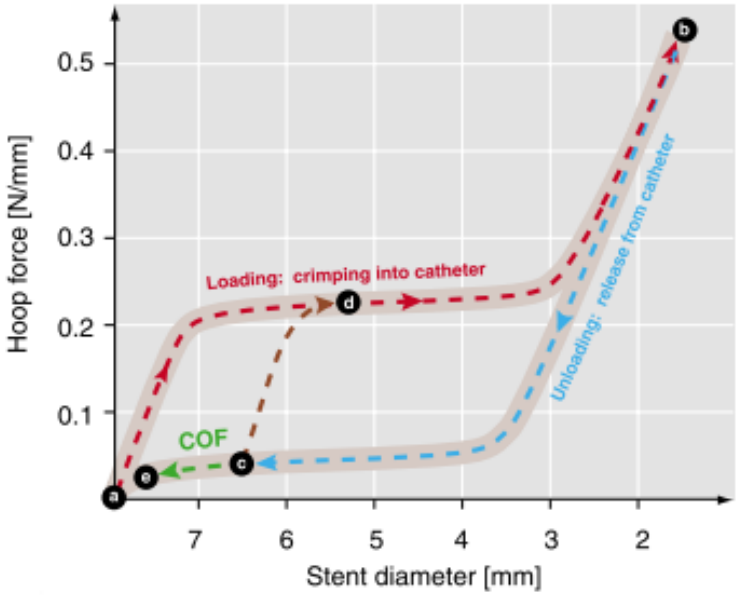

Figure 2.19 – A typical loading-unloading curve of superelastic self-expanding stents plotted as radial force vs stent diameter. Note the force plateaus during loading and unloading (reproduced from Duerig et al. 2000).

Furthermore, the nonlinear, path-dependent, temperature-dependent superelastic material property of nitinol, as reviewed in the previous section, results in a very important feature of self-expanding stent called "biased stiffness". Figure 2.19 uses the loading and unloading of an 8mm diameter self-expanding stent as an example to explain this concept. The loading phase of the stent is plotted in red, the radial force increases as its diameter decreases (from "a" to "b"). The unloading phase is plotted in blue, where radial force decreases as the stent expands back to its original diameter. It is important to see that once the stent diameter returns to about 4mm, the radial force enters a plateau

that it only slightly decreases as the diameter increases. Take point “c” on this plateau as an example. If the stent is to be crimped again, the loading curve will need to follow the brown line to reach point “d”, whereas if the stent is to be further released, the unloading curve will follow the green line to go to point “e”. Thus biased stiffness means that in this particular scenario the stent is much stiffer in loading than in unloading. The chronic outward force (COF), which is the continuing opening force the stent exerts on surrounding tissue, remains low throughout the unloading phase. Meanwhile, the radial resistive force (RRF) generated by the stent to resist being compressed again is much higher. In general, stents usually aim for a design that has as high a radial resistive force as possible to prevent collapsing, with as low a chronic outward force as possible to alleviate unnecessary pressure on biological tissue. For stent retractor design in this study, this biased stiffness concept should be applied so that minimal chronic outward force is exerted on brain tissue while a high radial resistive force ensures the retractor does not collapse after being deployed or during operation.

2.3.4 Finite element modelling approaches

Finite element method has been widely used in recent years to design and analyse stent fatigue life as well as the interaction between stent and artery. Traditionally new products were developed by prototyping and experimenting. This process is often time and money consuming and does not fully reveal potential design flaws. Finite element method not only reduces time and money in product development process but also exposes and solves design flaws in advance of any prototyping. This section focuses on reviewing finite element modelling of stents using commercial software Abaqus/Explicit. Material models for stent and graft are first reviewed. Then common modelling approaches are reviewed and a few representative models are described and compared.

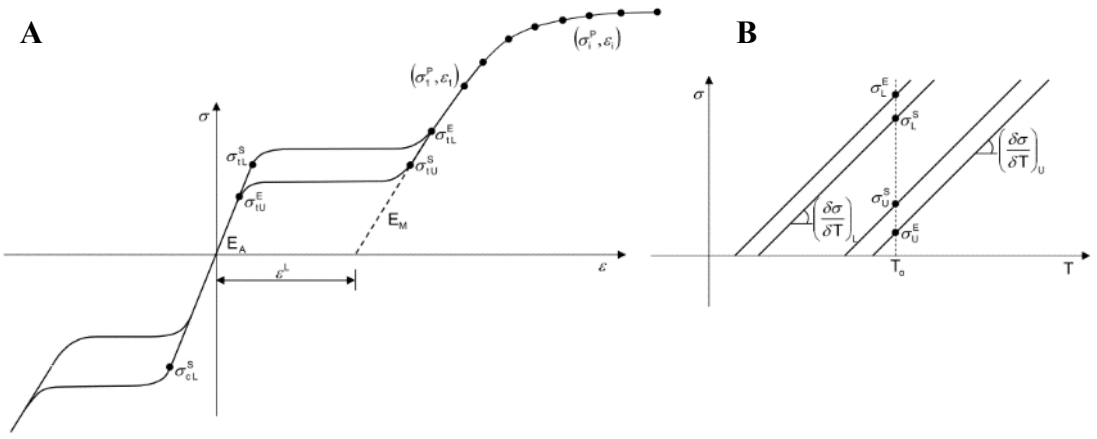

Figure 2.20 – User material subroutine (VUMAT) for nitinol in ABAQUS with all parameters shown on the (A) uniaxial loading – unloading curve and (B) temperature dependent stress behaviour plot (reproduced from Dassault Systèmes Simulia Corp. 2004).

The complex material property of nitinol is hard to model numerically but a user material subroutine (VUMAT) for superelastic material is already available in Abaqus/Explicit. Table 2.8 listed all the input material parameters and a few sets of data reported in literature while Fig. 2.20 explains these parameters on a loading-unloading curve based on uniaxial behaviour. With this subroutine, it is easy to characterise nitinol

in Abaqus using experimental data. Past studies usually conducted their own tests of nitinol wire or tube and extracted input parameters from experimental data to do finite element analysis. The experimental test is necessary because nitinol material property can be largely affected by material composition and austenite finishing temperature, as reviewed in the previous section. It is important to use parameters corresponding to one's own nitinol specimen because as shown in the table, some parameters such as austenite and martensite elasticity reported from different studies differ more than 30%.

Table 2.8 – VUMAT input parameters for nitinol.

VUMAT Input	Symbol	Simulia (2009)	Pelton (2013)	Simulia (2013)
Density	ρ	1.00E-2	6.45E-9	6.45E-9
Dependent variables	-	24	24	24
Austenite elasticity (MPa)	E_A	40000	51437	46728
Austenite Poisson's ratio	ν_A	0.33	0.33	0.33
Martensite elasticity (MPa)	E_M	32000	21588	25199
Martensite Poisson's ratio	ν_A	0.33	0.33	0.33
Transformation strain	ε^L	0.041	0.037	0.0426
ds/dT loading (MPa/°C)	$(\delta\sigma/\delta T)_L$	6.7	5.1	4.5
Start transformation loading (MPa)	σ_L^S	440	494	358.2
End transformation loading (MPa)	σ_L^E	540	557	437.8
Reference temperature	T_0	22	22	0
ds/dT unloading (MPa/°C)	$(\delta\sigma/\delta T)_U$	6.7	5.1	4.5
Start transformation unloading (MPa)	σ_U^S	250	336	124.5
End transformation unloading (MPa)	σ_U^E	140	311	17.75
Start transform stress compression (MPa)	σ_{CL}^S	660	755	537.3
Volumetric transformation strain	ε_V^L	0.041	0	0.0426

While the material definition for superelastic nitinol is rather complicated, the finite element modelling of the graft is usually very simple. A few studies even omitted the graft in their simulations to reduce computational cost because in some cases the stent

behaves the same way with or without the graft. Kleinstreuer et al. (2008) first modelled both PTFE and PET grafts as isotropic linear elastic material and this simplification is supported by De Bock et al. (2012), whose study found that the graft indeed only has a minimal effect on stent mechanical behaviour. However, in some cases when the addition of graft does make a difference, for example when bending a stent graft up to 180°, Demanget et al. (2012) modelled the PET graft as orthotropic linear elastic whose elastic moduli in longitudinal and transversal directions are very different.

Building a finite element model should follow the steps outlined in the standard guide ASTM F2514 – 08 (2011). Two most important aspects of a finite element analysis are accurate presentation of geometry and material properties and proper definition of loading and boundary conditions. Input data should include geometric data, preliminary models, material property tests, material property validation, loading conditions, boundary conditions and special considerations. The analysis should consider finite element choice, mesh requirement, and model validation and verification. The best practice for stent analysis (Dassault Systèmes Simulia Corp. 2011) provides a good guide for building a model using Abaqus. The guide suggests that although beam elements (B31) are used for stents, to reveal more insightful information, solid elements should be used to capture the local peak and strain. The guide compared solid element with incompatible mode C3D8I and with reduced integration C3D8R and concluded that C3D8I is the best option as it does not suffer from hourglassing, has integration points closer to element surface, and allows for a relatively coarse mesh to improve computation efficiency. When large deformations and complicated contacts are involved, ABAQUS/Explicit should be used but kinetic energy and internal energy of the model should be closely monitored to ensure that the analysis is within quasi-static range. Table 2.9 summarised some

representative material and mesh modelling approaches for stent and graft and what kind of analysis the models are intended for.

Table 2.9 – Finite element models of stent and stent grafts reported in the literature.

Study	Stent	Graft	Analysis
Kleinstreuer et al. (2008)	Material: Superelastic nitinol Mesh: C3D8I	Material: Linear elastic PET and PTFE Mesh: C3D8R	Crimping and pulsatile loading to stent grafts to study maximum strain and stress and its interaction with artery
Azaouzi et al. (2012)	Material: Superelastic nitinol Mesh: C3D8I	No graft	Deploying a self-expanding stent inside an artery and applying pulsatile pressure to simulate blood flow
Demanget et al. (2013)	Material: Linear elastic 316L stainless steel or superelastic nitinol Mesh: B31	Material: Linear elastic orthotropic PET or Isotropic PTFE Mesh: S3	Bending up to 180° and pressurisation at 150 mmHg of eight commercial stent grafts to study luminal reduction rate, stress in stent and strain in graft
De Bock et al. (2012)	Material: Superelastic nitinol Mesh: B31	Material: Linear elastic PET Mesh: M3D4	Virtual deployment of stent graft in artery and comparison with experimental result
De Bock et al. (2013)	Material: Superelastic nitinol Mesh: B31	Material: Linear elastic PET Mesh: S3	Mechanical testing of four commercial stents to find loading – unloading force

Kleinstreuer et al. (2008) and Azaouzi et al. (2012) both used solid C3D8I elements to mesh the stents and superelastic user material subroutine to model nitinol and conducted implicit analysis using Abaqus/Standard because the objectives of their studies involved finding peak stress or strain in the stents. They also considered the effect of temperature on nitinol material property and thus applied a temperature field in their

models. On the other hand, Demanget et al. (2013) and De Bock et al. (2013) both used beam B31 elements to mesh the stent despite the recommendations of solid element in best practice guide because their analyses involved complicated geometries and contact behaviours and thus required a lower computational cost. For example, De Bock's model was to deploy a stent-graft and see how it interacts with the artery. The priority of their study was to accurately model the radial force of stent instead of finding peak stress at some particular location. Hall & Kasper (2006) compared different mesh elements: solid C3D8, C3D8R C3D8I, shell S4, S4R and beam B31 elements in modelling stent expansion and concluded that B31 beam element is most computationally efficient by a significant margin while still capable of predicting nearly the same radial force and peak values of stress and strain. Figure 2. 21 shows that the radial force predicted by B31 element mesh is very similar to those by solid element meshes and a coarse beam element mesh does not affect the model's accuracy. In fact, De Bock's model only used 200 ~ 400 B31 elements per stent ring.

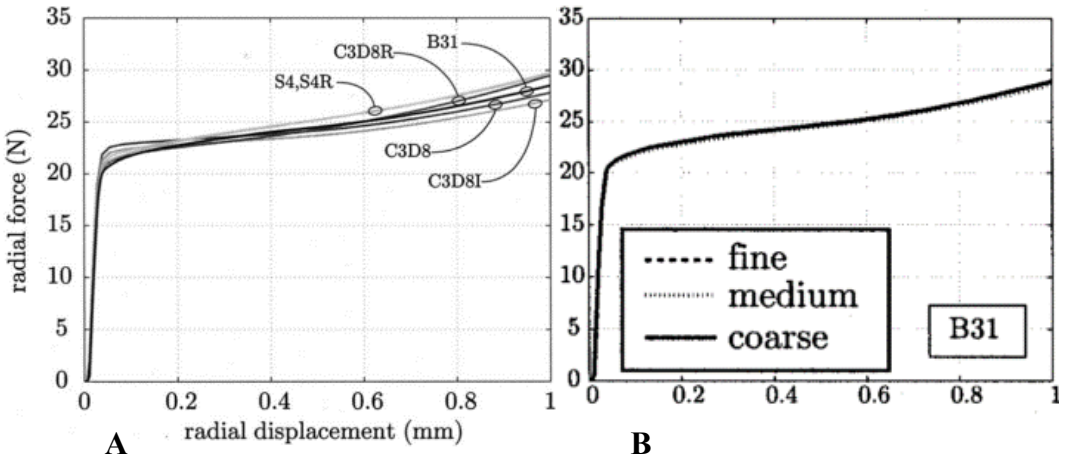

Figure 2.21 – Radial force prediction of a stent using (A) different mesh elements and (B) different B31 beam element mesh density (reproduced from Hall & Kasper 2006).

As for meshing the graft, an earlier study (Kleinstreuer et al. 2008) used solid C3D8R elements while the majority of new studies (Demanget, et al. 2012; De Bock et al. 2013) suggested that triangular shell elements S3 should be used. A very fine mesh (more than 60000 elements in De Bock's study) is necessary to avoid unrealistic excessive deformation in graft. Membrane elements M3D4 (De Bock et al. 2012) have also been used but in terms of contact formulations, they are not as good as shell elements because membrane elements exhibit sharp folds between elements when compressed. It is also worth mentioning that it is common practice to artificially reduce shell thickness of the graft so that it will have negligible bending stiffness; as a compensation, elastic modulus of the graft is artificially increased. According to the Kirchhoff-Love theory, the bending rigidity *D* of a shell element is defined by

$$D = \frac{Et^3}{12(1-v^2)}, \tag{2.9}$$

where E is the elastic modulus, t is the thickness of the shell element and v is the Poisson's ratio. For example, if the elastic modulus is multiplied by a factor of 5, the thickness is divided by a factor of 5 to compensate. This would reduce the bending rigidity to 1/25 of the original unrealistic value for fabric.

3. Brain Tissue Preliminary Studies

This chapter describes the preliminary studies performed on brain tissue in preparation for developing self-expanding stent retractors. It is critical to first study how brain tissue respond to mechanical loads because we need to understand the medium in which the retractor is deployed before moving to the detailed design process. Despite past efforts in studying the mechanical properties of brain tissue, there is no constitutive model that is completely suitable to simulate this surgical scenario. Nor is there a finite element model that can be directly borrowed and used for retractor deployment. Therefore, this thesis looks at the best available data from literature and develops an appropriate finite element model for designing and analysing the novel retractor. Preliminary experiments were also conducted to validate the finite element model as well as exploring what the experimental study could achieve in terms of evaluating retractor performance. The outline of this chapter is as the following. Section 3.1 describes the setup and validation of a finite element model of brain tissue phantom using the Coupled Eulerian Lagrangian method as reviewed in the literature review. The model is validated by comparing simulation results with experimental measurements reported in the literature. Section 3.2 analyses two surgical scenarios, application of rigid retractors and expansion of rigid shells, using the validated finite element model. Section 3.3 describes two preliminary experiments one conducted on porcine brains *in vitro* and the other on mice brains *in vivo*, to validate the finite element analyses and demonstrate how the experimental method is the better way of evaluating brain tissue injury. Section 3.4 discusses the finite element analysis and preliminary experiments results and finally Section 3.5 summarises the main findings of this chapter.

3.1 Finite element model of brain tissue phantom

3.1.1 Finite element model setup

This section describes the finite element model of a brain tissue phantom using the Coupled Eulerian Lagrangian (CEL) method in Abaqus/Explicit. Brain tissue is modelled as Eulerian while surgical tools are modelled as Lagrangian. The setup of the model, including geometry, material properties, mesh and boundary conditions of brain tissue phantom are first explained. The model is used to simulate three different surgical scenarios, insertion of a ventricular catheter, movement of a thermoseed and insertion of customised needles. Simulation results are compared with data reported in literature and experiment results to not only validate the finite element model but also finalise what parameters to use for future analysis.

Instead of modelling a brain tissue with geometric parameters that represent an actual human brain, a simple cubic phantom is modelled. By doing this we assume that although the brain is confined in the skull, which is a tight space, it is much bigger in size compared to surgical tools that the boundary conditions at the brain skull interface do not affect the interaction between brain tissue and surgical tools. For this validation model, the brain tissue phantom is defined in an Eulerian space using volume fraction control. The Eulerian space has a dimension of 30mm x 30mm x 42mm and it is meshed with EC3D8R elements. A reference cuboid with a dimension of 30mm x 30mm x 40mm is placed inside at the bottom of the Eulerian space. Mesh sensitivity study has been performed by the means of indentation test of a sphere with a diameter of 3mm. The maximum average computed Von Mises stress is derived for different level of mesh refinement of the phantom. By refining the mesh, the maximal Von Mises stress

converges. Element of size 0.5mm x 0.5mm x 0.5mm was chosen for the phantom as a good compromise between the accuracy of the solution and the computation time. Brain tissue phantoms that consist of solely white matter and both white and grey matters are considered. Using volume fraction control tool in Abaqus/CAE, the mesh inside the reference cuboid is defined as filled with brain tissue, while the mesh outside the reference cylinder is empty. For the phantom that consists of both white and grey matter, it is divided into two layers with the top 2.5mm layer being grey matter while the rest being white matter (Fischl & Dale 2000). Two boundary conditions are applied at the Eulerian space. All six faces of the space are fixed with no movement or rotations allowed. Eulerian boundary conditions of free inflow and non-reflecting outflow are also applied to all six faces to simulate an infinite domain at the truncated artificial boundary.

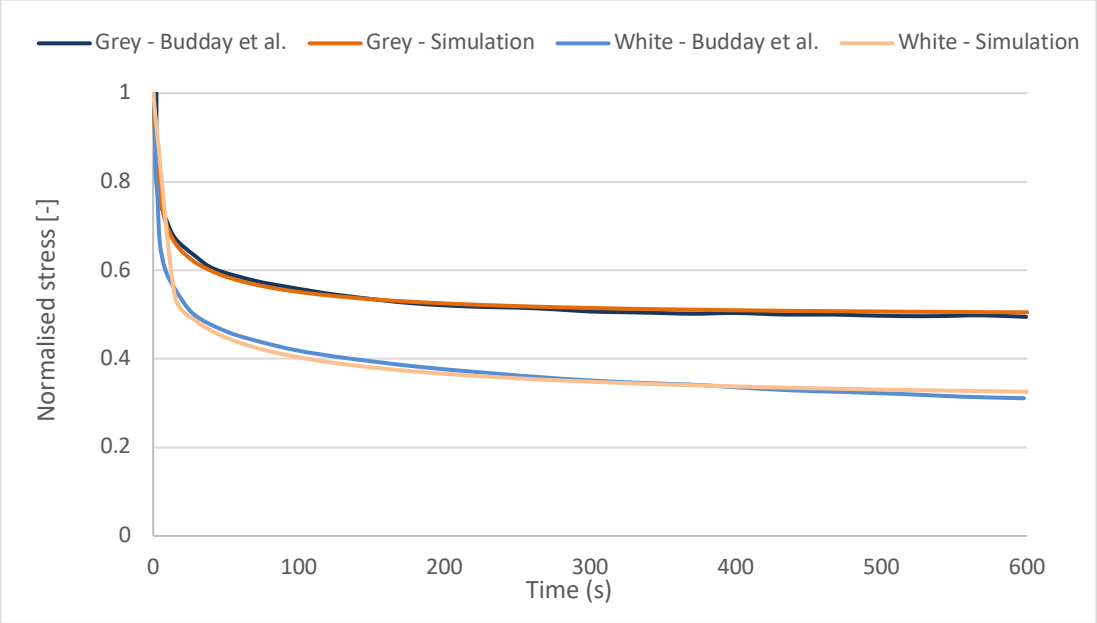

Figure 3.1 – Normalised stress relaxation plots for white and grey matter.

The constitutive material model of the brain tissue is based on experimental results reported by Budday et al. (2015). There are two main reasons that we chose to use data from this particular study. First, their tests were conducted at a slow loading rate that is

similar to surgery scenarios. Secondly, their experiments accounted for the regional variations of brain tissue and provided viscoelastic parameters for both white matter and grey matter.

The averages of reported values are used; the white matter has an elastic modulus of 1.895 kPa, while the grey matter has an elastic modulus of 1.389 kPa. The Poisson ratio of 0.495 is used to capture the almost incompressible behaviour. The viscoelastic parameters in Table 2.2 are evaluated in Abaqus and the normalised stress is used to show that simulation result and literature data match well (Fig. 3.1). It is important to note that this viscoelastic brain tissue model does not have any material failure criteria, meaning that the brain tissue is assumed to be pushed away during penetration, instead of being damaged at a certain stress or strain threshold and no longer support any load.

3..2 Finite element model validation

The brain tissue phantom is then used to simulate two surgery scenarios that were reported in the literature. The first one is an *in vivo* ventricular catheter insertion into the human brain during surgery reported by Howard et al. (1999). The second one is an *in vitro* movement of a thermoseed in canine brain tissue reported by in canine brain tissue Molloy et al. (1990). Simulation results are used to compare with data reported in the literature to validate the finite element model. Furthermore, small adjustments, such as material properties and contact formulations, are also made based on how simulation results compare with literature data.

3.1.2.1 Ventricular catheter insertion

The insertion of a catheter into brain tissue is simulated in Abaqus/Explicit. A typical ventricular catheter, with the same geometry as described in literature, is modelled as a Lagrangian deformable body. It has a diameter of 3mm, a tip length of 4.5mm and a total length of 60mm (Fig. 3.2 A). The length is not a big concern because the insertion depth does not exceed 35mm. The catheter is assigned material property of 316L stainless steel and meshed with C3D4 tetrahedral elements. Since it is much stiffer than brain tissue, rigid body constraint is applied. The reason for not directly modeling the catheter as a rigid body is that in the coupled Eulerian Lagrangian analysis, contact between the Eulerian body and analytical rigid body is not supported. At the beginning of the simulation, the catheter is positioned right above the centre of the brain tissue phantom as shown in Fig. 3.2 B.

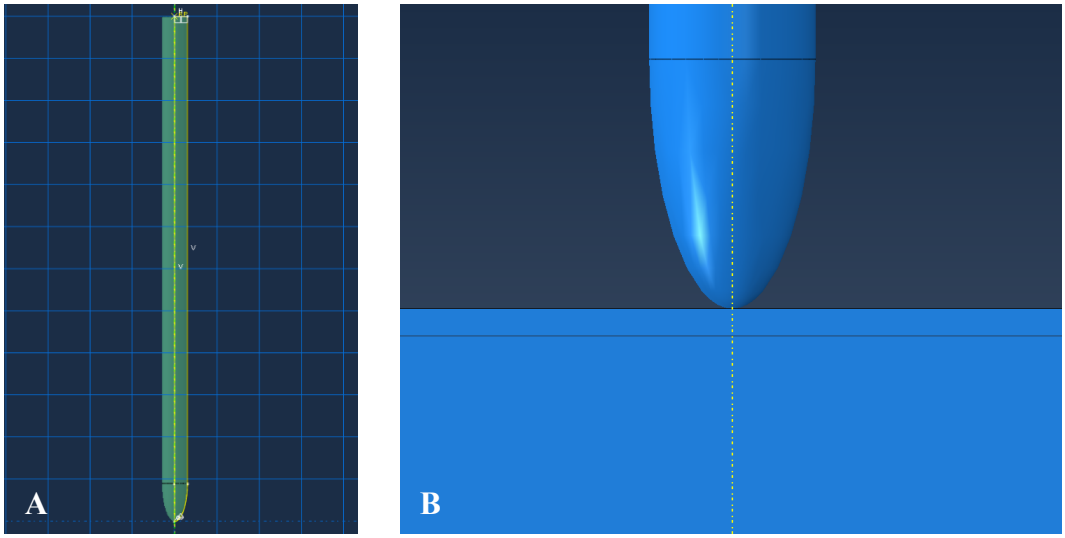

Figure 3.2 – (A) Section sketch showing the geometry of ventricular catheter. (B) The catheter is positioned just above brain tissue phantom before insertion.

The needle moves vertically downward into the brain tissue phantom at a speed of 0.33mm/s for 100s, in the same way as conducted during *in vivo* experiments. The interaction between the catheter and brain tissue is defined using a general contact algorithm with penalty tangential formulation for friction. History output of the reaction

force on the catheter is requested. Internal energy and kinetic energy of the whole model is monitored to ensure kinetic energy is less than 5% of internal energy so that the simulation can be considered quasi-static.

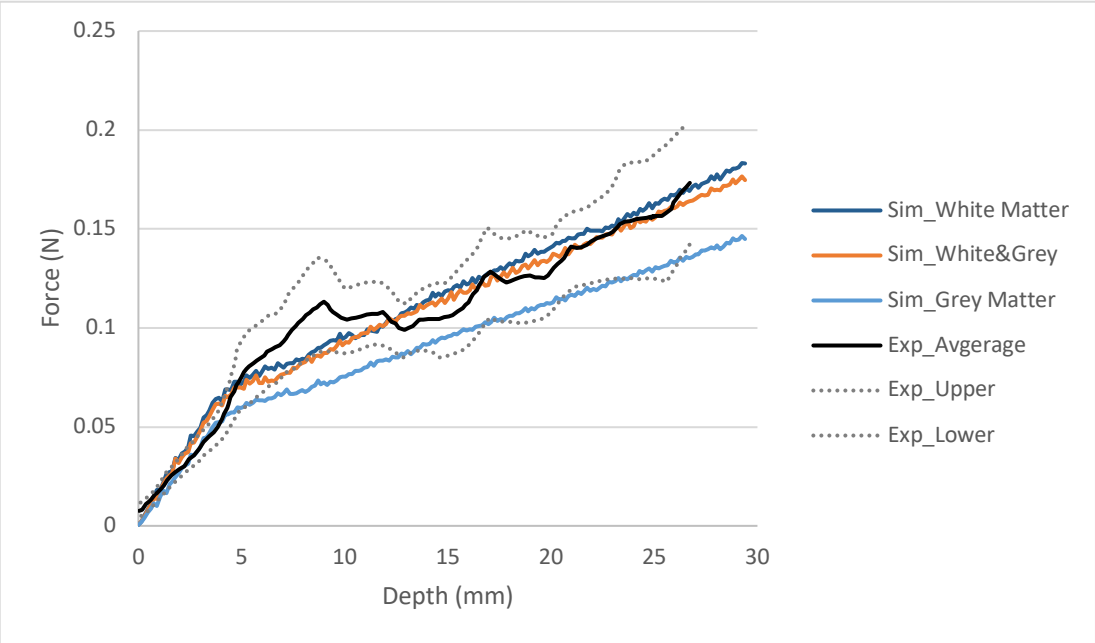

Figure 3.3 – Catheter insertion forces for different brain phantom definitions.

First, three different brain tissue phantoms, purely white matter, purely grey matter and a combination of white and grey matter, are used to find whether the grey matter layer should be considered. As shown in Fig. 3.3, simulated catheter insertion forces are plotted against data reported by Howard et al. (1999); the black solid line is the average value of 17 experiment trails while black dotted lines are upper and lower bounds of experimental measurements. The phantom of purely grey matter results in an insertion force too small, sometimes even smaller than the lower bound of experiment measurement, while the phantom of purely white matter results in an insertion force that closely follows experimental average. The addition of a 2.5mm thick grey matter layer does not change the insertion force very much. This is understandable because, despite the measurable difference in stiffness between grey and white matter, the white matter is

much more present in the phantom than grey matter in terms of volume, thus making the consideration of grey matter insignificant. Therefore, for all subsequent simulations, brain phantom of only white matter is used.

Next, the effect of different friction coefficients between the catheter and brain tissue is explored. Figure 3.4 plots catheter insertion forces into white matter brain tissue phantom for different friction coefficients of 0.1, 0.125, 0.15 and 0.2. Note that the friction coefficient has a big impact on insertion force, as increasing the coefficient from 0.1 to 0.2 would result in a 70.1% increase in peak insertion force at 30mm depth. The friction coefficient of 0.125 provides the best fit with experimental average and thus is used in subsequent simulations.

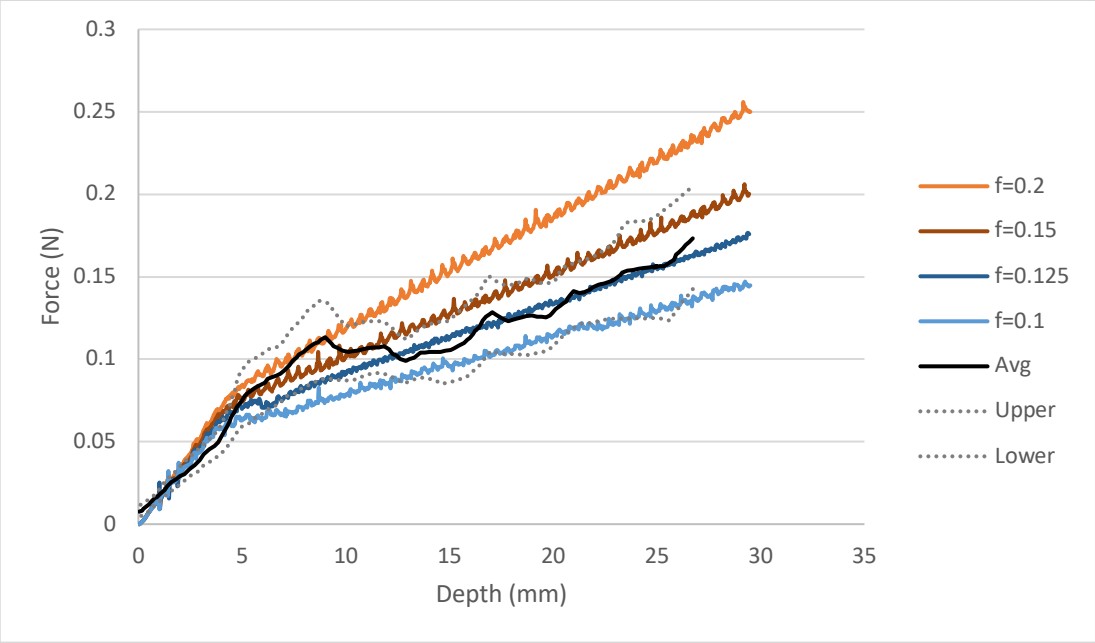

Figure 3.4 – Catheter insertion forces for different friction coefficients.

Finally, to expand on the *in vivo* experiment in literature, different insertion speeds are considered. In three different simulations, the catheter moves into white matter brain tissue phantom at 0.33mm/s, 0.1mm/s, and 3.3mm/s, respectively. The friction coefficient used in these simulations is 0.125. As shown in Fig. 3.5, a higher insertion speed results

in a higher insertion force, which is understandable given the viscoelastic nature of brain tissue, however, the influence is not as significant as the friction coefficient.

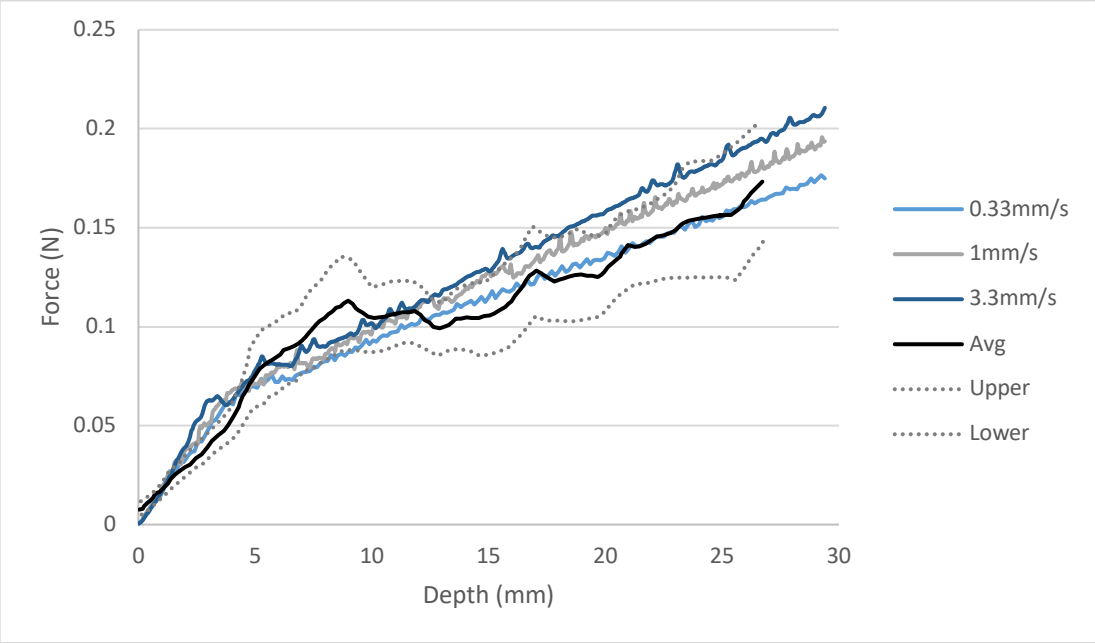

Figure 3.5 – Catheter insertion forces for different insertion speeds.

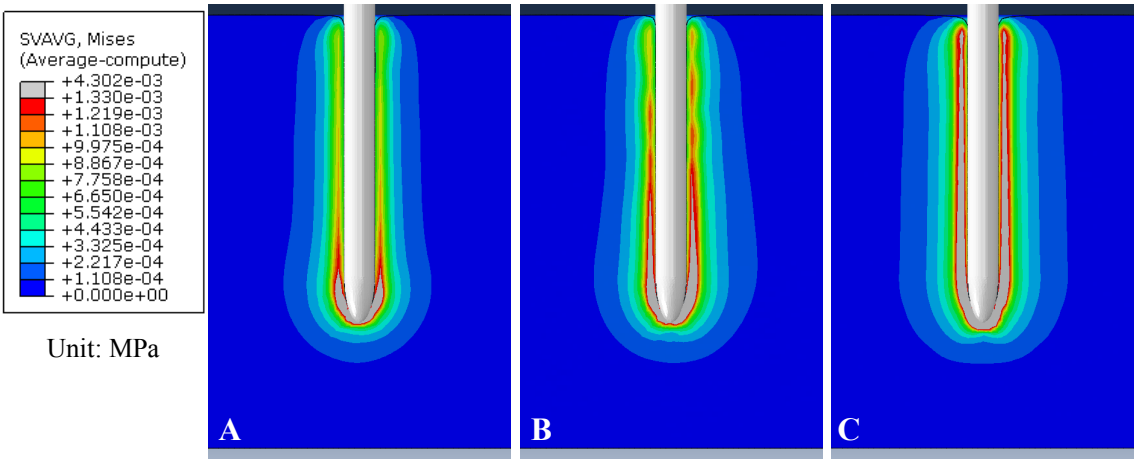

Figure 3.6 – Cross-section view of stress contours of brain tissue phantom for different insertion speeds (A) 0.33mm/s, (B) 1mm/s, and (C) 3.3mm/s.

The stress induced in the brain tissue shows more sensitivity to insertion speed as shown in Fig. 3.6. Average-computed von Mises stress is used and a reference stress of

1.33 kPa is applied to better visualise the stress contour. The grey areas represent regions of the brain under stress over 1.33 kPa, the stress level over which Ogura et al. (2006) claimed to be potentially harmful during neurosurgeries. Peak stresses in brain tissue phantom at the end of simulations are 2.598 kPa, 3.903 kPa and 4.302 kPa for 0.33mm/s, 1mm/s and 3.3mm/s insertions, respectively. Although the increase in peak stress is not significant as the insertion speed increases, there is a notable increasing amount of brain tissue subject to stress over 1.33 kPa.

3.1.2.2 Thermoseed movement

The movements of a thermoseed in brain tissue is then simulated in Abaqus/Explicit. As described in Molloy et al. (1990), the thermoseed is a sphere with a diameter of 3mm. In Abaqus/CAE, this is modelled as a Lagrangian deformable body. It is assigned material property of 316L stainless steel, meshed with C3D4 tetrahedral elements, and applied with rigid body constraint. Brain tissue phantom is considered to consist of purely white matter. At the beginning of the simulation, the thermoseed is positioned right above the centre of the brain tissue phantom. The thermoseed moves vertically downward into the brain tissue phantom at a speed of 0.7mm/s for 30 seconds, and then moves horizontally to the side for 10 seconds. The thermoseed speed is the same as was conducted during *in vitro* experiments. The interaction between thermoseed and brain tissue is defined using general contact algorithm with penalty friction using a coefficient of 0.125. History output of the reaction force on the catheter is requested. Internal energy and kinetic energy of the whole model is monitored to ensure kinetic energy is less than 5% of internal energy so that the simulation can be considered quasi-static. Figure 3.7 shows the stress induced

in the brain tissue due to movements of thermoseed. Average-computed von Mises stress is used and a reference stress of 1.33 kPa is applied to better visualise the stress contour. Peak stress experienced by brain tissue is 2.272 kPa.

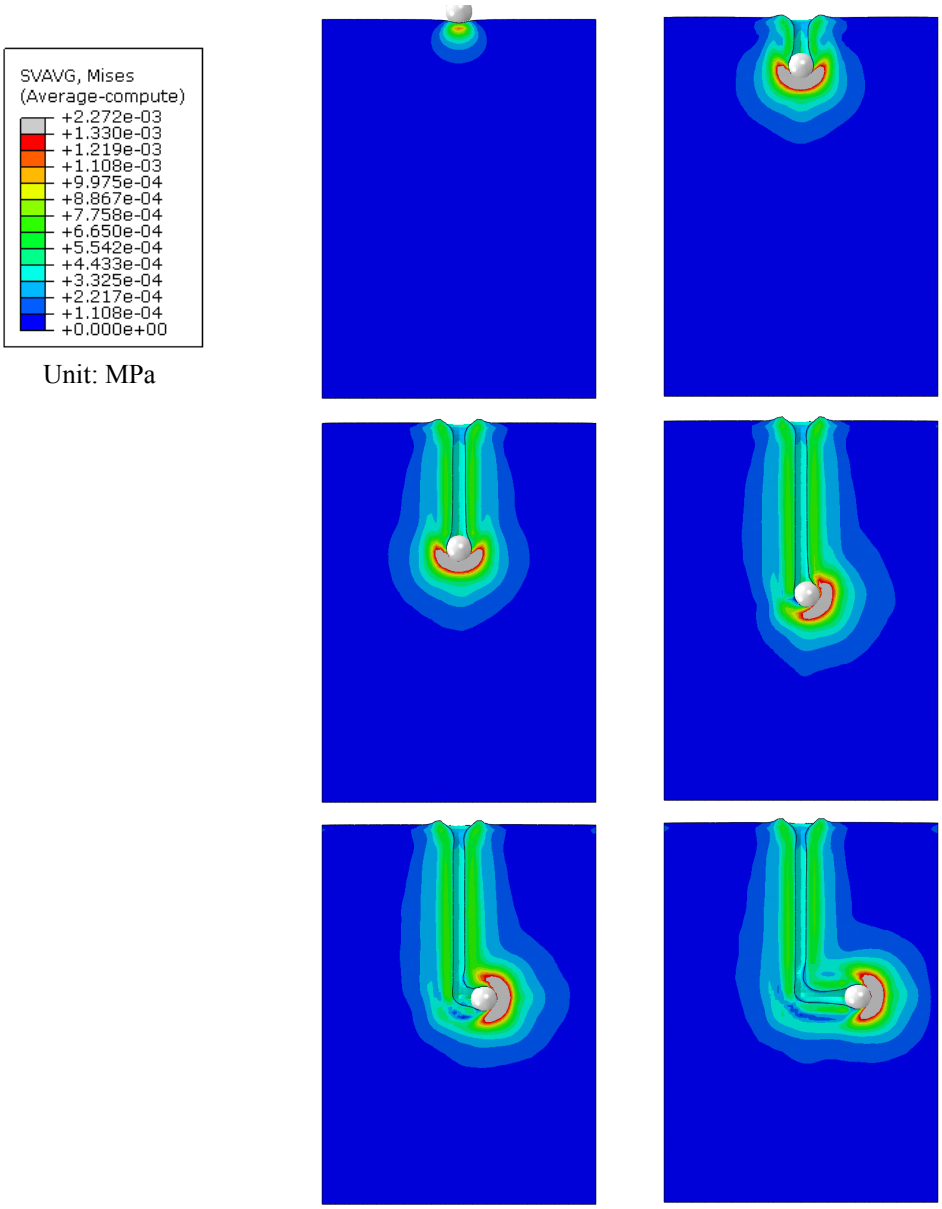

Figure 3.7 – Cross-section view of stress contours of brain tissue phantom as the thermoseed moves first vertically then horizontally inside.

The force required to move the theromseed inside brain tissue agrees well with experimental measurement of 0.074 +/- 0.023N (Molloy et al. 1990). As shown in Fig.

3.8, the peak force reaches 0.09N as the thermoseed moves vertically downward into brain tissue. Once it fully enters the brain tissue, the force decreases and fluctuates around 0.07N. As the horizontal movement starts, the force in vertical direction quickly drops while the force in horizontal direction immediately increases and reached around 0.07N.

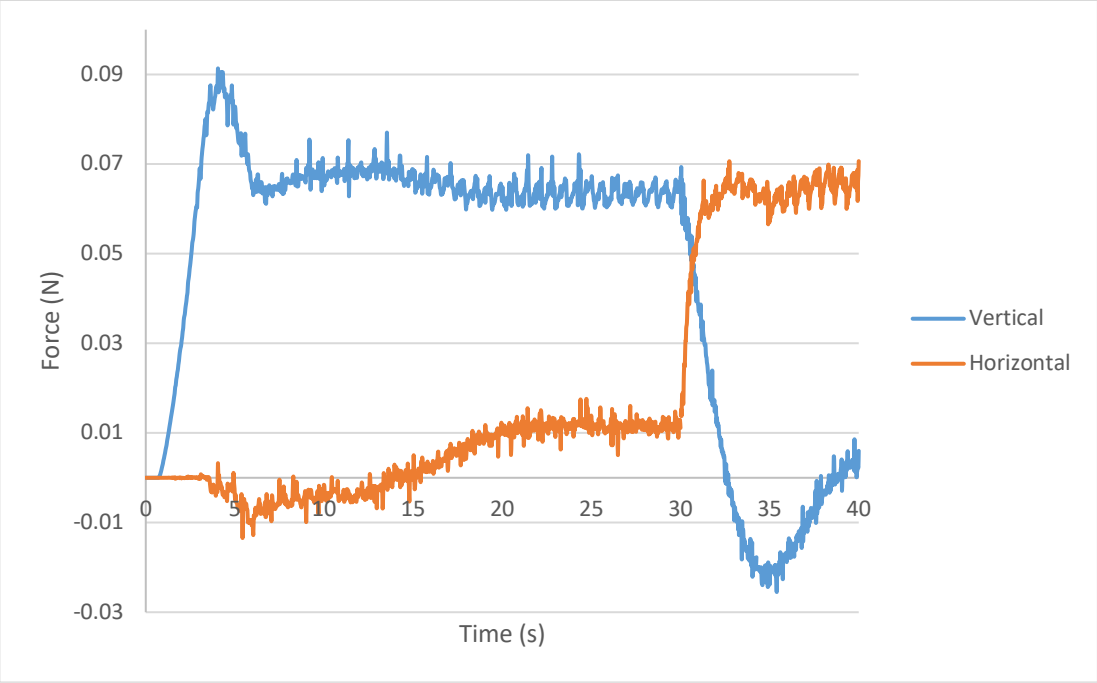

Figure 3.8 – Magnitudes of vertical and horizontal forces required to move the thermoseed.

3.1.2.3 Customised needle insertion force

To further validate this finite element model of brain tissue phantom, needle insertion of two different customised needles are also simulated, and the insertion forces are compared with experimental results. Although the brain phantom is already validated using literature data in the previous two sections, it is necessary to conduct experiments of our own because the catheter and thermoseed used by Howard et al. (1999) and Molloy et al. (1990) both have a diameter of 3mm. Further proof of whether the model can provide reliable results when interacting with surgical tools is needed. Thus we designed two customised needles, one small and one big, to insert into the brain phantom (Fig. 3.9). Needle A has a diameter of 1.5mm and a 45° conical tip that is 2mm long. Needle B has a square cross-section with a side length of 7.5mm and a conical tip of 13.2mm long. They are both modelled as Lagrangian deformable bodies, assigned material property of 316L stainless steel, meshed with C3D4 tetrahedral elements, and applied rigid body constraints. The model setup and output are the same as catheter insertion described in Section 3.1.2.1, except that the needles move at a speed of 0.5mm/s for 50 seconds, as it would be conducted in experiments. The simulated reaction forces on the needles are plotted in Fig. 3.10 and they will be used to compared with experimental measurements in Section 3.3.1.

In short summary, this section builds and validates a finite element model of brain tissue phantom interacting with surgical tools. We find out that although there is a considerable difference between white matter and grey matter brain tissue, it is sufficient to consider that the phantom only consists of white matter. We also find out the influence of friction coefficient and surgical tool speed on reaction force and induced stress in brain

tissue. This finite element model is ready to be used for further analysis of other surgical scenarios in next section.

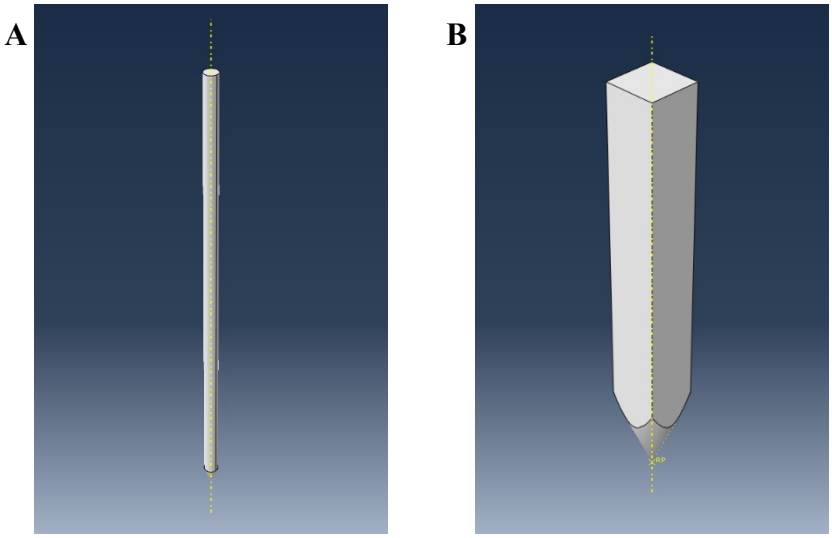

Figure 3.9 – Geometry of customised needle (A) and (B).

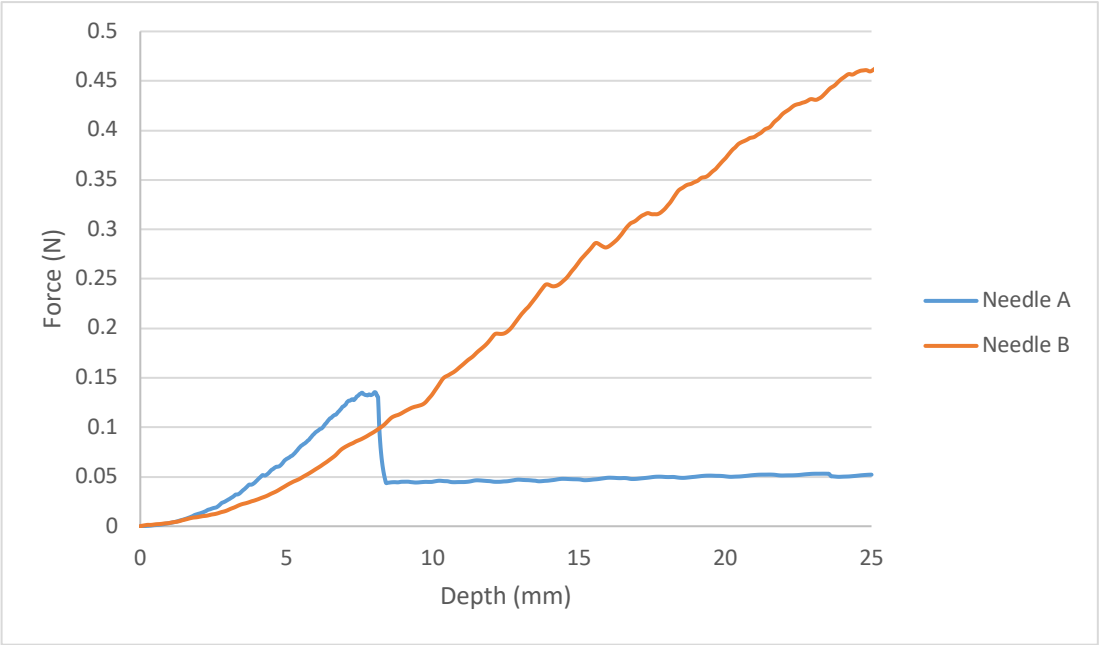

Figure 3.10 – Simulated insertion forces for customised needle A and B.

3.2 Finite element analysis of surgical scenarios

This section describes finite element analysis of two surgical scenarios, insertion of rigid retractors in brain tissue phantom and expansion of rigid shells after insertion, using Abaqus/Explicit. The objective is to find out the impact rigid retractors exert on brain tissue during surgery, as well as the force and pressure needed for something to expand inside brain tissue. This is essential for proving the motivation of designing a new self-expanding stent retractor, and understanding how strong in terms of radial pressure the proposed retractor should be.

3.2.1 Insertion of rigid retractors

Insertion of rigid retractors, such as commercially available BrainPath products, into brain tissue phantom, is simulated using the Coupled Eulerian Lagrangian method in Abaqus/Explicit. The brain tissue phantom is defined in a Eulerian space using volume fraction control. The Eulerian space has a dimension of 100mm x 100mm x 80mm and it is meshed with EC3D8R elements. A reference cuboid with a dimension of 100mm x 100mm x 78mm is placed inside at the bottom of the Eulerian space. Mesh sensitivity study has been performed by the means of indentation test of a sphere with a diameter of 7mm. The maximum average computed Von Mises stress is derived for different level of mesh refinement of the phantom. By refining the mesh, the maximal Von Mises stress converges. Element of size 1mm x 1mm x 1mm was chosen for the phantom as a good compromise between the accuracy of the solution and the computation time. Brain tissue consists of purely viscoelastic white matter with an elastic modulus of 1.895 kPa and stress relaxation parameters as described in Section 3.1.1. Two boundary conditions are

applied at the Eulerian space. All six faces of the space are fixed with no movement or rotations allowed. Eulerian boundary conditions of free inflow and non-reflecting outflow are also applied to all six faces to simulate an infinite domain at the truncated artificial boundary. On the other hand, the BrainPath retractor consists of two parts, the dilator (Fig. 3.11 A) and the retractor (Fig. 3.11 B). They are modelled as Lagrangian deformable bodies. The dilator has a diameter of 15mm, length of 67.5mm and 45° tip that is 7.5mm long. The retractor has an inner diameter of 15mm, a outer diameter of 16mm, and a length of 60mm. They are both assigned material property of 316L stainless steel and meshed with C3D4 tetrahedral elements. Since they are considerably stiffer than brain tissue, rigid body constraints are applied. At the beginning of the simulation, the dilator and retractor are paired together and positioned right above the centre of the brain tissue phantom as shown in Fig. 3.11 C.

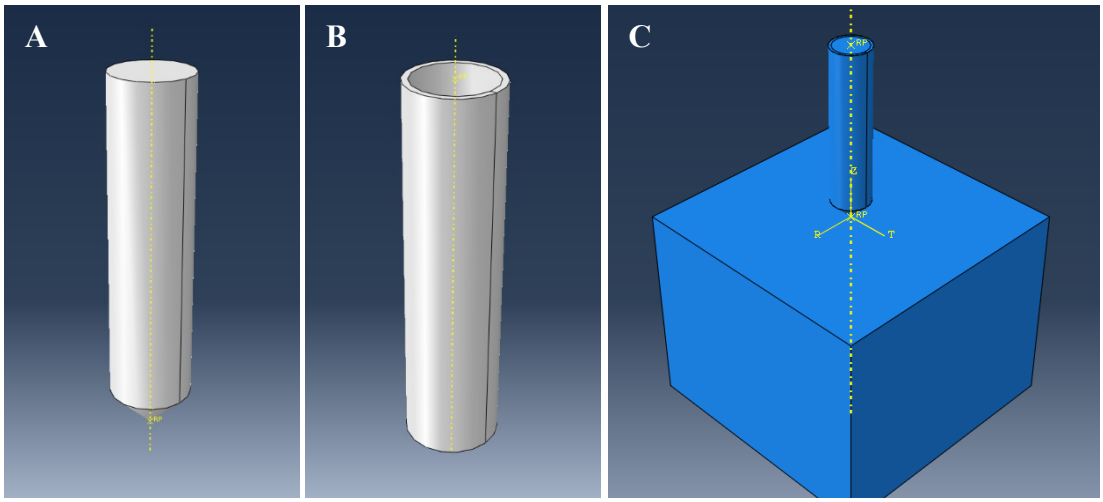

Figure 3.11 – Rigid BrainPath (A) Dilator and (B) Retractor. (C) Position of the dilator and retractor at the beginning of insertion.

The simulation is conducted in three steps. Step 1, both dilator and retractor move downwards into the brain phantom at a speed of 10mm/s for 5 seconds, so that a depth of 50mm is reached. Step 2, both dilator and retractor remained idle for 1 second to let things

settle. Step 3, dilator vertically moves out at 10mm/s for 6 seconds while retractor remains inside brain. Contact between dilator and retractor is ignored, while their interaction with brain tissue is defined using general contact algorithm. Tangential behaviour is Penalty friction formulation with a friction coefficient of 0.125. Normal behaviour is hard contact that allows separation after contact. History output of the reaction force on the dilator is requested. Internal energy and kinetic energy of the whole model is monitored to ensure kinetic energy is less than 5% of internal energy so that the simulation can be considered quasi-static. Insertion of a thinner pair of dilator and retractor is also simulated to study the effect of a smaller profile on stress caused in the brain. The thinner pair has an outer diameter of 7 mm, the same profile as the proposed self-expanding stent retractor (SESR) is intended to be packaged into.

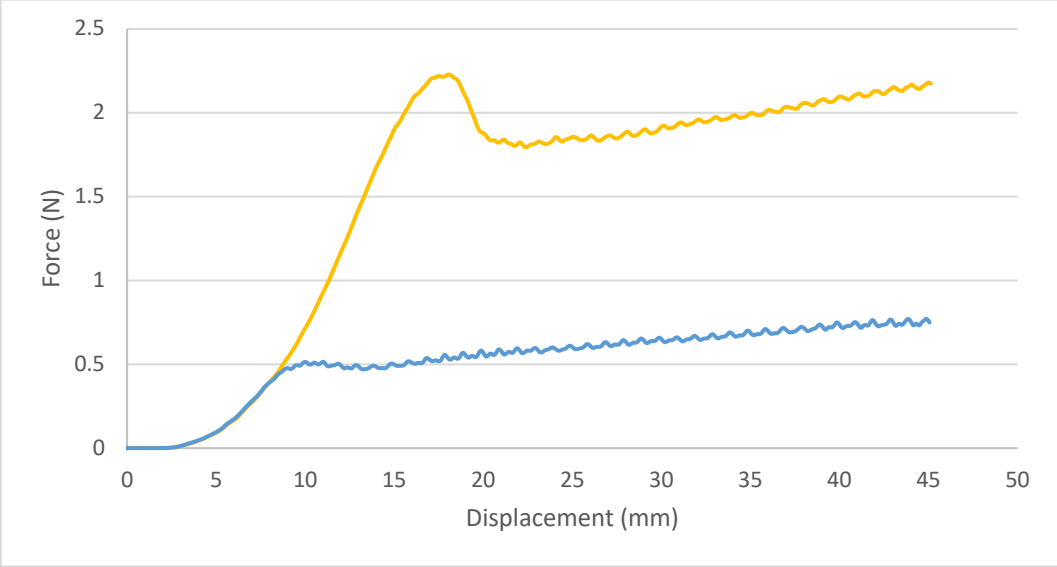

Figure 3.12 – Comparison of insertion forces of BrainPath (yellow) and thin retractors (blue).

Figure 3.12 compares the insertion force for BrainPath and the thinner pair. A smaller dilator results in an insertion force almost 1/3 of the BrainPath dilator. The maximum force required is 0.749 N for the thinner pair and 2.183 N for the thicker BrainPath. The stress induced in brain tissue during insertion of d =16 mm and d =7 mm dilators and

retractors are compared in Fig. 3.13. Cross section views are shown here to better visualise the results. Average-computed von Mises stress is used and a reference stress of 1.33 kPa is applied in all plots to better visualise the stress contour. Peak stresses in brain tissue phantom during insertions are 3.658 kPa and 3.160 kPa for thick and thin pairs, respectively. At the end of insertions, peak stresses decrease to 2.458 kPa and 2.154 kPa for thick and thin pairs, respectively.

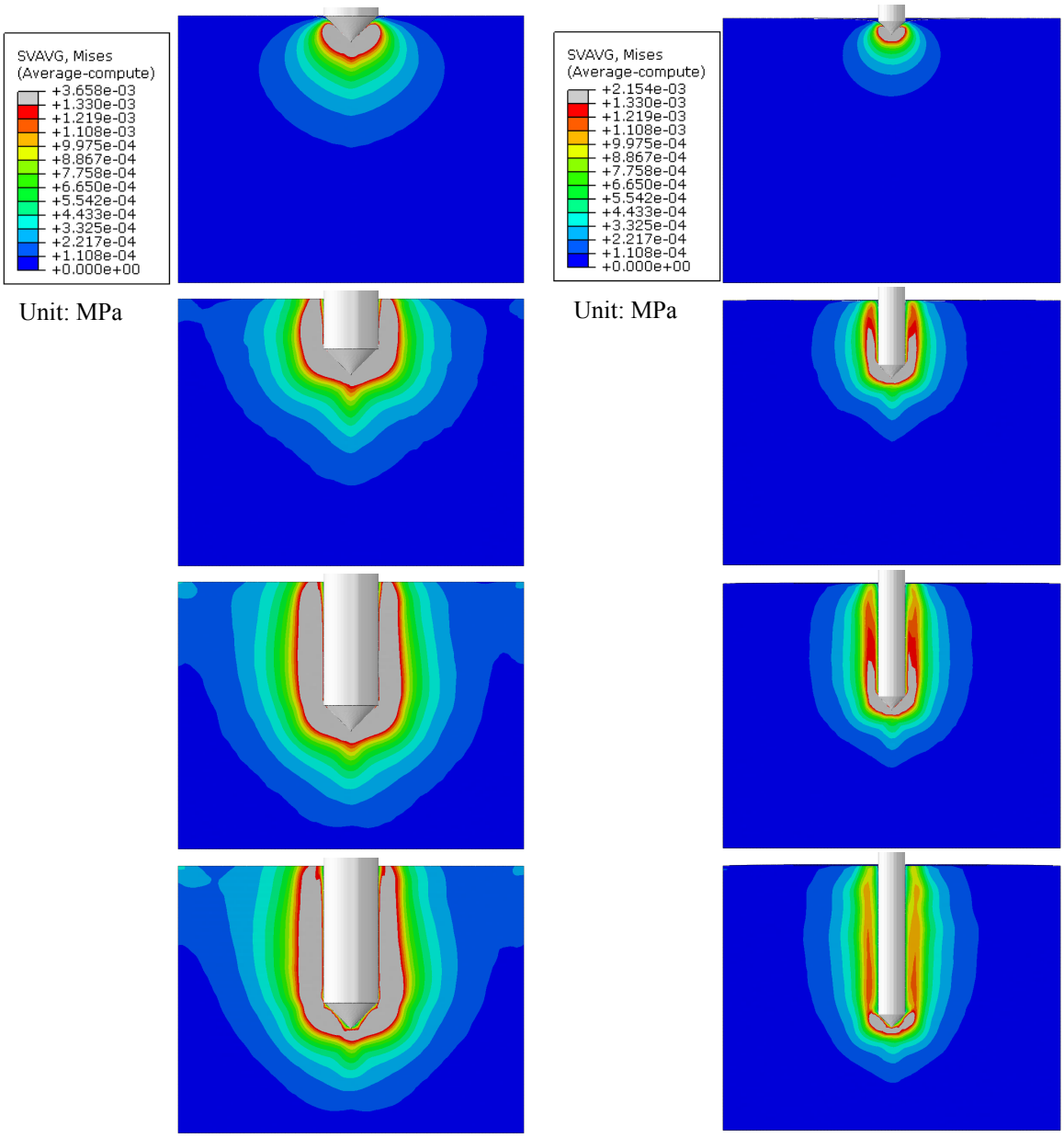

Figure 3.13 – Cross section view of stress contours induced by (A) BrainPath and (B) thin retractor insertions.

Although the difference in peak stress is not big, the amount of brain tissue subject to high stress is significantly less in the thin pair case than that for BrainPath. Thus, it is safe to conclude that introducing a pair of dilator and retractor of smaller profile will reduce damage in brain tissue. Finally, the stress contour during BrainPath dilator withdrawal is shown in Fig.3.14. The stress relaxes overtime because of the viscoelastic property of brain tissue. The remaining peak stress is 2.588 kPa after withdrawal of dilator.

It is important to note that the average-computed von Mises stresses obtained from these two simulations are mainly for comparison purpose, i.e., to show that inserting a smaller dilator into the brain causes less stress than that from inserting BrainPath. Due to the geometric and material simplification of the brain tissue, the stress values obtained are not used to compare with an injury criteria reported in literature to predict brain injury.

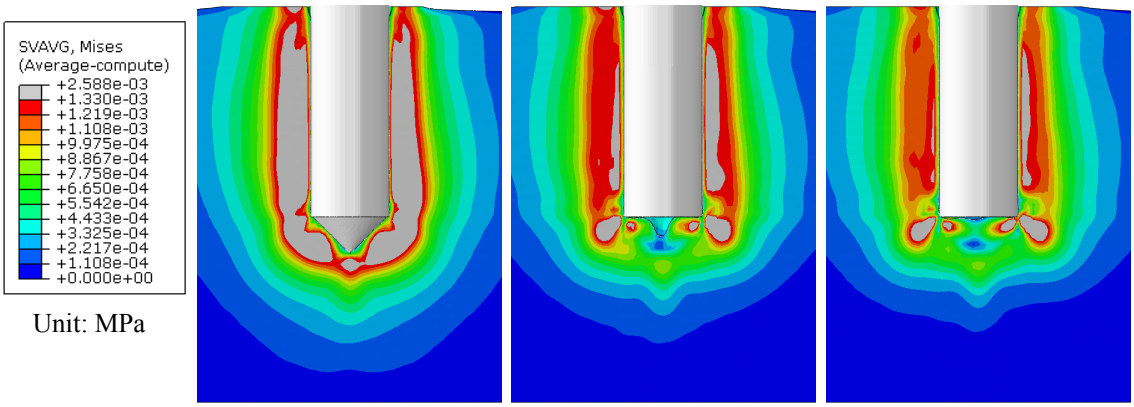

Figure 3.14 – Cross-section view of stress contours during withdrawal of dilator.

3.2.2 Rigid expansion after insertion

Rigid expansion of the thinner retractor after insertion is simulated in this section because it is necessary to understand the force and pressure required for one to expand once inside brain tissue phantom. Moreover, the concept of expansion after insertion needs to be verified. Specifically, it is important to make sure that to create the same amount of space in brain phantom, the stress induced by insertion and expanding a thinner retractor is not significantly larger than that induced by a conventional rigid retractor like BrainPath. The rigid expansion is simulated using two different methods. In method one, 16 half-cylinder shells are placed overlapping in the same position as the dilator. Each shell is 50mm in length, 3.5mm in outer diameter and 0.5mm in wall thickness (Fig. 3.15 A). They are assigned material property of 316L stainless steel, meshed with C3D8R solid elements and applied rigid body constraints. After the insertion step, the shells move radially outward at speed of 4.5mm/s for 1 second, so that a cylindrical space of 16mm in diameter is created at the end of expansion. History output of reaction forces in X and Y direction on each shell are requested and used to calculate the radial expansion force and pressure. Detailed calculation is described in Appendix 1.

In method two, a deformable surface is used in place of the rigid shells for expansion (Fig. 3.15 B). The deformable surface is meshed with eight layers of SF3D4R surface elements, each layer consisting of 50 elements, and placed inside the brain phantom as shown in Fig. 3.16. The depth inside brain tissue for each layer of nodes is also labelled. With this setup, we are able to obtain radial expansion force at every 5mm deep inside the brain and thus extrapolate the pressure required at different depths. The expansion is controlled by radially displacing all surface nodes outward at speed of 4.5mm/s for 1 second, while keeping displacements and rotations in other directions zero,

thus creating a cylindrical space the same size as in method one. History output of reaction forces in X and Y direction for each layer of nodes are requested and used to calculate the radial expansion force and pressure at different depth. Detailed calculation is described in Appendix 2. In both methods, after expansion, rigid shells and deformable surface remain in place while the thin dilator vertically withdraws from the brain phantom at 10mm/s for 6 seconds.

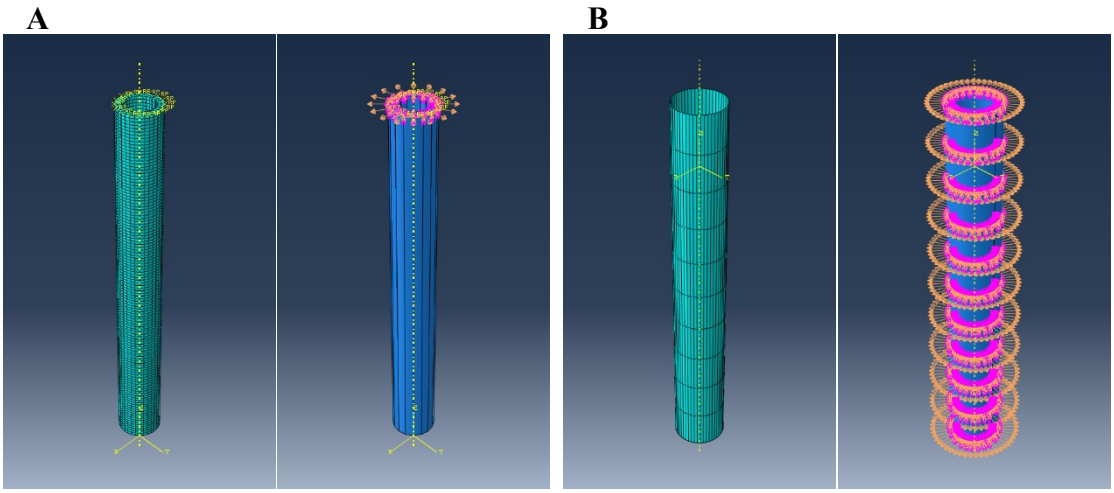

Figure 3.15 – Expansion by (A) Rigid shells and (B) deformable surface.

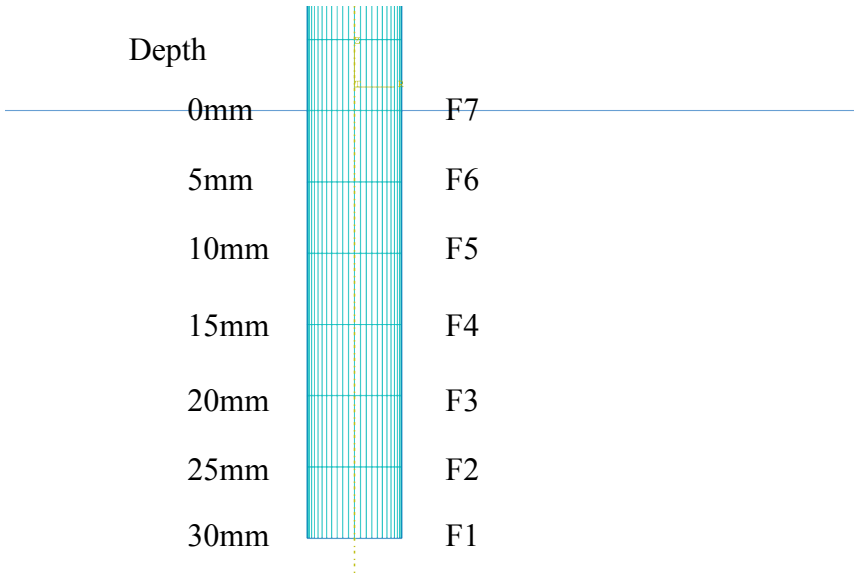

Figure 3.16 – Expansion using a deformable surface at different depths.

It is important to study the expansion using both methods. As explained in the last section, in the Coupled Eulerian Lagrangian analysis, contact is best modelled between Eulerian body and 3D Lagrangian body. Hence method one is better at predicting the stress induced on brain tissue phantom, as well as finding out the average force and pressure needed to expand these 16 rigid shells. On the other hand, method two using deformable surface enables us to find radial force and pressure at different depth inside brain tissue through nodal force output. This is critical because as speculated earlier, the radial force and pressure at different depth inside brain phantom should be different, with increasing depth correlating to increasing force and pressure.

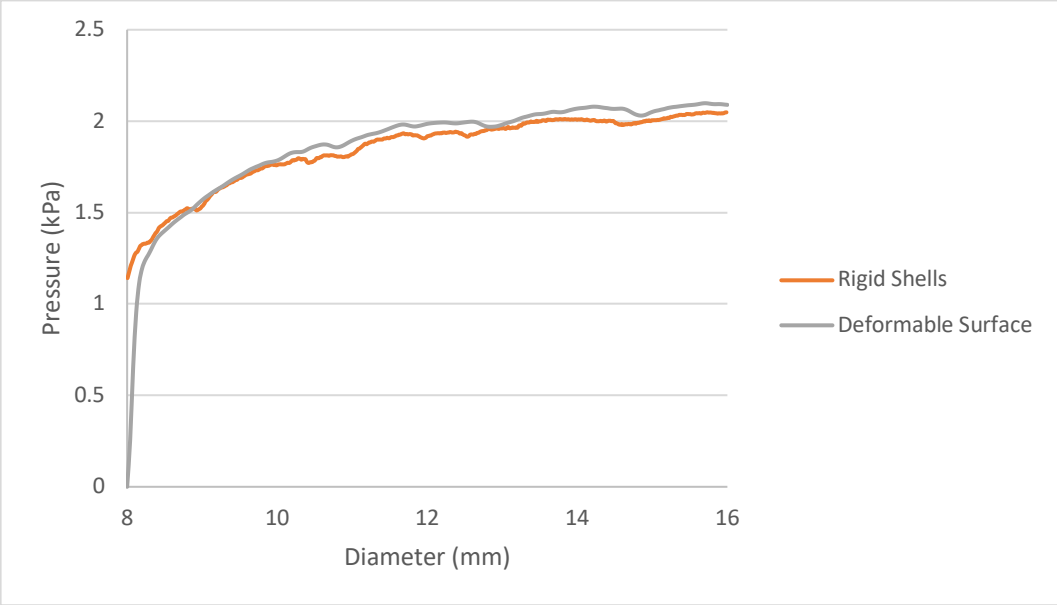

Figure 3.17 – Comparison of expansion pressure vs diameter results between two methods, rigid shells and deformable surface.

These two methods are compared to each other. Figure 3.17 plots the radial expansion pressure calculated from two methods. Two results show very little difference except at the beginning of expansion, radial pressure increases slower in method two. This is understandable because contact between the Eulerian body and surface elements are not as good as that between Eulerian body and 3D solid elements.

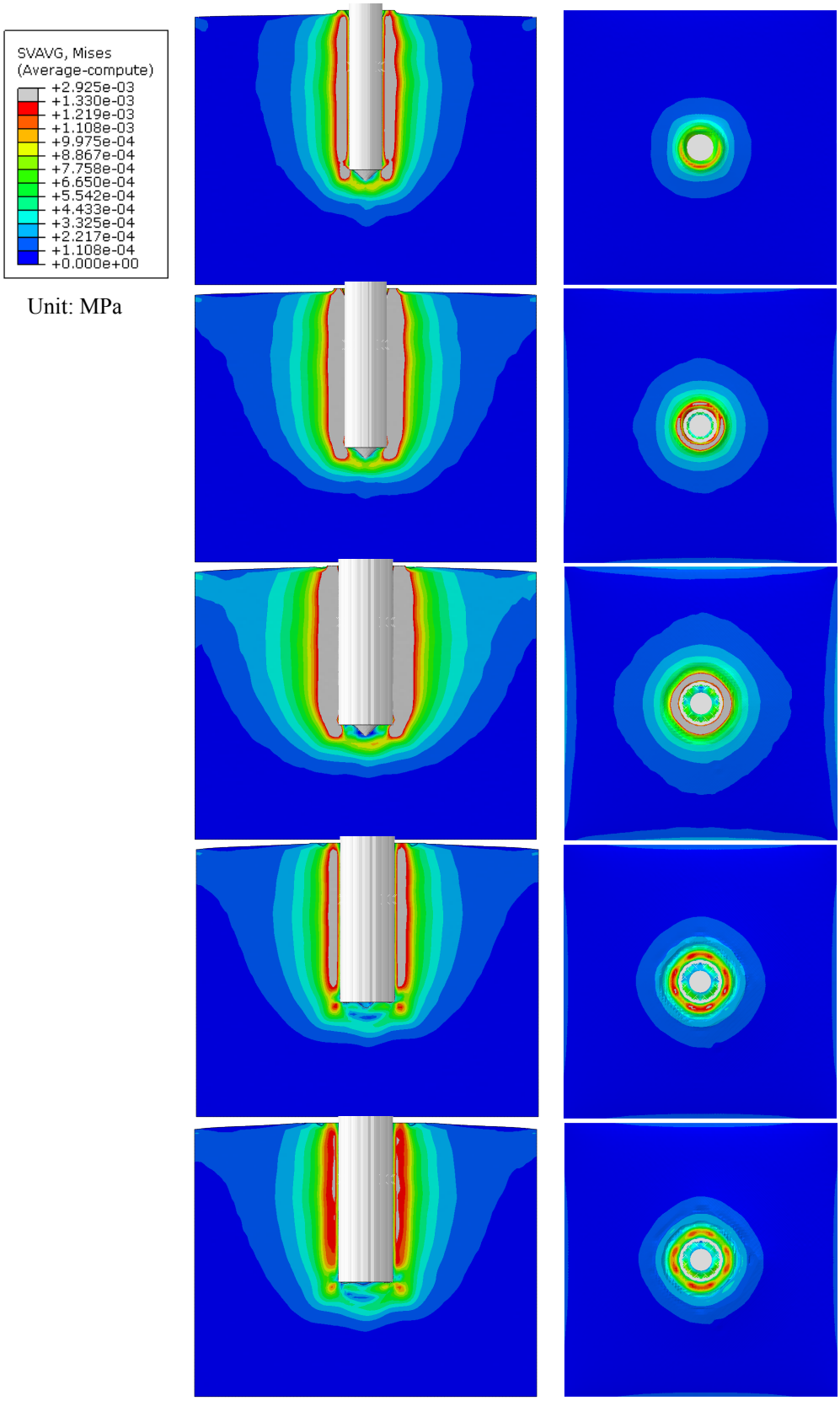

Figure 3.18 – Stress contours of brain tissue phantom during rigid shell expansion.

Nevertheless, radial pressures at 16mm expansion are almost identical, 2.085 kPa and 2.089 kPa for rigid shells and deformable surfaces, respectively. The peak stress induced during expansion are very similar too, 2.925 kPa and 3.035 kPa for rigid shells and deformable surfaces, respectively. Figure 3.18 shows the expansion of rigid shells and relaxation of brain tissue as the dilator is withdrawn. Average-computed von Mises stress is used and a reference stress of 1.33 kPa is applied to better visualise the stress contour. Note that at the end of expansion, the stress in brain phantom is relatively high. The amount of brain tissue that exceeds 1.33 kPa stress limit is significantly more than the BrainPath case. However, during the 6 seconds that the dilator is withdrawn, the stress relaxes significantly with the peak stress decreased to 2.398 kPa. At the end of relaxation, almost no brain tissue has stress over 1.33 kPa. Similar to Section 3.2.1, it should be noted that the average-computed von Mises stress from this simulation is mainly for comparison purpose. It is not used to compare with an injury criteria reported in literature to predict brain injury.

The average radial expansion force and pressure, calculated from rigid shell expansion, are then plotted against time and retractor diameter in Fig. 3.19 A and B and Fig. 3.20 A and B, respectively. The radial expansion force and pressure at different depth inside brain tissue, calculated from deformable surface expansion, are plotted against retractor diameter in Fig. 3.19 C and Fig. 3.20 C, respectively. The viscoelastic property of brain tissue can be seen in Fig. 3.19 A and Fig. 3.20 A. Force and pressure increase during the expansion step between 5s and 6s on the time axis, and gradually decrease as the expansion stops and brain tissue starts to relax between 6s and 12s on the time axis. From Fig. 3.19 B and Fig. 3.20 B, we find that the relationship between expansion force and retractor diameter is basically linear, while the expansion pressure reaches close to a

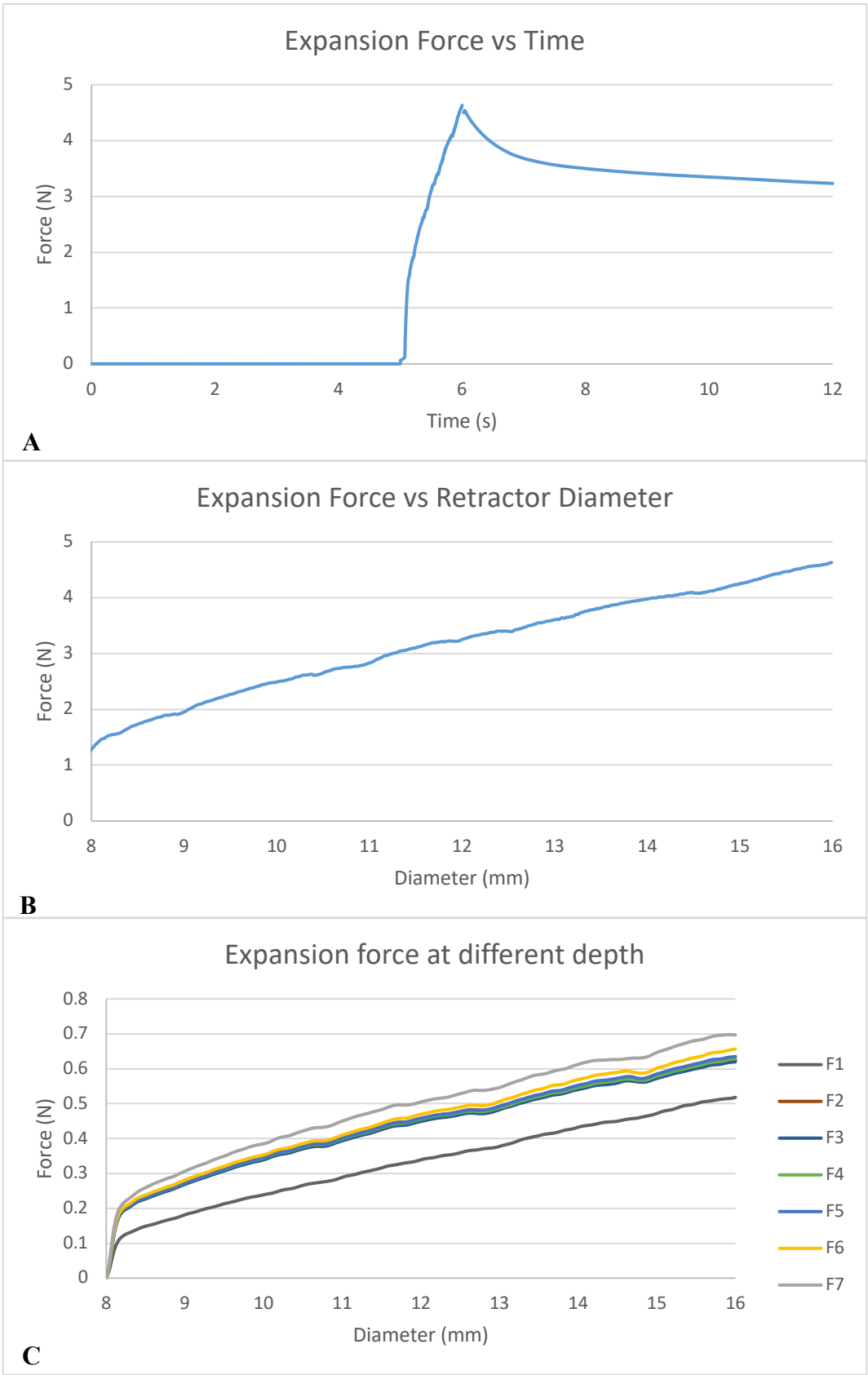

Figure 3.19 – Average radial expansion force plotted against (A) time and (B) retractor diameter. (C) Radial expansion force at different depth inside brain tissue phantom.

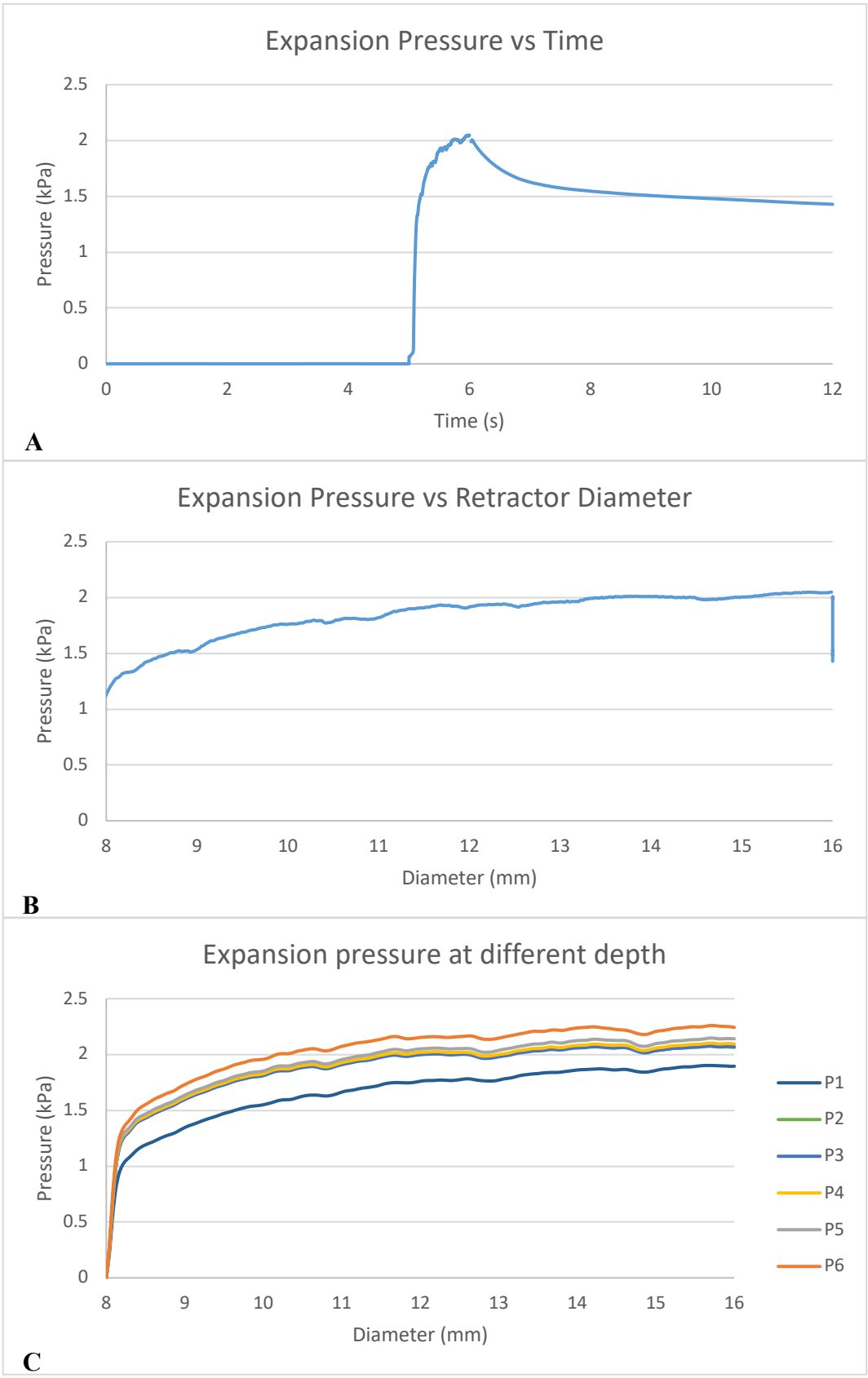

Figure 3.20 – Average radial expansion pressure plotted against (A) time and (B) retractor diameter. (C) Radial expansion pressure at different depth inside brain tissue phantom.

constant as the retractor diameter gets larger. The depth-dependent expansion force and pressure are shown in Fig. 3.19 C and Fig. 3.20 C. At the middle part of the retractor, there is a trend of slight increase in force and pressure with decreasing depth. At 16mm retractor diameter, the expansion pressure at the very bottom (30mm inside brain tissue) is 1.89 kPa, which is noticeably 18.5% smaller than that at the very top (0mm inside brain tissue), 2.24 kPa. The expansion pressures at 0-10mm, 10-20mm, and 20-30mm deep inside brain tissue are then calculated and plotted in Fig. 3.21. At 16mm expansion, the pressures required are 2.192 kPa, 2.083 kPa and 1.980 kPa, respectively. The required pressure difference along the depth inside brain urges us to consider designing a SESR with varying radial pressure if the SESR was to expand to a tubular shape instead of funnel shape.

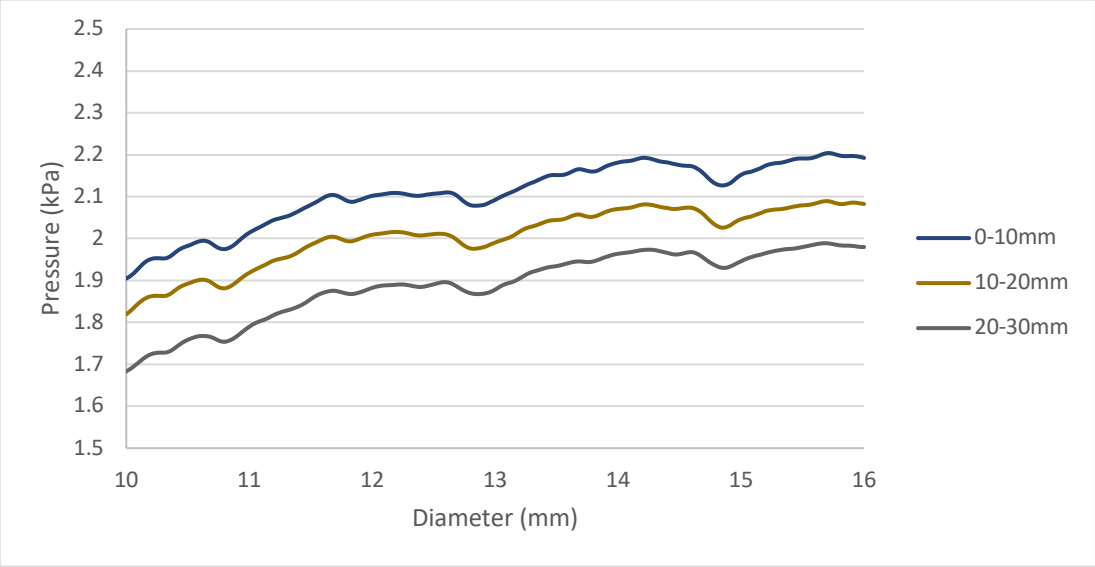

Figure 3.21 – Average radial expansion pressure estimated for 0-10mm, 10-20mm and 20-30mm deep inside brain tissue.

In short summary, this section analyses two surgical scenarios relevant to the SESR design. The first analysis finds out the impact rigid retractors exert on brain tissue during surgery in terms of insertion force and induced stress contour and proves the

motivation of designing a smaller retractor for insertion. The second analysis proves the concept of expanding after insertion of a thin pair of dilator and retractor and finds out average and depth-dependent force and pressure required for expansion.

3.3 Preliminary experiments

Two preliminary experiments are described in this section. The first experiment is insertion of two customised needles into the porcine brain *in vitro*. The results are to be compared with finite element analysis results and further validate the finite element model. The second experiment is an *in vivo* study on mice brain in which stab wound injury is visualised and quantified using histology technique. The objective is to demonstrate how experimental technique can be used to evaluate brain tissue injury.

3.3.1 Customised needle insertion force

Two customised needles were used for this experiment (Fig. 3.22 A and B). They have the same geometry as described in finite element analysis in Section 3.1.3. Needle A is a 17-gauge needle that is commonly used for fluid injection. Needle B is machined from stainless-steel, with a square cross-section 7.5mm on each side and a conical tip of 13.2mm in length. Porcine brains were obtained from local butcher shop six hours post-mortem. For each test, a new porcine brain was placed in a glass container which has a diameter of 70mm and height of 75mm. The opening at the top of the container is 36mm in diameter. The reason of this container size is that we wanted the porcine brains to almost fill the space, yet still have some room to move around at the opening, as it was simulated in the finite element model in the last section. Although porcine brain samples differed in size, most of the samples were able to fill the container to a height of 50mm. The experiment setup is shown in Fig. 3.22 C. Needles were attached to a force transducer, which was controlled by the stereotaxic apparatus (ST-5ND-B, Chengdu, China), and positioned right above the porcine brain in glass container. Insertions were

controlled by the stereotaxic apparatus; needles were moved vertically downward at a speed of 0.5mm/s for 50 seconds so that a depth of 25mm was reached. For each needle, five porcine brains were tested. Reaction forces on the needles were recorded. Examples of both needle insertions are shown in Fig. 3.23. Note that needles do not appear vertical in these photos because the camera angle was tilted. Also, note that the different colour of porcine brain in these two sets of photos is because of the different lengths of time they were exposed to air.

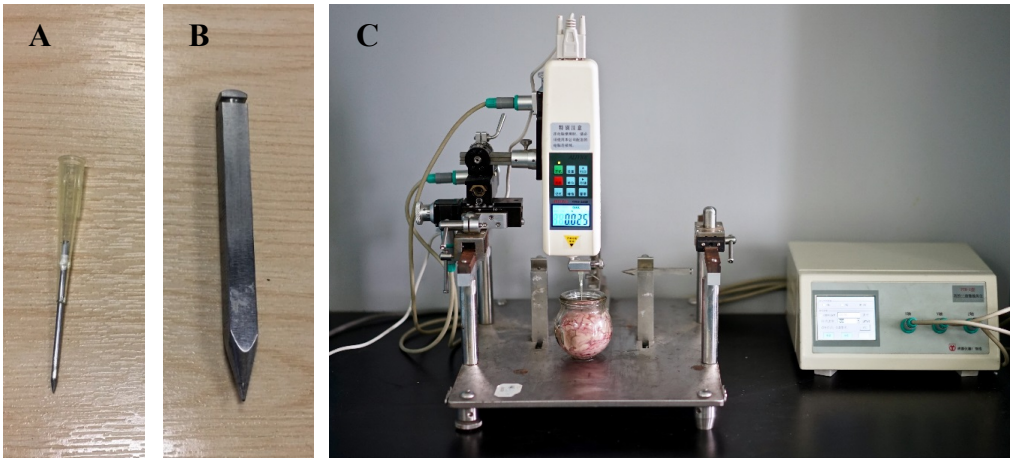

Figure 3.22 – Customised needle (A) #1 and (B) #2. (C) Experiment setup.

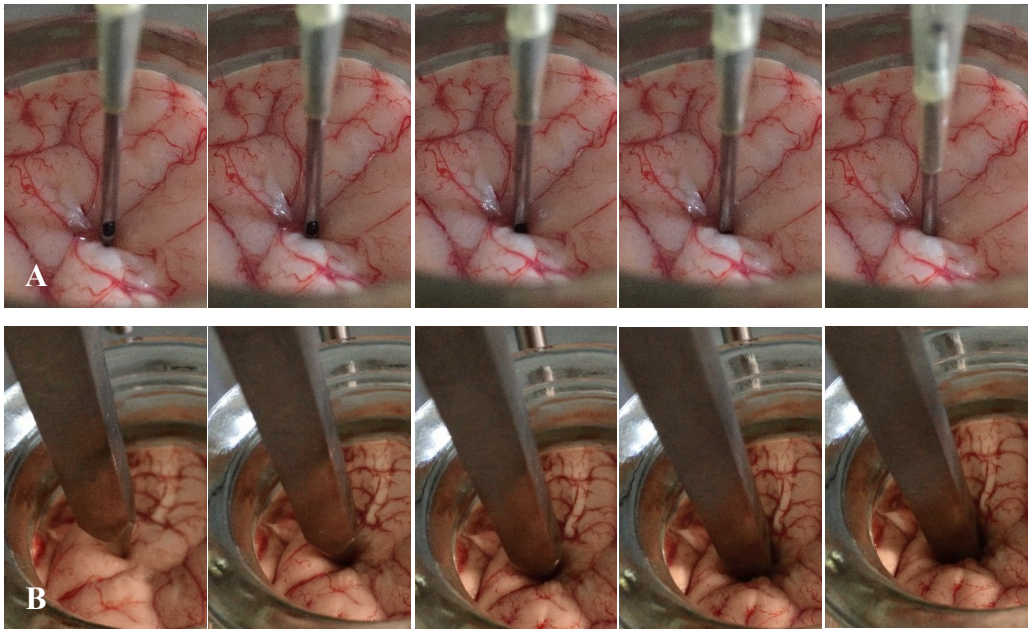

Figure 3.23 – In vitro needle insertions of customised needles into the porcine brain.

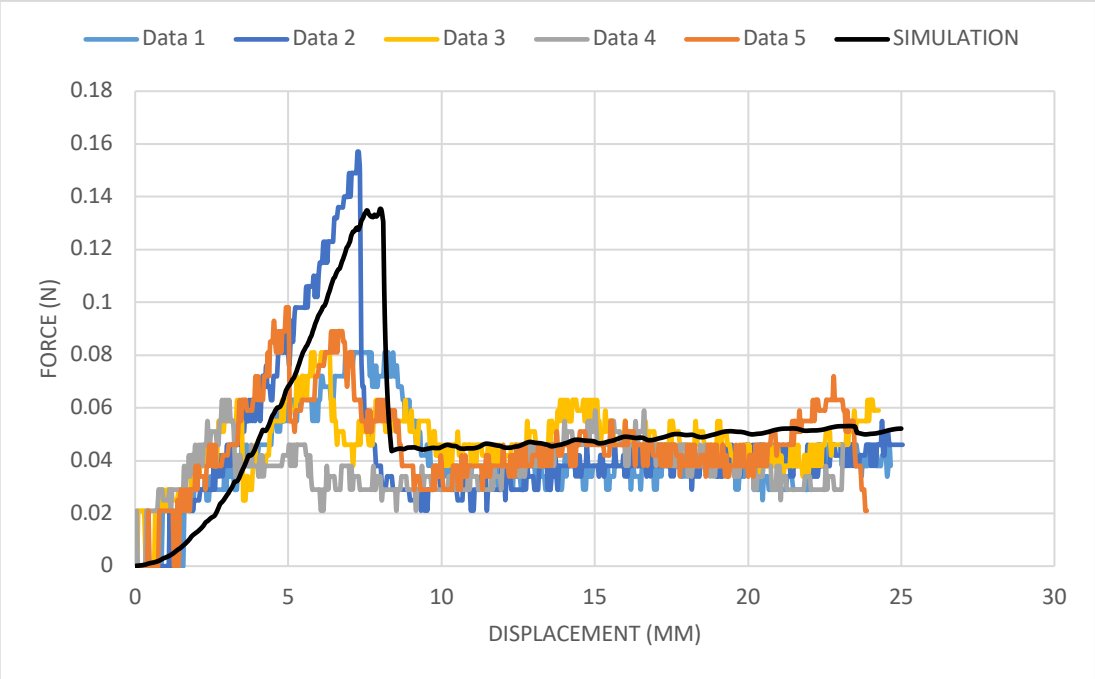

Figure 3.24 – Insertion force vs depth plot for needle A.

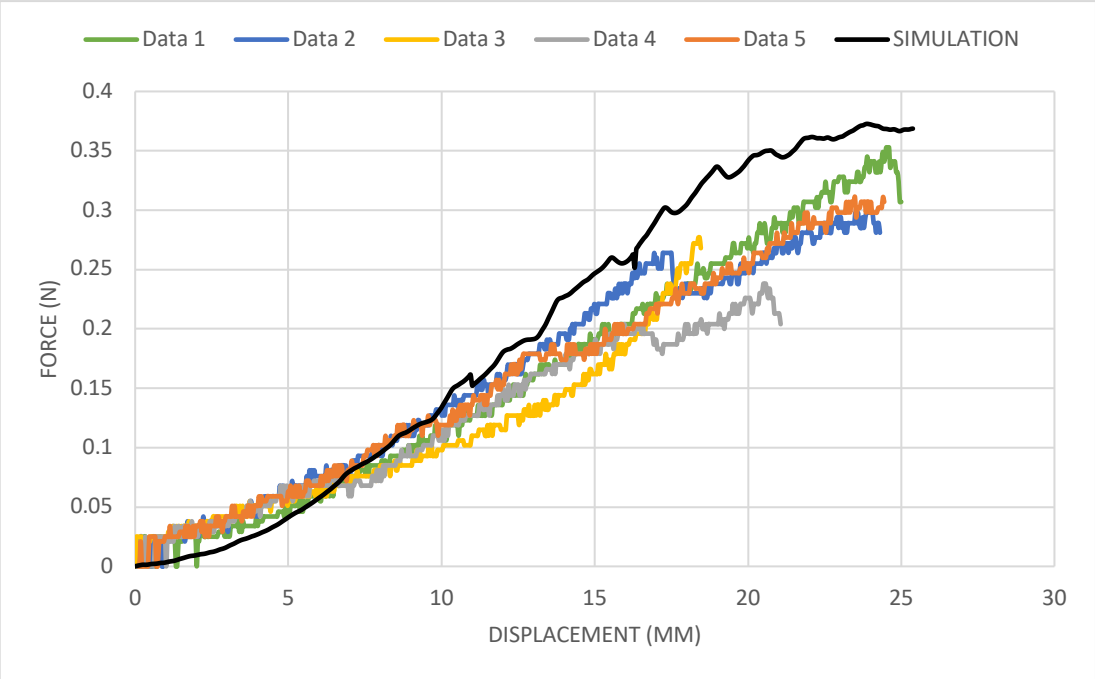

Figure 3.25 – Insertion force vs depth plot for needle B.

Experiment insertion forces from each test were plotted against simulation results from Section 3.2.1 for needle A and B, as shown in Fig. 3.24 and Fig. 3.25, respectively.

In principle, experiment measurements agree well with finite element model predictions. The reason for not averaging experimental results is to show variations of insertion forces for the same needle. Because the brain is such a complex biological tissue, there will indeed be some differences for each test. For example, Data 2 in Fig. 3.24 shows a late puncture of brain tissue and a much higher puncture force than other tests.

3.3.2 Stab wound injury and cavity size quantification

Due to the limitations of finite element models in terms of evaluating brain tissue injury as reviewed earlier, experimental method is sought after. *In vivo* needle penetrations into mice brains have been conducted as preliminary animal experiments with the objective to verify that the histology technique is an applicable method for future evaluation of brain tissue injury and stent retractor performance. Simple stab wounds are made in mice brains to induce injury that mimic that which occurs during minimally invasive neuroendoscopy. Mice are used instead of larger animals such are rabbits or pigs because they are not only very common in histology laboratory practices but also less costly. For preliminary experiments, using mice would be sufficient enough to validate the experimental method. Hematoxylin and eosin (H&E) stain is chosen as the staining method because it has the ability to demonstrate a wide range of normal and abnormal cells and yet is a relatively simple stain to carry out on paraffin or frozen sections. The experimental setup is described as the following.

Mice were housed under a 12-h light/dark cycle, with food and water freely available. All animal procedures were performed under the guidelines set by Liaoning University of Traditional Chinese Medicine, Institutional Animal Care and Use Committee and are in accord with those set by the National Institutes of Health (License No. SYXK (Liao) 2012-0010). Stab wound injury was performed on 15 mice. Mice were anaesthetized with sodium pentobarbital (40 mg/kg body weight) and fixed to a stereotaxic apparatus (ST-5ND-B, Chengdu, China). A midline incision was made through the scalp, and the skin was retracted laterally. The periosteum was cleaned from the skull, and a small rounded hole was made with a dental drill over the left cerebral hemisphere, exposing the dura. A 20-gauge needle with a diameter of 0.9mm was

attached to the vertical bar of the stereotaxic frame, and the tip of the needle was inserted stereotaxically (at 2.0mm lateral to the midline, 2.5mm posterior to the lambdoidal suture and at a depth of 2.0mm from the surface of the brain). The needle was allowed to remain in place for 30min before being removed. The skin was sutured, and the mice were allowed to recover and returned to their cages. Figure 3.26 A shows a schematic drawing of the position of needle penetration relative the mouse's brain. Figure 3.26 B shows the *in vivo* needle penetration while a mouse is anaesthetized and fixed to the stereotaxic apparatus.

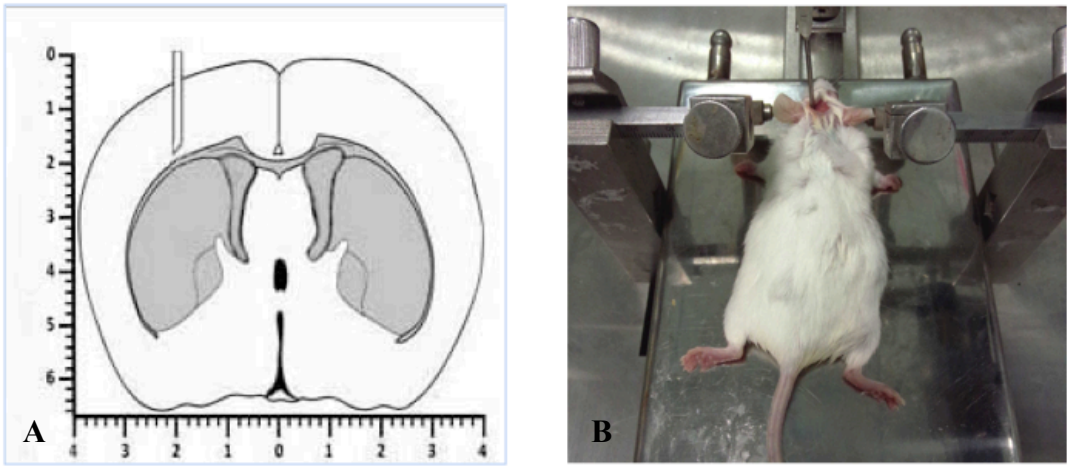

Figure 3.26 – (A) Schematic drawing of needle penetration into mouse brain. (B) *In vivo* needle penetration into mouse's brain.

Injured mice were randomly divided into 5 groups: 24 hours, 3, 7, 14 and 21 days group, 3 for each group. 24 hours post-injury, three mice were anaesthetized and transcardially perfused with 100ml cold phosphate buffered solution (PBS). The brains were immediately harvested, fixed in 10% buffered formalin and embedded in paraffin. 7μm consecutive coronal sections of the brain, in a direction parallel to needle penetration line, were cut at 10μm intervals from bregma -2.0mm to bregma -7.0mm to collect the entire lesion site. The sections were mounted on glass slides and prepared for an H&E

stain in order to visualize overall changes in morphology and architecture, as well as cellular damage. At 3, 7, 14, and 21 days post stab wound injury, other groups of mice were anaesthetized and transcardially perfused with 100 ml cold PBS respectively. The brains were immediately harvested, snap-frozen in cold isopentane on dry ice and stored at -80°C until sectioning. Consecutive coronal sections, in a direction that parallel to needle penetration line, were cut at 10μm intervals from bregma -2.0mm to bregma -7.0mm to collect the entire lesion site. 7μm frozen sections were prepared using a cryostat microtome (Leica, Nussloch, Germany) and mounted on glass slides for H&E stain and further evaluations.

The H&E staining was performed with the slides in glass staining racks and the solutions in square glass staining jars. Glass racks with slides were stained in the following steps. Deparaffinize and re-dehydrate the paraffin sections; air dry frozen sections and then fix the frozen sections before the staining; incubated slide with hematoxylin for 3-5 minutes; wash with tap water for 1-3 minutes; dip the slides into 1% alcohol for 1 second; wash with tap water until the sections turn blue; dip the slides into 95% alcohol for 1 dip; incubate the slides with alcoholic eosin for 1 minute; 95% alcohol one time, 100% alcohol two times, xylenes three times, 10 seconds each; mount with xylene-based mounting medium. The sections were then left to dry and placed under Nikon Eclipse 600 microscope for examination.

A 4× magnification, hematoxylin and eosin stained whole coronal section of mouse's brain, harvested from 24 hours post stab wound injury, is shown in Fig. 3.27 A. Hematoxylin colours the nuclei of cells blue, while eosin colours the protein and other structures in various shades of orange, pink and red, with the red blood cells being intensely red. Needle penetration causes traumatic damage to the central nervous system

(CNS) that destroys the blood-brain barrier and provokes the invasion of hematogenous cells into the neural tissue. Invading leukocytes, macrophages and lymphocytes secrete various cytokines that induce an inflammatory reaction in the injured CNS and result in local neural degeneration, the formation of a cystic cavity and activation of glial cells around the lesion site. The right side shows no damage while diffuse damages due to needle insertion are observed on the left side of the brain cortex, hippocampus, and corpus callosum. Intense red dots around the lesion site indicate accumulation of blood cells. In this case, the penetration depth was not controlled well and went deeper than 2mm. Nevertheless, the morphology changes due to stab wound injury are very well presented.

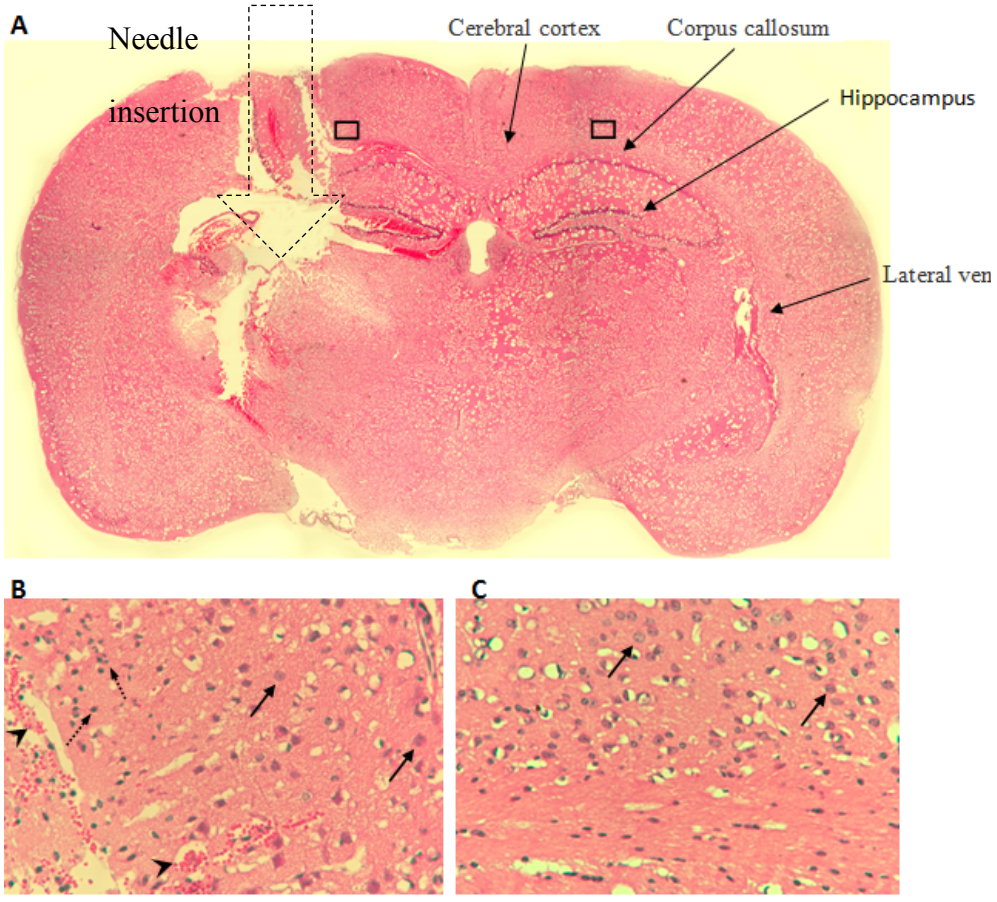

Figure 3.27 – Histological examination of the mice brain by H&E staining. (A) A whole coronal section of mouse's brain, harvested from 24 hours post stab wound injury. Magnifications 4×. Cells in boxed areas of stab wound (B) and undamaged region (C) appear at higher magnification in the insets (40×). Arrows indicate normal neurons; dash arrows indicate damaged neurons; arrowheads indicate the invasion of hematogenous cells into the neural tissue.

A closer look at this section would further reveal the injury on a cellular level. At 40 × magnification level, tissue in the vicinity of stab wound, Fig. 3.27 B and tissue in undamaged region, Fig. 3.27 C are compared. A strongly reduced number of viable neurons in the damaged cortical region was observed as compared with the normal side of the brain. The appearance of damaged neurons was dark, with nuclear pyknosis, or enlarged, shrunken, triangular cell bodies, while normal neurons were round, light with nuclei in large, round appearance. In the wounded areas, stab wound injury destroys the blood vessels and provokes the invasion of hematogenous cells into the neural tissue, while no morphological changes, as well as blood cells, were observed in the normal areas.

Another way to measure damage is to see how well the wound heals over time. Consequently, after the traumatic injury to central nerve system, two types of scarring tissue are formed at the lesion site. One is a glial scar that consists of reactive astrocytes, reactive microglia and glial precursor cells. The other is a fibrotic scar formed by fibroblasts, which have invaded the lesion site from adjacent meningeal and perivascular cells (Kawano et al. 2012). At the interface, the reactive astrocytes and the fibroblasts interact to form an organized tissue, the glia limitans. The astrocytic reaction has a protective role by reconstituting the blood-brain barrier, preventing neuronal degeneration and limiting the spread of damage. Although H&E stain could not visualize scarring tissue, it is capable of visualizing the overall morphology and thus exposing the cavity, an empty region where brain tissue is damaged or pushed away due to needle penetration. The cavity size, defined as the empty area of the coronal section, is measured for each mouse at 3, 7, 14 and 21 days post-injury. At each time point, three mice are randomly selected and anaesthetized. Their brains are removed, sectioned and

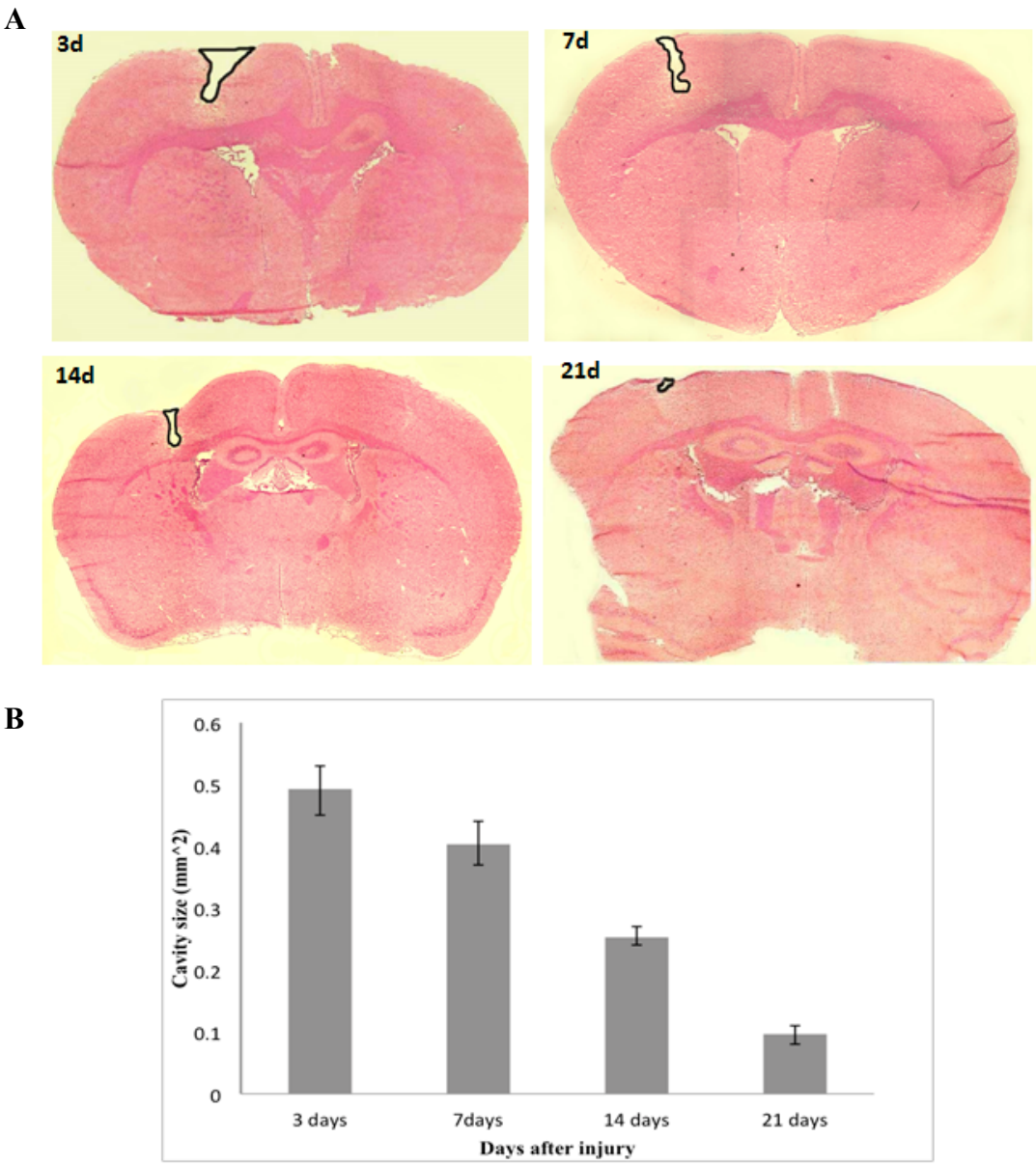

Figure 3.28 – Measurements of the wound closure. (A) H&E stained mice brain coronal sections of at 3, 7, 14 and 21 days' post-injury. Magnifications 4 ×; (B) Cavity size quantification. The cavity size at each time point post-injury was measured using ImageJ software. Six non-adjacent sections from each mouse were assessed, 3 mice per group were evaluated.

stained for cavity size measure meant. The size is measured by drawing a smooth line across the top of the lesion and tracing the edge of tissue lining the lesion with tools provide in ImageJ software (Abràmoff et al. 2004). Figure 3.28 A shows examples of mice brain sections at 3, 7, 14 and 21 days post-injury, with their cavity circled by black

lines. It is obvious that the cavities keep shrinking as the mice heal day by day; the cavity size at 21 days post-injury is significantly smaller than that at 3 days post-injury. The cavities have different shapes largely because the needle penetration processes are not perfectly consistent; mice could not be fixed to the apparatus at identical positions each time and their brains have slightly different shapes. Also, healing is a biological process which means each mouse heals differently and would form different scars. The tissue sectioning and staining process might as well marginally contribute to the differences. Nevertheless, the cavity sizes for samples at same time point agree very well. Figure 3.28 B shows the histogram of average cavity size at each time point, with upper and lower limits indicated by the error bars. Small error bars suggest that deviation is small among each set of data. The gradual and consistent closure of cavity is also very well presented as the average cavity size keeps decreasing from day 3 to day 21.

3.4 Discussion

3.4.1 Prediction of reacting force on surgical tools and stress in brain tissue

The finite element model of brain tissue phantom is built by borrowing material properties from literature. Although a comprehensive material definition with failure criteria for brain tissue is missing, the model applies calibrated parameters, i.e. friction coefficient, that produce adequate results. The interactions between brain tissue and surgical tools are modelled using Coupled Eulerian Lagrangian (CEL) method, which is excellent in dealing with extreme deformations as no distortion has occurred during any simulations. For future studies, if necessary, it would also be easy to replace the cubic phantom with an actual brain geometry because the Eulerian part is defined using volume fraction control with no complicated meshing technique involved.

Although the CEL method has been mainly used in soil mechanics in the past, it, in fact, has been used for needle insertion analysis (Kataoka et al. 2008). Results from this chapter further prove that satisfactory results can be obtained using this method. Simulations of surgical tools of different geometries and dimensions all yield matching results with both literature data and experimental measurement. Moreover, results also compare favourably with other finite element analysis reported in the literature. For example, Wittek et al. (2008) reported a finite element analysis of needle insertion into the brain using purely Lagrangian approach. The insertion force of a 1.15-mm diameter needle at 7 mm depth is 0.065 N, which is similar to the simulated insertion force 0.082 N for our 1.5-mm diameter needle at the same depth. Wittek et al.'s needle insertion simulation was not able to go deeper than 10 mm because of element distortion. Oldfield et al. (2013) used a cohesive approach to solve the distortion problem and thus simulated

much deeper insertion. Their insertion force of an 8-mm diameter needle once it is deep inside ranges between 0.5N to 0.9N, depending on needle tip geometry and friction coefficient. This also matches well with our 7-mm dilator insertion force, which is 0.74 N at 45mm deep inside the brain. Furthermore, the stress in brain tissue predicted by our model also falls in the same range of results reported in the literature. For their 8-mm needle insertion, Oldfield et al. reported maximum von Mises stress of 5.126 kPa during insertion and 2.600 kPa at the end of insertion, while our 7-mm dilator insertion caused maximum von Mises stress of 3.160 kPa during insertion and 2.154 kPa at the end of insertion.

3.4.2 Expansion of a thin rigid retractor after insertion

The concept of expanding a thin retractor after insertion is verified by comparing the stress level inside brain tissue. The initial idea of having the retractor inserted and expanded through gaps between brain fibre tracts is not simulated because brain tissue is simplified as an isotropic phantom. Nonetheless, average-computed von Mises stress is used as a metric for comparison between a rigid retractor like BrainPath and thin rigid shell expansion after insertion. A reference stress of 1.33 kPa (10 mmHg) is used in all figures to best visualise the stress contour. Ogura et al. (2006) claimed in their trans cylinder technique pressure around retractor is always less than 10 mmHg but did not provide detail information on how they obtained this measurement. Our thin rigid shells expansion yields a stress level slightly higher than 1.33 kPa at the end of the simulation. During the expansion phase, stress in brain tissue is momentarily higher than that in the BrainPath rigid retractor case. After expansion, brain tissue soon relaxes in both cases and the stress decreases significantly. At the same time point with the same amount of space created inside the brain, stress induced by thin rigid shell expansion is lower and more consistent along longitudinal direction than that by BrainPath retractor. It is thus extrapolated that if the proposed self-expanding stent retractor (SESR) was used, the stress induced in brain tissue would be even lower because SESR is very flexible in the radial direction.

The pressure required for expansion is obtained from thin rigid shells expansion simulation. Average pressure of 2.085 kPa is required for a final expansion size of 16-mm diameter. If the retractor was to be uniformly expanded, i.e., there is no difference in diameter along the longitudinal direction of the retractor, then the depth inside brain tissue needs also be considered. The pressures required at 0-10 mm, 10-20 mm and 20-30 mm

depth for 16-mm diameter expansion are 2.192 kPa, 2.083 kPa and 1.980 kPa, respectively. It might be counterintuitive that a higher pressure is required at a shallower depth, but this agrees with needle-tissue interface pressure experimentally measured by Casanova et al. (2014) using rats' brain. Their result shows even more dramatic difference along the needle tract because of different material composition in different regions. Although our finite element model is a simplified isotropic brain phantom, it does provide with a basic pressure range for SESR design.

3.4.3 Evaluating brain tissue injury

Despite the accuracy in predicting reaction force and pressure on surgical tools and the capability of showing induced stress and strain in brain tissue, the finite element model cannot predict brain tissue injury mainly because a comprehensive material definition is missing. Without any material failure criteria, the brain tissue is assumed to be pushed away during the penetration and expansion, instead of being damaged at some failure threshold and no longer support any load. The isotropic assumption of the brain tissue as well as geometric simplification of a cubic phantom also makes injury prediction unrealistic because the brain is such a complicated biological organ. Stress or strain can be used to compare different surgical scenarios; however, it is irresponsible to just pick a stress or strain threshold and conclude which part of the brain is injured. After all, it is not the main objective of this study to develop a finite element model capable of pinpoint injury in a specific location in the brain, which itself might warrant another thesis.

Nevertheless, experimental method is explored to demonstrate that it is indeed possible to evaluate tissue injury for this specific surgery. Histology analysis using H&E staining and post-processing using ImageJ software image analysis prove to be capable of showing tissue damage on both morphological and cellular level. Measurement of cavity sizes from different days' post-injury provides a good quantified method of evaluating how the injury heals over time. This is one of the advantages that histology technique has over conventional mechanical stress-strain measurement because it directly shows what happens inside the tissue. Although photoelastic and digital image correlation technique can investigate the strain in tissue (Kerl et al. 2012), it cannot evaluate injury from a biological perspective. In addition to H&E staining, other histology technique can be very versatile in showing many other things inside the tissue. For example, glial

fibrillary acidic protein (GFAP) stain could visualize the glial scar and help analyse how the wound heals after injury (Wang et al. 2007). Last but not least, histology analysis is a convenient method. Although it might require a little more effort in setting up the experiments, the post-experiment analysis is relatively simple. No computational codes need to be developed to correlate and analyse the data.

It is beyond the scope of this thesis to conduct comprehensive histology analysis, or any other experimental studies to evaluate brain tissue injury. However, the brief experiment does point us in the right direction, if retractor performance was to be studied in the future. Other biomechanical methods such as magnetic resonate imaging method could also be pursued, albeit more costly. Recent development in magnetic resonance imaging has reached the point that it has sub-nanometre spatial resolutions, which proves to be more than sufficient for evaluating the cavity shape and size, which is in sub-millimetre scale.

3.5 Summary

In summary, this chapter covers the preliminary studies on brain tissue that are essential to set up an appropriate medium for surgical scenarios and retractor deployment. Finite element analysis of brain tissue phantom is conducted in Abaqus/Explicit. The Coupled Eulerian Lagrangian method is used to simulate the interaction between brain tissue and surgical tools. The finite element model is validated by comparing simulation results with data in literature as well as experimental measurements. Two surgical scenarios are analysed to prove the concept of inserting a thinner retractor and expanding it inside brain tissue. Force and pressure on surgical tools predicted by the finite element analysis will be used for designing the proposed self-expanding stent retractor in next chapter. Moreover, two experiments are also conducted. Firstly, customised needled insertion experiment on the porcine brain *in vitro* further validates the finite element model. Secondly, stab wound injury experiment on mice brain *in vivo* explores the histology technique of analysing tissue injury, which fills the void left by our finite element model's lack of capacity in predicting damage in brain tissue.

4. Design and Analysis of Self-Expanding Stent Retractors

This chapter describes the design and analysis process for the proposed self-expanding stent retractor (SESR). The main objective is to find a functional design based on results from the brain tissue preliminary studies in Chapter 3. Section 4.1 explains the conceptual design in detail, including SESR system components, their geometric parameters as well as the reasoning of material choices. Section 4.2 uses a theoretical approach to predict the radial force and pressure of a z shape stent. This helps us identify an approximate range for the detailed geometric design of the SESR. Section 4.3 describes the uniaxial tension test of nitinol wires. Section 4.4 describes the finite element analysis of z shape stents and SESR's. Radial pressure is thoroughly studied. Radial crimp and release of the SESR is simulated to prepare for deployment in brain tissue phantom in Chapter 5. Section 4.5 describes the prototyping process of the z shape stent as well as the SESR. Flat compression test is conducted to validate finite element analysis results. Section 4.6 compares and discusses theoretical analysis, finite element analysis and experimental results. And finally, Section 4.7 summarises the main findings of this chapter.

4.1 Conceptual design of a self-expanding stent retractor system

This section describes the conceptual design of the self-expanding stent retractor (SESR), the components of the SESR system, basic geometric parameters of each component and choice of materials for each component. The system consists of one main component, which is the SESR, and three accessory components, the outer sheath, the dilator and the stopper. To better explain the concept of the proposed SESR system, we revisit the schematic drawings from Chapter 1. Before deployment, the SESR is compressed and confined inside the outer sheath and packaged with the dilator and stopper (Fig. 4.1 A). The surgeon then inserts the SESR system into patient's brain and after reaching the desired location, the outer sheath is slowly withdrawn while the stopper stays in place to keep the SESR from being drawn out (Fig. 4.1 B and C). After the SESR fully self-expands, the dilator and stopper are also withdrawn, leaving a corridor to the lesion site (Fig. 4.1 D). The stopper is not shown in this schematic drawing.

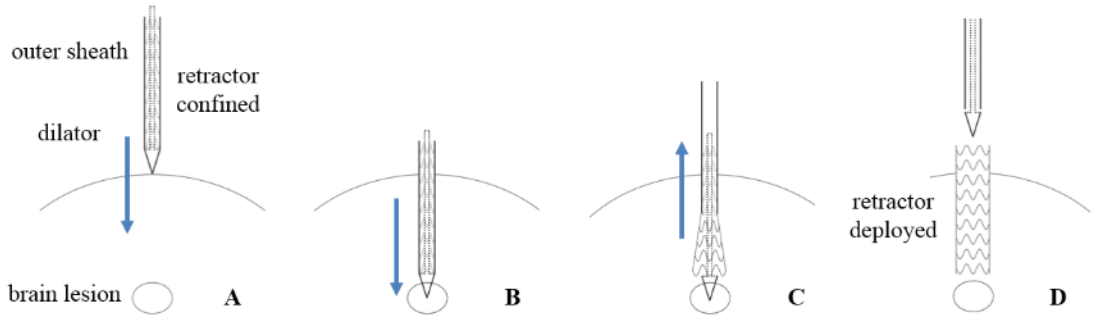

Figure 4.1 – Schematic drawings of deploying a self-expanding stent retractor in patient's brain to create an access corridor to the lesion site.

Based on neurosurgical needs and current commercial rigid retractors, which have diameters from 8mm to 28mm and lengths from 30mm to 70mm, we propose SESRs with a diameter of 18mm and length of 32mm. The SESR consists of several z shape stents

and a layer of covering fabric. Note that the length of SESR can be easily varied by increasing or reducing the number of stents in the SESR. Figure 4.2 A shows three SESRs with lengths of 32mm, 43mm and 54mm; they are made of 3, 4 and 5 z shape stents, respectively. Figure 4.2 B takes the 32mm SESR as an example and shows isometric, top and side views. The retractors would be compressed and confined in an outer sheath of 7mm in diameter, and after deployment, aim to expand to a diameter of 16mm. The reason for aiming to expand to 16mm instead of the original diameter of 18mm, is that we want the SESRs to be very soft that they do not exert unnecessary pressure on the patient's brain. If they were to be able to expand back to their original diameters, they would be too stiff, being essentially rigid compared to brain tissue and thus lose their advantage over current commercial rigid retractors.

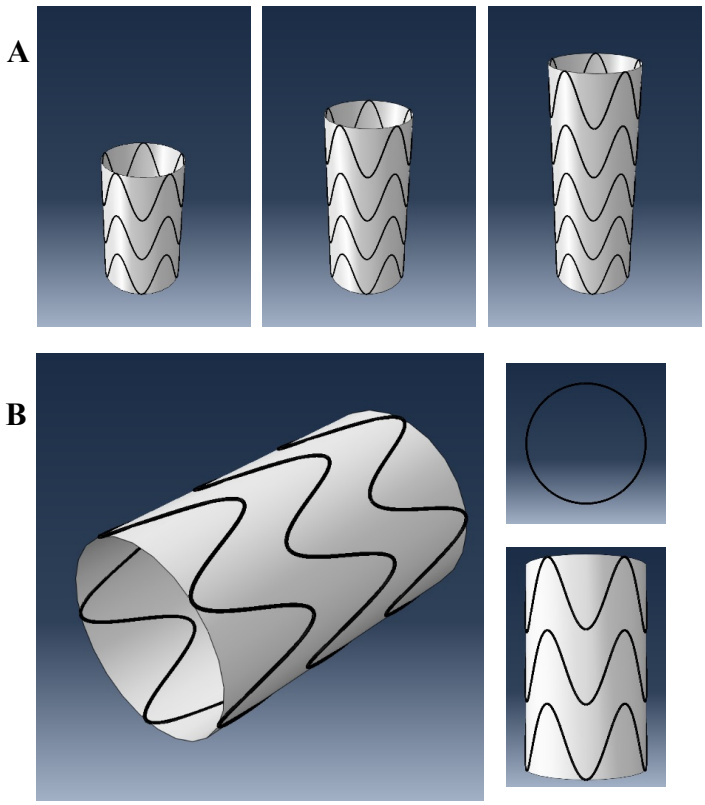

Figure 4.2 – (A) Three self-expanding stent retractors of length 30mm, 40mm and 50mm, respectively. (B) Isometric, top and side views of a 30mm long self-expanding stent retractor.

To complete the SESR system, the other three components are the dilator, the outer sheath and the stopper (Fig. 4.3 A B and C). The main function of the dilator is to penetrate the patient's brain and deliver the SESR to the desired location. It has a 45° tip which is 7mm in diameter and a thin shaft attached to the tip for surgical ergonomics. The main function of the outer sheath is to package the compressed SESR and keep it in a slim profile prior to deployment. It has an outer diameter of 7mm and a length of 60mm. The stopper is a hollow tube of 60mm in length, with an outer diameter of 5mm and an inner diameter of 3mm so that it fits inside the outer sheath without any friction, while the dilator shaft passes through its hole without any friction either. As its name indicates, its role is to stop the SESR from being vertically withdrawn during deployment. Figure 4.3 D is an isometric drawing that illustrates how these three pieces would fit with each other, while in the cross-section view in Fig. 4.3 E, the red box indicates where the SESR would be packaged prior to deployment.

Next, we consider the material choices for the SESR system. In principle, the SESR is very similar to a conventional stent graft used for cardiology. However, in term of functionalities, they are very different. For a cardiology stent graft the aim is to stay in patient's artery for ten years or longer, and so fatigue life is of one the most important factor in design. Whereas for the proposed SESR, which would only be used for the duration of the surgery, fatigue life is not a concern. The most important objective is to package the SESR into a slim profile, while maintaining the capacity of expanding back to almost its original size. Therefore, we choose nitinol to make the stents and Dacron as the cover material. The superelastic property of nitinol enables us to design a SESR that can be compressed to as much as 8-10% recoverable strain. Conventional materials for

stent graft, PTFE (Polytetrafluoroethylene) and Dacron (polyethene terephthalate) are both

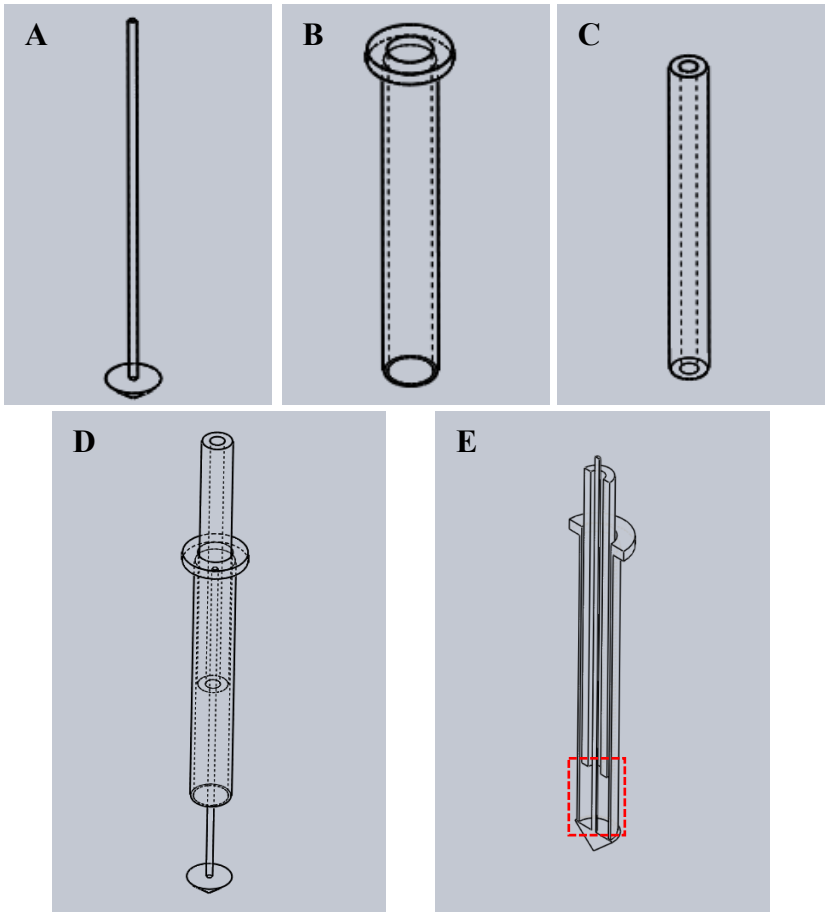

Figure 4.3 – Components of the SESR system (A) the dilator, (B) the outer sheath and (C) the stopper. (D) Isometric and (E) cross section cut views of the assembly of the dilator, outer sheath and stopper.

considered for covering and connecting the stents. We choose Dacron over PTFE for the following two reasons. First, there are many colour choices for Dacron that if necessary, we can select a dark colour to reduce glare in endoscopes during surgery. Secondly, Dacron is easier to prototype than PTFE, which is infamous for its ability of not sticking to anything. Since the cover only acts as an insulating layer between stents and brain tissue, its mechanical behaviour is of less importance here. For accessory components, the dilator, outer sheath and stopper, first round of prototypes should be 3D printed using

ABS plastic. This is a time and cost effective way of prototyping to test if the proposed conceptual design works. Once the idea is proven, they would be prototyped again using stainless steel because of its biocompatibility and wide application in medical devices. A summary of the proposed SESR system components, dimensions, material choices and functions are listed in Table 4.1.

Table 4.1 – Summary of the SESR system components, dimensions, materials and functions.

Components	Self-expanding stent retractor	Dilator	Outer sheath	Stopper
Dimensions	Diameter=18mm Length=32mm	Tip diameter=7mm Tip angle=45° Shaft diameter=2mm Shaft length=60mm	Diameter=7mm Length=60mm	Outer diameter=5mm Inner diameter=3mm Length = 60mm
Material	Stent = Nitinol Cover = Dacron	3D print ABS plastic/ stainless steel	3D print ABS plastic/ stainless steel	3D print ABS plastic/ stainless steel
Function	Create an access corridor to deep brain lesions; minimize damage to surrounding healthy brain tissue.	Penetrate patient's brain; deliver the SESR to the desired location for deployment.	Package the SESR into a slim profile to minimize damage during insertion.	Stop the SESR from being vertically withdrawn during deployment.

For the SESR to successfully expand and create a corridor for surgical operation, the determining factor is the radial pressure, which mainly depends on the geometry and dimension of the stents. There are many different stent geometries that might fulfil the design criterion; this thesis chooses to focus on the z shape stent made of nitinol wires with circular cross-sections because it is simple and efficient in radial contraction and expansion. To start the design process, we first investigate how key geometric parameters of one ring z shape stent affect its radial force and pressure.

4.2 Theoretical analysis of z shape stent radial force and pressure

This section is a theoretical analysis of radial force and pressure of one ring z shape stent. This analysis, albeit making many assumptions and not as accurate as finite element analysis, is a time efficient way to understand the relationships between stent geometric parameters and the radial force and pressure. Furthermore, this analysis will help find out a general range of geometric parameters for SESR design, which sets up the finite element analysis in later sections.

4.2.1 Theoretical model of radial force and pressure for a z shape stent

To develop a theoretical model that can predict radial force and pressure, we first identify key geometric terms of a z shape stent. Figure 4.4 A shows a typical z shape stent with five crowns. A crown is a bend in nitinol wire that eventually gives the stent a z shape, this example stent has five tops crowns and five bottom crowns. The wire has a circular cross-section and diameter d. To look from the side (Fig 4.4 B), it has height H, and to look from top (Fig. 4.4 C), it has diameter D. If we cut somewhere in the middle of the stent and lay the nitinol wire on a flat surface, we have a planar view of the stent as shown in Fig 4.4 D. We define one straight segment as one strut with length L and the angle between two struts is 2θ. The circumference C is related to the stent diameter as $C = \pi D$.

The deduction of theoretical radial force of a z shape stent follows the method reported by Snowhill et al. (2001), which combines Castigliano's theorem and the law of Laplace. The theoretical model takes wire diameter d, stent height H, stent original diameter D and number of crowns n as input, and predicts the radial force and pressure at a certain diameter to which the stent is compressed. The relationship between radial

force and stent geometry can be approximated by considering the planar configuration of z shape stent shown in Fig. 4.4 D.

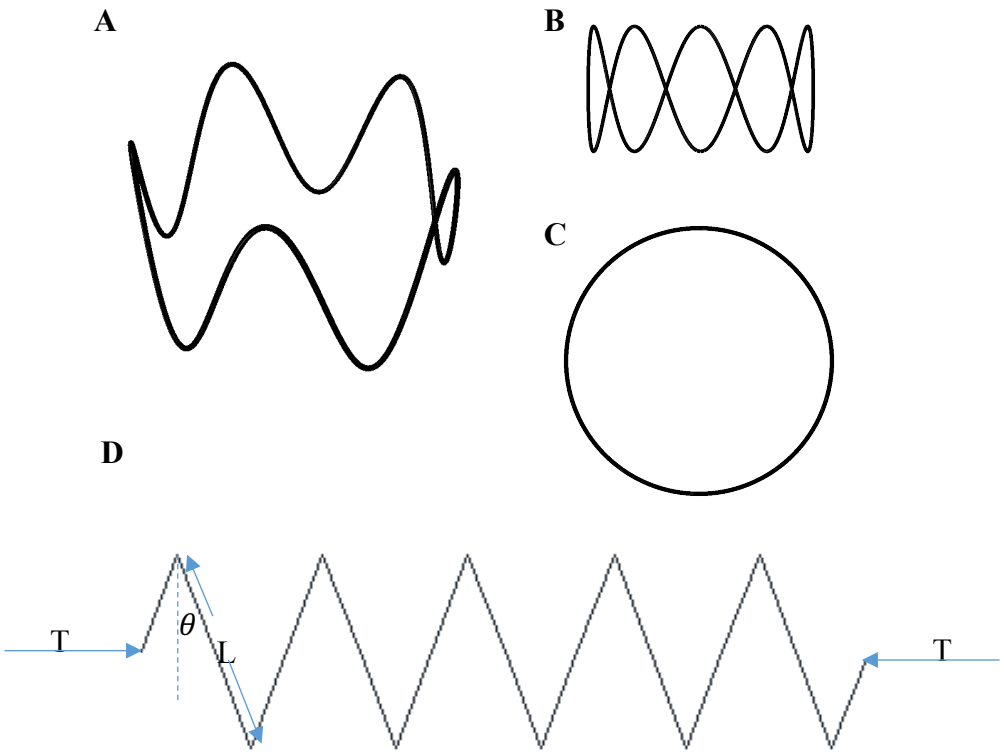

Figure 4.4 – (A) Isometric, (B) side, (C) top and (D) planar views of a z shape stent. Important geometric parameters are labelled.

If a horizontal force T is applied to one end of the stent at equilibrium, then the shear component of this force is $Tcos\theta$, the axial component is $Tsin\theta$ and the bending moment is $Tcos\theta$ multiplies half of the strut length L. Per Castigliano's second theorem, which applies for any linear elastic beam, the first partial derivative of the strain energy δU, the external force T and the deflection Δ of the point where force is applied, can be described as

$$\frac{\delta U}{\delta T} = \Delta\,. \tag{4.1}$$

There are five underlying assumptions made to apply this theorem to the planar stent. (1) The stent material is considered linear elastic; (2) the stent wire cross section remains planar after bending; (3) the center points of the stent rotate but do not translate vertically; (4) the stiffness of the crowns is less than that of the struts; and (5) the deflection due to axial force *P* and shear force *V* are negligible when compared with the bending moment *M*. For a simple beam of length s, the strain energy *U* stored in it can be expressed as

$$U = \int \left\{ \left(\frac{P^2}{2EA} \right) + \left(\frac{M^2}{2EI} \right) + \left(\frac{KV^2}{2GA} \right) \right\} ds \,. \tag{4.2}$$

where *E* is the Young's modulus, *G* is the shear modulus, *K* is the transverse shear stiffness, *A* is the cross-section area and *I* is the second moment of area. With the assumption that deflection due to axial and shear forces are negligible when compared with the bending moment, we consider only the bending moment contributes to the storage of strain energy, the strain energy *U* and the deflection Δ are simplified to

$$U = \int \left\{ \left(\frac{M^2}{2EI} \right) \right\} ds \,. \tag{4.3}$$

$$\Delta = \frac{\delta U}{\delta T} = \int \left\{ \left(M \frac{\delta M}{\delta T} \right) \right\} ds \,. \tag{4.4}$$

In this particular case, the bending moment for one segment is

$$M = (T cos\theta) s \,. \tag{4.5}$$

Now to apply Castigliano's second theorem, the deflection of this beam segment can be expressed as

$$\Delta = \frac{\delta U}{\delta T} = \int_0^{\frac{L}{2}} \left\{ \left[\frac{(T cos^2 \theta) s^2}{EI} \right] \right\} ds = \frac{TL^3 \cos^2 \theta}{24EI}, \tag{4.6}$$

where E is the Young's modulus of the wire and I is the second moment of area. For one crown, there are four such deflections and thus for a stent with n crowns, the tension force can be expressed as

$$T = \frac{6EI\Delta C}{nL^3 \cos^2 \theta}, \tag{4.7}$$

where ΔC is the total circumferential deflection. Now according to the Law of Laplace

$$\sigma = \frac{Pr}{t}, \tag{4.8}$$

and because circumferential stress also equal to tension divided by cross section area of the cylinder, we can express wall tension P as

$$P = \frac{T}{rl}, \tag{4.9}$$

where r is the radius, t is the thickness and l is the length of the cylinder. Wall tension can also be expressed as radial force divided by surface area

$$P = \frac{F}{2\pi rl}, \tag{4.10}$$

hence we can derive the radial force as

$$F = 2\pi T = \frac{12\pi EI\Delta C}{nL^3 \cos^2 \theta}, \tag{4.11}$$

where second moment of area I, wire diameter G, stent diameter D, stent height H, angle between struts θ and strut length L and can all be described using basic stent geometric parameters as

$$\mathrm{I} = \frac{\pi\left(\frac{\mathrm{G}}{2}\right)^4}{4}, \tag{4.12}$$

$$\theta = tan^{-1}\left(\frac{\pi D}{2nH}\right), \tag{4.13}$$

$$L = \frac{H}{cos(\theta)}. \tag{4.14}$$

And finally, the radial pressure is expressed as

$$P = \frac{F}{\pi D l} = \frac{12EI\Delta C}{nL^3 \cos^2\theta \times Dl}. \tag{4.15}$$

4.2.2 Relationship between geometric parameters and radial behaviour

The theoretical model is then implemented in MATLAB to investigate the relationships between z shape stent geometric parameters and its radial force and pressure. For input parameters wire diameter (*d*), stent height (*H*), stent original diameter (*D*) and number of crowns (*n*), the MATLAB code calculates the radial force and pressure at different diameters to which the stent is compressed. For our SESR design purpose, we look at stents with an original diameter of 18mm and investigate how they behave when compressed to 6mm in diameter. For simplicity of comparing different geometry parameters, a "baseline" stent geometry is set to have wire diameter 0.32mm, stent diameter 18mm, height 10mm and 5 crowns.

Table 4.2 – Geometric parameters for z shape stent radial force and pressure theoretical analysis.

	d (mm)	*H* (mm)	*D* (mm)	*n*
A1	0.16	10	18	5
A2	0.24	10	18	5
A3	0.32	10	18	5
A4	0.40	10	18	5
A5	0.48	10	18	5
B1	0.32	6	18	5
B2	0.32	8	18	5
B3	0.32	10	18	5
B4	0.32	12	18	5
B5	0.32	18	18	5
C1	0.32	10	18	4
C2	0.32	10	18	5
C3	0.32	10	18	6
C4	0.32	10	18	8
C5	0.32	10	18	10

Three groups of geometric parameters are analysed. Group A varies stent wire diameters from 0.16mm to 0.48mm and keeps everything else constant; Group B varies stent heights from 6mm to 14mm and keeps everything else constant; Group C varies

numbers of crowns from 4 to 10 and keeps everything else constant. The detailed geometric input parameters are listed in Table 4.2. 40GPa is used for stent elastic modulus E, which is for nitinol, assumed to be pure Austenite throughout deformation.

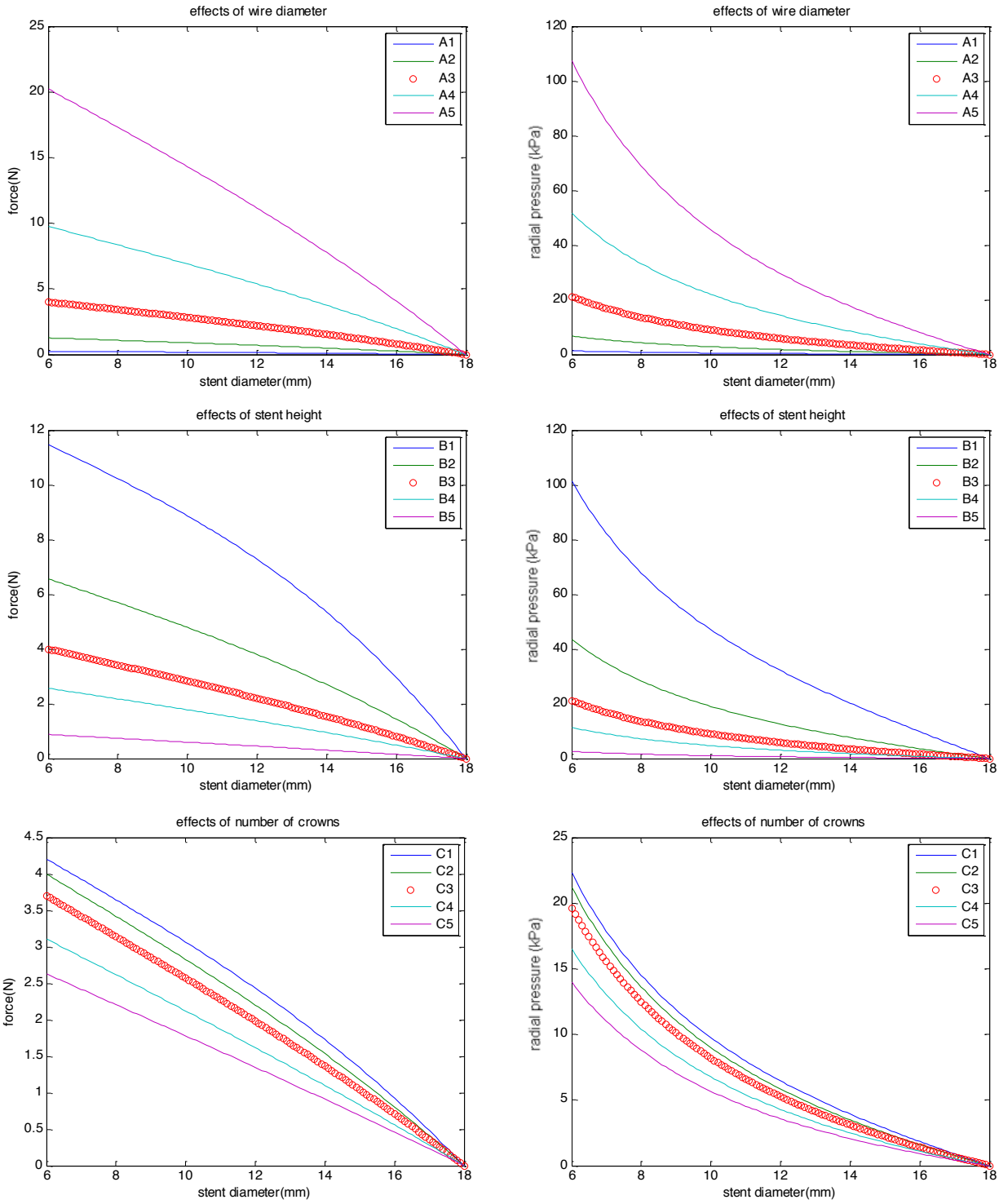

Figure 4.5 – Theoretical radial force and radial pressure plots for different stent geometries.

Theoretically predicted radial forces and pressures vs stent diameters plots (Fig. 4.5) reveal valuable information on how stent wire diameter, height and number of crowns influence its radial pressure. Group A shows that increasing stent wire diameter causes a dramatic increase in radial force and pressure. By increasing wire diameter 3 times from 0.16mm to 0.48mm, predicted radial force for stent A5 at 6mm diameter (20.23N) is about 81 times greater than that of stent A1 (0.2498N). Group B shows that increasing stent height causes a moderate decrease in radial force and pressure. By increasing stent height 3 times from 6mm to 18mm, predicted radial force for stent B5 at 6mm diameter (0.8809N) is about 13 times less than that of stent B1 (11.47N). Group C shows that increasing numbers of crowns also causes a decrease in radial force and pressure, albeit the decrease is not significant. By increasing stent numbers of crowns from 4 to 10, predicted radial force for stent C5 at 6mm diameter (2.6305N) is about 62.6% of that of stent C1 (4.2045N). In conclusion, changing stent wire diameter is the most effective way of changing the radial force and pressure of a z shape stent. If slight change is needed, changes in stent height and number of crowns can be changed to meet the demand. In this thesis, for the simplicity of finding a SESR that has enough radial pressure to expand inside brain tissue, we decide to keep stent diameter, height and number of crowns fixed and solely adjust the wire diameter to alter radial pressure.

Next, a geometry that enables the stent to expand to 16mm once deploy inside brain tissue is sought. As found in Chapter 3, the radial pressure needed to expand inside brain tissue from 8mm to 16mm is on average is approximately 2kPa, regardless of depth inside the brain phantom. Therefore, the stent, with original diameter 18mm, should have a radial pressure of at least 2kPa when compressed to diameter of 16mm. For stents with diameter of 18mm, height of 10mm and five crowns, we look at six different designs D1

– D6, with wire diameters 0.30mm, 0.31mm, 0.32mm, 0.33, 0.34mm and 0.35mm, respectively. The radial pressure versus stent diameter plot is shown in Fig. 4.6. An expanded view shows that at between D3 and D4, wire diameter 0.32mm and 0.33m is where the radial pressure reaches 2kPa at 16mm.

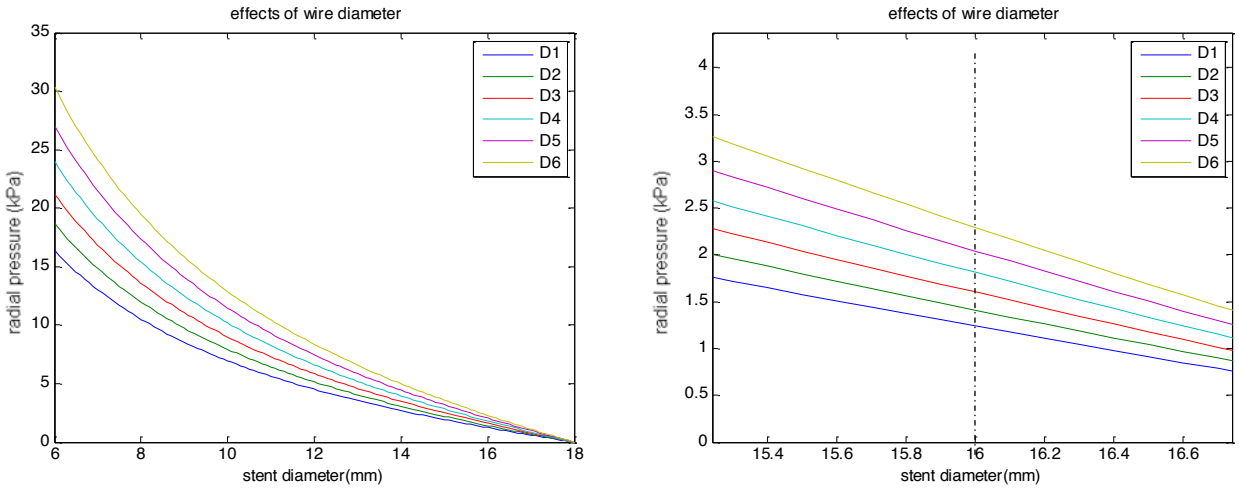

Figure 4.6 – Stent designs that are suitable for SESR application. (A) Radial pressure vs Stent diameter plot (B) Same plot zoom into stent diameter of 16mm.

In summary, this theoretical model enables us to predict a z shape stent's radial force and pressure at any diameter using basic stent geometries. We now understand among stent diameter, height, number of crowns and wire diameter, which one to change and how to change it if we want to increase or decrease stent radial pressure. Furthermore, a geometric parameter range has been identified for stent wire diameters, so that the resulting radial pressure would enable SESR to successfully expand inside brain tissue. However, this theoretical model is a very raw approximation in terms of accuracy. First, among all assumptions made to deduct the radial force and pressure, the most glaring one is to assume the stent material to be linear elastic, which is far from the fact for nitinol. For stent made of nitinol, the force and pressure curve during loading and unloading should be different because of the superelasticity of nitinol. Once the transformation

strain is reached, austenite-martensite phase transformation starts and there is a period of plateau for stress. Hence, although we have identified that radial pressure reaches 2kPa at 16mm diameter for a stent with wire diameters between 0.32mm and 0.33m, a broader range should be considered when conducting finite element analysis because the theoretical results might not be accurate. Secondly, this theoretical model cannot predict strain in the stent. Though fatigue life is not a major concern in this SESR design, we still need to know if any region of the stent has gone over 8% strain, which is most likely irrecoverable. Therefore, further finite element analysis is needed to develop the SESR.

4.3 Nitinol material property

The remarkable superelastic behaviour of nitinol is of key importance in designing and modelling the SESR, for it enables the stents to undergo very large deformations and recover from strains up to 8 – 10%. The exact superelastic behaviour of nitinol depends on many factors such as material composition and austenite finish temperature; for a given specimen, the environment temperature also greatly impacts its mechanical responses. Therefore, it is important to experimentally characterise the Nitinol wires that will be used to prototype the SESRs and then use this data for finite element analysis. This section describes the uniaxial tension test of nitinol wires and how the experimental data is used to calibrate a user material subroutine for Abaqus/Explicit.

4.3.1 Uniaxial tension test

Five samples of nitinol wire (EUROFLEX GmbH, Stuttgart, Germany) of 0.32mm wire diameter and 150mm length were obtained. The austenite finishing temperature for this wire is 18 °C. A pair of grips were also made to hold the specimen at both ends so that the gage length for wire under tension is 100mm. To mount the wire on the grips, one end of the wire is first tightly secured between two plates on the grip. It then passes around a shaft and goes to the other grip. Specimens were tested using Instron 5982 universal testing system (Instron, Norwood, MA, United States) configured with a 1kN load cell (Fig. 4.7). Per ASTM F 2516-06, standardised tension test method for superelastic material was followed. First, the force transducer is zeroed and the specimen was gripped. Each wire was first pulled to 6% strain, then unloaded to less than 7 MPa, and finally pulled to failure. Measurements were conducted at room temperature of 21 °C; crosshead

speed of 4mm/min was used to prevent significant temperature increase in wire specimen. Measurements were recorded for force and displacement. True stress and strain were then calculated from the measurements. Results from five specimens showed little deviation and the average is plotted in Fig. 4.8. Upper plateau strength, the stress at 3% strain during loading of the sample, is identified as 520 MPa. Lower plateau strength, the stress at 2.5% strain during unloading of the sample after loading to 6% strain, is 154 MPa. Residual elongation, the difference between the strains at 7 MPa stress during loading and unloading, is 0.09%.

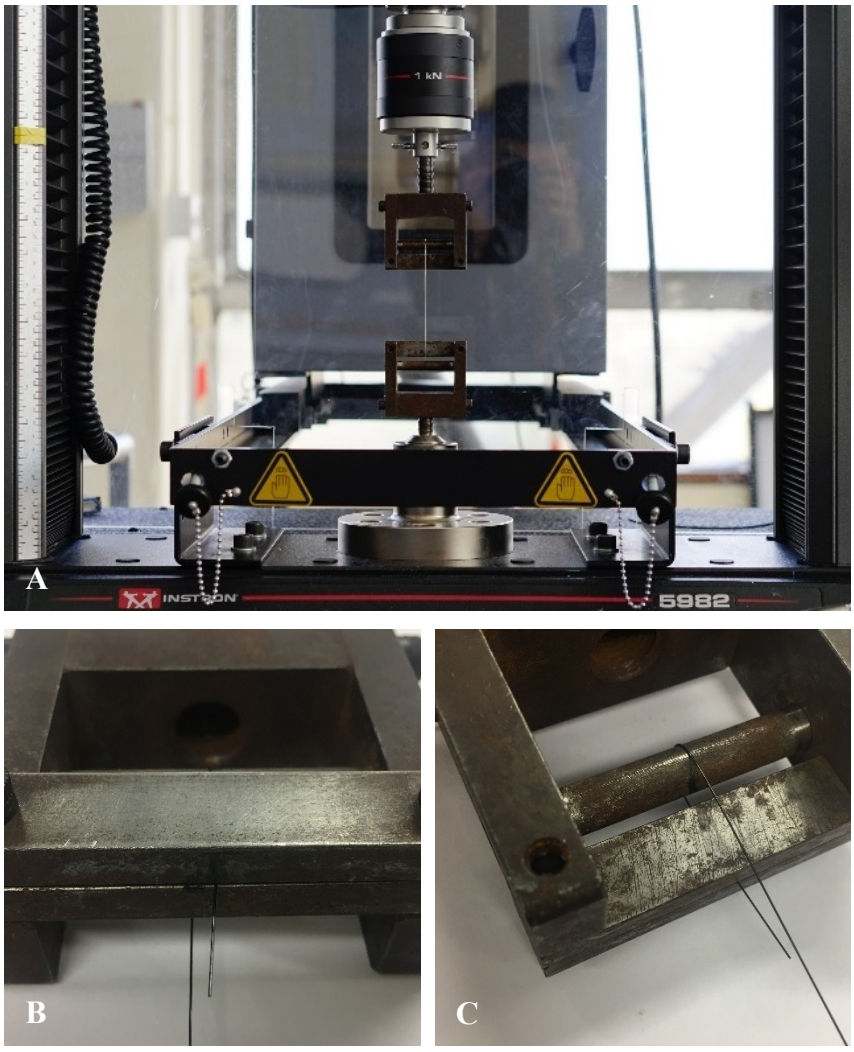

Figure 4.7 – (A) Uniaxial tension test of a nitinol wire sample. (B) The end of the wire is tightly secured between two plates on the grip and (C) then the wire passes around a shaft to go to the other grip.

4.3.2 Abaqus/Explicit user material subroutine

The average of experimental data was then used to import into Abaqus/CAE to determine and calibrate the parameters of a user material subroutine (VUMAT) for nitinol. The user material subroutine is based on the model proposed by Auricchio and Taylor (1997) and readily available in Abaqus/CEA as a plug-in utility. In the VUMAT plug-in user interface, four data points, start and end of transformation during loading and start and end of transformation unloading, need to be picked for the calibration. The input parameters generated based on the four picked data points are listed in Table 4.3. Four sets of parameters reported in the literature are also shown in Table 4.4 for comparison purposes. Our result falls in range of the data reported in literature and is most similar to those reported by De Bock et al. (2012). Uniaxial tension test of a unit nitinol cube was also simulated in Abaqus/Explicit to verify these calibrated parameters. The cube is pulled to 7.76% strain and then unloaded to zero strain. The strain-stress curve from the finite element analysis is plotted against experimental measurement average in Fig. 4.8.

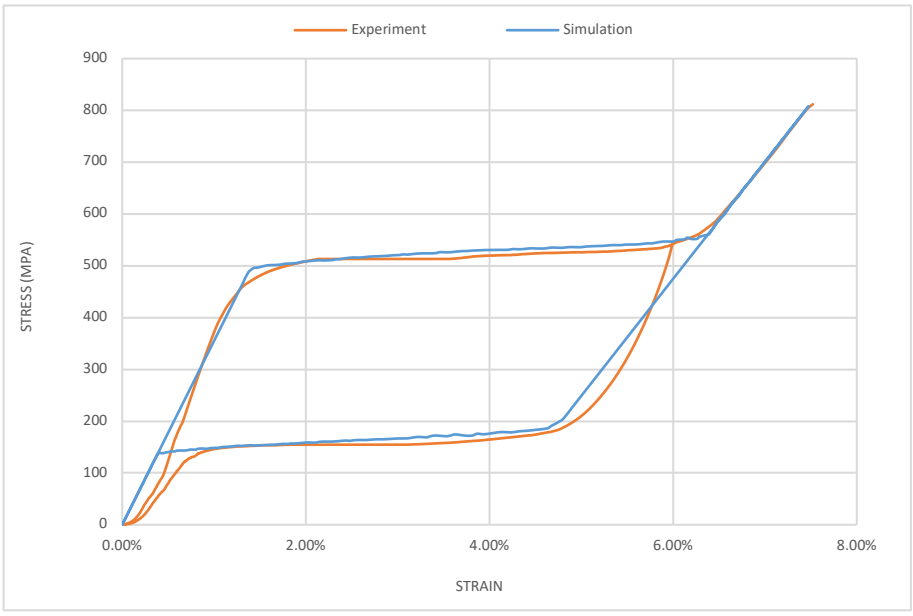

Figure 4.8 – Stress vs strain plots of nitinol wires uniaxial tension test.

Table 4.3 – Calibrated Nitinol VUMAT parameters.

VUMAT Constant	Symbol	Value
Density	ρ	6.5×10^{-9}
Austenite elasticity (MPa)	E_A	35507
Austenite Poisson's ratio	ν_A	0.33
Martensite elasticity (MPa)	E_M	22604
Martensite Poisson's ratio	ν_M	0.33
Transformation strain	ε^L	0.039
ds/dT loading (MPa/°C)	$(\delta\sigma/\delta T)_L$	6.7
Start transformation loading (MPa)	σ_L^S	490
End transformation loading (MPa)	σ_L^E	565
Reference temperature	T_0	22
ds/dT unloading (MPa/°C)	$(\delta\sigma/\delta T)_U$	6.7
Start transformation unloading (MPa)	σ_U^S	190
End transformation unloading (MPa)	σ_U^E	135
Start transform stress compression (MPa)	σ_{CL}^S	612.5
Volumetric transformation strain	ε_V^L	0.039

Table 4.4 – Nitinol VUMAT parameters reported in literature.

Variables	Simulia (2013)	Kleinstreuer et al. (2008)	De Bock et al. (2012)	Nematzadeh et al. (2013)
ρ	6.5×10^{-9}	-	-	-
E_A	40000	51700	35850	20700
ν_A	0.33	0.3	0.3	0.33
E_M	32000	47800	13950	11700
ν_M	0.33	0.3	0.3	0.33
ε^L	0.041	0.063	0.0532	0.055
$(\delta\sigma/\delta T)_L$	6.7	652.7	-	5.32
σ_L^S	440	600	480	344
σ_L^E	540	670	640	363
T_0	22	37	22	37
$(\delta\sigma/\delta T)_U$	6.7	652.7	-	5.32
σ_U^S	250	288	270	58
σ_U^E	140	254	200	42
σ_{CL}^S	0	900	480	0
ε_V^L	0.041	0.063	-	0.055

The finite element analysis result and experimental measurement match well, both falling in line with the range of data reported in literature. There are indeed many sources for deviations and errors. First, the grips were custom made for this specific test. Better, lighter pneumatic grips could be purchased from vendors like Instron as suggested in literature. Secondly, the strain is calculated from crosshead speed instead of using an extensometer because wire diameter is small. However, these should not cause major concern as the mechanical property of nitinol can be also affected by many other factors. For example, nitinol material composition, the percentage of nickel and percentage of titanium, influences the stiffness of the wires. Furthermore, austenite finishing temperature affects the transformation phase of the material. A higher austenite finishing temperature (A_f) will result in a longer and flatter plateau, which means lower stress and force at the same strain, making it more suitable for our design purpose. However, if the A_f is too high, for example, higher than normal body temperature 37 °C, there would be risk of resulting in a stent too soft to expand inside the brain. We chose wires with A_f of 18 °C, because for the proposed SESR, which expands quickly after being introduced into patient's brain, there is a need to have adequate stiffness even at room temperature 22 °C. In summary, we are confident of the experiment measurements and calibrated VUMAT parameters, and thus proceed to finite element analysis of stents and SESRs.

4.4 Finite element analysis

This section covers the finite element analysis of self-expanding stent retractors (SESR) conducted using Abaqus/Explicit. The objective is to find a workflow of SESR design that is capable of desired expansion inside brain tissue. Section 4.4.1 describes the model setups, including construction of z shape nitinol stents using both C3D8I solid elements and B31 beam elements, and construction of Dacron fabric. Section 4.4.2 analyses z shape stents through three studies, flat plate compression, radial compression and release, and parametric study on radial pressure. Section 4.4.3 analyses SESRs through three studies, stent alignment and influence of Dacron, radial crimp and vertical release, and varying radial pressure.

4.4.1 Finite element model setup

4.4.1.1 Stent meshed with C3D8I elements

The z shape stent is constructed by creating a planar 3D deformable part and wrap it into stent ring shape in Abaqus/Explicit. The following script is an example of how the planar zig zag part is sketched.

```
m = mdb.models['Stent']
s = m.ConstrainedSketch(name='D18H10C5', sheetSize=50.0)
xMax = 6.28315307*9
points = []
for i in range(1000):
   x = (float(i)/999)*xMax
   y = 5*sin(x/9*5)
   points.append([x,y])

s.Spline(points=points)
```

Part name D18H10C5 indicates that the stent has an outer diameter of 18mm, a height of 10mm and 5 crowns. xMax is the circumference of stent.range(1000) means there are 1000 points to be generated. In y = 5*sin(x/9*5), 5 is half of the stent height, 9 is stent radius, 5 is the number of crowns. By using a sine curve to define the zig-zag shape, we eliminate sharp turns at the crowns that would be caused by using straight lines, and thus as a precaution, avoid large strain at the crowns when stents are radially compressed. Circular section is used for solid sweep and the planar stent is generated as shown in Fig. 4.9. The diameter of the circle in Fig. 4.9 B is the wire diameter of the stent. In this chapter, three different wire diameters, 0.24mm, 0.32mm and 0.44mm are used to construct stents meshed with C3D8I elements.

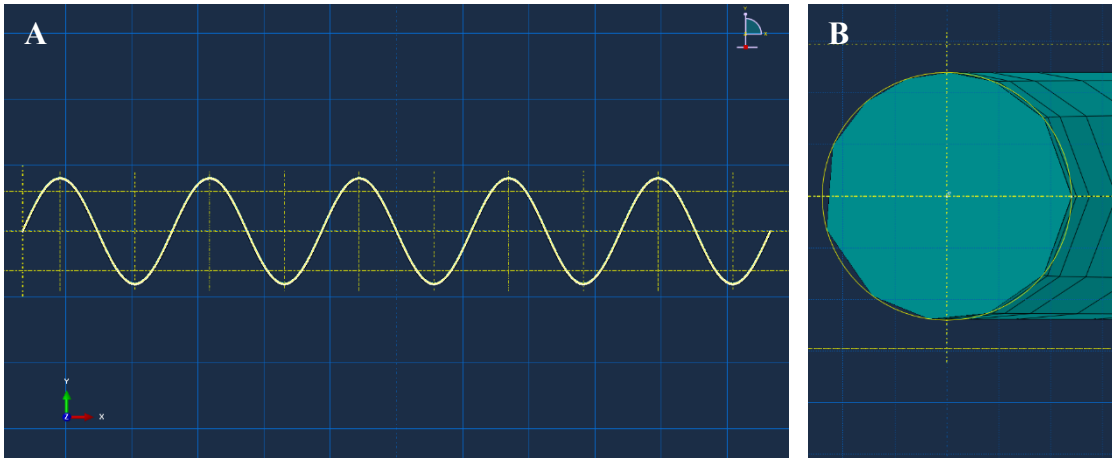

Figure 4.9 – (A) Planar zig-zag stent. (B) Circular cross-section of stent wire.

The planar stent is partitioned and biased seeding is used so that the crowns of the stent have denser meshes while the relatively straighter struts have less dense meshes (Fig. 4.10 A). Sweep mesh technique that minimizes the mesh transition along the medial axis is used. In total 7200 C3D8I elements are generated. The fine mesh is necessary for avoiding element distortions as well as accurately predicting stress and strain in the stents. Mesh sensitivity study has been performed by the means of radial compression test. The

maximum average computed Von Mises stress is derived for different level of mesh refinement of the stent. By refining the mesh, the maximal Von Mises stress converges. A discretisation of 7200 elements was chosen for the stent as a good compromise between the accuracy of the solution and the computation time. The planar stent is then imported into assembly; 3 datum axes are created. Wrap Mesh function is used to wrap the meshed planar stent into a ring shape. Circumferential direction is along the crowns while the axial direction is perpendicular to it (Fig. 4.10 B). The wrapped mesh stent appears as a new part (Fig. 4.10 C). Two free ends of the wire are connected in mesh control by merging adjacent nodes. Superelastic material property of nitinol obtained from uniaxial tension tests in Section 4.3 is used. Input parameters are the ones listed in Table 4.3. The material is named "ABQ_SUPER_ELASTIC_N3D" so that the user material subroutine (VUMAT) can be called upon in Abaqus/Explicit. As stated earlier, this VUMAT is a user material subroutine already available in Abaqus based on the superelastic material model described by Auricchio and Taylor (1997). A solid homogeneous section is created and assigned to the stent.

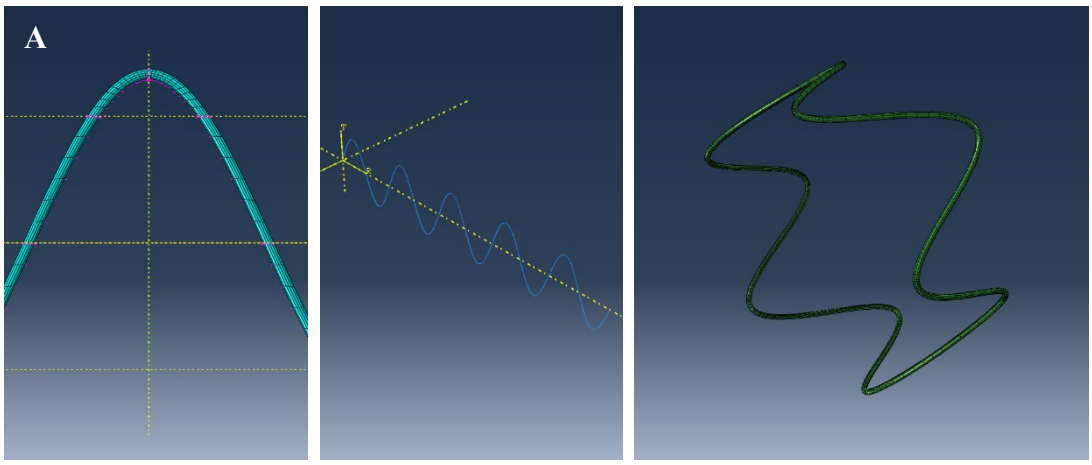

Figure 4.10 – (A) Biased mesh of a (B) planar stent, which is to be wrapped into (C) a stent ring.

4.4.1.2 Stent meshed with B31 elements

The construction of z shape stents using B31 beam elements is similar to that using C3D8I solid elements. The planar zig-zag shape is created using the same script as a 3D deformable wire. After being uniformly meshed with 400 B31 beam elements, it is imported into assembly and wrapped into stent ring shape; adjacent nodes are merged to complete the stent (Fig. 4.11 A). Mesh sensitivity study has been performed by the means of radial compression test. The maximum average computed Von Mises stress is derived for different level of mesh refinement of the stent. By refining the mesh, the maximal Von Mises stress converges. A discretisation of 400 elements was chosen for the stent as a good compromise between the accuracy of the solution and the computation time. As shown in Fig. 4.11 B, the mesh at stent crown is very coarse, yet it is acceptable as literature has shown that coarse uniform mesh is capable of producing good results (Demanget, Avril, et al. 2012; De Bock et al. 2013).

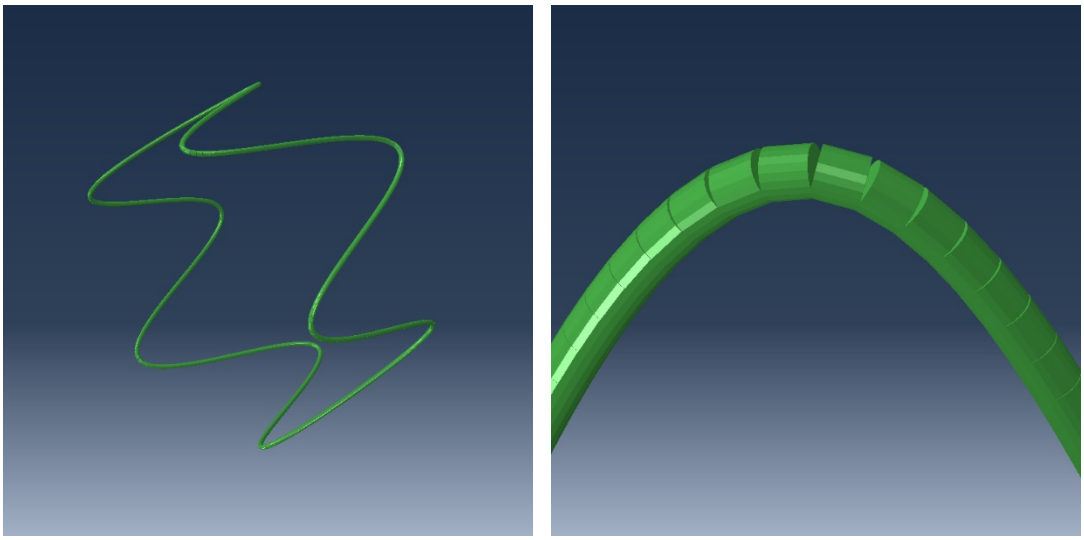

Figure 4.11 – (A) A stent meshed with B31 elements. (B) Uniform coarse mesh at stent crown.

Note that the wire diameter is not defined when creating the stent. It is rather controlled by the beam section that is assigned to the part. A circular profile is selected and transverse shear stiffness is defined for each profile. Beam section orientation is assigned with default parameter (0, 0, -1). Material name for nitinol is changed to "ABQ_SUPER_ELASTIC_N1D" so that the VUMAT can be properly called upon for beam elements. As stated earlier, this VUMAT is a user material subroutine already available in Abaqus based on the superelastic material model described by Auricchio and Taylor (1997).

4.4.1.3 Dacron fabric

Dacron fabric is created as a cylindrical 3D shell part. It has a diameter of 18mm and length of 34 mm. It is 2 mm longer than the proposed SESR because there is 1 mm at each end to prevent severe element distortion at the edges of the fabric. Fabric thickness is 0.1mm. The in-plane orthotropic elastic behaviour of Dacron characterized by Demanget et al. (2013) is used. Homogeneous shell section is assigned to the graft. As explained by Eq. 2.9 in Chapter 2, an adjustment factor of 10 is used. Shell thickness is artificially reduced by 10 times while material elastic modulus is artificially increased by 10 times so that the bending rigidity of shell elements is decreased by 100 times to make Dacron exhibit fabric behaviour in simulations. The fabric is meshed with S3R shell elements of size 0.25mm with all default settings. The fine mesh is necessary for the fabric to be properly tied to stents, as well as avoiding element distortions during folding. Mesh sensitivity study has been performed by the means of radial compression test. The maximum average computed Von Mises stress is derived for different level of mesh

refinement of the fabric. By refining the mesh, the maximal Von Mises stress converges. A discretisation of 61427 elements was chosen for the fabric as a good compromise between the accuracy of the solution and the computation time. With its inner and outer surfaces defined, the Dacron fabric is imported into assembly and coaxially aligned with stents to form the SESR. Tie constraints are used to tie the stents and the inner surface of Dacron fabric, with fabric surface being the master surface while stent surface being the slave surface. Alignment of the stents and influence of the fabric is investigated in section 4.4.3.

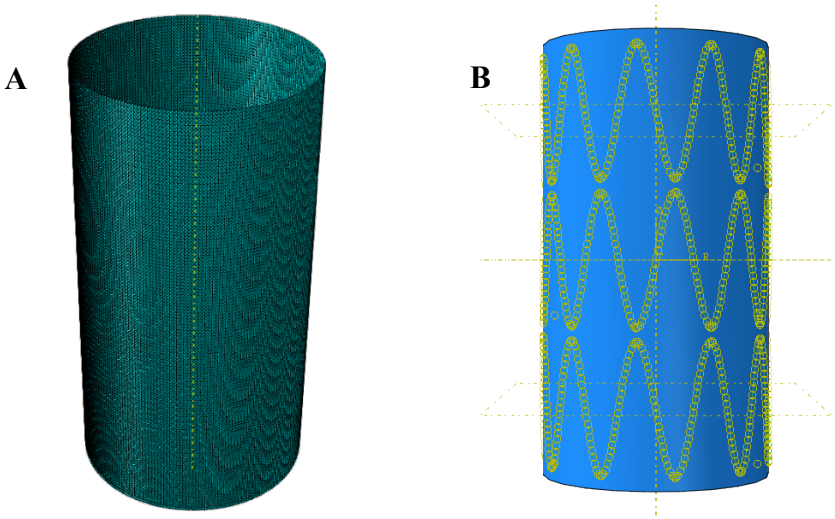

Figure 4.12 – (A) Dacron fabric with fine mesh. (B) Constraints that tie stents and fabric together to form the self-expanding stent retractor.

4.4.2 Finite element analysis of z shape stents

4.4.2.1 Flat plate compression

Flat plate compression tests of single z shape stents are simulated with two objectives. The first objective is to compare results between C8D3I element mesh and B31 beam element mesh of the same stent. The second objective is to compare simulation results with experimental measurements to validate the finite element model. Two analytical rigid flat plates are used to compress the stents meshed with both C3D8I and B31 elements. Tested stents all have a diameter of 18mm, height of 10mm and 5 crowns, with varying wire diameters of 0.24mm, 0.32mm and 0.44mm. At the beginning of the simulation, the rigid plates are placed right above and below the stent. In a dynamic explicit step of 0.024 seconds, they move towards each other for a compression distance of 12mm (Fig. 4.13). One stent node is pinned to avoid rigid body movement. All stent nodes are subjected to a temperature field of 37 °C, same as normal human body temperature. Interaction is defined using general contact algorithm, with Penalty friction coefficient of 0.1 in the tangential direction and Hard contact in the normal direction. History output of the reaction forces and displacements of rigid plates are requested. Internal energy and kinetic energy of the whole model is monitored to ensure kinetic energy is less than 5% of internal energy so that the simulation can be considered quasi-static.

Figure 4.14 is an example of maximum principal strain comparison in stents of 0.32mm wire diameter at 12mm compression using C3D8I elements and B31 elements. Because of the fine mesh at crowns, the C3D8I stent can predict which portion of the stent has higher strain. On the other hand, the B31 stent can only tell that maximum strain

happens at two of the crowns. Furthermore, both maximum principal strain and maximum von Mises stress predicted in B31 stents are lower than those of C3D8I stents, as summarised in Table 4.5 and 4.6.

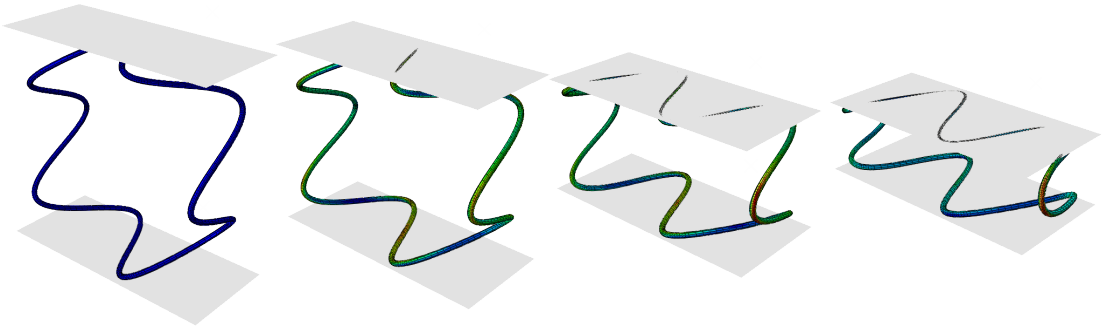

Figure 4.13 – Flat plate compression of a z shape stent.

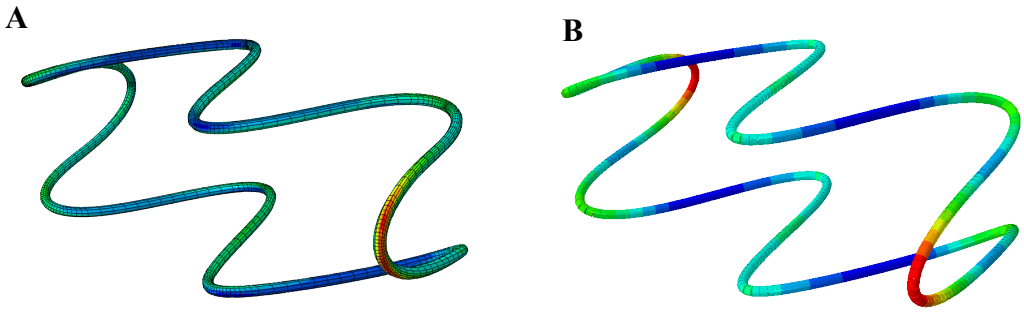

Figure 4.14 – Maximum principal strain in (A) C3D8I and (B) B31 stents at 12mm compression.

Table 4.5 – Comparison of maximum principal strain

Wire diameter	B31	C3D8I
0.24mm	0.764%	1.262%
0.32mm	1.027%	1.551%
0.44mm	1.457%	1.839%

Table 4.6 – Comparison of maximum von Mises stress

Wire diameter	B31	C3D8I
0.24mm	306.5 MPa	526.9 MPa
0.32mm	413.5 MPa	697.7 MPa
0.44mm	579.1 MPa	971.6 MPa

Table 4.7 – Comparison of maximum compression force

Wire diameter	B31	C3D8I
0.24mm	0.203 N	0.190 N
0.32mm	0.613 N	0.593 N
0.44mm	2.546 N	2.454 N

Nevertheless, the compression force from both models shows very good agreement (Fig. 4.15 and Table 4.7). The percentage differences in maximum compression force at 6.8%, 3.37% and 3.75% for stents with wire diameters of 0.24mm, 0.32mm and 0.44mm, respectively. This simulated compression results will also be used to compare with experimental measurements in next section to further validate the finite element model.

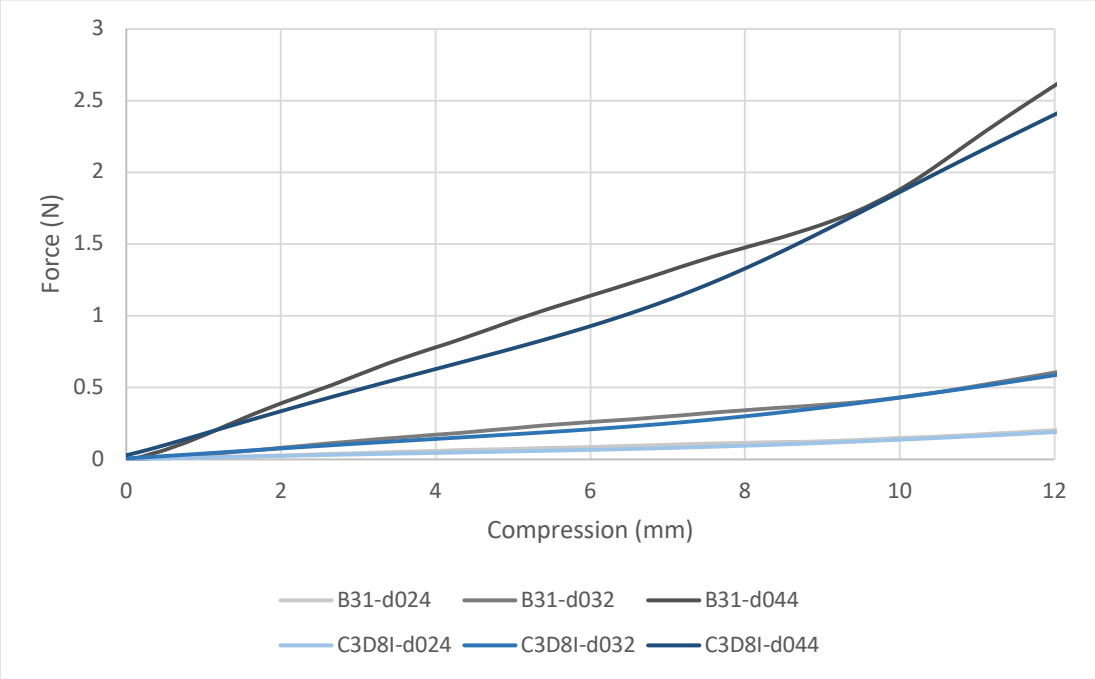

Figure 4.15 – Compression force versus distance plot for C3D8I and B31 stents.

4.4.2.2 Radial compression and release

Radial compression and release of single z shape stents are then simulated to further compare results between C8D3I element mesh and B31 beam element mesh of the same stent. Tested stents are the same as those for the flat plate compression test. The model setup is also similar to the flat plate compression test, except that this time a circular crimp tool is used to radially compress and release the stents. It is defined as a deformable 3D part and assignment shell surface section with its inner surface used for contact with stents. It is meshed with 50 surface SFM3D4R elements, so that there are 50 nodes at each end of the crimp tool, and imported into the assembly to coaxially align with the stent. A cylindrical coordinate system is created to manipulate the crimp tool.

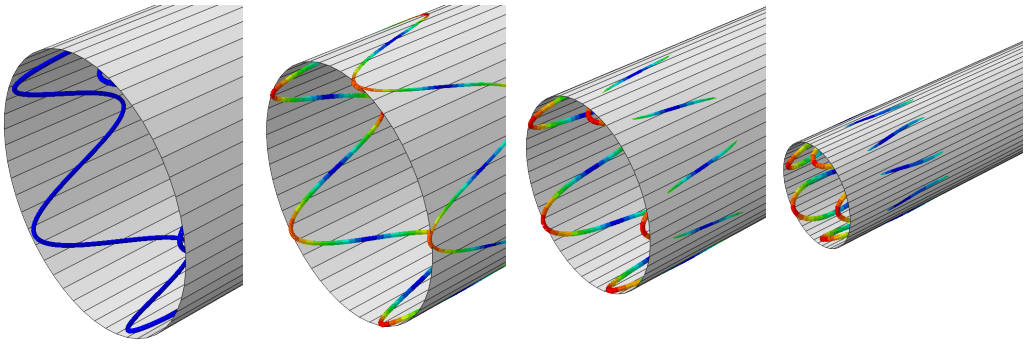

Figure 4.16 – Radial compression of a z shape stent.

In step 1, all crimp tool nodes move radially inward to crimp the stent from 18mm original diameter to 7mm diameter (Fig. 4.16). Crimp tool nodes are controlled with velocity boundary conditions and a smooth step amplitude. In step 2, all stent nodes radially move outward with the same boundary condition to release the stent. History output of nodal force on all crimp tool nodes in X and Y directions are requested with antialiasing filter applied. Displacement of one crimp tool node is also requested. The nodal force data is then exported from Abaqus .odb and imported into MATLAB. The

same script as in Appendix 2 is used to combine nodal force outputs in X and Y directions into a scalar radial force.

Table 4.8 – Comparison of maximum principal strain

Wire diameter	B31	C3D8I
0.24mm	1.790%	2.574%
0.32mm	2.530%	4.067%
0.44mm	4.048%	5.538%

Table 4.9 – Comparison of maximum von Mises stress

Wire diameter	B31	C3D8I
0.24mm	71.0 MPa	102.2 MPa
0.32mm	96.1 MPa	104.3 MPa
0.44mm	131.7 MPa	131.0 MPa

Table 4.10 – Comparison of maximum radial force

Wire diameter	B31	C3D8I	Theoretical
0.24mm	1.350 N	1.578 N	1.192 N
0.32mm	4.075 N	4.310 N	3.767 N
0.44mm	12.924 N	12.870 N	13.465 N

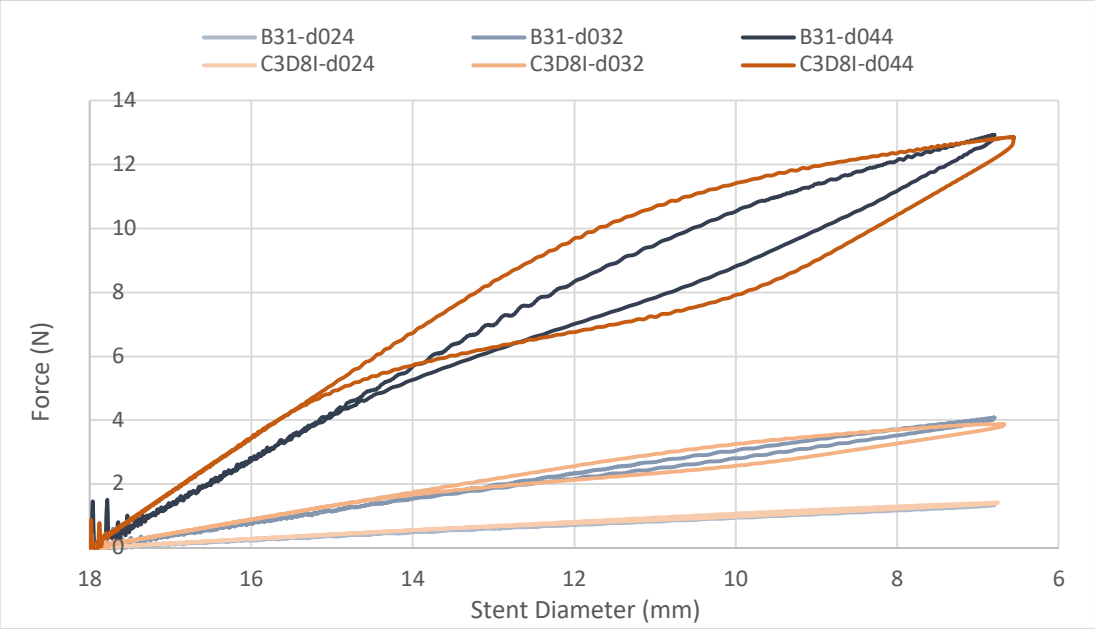

Figure 4.17 – Radial force during loading and unloading of B31 and C3D8I stents.

The comparisons of maximum principal strain, maximum von Mises stress and maximum radial force are summarised in Table 4.8, 4.9 and 4.10. As expected, B31 stents under predicts both strain and stress because of their coarse meshes at the crowns. Nevertheless, as with the flat plate compression force, the radial force during loading and unloading show good agreement between B31 and C3D8I stents, as shown in Fig. 4.17.

Despite the inaccuracies in predicting strain and stress at one specific location of the stent, we decide to move forward with B31 mesh stent for two reasons. First, the B31 mesh is much more computationally efficient than C3D8I mesh. With future additions of graft elements and their interactions with brain tissue elements, we need to keep the computational cost as low as possible. Secondly, B31 element is sufficient in predicting radial force, which is the key design parameter in this thesis. Furthermore, the maximum principal strain in 0.44mm wire diameter C3D8I stent is 5.538%, which is much lower than the 8% limit of nitinols recoverable strain. Since the 0.44mm wire diameter stent is already much stiffer than stents we would use, it is safe to say that SESR designs in this thesis do not have the risk of going over the 8% limit of recoverable strain for nitinol.

4.4.2.3 Parametric study on radial pressure

A parametric study on radial pressure is then conducted using B31 element stent, in an attempt to find the range of geometric parameters for a single stent that is capable of expanding to certain diameters inside brain tissue. Stents have diameter of 18mm and height of 10mm. Stent type A has 5 crowns while stent type B has 10 crowns. For each stent type, wire diameter varies from 0.27mm to 0.36mm. In total 20 different geometries are studied as summarised in Table 4.11.

Table 4.11 – Geometric parameters used for radial pressure study

Stent diameter = 18mm, height = 10mm										
Number of crowns	Type A: 5 crowns									
	Type B: 10 crowns									
Wire diameters (mm)	0.27	0.28	0.29	0.30	0.31	0.32	0.33	0.34	0.35	0.36

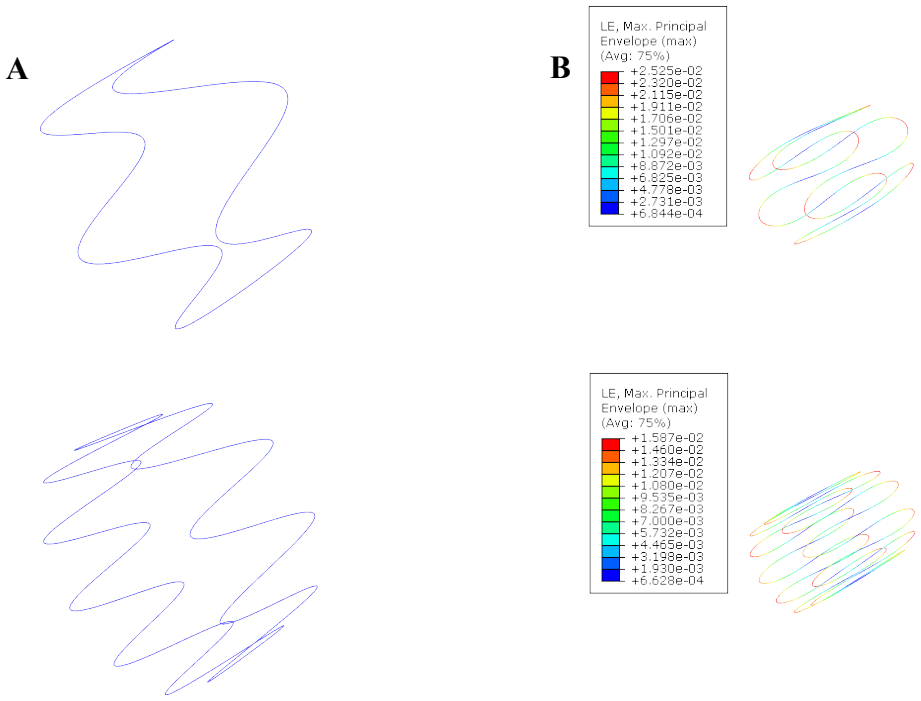

Figure 4.18 – 5-crown stent and 10-crown stent (A) original shape and (B) at the end of radial compression. Maximum principal strain contour.

The finite element model setup is the same as the radial compression and release test in the last section. Figure 4.18 shows the geometries of type A 5-crown stent and type B 10-crown stent with wire diameter of 0.32mm. The maximum principal strain contours at the end of radial compression are also shown. Note that the peak strain in type A stent (2.525%) is higher than that in type B stent (1.587%) because the deflection gets more

distributed among crowns. Although the exact value of strain is underestimated when using B31 elements, it is important to understand the trend that a higher number of crowns decreases the peak strain in the stent if all other parameters are kept the same.

With the radial force obtained the same way as in the last section, the radial pressure of the stent is calculated as

$$k_\theta = \frac{F}{\pi(D - \Delta d) \times H}, \tag{4.1}$$

where F is the radial force, D is original stent diameter which is 18mm, Δd is change in diameter and H is stent height which is 10mm. The radial pressure for type A and B stents during radial loading and unloading is plotted in Fig. 4.19. In the legend, "d027", "d028", "d029", …, "d035", "d036" denotes the stents with wire diameter of 0.27mm to 0. 36mm.There are three main findings from this result. First, as predicted by the theoretical model, the radial pressure increases dramatically with increasing wire diameter. The peak pressure at 7mm for Type A wire diameter 0.36mm stent (22.7 kPa) is almost 3 times of that for Type A wire diameter 0.27mm stent (7.68 kPa). Secondly, increasing number of crowns will cause the radial pressure to decrease. For the same wire diameter, Type B 10-crown stents have radial pressure that is 20-25% smaller than those of Type A 5-crown stents. Thirdly, the biased stiffness effect discussed earlier in literature review is not significant here because not enough portion of the stent has reached nitinol's stress plateau. Because of the thin wire diameter, the strain in stents almost never reaches transformation strain, thus the loading and unloading path show little to no difference.

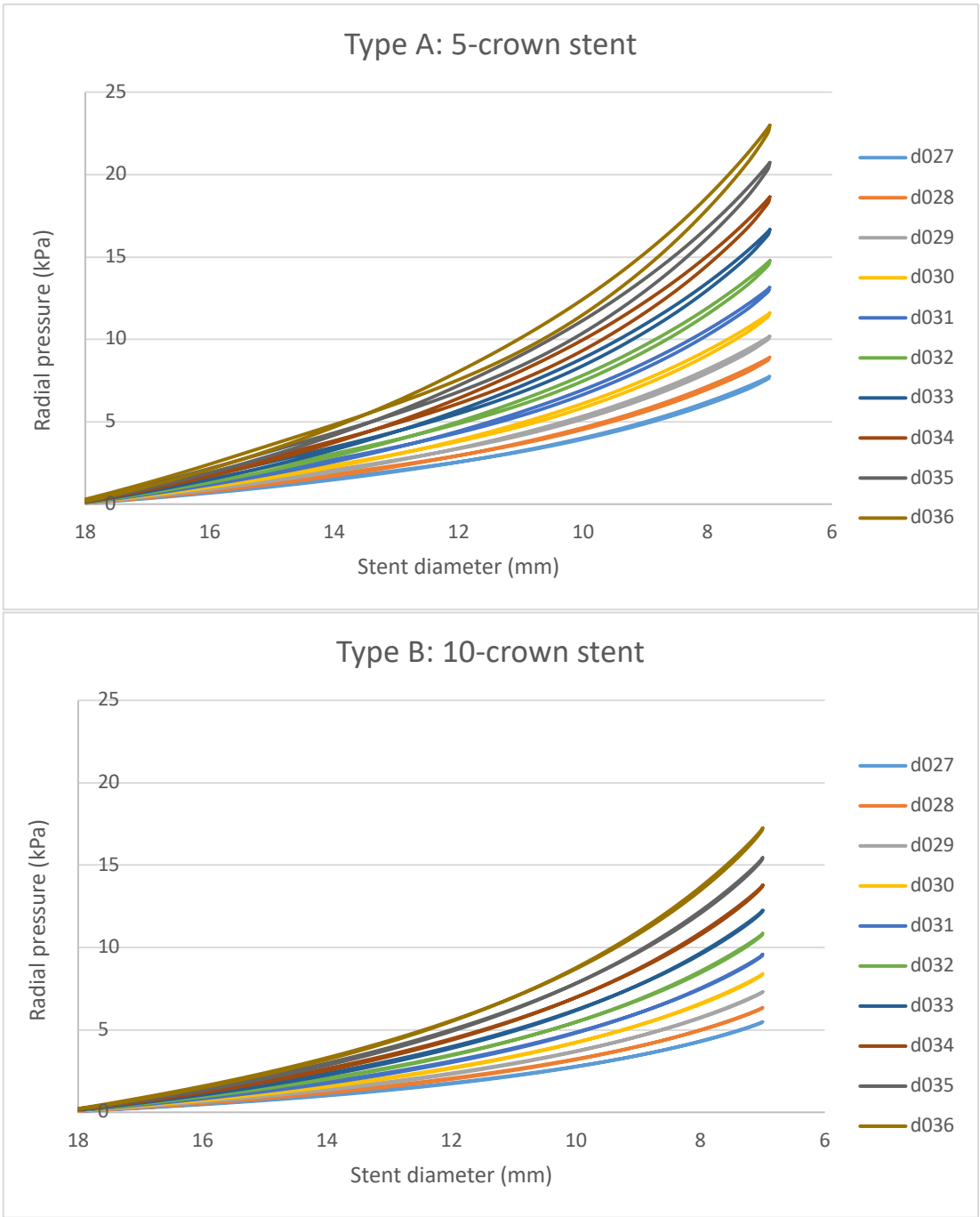

Figure 4.19 – Type A and Type B stents radial pressure during loading and unloading.

A closer look of radial pressure between stent diameter 15.5mm and 16.5mm is shown in Fig. 4.20 because this is the diameter that we would like the SESR to expand inside the brain. As we learned from the last chapter, the average pressure needed for 16mm expansion inside the brain is 2.085 kPa and this pressure gradually decreases to 1.473 kPa

over time because of the viscoelastic property of brain tissue. If the depth inside brain is considered, expansion deeper inside the brain requires as much as 2.24 kPa while expansion near the top requires as little as 1.89 kPa. Therefore, we look for stents whose radial pressure at 16mm diameter fall in the range between 2.24 kPa and 1.473 kPa. Because the influence of adding a covering layer of Dacron fabric is yet studied, a broader range is taken. For type A 5-crown stents, wire diameter from 0.31mm to 0.33mm will be considered for SESR application. For type B 10-crown stents, wire diameter from 0.34mm to 0.36mm will be considered.

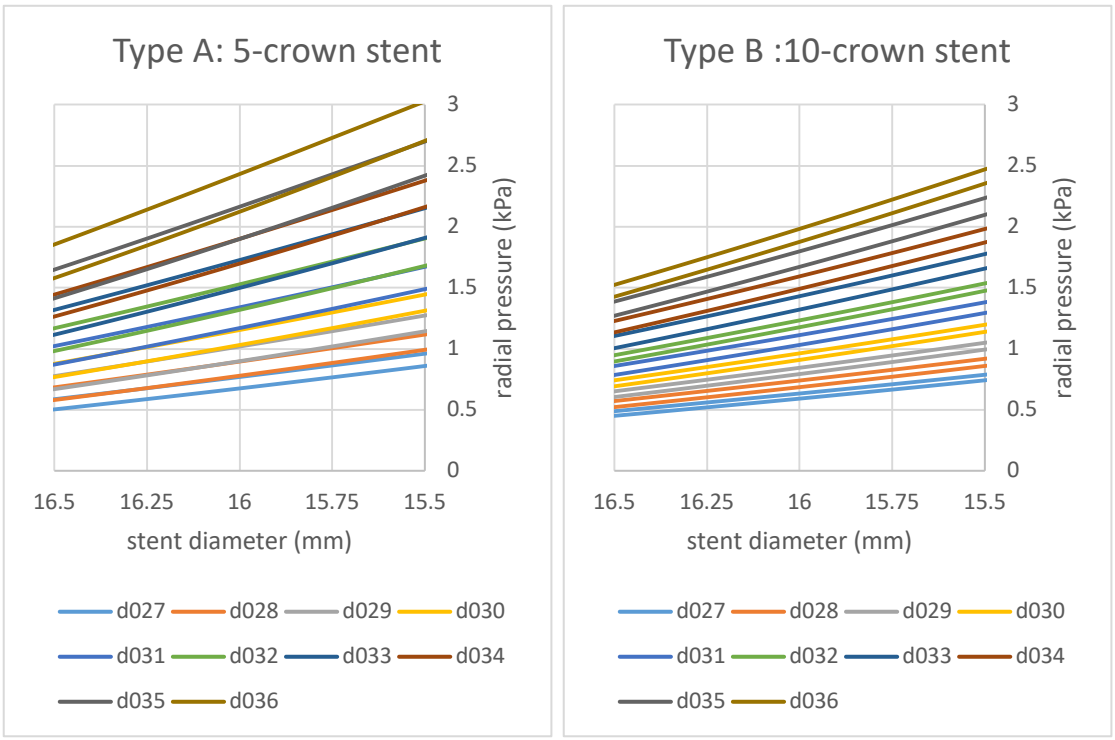

Figure 4.20 – Close-up look of stent radial pressure between diameter 15.5mm and 16.5mm.

4.4.3 Finite element analysis of self-expanding stent retractor

In this section, two aspects of the self-expanding stent retractor are analysed in Abaqus/Explicit. First, the radial compression and vertical deployment process of SESR is simulated. Four different SESR designs are used to find the influence of Dacron fabric as well as the alignment of stents on SESR's geometry and size during deployment. Secondly, the radial pressure of two SESR designs is studied. Specifically, with the addition of Dacron fabric, the radial pressure during unloading between 17-mm and 15-mm diameter is investigated in order to find a range of wire diameters that provides adequate pressure for the desired diameter.

4.4.3.1 Radial compression and vertical deployment

Four different SESR designs, as shown in Fig. 4.21, are studied in the radial compression and vertical deployment simulation. They are named C5A1, C5A2, C10A1 and C10A2, with "C" indicating the number of crowns in a stent and "A" indicating stent alignment options. All stents have height of 10mm and diameter of 18mm, the same as the ones in the parametric study in the last section. The first two designs use stents with 5 crowns while the second two designs use stents with 10 crowns. Alignment A1 means that stents are attached to the fabric in the same orientation one by one so that the stent crowns face the valleys of adjacent stents. Alignment A2 rotates the middle stent by an angle so that stent crowns face the crowns of adjacent stents. For comparison purposes, all four designs have stent wire diameter of 0.32mm. Dacron fabric has a length of 34 mm, with 1mm between the stent crowns and fabric edge at each free end. Thus, the effective length of the SESR is 32mm. Stents and fabric are connected using tie constraints. Figure 4.22 A

shows the connection at one of the crowns. Red dots indicate the fabric nodes that are tied to the stent. All stent nodes are subjected to a temperature field of 37 °C. Interaction is defined using general contact algorithm, with Penalty friction coefficient of 0.1 in the tangential direction and Hard contact in the normal direction. History output of displacements of stent nodes is requested. Fig. 4.22 B shows the top, middle and bottom nodes of a 5-crown stent. The displacements of these nodes will be used to calculate the geometry of each SESR design during radial compression and vertical deployment.

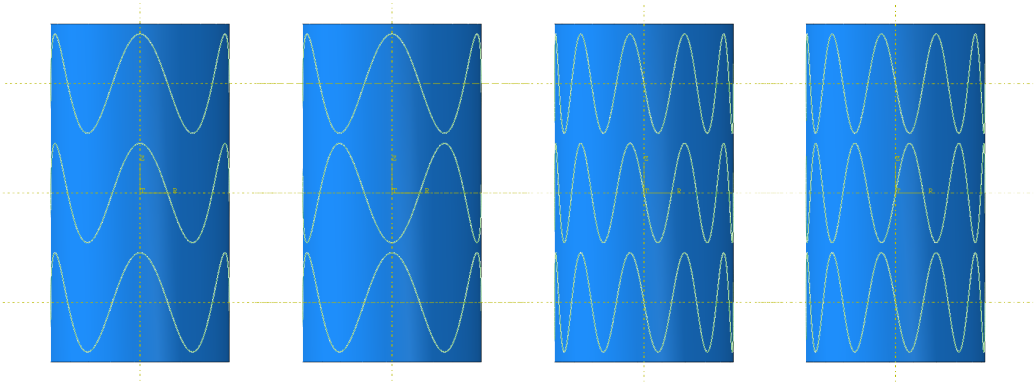

Figure 4.21 – Four different SESR designs named as “C5A1”, C5A2”, “C10A1” and “C10A2”.

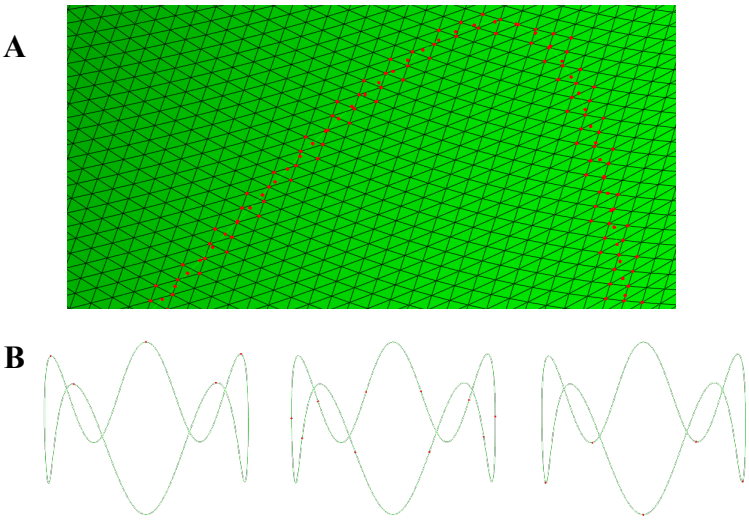

Figure 4.22 – (A) Dacron fabric nodes connected to stents using tie constraints. (B) Top, middle and bottom nodes of a 5-crown stent.

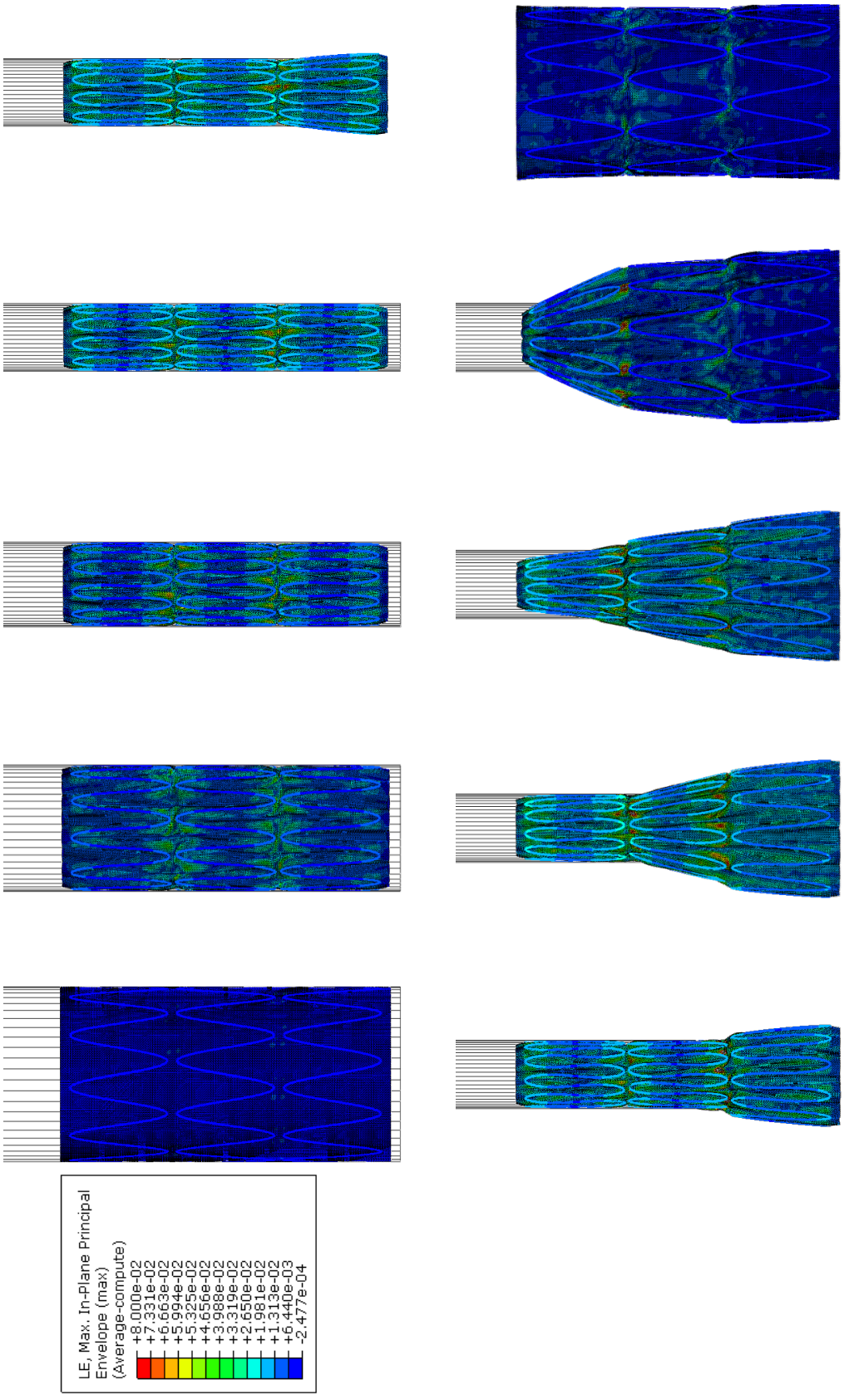

Figure 4.23 – Radial compression and vertical deployment of a C10A2 SESR

The radial compression step is the same as that of radial compression of a single stent in the last section. In a step of 0.024 seconds, the crimp tool radially compressed SESR from 18mm in diameter to 7mm in diameter. No stent nodes are pinned in this step. For vertical deployment, stent node boundary conditions are used to serve the purpose of the stopper. Middle nodes, as marked by red dots, of each stent are pinned so that SESR does shift in longitudinal or latitudinal direction. In a step time of 0.036 seconds, the crimp tool moves vertically for 54mm to deploy SESR and give it a little time to settle from vibration. Simulations are performed in Abaqus/Explicit. The compression and deployment of a C10A2 SESR is shown in Fig. 4.23 as an example.

The lengths of four SESR designs are compared in Fig. 4.24. There is a temporary decrease of length around 0.045s, which is when the SESR is just about to be fully deployed. The top crowns dip downward while the crimp tool moves upward (Fig. 4.23 - 8 and 9). We found that C5 SESRs have a shorter length than C10 SESRs both at the end of compression and at the end of the deployment. As for stent alignment, A1 SESRs are shorter than A2 SESRs during the entire compression and deployment process.

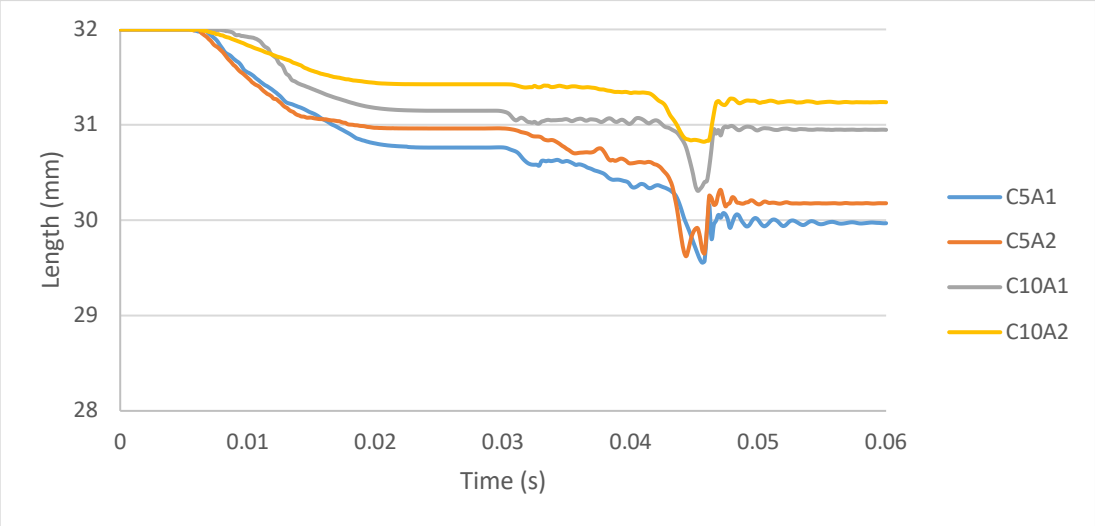

Figure 4.24 – Comparison of SESR lengths during radial compression and vertical deployment.

The diameters of four SESR designs are compared in Fig. 4.25. The diameter of each stent of the SESR is plotted so that it can be clearly seen that the stents are deployed one by one. There are notable fluctuations in diameter during deployment, especially for the stent. It is sensible because the deployment is a rather dynamic process. No matter how slowly the crimp tool moves, the moment where one stent is fully deployed will release a considerable amount of strain energy. We found that both C5A2 and C10A2 SESRs are able to fully return to their original diameter of 18 mm after deployment, while C5A1 and C10A1 SESRs have some stents with deployed diameters smaller than 18 mm. This is most likely due to the tie constraints between stents and fabric.

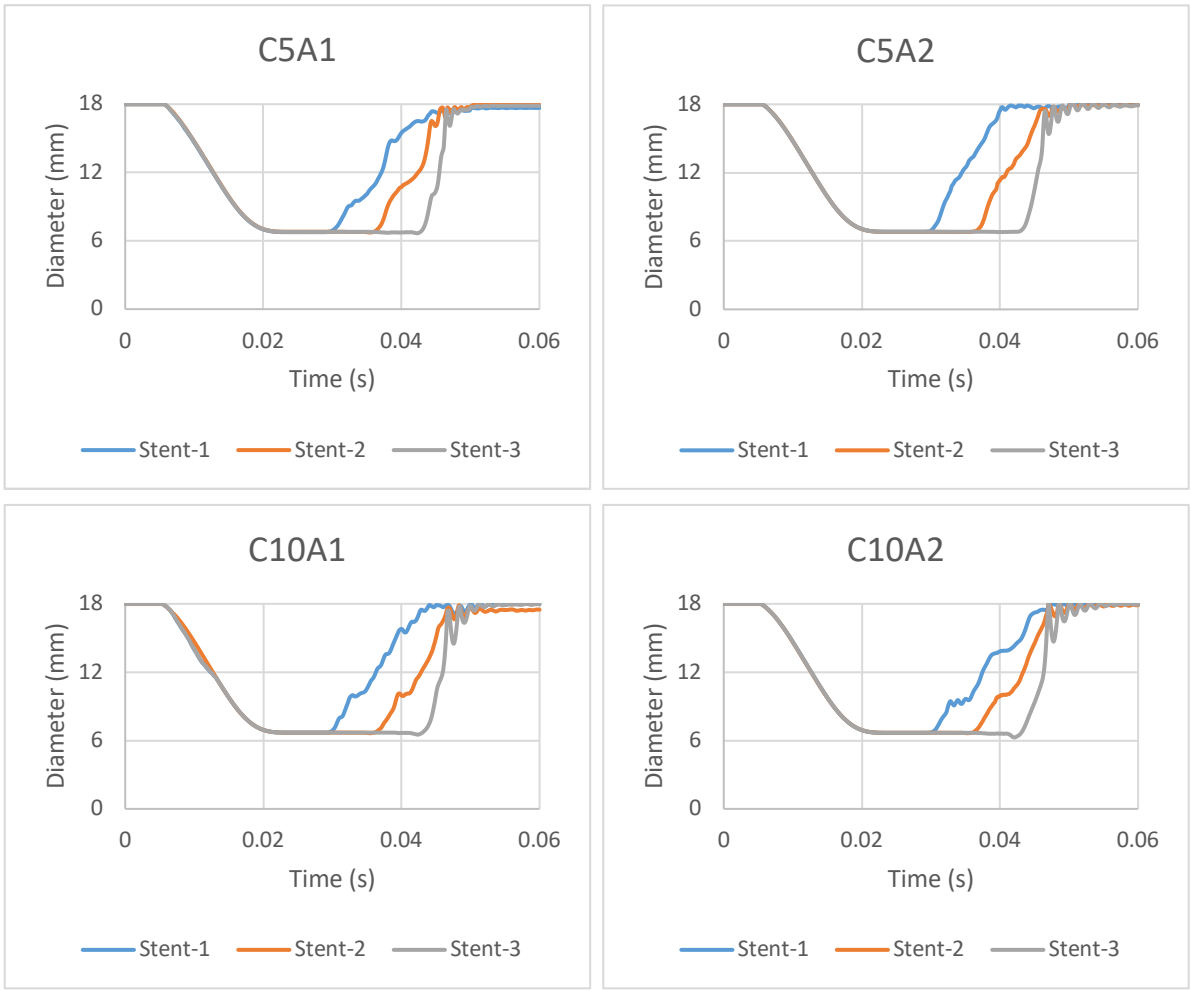

Figure 4.25 – Comparison of SESR diameters during radial compression and vertical deployment.

Therefore, the strains in stents and fabrics are further investigated to understand the influence of fabric. Table 4.12 summarises the maximum true strains (LE) in stents and fabric at the end of compression and the end of the deployment. Values for 5-crowns and 10-crowns stents without fabric are listed for comparison. Maximum radial forces are also compared.

Table 4.12 – Comparison of SESR strains and maximum radial forces.

	Stents Max. LE compression	Stents Max. LE deployment	Fabric Max. LE compression	Fabric Max. LE deployment	Max. radial force
C5 (no fabric)	2.525%	0.01920%	N/A	N/A	9.77 N
C5A1 (with fabric)	2.788%	0.1675%	11.57%	7.523%	11.70 N
C5A2 (with fabric)	2.696%	0.1612%	15.57%	10.97%	10.52 N
C10 (no fabric)	1.587%	0.02762%	N/A	N/A	7.16 N
C10A1 (with fabric)	1.650%	0.1884%	6.417%	5.699%	9.21 N
C10A2 (with fabric)	1.599%	0.1786%	9.458%	6.866%	8.56 N

Addition of fabric results in a 10-20% increase of maximum radial force at the end of compression. This is comprehensible because when the 18-mm diameter SESR is compressed to 7 mm in diameter, there is considerable amount of contact between stents and fabric, as well as self-contact among fabric. However, since the fabric is just a thin layer that is easily foldable, the resultant increase is not very significant. The influence on radial force and pressure will be studied more in Section 4.4.3.2. As for the four different designs, C10 SESRs have lower radial forces and strains in both stents and fabric than C5 SESRs because of the same wire diameter used for their stents. A1 SESRs have higher maximum radial force and maximum strain in stents than A2 SESRs. However,

maximum fabric strains are lower in A1 SESRs than in A2 SESRs. Figure 4.26 shows the strains in four SESR's at the end of the deployment. Although C5A2 and C10A2 SESRs have higher maximum strains between stent crowns, the overall strain levels are much lower than those in C5A1 and C10A1 SESRs. A1 alignment results in more shortening of the SESRs because stent crowns slide slightly into the valleys of adjacent stents. The fabric between them folds inwards and has considerably more remaining strain after deployment. The higher maximum strains in A2 SESRs should not be a concern because they are far below the elastic limit of Dacron.

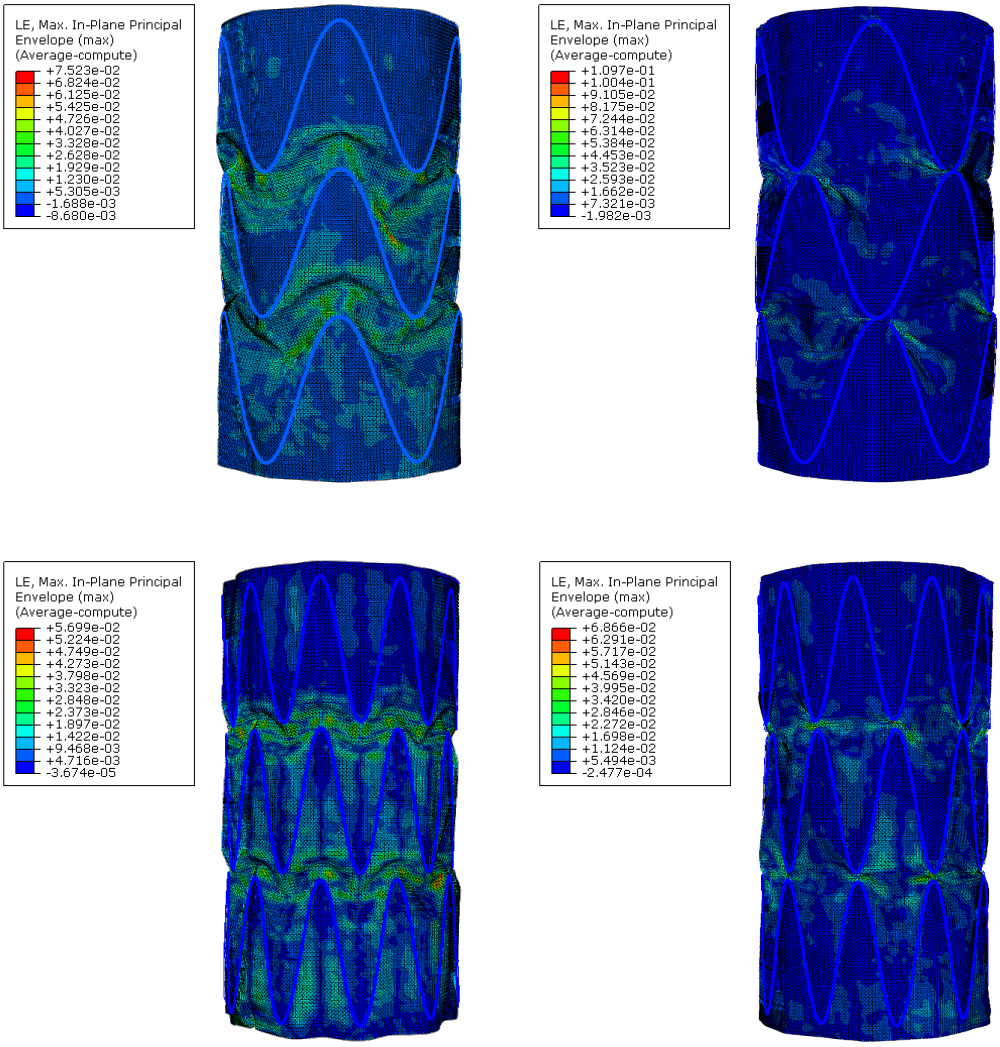

Figure 4.26 – Comparison of remaining strain in Dacron fabric after vertical deployment.

In short summary, this section investigated the radial compression and vertical deployment of four different SESR designs. We learnt that the A2 alignment, which is to have stent crowns facing towards adjacent stent crowns, results in less shortening, more uniform and complete radial expansion of the SESR. It also reduces the constraints that fabric put on stents, causing less change in strain and radial force when compared to stents without fabric. Therefore, we use C5A2 and C10A2 SESRs to further investigate the influence of fabric on radial force and pressure.

4.4.3.2 Radial pressure during unloading

SESR radial pressure during unloading is the metric to be used for comparison because the biased stiffness effect, albeit not significant when stents are not subject to high strains, could still cause considerable difference between loading and unloading phase at the same diameter. C5A2 SESR with stent wire diameter of 0.31 mm, 0.32 mm and 0.33mm and C10A2 SESR with stent wire diameter of 0.34 mm, 0.35 mm and 0.36 mm are studied. The finite element analysis performed is the same as the parametric study on radial pressure in the last section, except that the single z shape stent is replaced by SESR.

Figure 4.27 shows C5A2 SESR with a wire diameter of 0.32 mm as an example to illustrate the influence of fabric on radial pressure. In this case, radial pressure of SESR is on average 23.4% more than that of stents without fabric. More importantly, radial pressure increase during loading phase is 34.3% while the increase during unloading phase only 12.5%. This is because the addition of fabric causes higher strains in stents during the loading phase so that more portions of the stents would reach nitinol's stress plateau, resulting in a more visible biased stiffness effect during unloading. The exact

increase percentage differs slightly for different SESR designs and wire diameters and is not of concern because in this thesis we only consider SESR designs with fabric. Radial pressures during the unloading phase of C5A2 and C10A2 SESR's are shown in Fig. 4.28, while maximum true strains (LE) in stents and fabric are compared in Table 4.13.

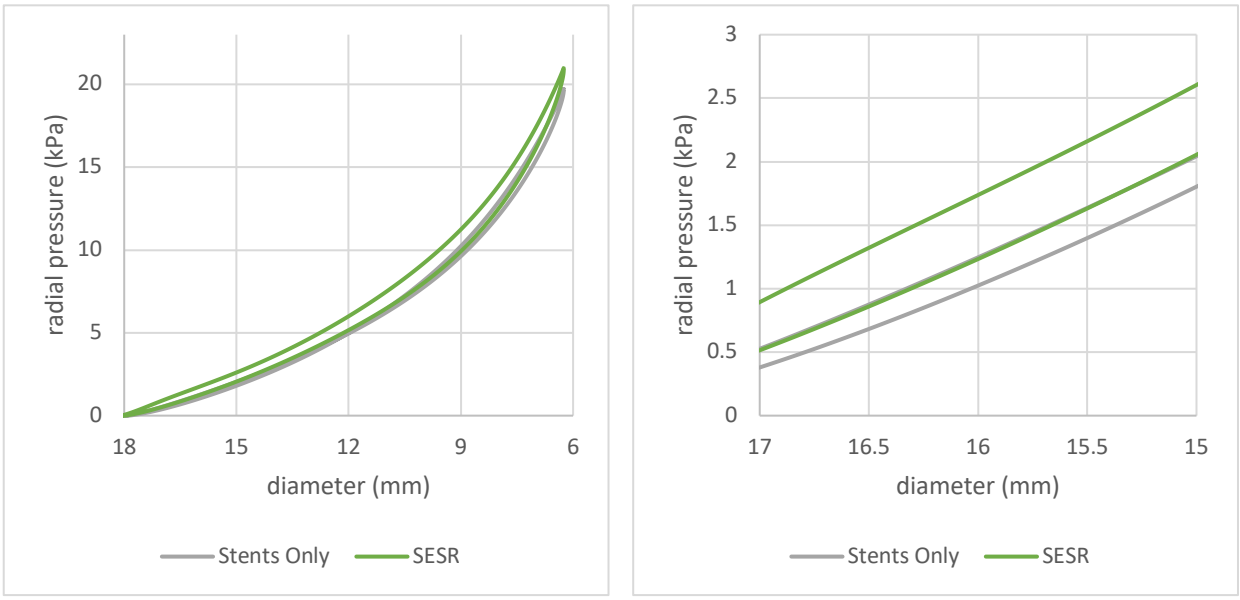

Figure 4.27 – Influence of fabric on radial pressure.

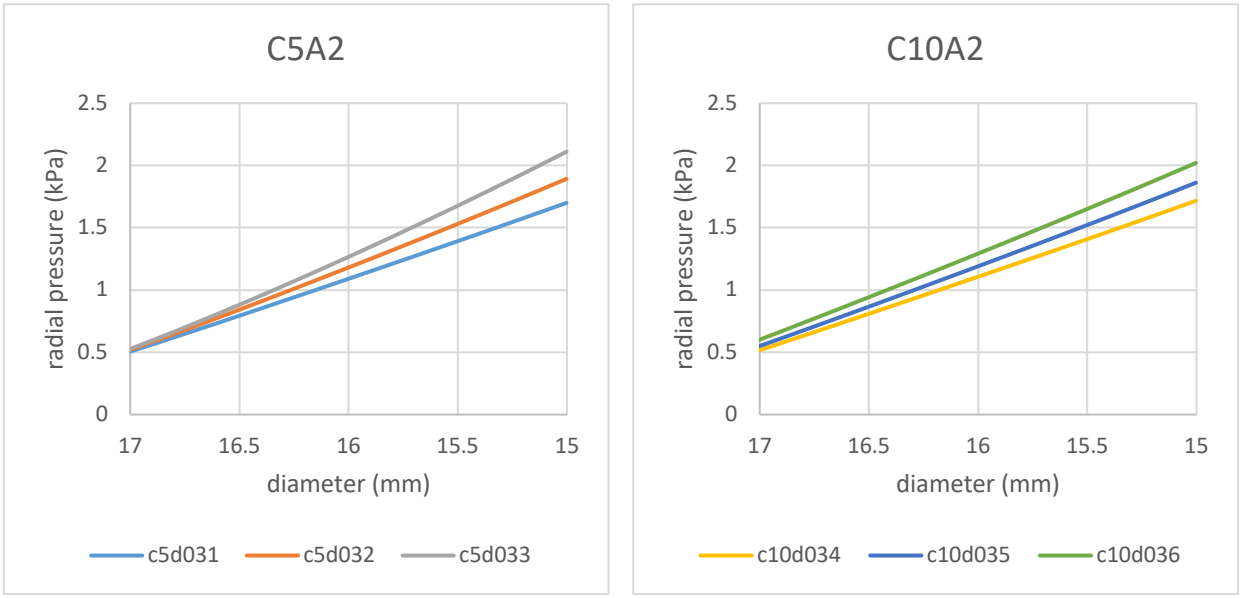

Figure 4.28 – Radial pressure during unloading phase.

With larger stent wire diameters, C10A2 SESRs could produce almost identical radial pressure versus diameter plots as the C5A2 SESRs with smaller wire diameter. To achieve a similar level of radial pressure, the maximum strains in stents after compression are also similar. On the other hand, fabric strains after compression and deployment are always smaller in C10A2 SESRs than in C5A2 SESRs. However, this does not matter much because no strains are even close to Dacron's elastic limit. Therefore, we find neither 5-crown or 10-crown SESRs has a distinct advantage over the other. No matter which SESR design we choose, to cover the range of 1.472 kPa to 2.24 kPa, which is the required expansion pressure inside brain considering depth, unloading radial pressure at certain diameter can be easily adjusted by changing nothing but stent wire diameter.

Table 4.13 – Comparison of strains in stents and fabrics

Comparison	Set #1		Set #2		Set #3	
	C5A2-d031	C10A2-d034	C5A2-d032	C10A2-d035	C5A2-d033	C10A2-d036
Stent Max. LE after Compression	2.599%	2.459%	2.696%	2.76%	2.845%	3.024%
Fabric Max. LE after Compression	16.4%	13.25%	15.57%	13.74%	16.93%	14.34%
Fabric Max. LE after Deployment	9.46%	8.56%	10.97%	8.436%	12.97%	6.13%

It should be noted that a SESR design with precise wire diameter is yet determined here because how SESR interact with brain tissue phantom remains unknown. Instead, reasonable ranges for the stent wire diameter, 0.31mm to 0.33mm for 5-crown SESR and

0.34mm to 0.36mm for 10-crown SESR, are identified. Lots of factors, for example, friction, contact between fabric and brain tissue, depth inside the brain and viscoelastic property of brain tissue, could all potentially affect the deployment diameter predicted merely from radial pressure. What we have achieved here is a design range that is to be further tested for deployment in next chapter.

4.5 Prototyping and Experiments

This section describes the prototyping process of 5-crown z shape stents, self-expanding stent retractors with C5A2 design and delivery system. Experimental flat plate compression tests are also conducted. The objectives of prototypes and experiments are to prove the concept of SESR, further validate finite element analysis results and prepare for deployment experiment in Chapter 5.

4.5.1 Prototypes and proof of concept

Based on finite element analysis in the last section, stent prototypes with three different wire diameters, 0.24mm, 0.32mm and 0.44mm are made from nitinol wires (EUROFLEX GmbH, Stuttgart, Germany) used for uniaxial tension test. The stents all have diameter of 18mm, height of 10mm and 5 crowns. A pair of rigs (Fig. 4.29 A), one flat and one cylinder, were custom made from brass to set the wires into z shape stent geometry via heat treatment. The goal of the heat treatment is to anneal residual stress in nitinol wires when they are bent and confined into stent shape; the procedure is based on literature (Drexel et al. 2006) as well as trial and error. First, the wire was fixed into the notch on the flat rig as shown in Fig. 4.29 B and put into Carbolite chamber furnace (Carbolite Gero Limited, Hope Valley, United Kingdom) and heat-treated at 450 °C for 20 minutes. It was water quenched right after being taken out from the furnace. The point of the first step was to give the wire a zigzag shape as shown in Fig. 4.29 C, so that it would be easier to be fixed into the notch on the cylinder rig as shown in Fig. 4.29 D. Without the flat rig step, it was virtually impossible to fix the wires into the cylinder rig by hand because of the superelastic nature of nitinol. Once fixed on the cylinder rig, the wire was put back

into the furnace and heat-treated at 500 °C for 12 minutes. Finally, it was taken out and water quenched again. A z shape stent was thus formed except that the two free ends of the wires were not connected.

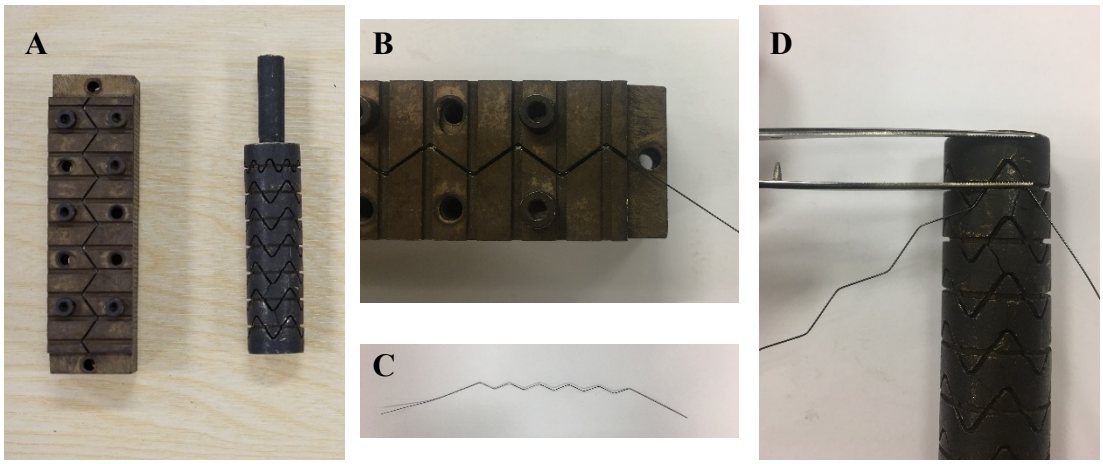

Figure 4.29 – (A) Custom made flat and cylinder rigs for nitinol wire heat treatment. A nitinol wire (B) fixed into the notches of the flat rig, (C) after the first step of heat treatment, and (D) being fixed into the notch on the cylinder rig for the second step of heat treatment.

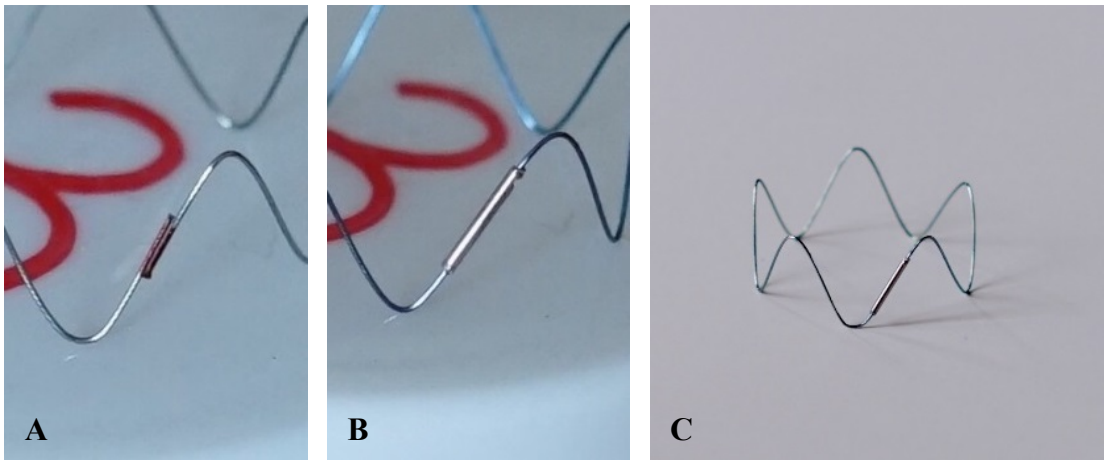

Figure 4.30 – Stent prototypes whose free ends connected by (A) laser welding and (B) 6mm long stainless-steel tube. (C) A z shape stent prototype, wire diameter 0.24mm.

Two methods were tried to connect the free ends. Figure 4.30 A shows the free ends laser welded together while Fig. 4.30 B shows the free ends connected by a thin stainless-steel tube 6 mm in length. After some pinching and experimenting, the laser-

welded prototypes broke apart easily while the ones connected by stainless-steel tube stayed intact. The addition of stainless-steel tube should not be a big concern regarding the mechanical behaviour of the stent because it is added at mid-strut, an area that is subjected to minimal strain when the stent is compressed. Therefore, all prototypes used in later sections are connected using this stainless-steel tube method. 10 prototypes were made for each wire diameter and in total 30 stents were made in preparation of prototyping the self-expanding stent retractor and flat plate compression experiments.

SESR prototypes were then made by stitching Dacron fabric (Shelby Ltd., Finland) of 0.1mm thickness onto 5-crowns stents. Stents were aligned in the way same as the C5A2 design described in the last section. The stitching is a difficult process given the small dimensions of the prototypes. The crowns of the stent were first stitched to the fabric as shown in Fig. 4.31 A; once all crowns were fixed, two ends of the fabric were stitched together so that a tubular shape is formed as shown in Fig. 4.31 B. Figure 4.31 C shows an example of the stitched SESR prototype on the left; on the right is a SESR prototype covered by PTFE film. Though it was not the proposed design or analysed in finite element study, this prototype was nevertheless made because the transparent PTFE enables us to better visualise stents behaviour during deployment.

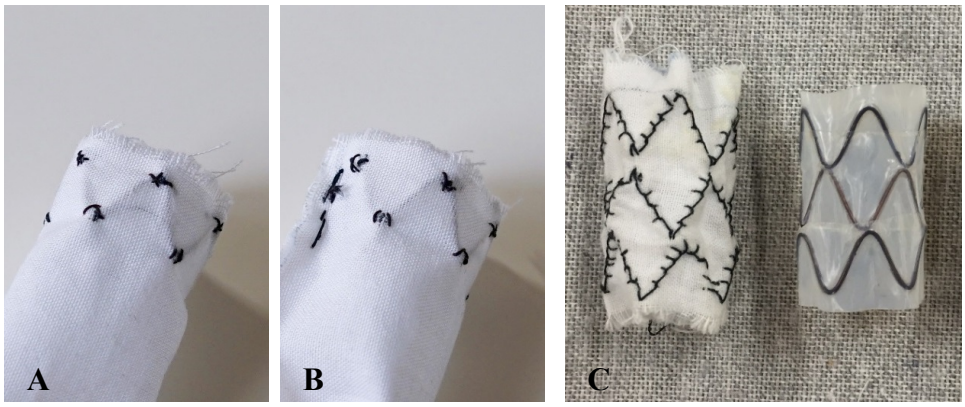

Figure 4.31 – (A) The crowns of the stent were first stitched on the Dacron fabric. (B) The side of the SESR being stitched to form a tubular shape. (C) Two examples of the C5A2 SESR, one covered by Dacron the other covered by PTFE.

Finally, the accessory components of the SESR system were prototyped. First round of prototypes was 3D printed using ABS plastic as shown in Fig. 4.32 A. Once their basic functionalities were tested and proven, the outer sheath was machined from a stainless-steel tube with outer diameter of 7mm and wall thickness of 0.05mm; dilator tip was machined from and attached to a thin shaft (Fig. 4.32 B). The metal parts allowed for a larger inner diameter of the outer sheath and a sharper tip for the dilator. A glass tube was also obtained to function as the outer sheath and used together with the SESR prototype covered by PTFE film to visualise the deployment process as shown in Fig. 4.32 C. This experiment not only confirmed the conceptual but also prepared us to experimentally deploy the prototypes in different mediums in next chapter.

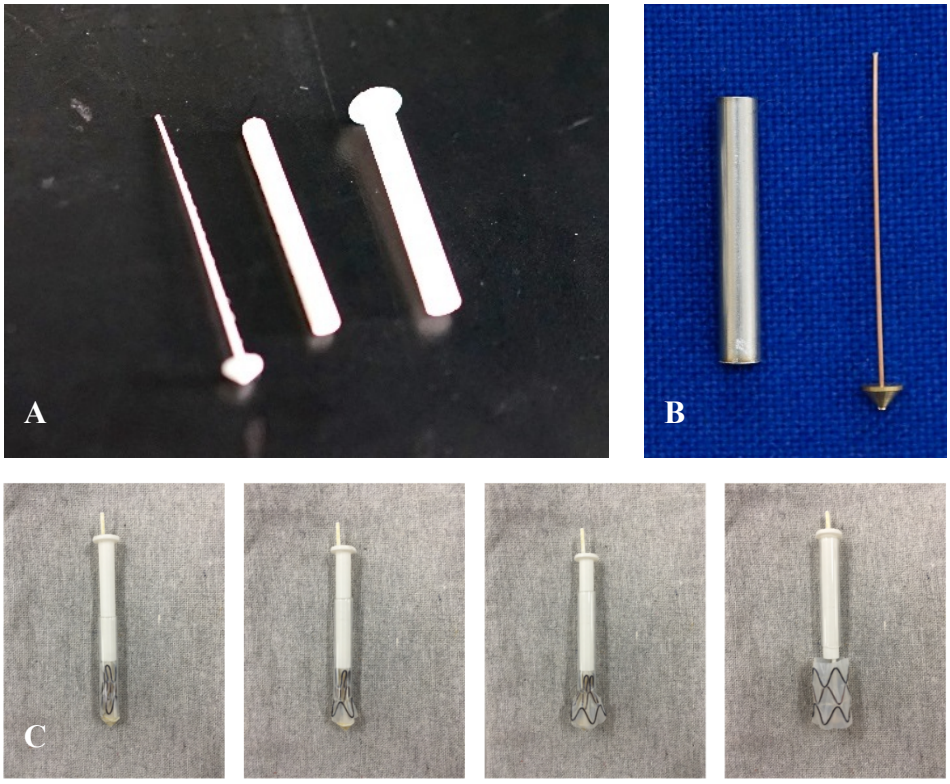

Figure 4.32 – (A) The dilator, stopper and outer sheath prototypes 3D printed from ABS plastic. (B) Stainless-steel outer sheath and brass dilator. (C) A C5A2 SESR prototype covered by PTFE film being deployed from a glass tube.

4.5.2 Flat plate compression experiments

With prototypes of z shape stents and SESRs two sets of flat plate compression tests were conducted experimentally to validate finite element analysis results. Set one intended to compare the experimental compression forces of a single stent with results from finite element analysis. For each wire diameter of 0.24mm, 0.32mm and 0.44mm, three prototypes were tested and the average was obtained. Set two intended to verify the influence of fabric on stents. A SESR composed of two stents with a wire diameter of 0.44mm was compressed. All compression followed the same procedure. Prototypes were placed between two custom-made flat plates mounted on Instron 5982 universal testing system (Instron, Norwood, MA, United States) configured with a 100N load cell. The load was applied by vertically moving down one plate at a speed of 6mm/min for a total displacement of 12mm. The compression of a single z shape stent is shown in Fig. 4.33 A while the compression of a two-stent SESR is shown in Fig. 4.33 B.

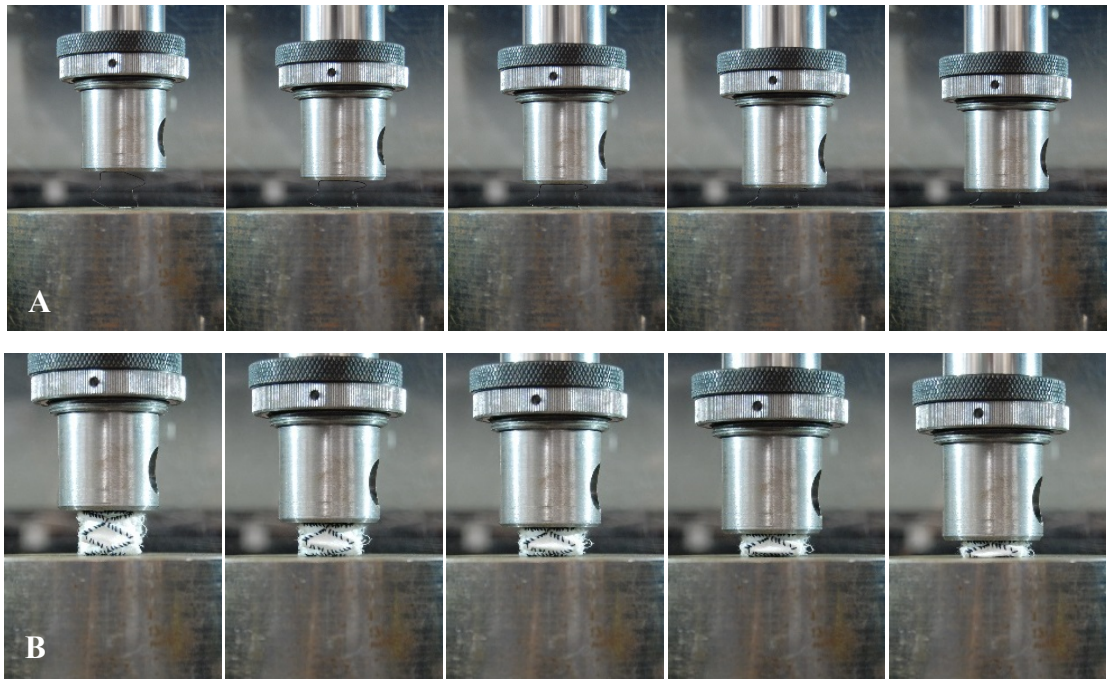

Figure 4.33 – Flat plate compression of (A) a stent and (B) a SESR composed of two stents.

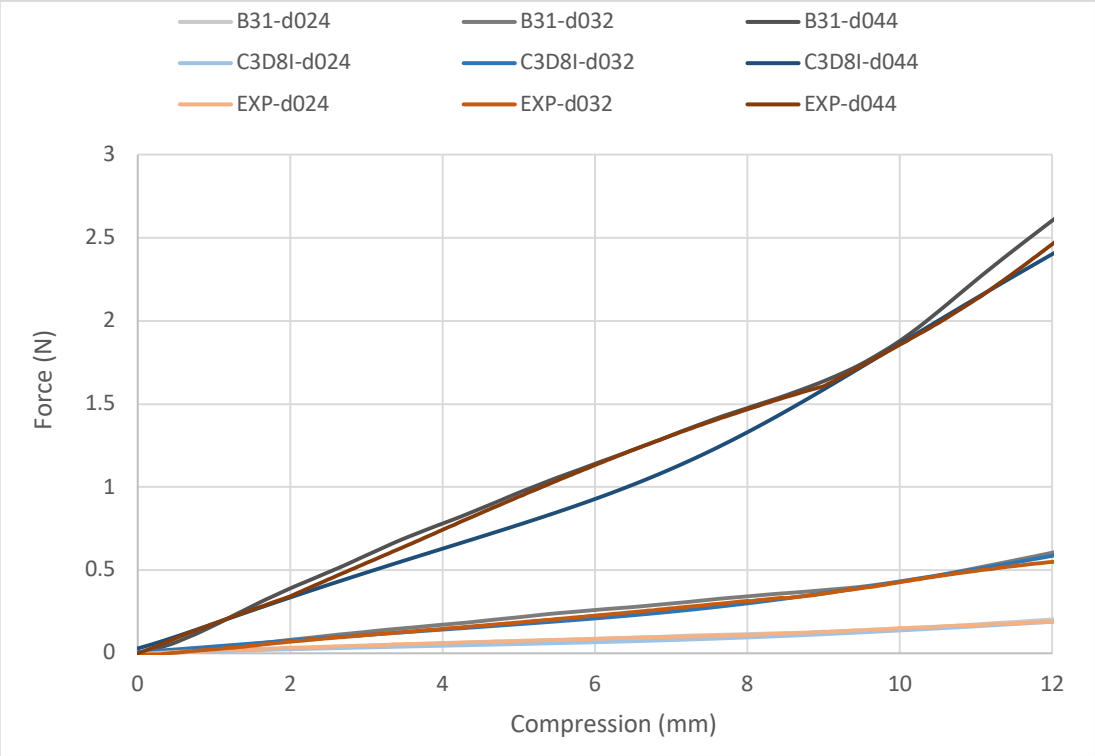

Figure 4.34 – Comparison of flat plate compression forces between experimental results and finite element analysis results using B31 and C3D8I elements.

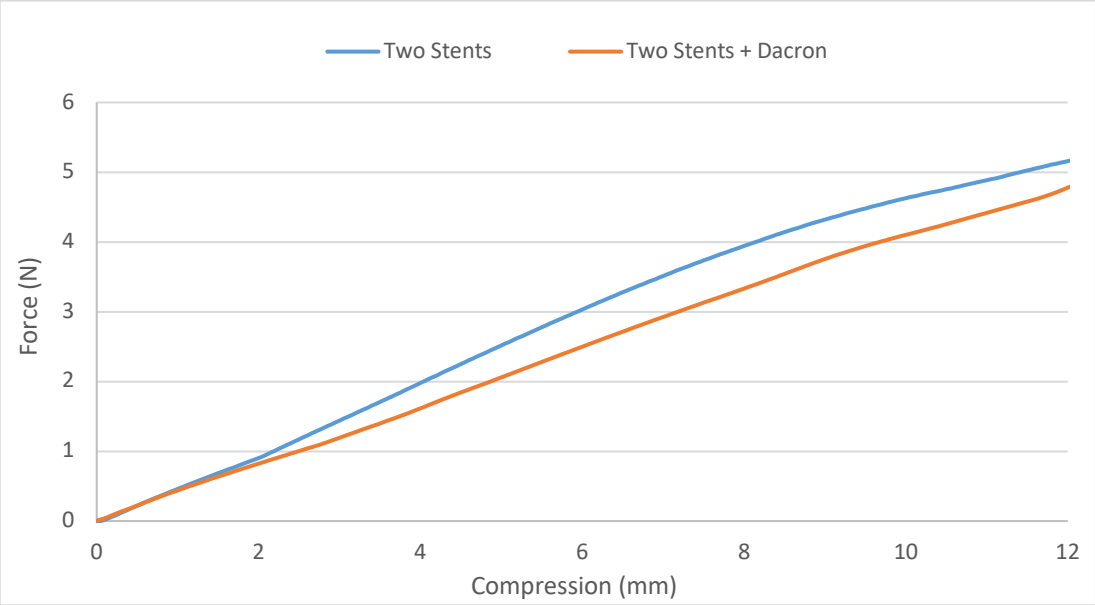

Figure 4.35 – Comparison of flat plate compression forces between two stents and two stents stitched to Dacron fabric. Stents all have a wire diameter of 0.44mm.

As shown in Fig. 4.34, experimental compression forces of single stents agree with finite element results very well. The maximum difference in peak forces at 12mm compression are 6.8%, 10.4% and 7.8% for stents with wire diameter of 0.24mm, 0.32mm and 0.44mm respectively. Although there is a slight difference in loading curves between experiment and finite element results, we are confident to conclude that the prototypes of z shape stents behave in the same way as previously analysed in finite element models. Figure 4.35 shows the marginal influence that Dacron fabric has when stitched onto multiple stents. For two stents with wire diameter of 0.44mm, the peak compression force at 12mm increases by 7.3% if Dacron fabric is stitched. This result agrees qualitatively with the influence of fabric on radial pressure analysed in finite element analysis in Section 4.4.3.

4.6 Discussion

4.6.1 Design and analysis workflow

This chapter presents a complete workflow of SESR design and analysis. In conceptual design, basic dimension, material choice and delivery system are proposed based on surgical needs. The theoretical model is used to better understand z shape stent and thus narrow down a geometric range for finite element analysis. Next, both z shape stent and SESR are thoroughly studied with finite element analysis, with special attention paid to their radial force and pressure. The size and geometry of SESR's are also studied to identify final design. In the end, prototypes made and experimented serve as a proof of concept step, before we move on to further deployment analysis.

The whole workflow is easy to follow and highly repeatable. If there were changes in surgical needs or assumptions that we have made, it is easy to modify the conceptual design. For example, if further experiments found that a tubular delivery device is not ideal, we can modify the geometry of delivery system in conceptual design. If Dacron fabrics cause implications in clinical trials, we can replace it with PTFE and conduct the whole analysis in the same way. If another stent geometry, instead of z shape stent, were to be used, the same steps of theoretical analysis to finite element analysis to experimental validation can be repeated.

4.6.2 Finite element analysis results

The primary aim of finite element analysis is to investigate the radial pressure and geometry of SESR during deployment so that an adequate design can be tested for interaction with brain tissue phantom. First, the model is validated through analysis of single z shape stents. Radial forces calculated from stents meshed with C3D8I continuum elements and B31 beam elements show good agreement. B31 beam elements are then chosen for all further analysis because of its computation efficiency. Flat plate compression forces are also compared with experimental measurements to further validate the model. Although the main focus of our design is the stent's radial behaviour, only flat plate compression tests are conducted because of low cost and convenience. Experimental measurement of radial force needs specialized equipment for loop test. Although usually the influence stent geometry has on a stent's radial pressure and pinch stiffness are different, with radial pressure more dependent on strut thickness and pinch stiffness more depended on strut width, it does not matter in our case because our stent has circular cross-section, meaning that strut thickness and width are the same. Therefore, the flat plate compression test is sufficient for validating the finite element model.

Secondly, geometry and radial pressure of SESR during deployment are analysed. Dacron fabric is meshed with very small S3R shell elements and connected to stents with tie constraints. The fine mesh of fabric adds a lot of burden on computing power, but it is necessary for Dacron to exhibit fabric behaviour. An adjustment factor, a technique reported by (Demanget, Avril, et al. 2012), is also used to make sure Dacron can properly fold during simulation. The addition of fabric would cause a noticeable but marginal increase in radial pressure of SESR comparing to that of only stents. Experimental flat

compression tests also show compression force for SESR slightly higher than that for only stents. It is unreasonable to use experimental measurements to quantitatively validate finite element results in this case, due to the crude prototyping process. Nevertheless, this trend agrees with findings reported by De Bock et al. (2013).

4.6.3 Features of self-expanding stent retractor

Through conceptual design, theoretical analysis, finite element analysis, prototyping and experiments, we have come to a SESR design that has the following three features. First, there is a great design flexibility in dimension and size. The SESR analysed in this chapter is 32 mm in length and 18mm in diameter, consisting of three 10-mm tall stents in series. The SESR length can vary easily by adding or removing stents, or changing the height of stents. Its diameter can also be easily adjusted by changing stent's original diameter. The number of crowns in each stent can also change based on surgical need because from analysis on C5A2 and C10A2 designs, we have learned that no matter the number of stent's crowns, the same radial pressure can always be achieved.

Secondly, there is great flexibility in SESR itself. The current SESR design has an original diameter of 18 mm and is to be packaged into a 7-mm outer sheath, resulting in a contraction/expansion factor of 2.57. This value can be easily pushed higher, i.e. compress the SESR further and confine it in an even thinner outer sheath because current SESR only have less than 3% strain in stents, far below nitinol's superelastic limit. However, this option is not explored because what effect the deployment would cause on brain tissue is yet known. If the SESR was to be packaged into a very small outer sheath, it will store more strain energy in stents and make the deployment process more dynamic. On the other hand, current SESR features no connection between stents except for Dacron fabric. This design is intuitively more flexible in terms of bending, comparing to SESR with peak-to-peak or peak-to-valley strut connections. The bending behaviour is not analysed because once deployed in brain tissue, the amount of bending required for SESR is small. If the surgical tools need to be tilted more than 45 degrees to reach certain lesion

(which would cause a less than 45-degree bending of SESR), it is very like that SESR is deployed at the wrong location at the first place. Demanget et al. (2013) have performed finite element analysis of bending 8 commercial stent graft devices up to 180 degrees and found no significant high strain in stent or fabric. Thus, it is safe to say current SESR can easily withstand the amount of bending required for neuroendoscopy.

Thirdly, the SESR could have varying radial pressure along the longitudinal direction by connecting stents with different wire diameter onto Dacron fabric. For example, if depth sensitivity of radial expansion required turns out to be significant in future analysis, stiffer stents should be used at shallower depth while softer stents should be used deeper down. If for some specific surgery where a funnel-shaped corridor is preferable than a straight tubular one, we can also adjust wire diameter of the stents to achieve the desired shape. It is an idea similar to the variable radial force stent aiming to improve interaction between vessel and stent, reported by García et al. (2012), who claims it can cause a notable decrease in contact pressure over arterial wall comparing with a stent that has constant radial force.

4.7 Summary

This chapter presents a complete workflow of designing and analysing the self-expanding stent retractor for neuroendoscopy. Starting with conceptual design, we identify the design parameters, including dimensions, materials and functions, of SESRs as well as a set of delivery devices. A theoretical approach is then taken to determine a suitable range of geometric parameters for z shape stents. The unique material property of nitinol is tested in uniaxial tension test and used in the finite element models to analyse z shape stents and SESRs. Finite element analysis on single z shape stents is first performed using both continuum C3D8I elements and beam B31 elements and the results are validated against each other. A parametric study on radial pressure is also conducted to further narrow down the geometric parameters that can be used in SESR. Then, finite element analysis on SESRs is performed to simulate the compression and deployment process. The influence of Dacron fabric and alignment of stents are studied, with special attention to SESR radial pressure during unloading. Experimentally, prototypes of the SESR and delivery devices are made as a proof of concept. Flat plate compression test is conducted on SESR prototypes to validate the finite element model. Eventually, final designs of SESR are achieved and ready to be tested for deployment in brain tissue phantom.

5. Deployment of Self-Expanding Stent Retractors

This chapter covers the deployment of self-expanding stent retractors in brain tissue phantom. The main objective is to see how SESR designs from Chapter 4 interact with brain tissue phantom developed in Chapter 3. Section 5.1 describes finite element analysis of retractor deployments. SESRs with uniform and varying radial pressure along the longitudinal direction are both analysed. BrainPath retractor and thin rigid retractor expansion are also revisited for comparison purpose. Section 5.2 explains SESR deployment experiments in agarose gel and porcine brain *in vitro*, which serve to validate finite element analysis results. Section 5.3 discusses the deployed geometry of different SESR designs, advantages of SESR over rigid retractors, and limitations of this study. Finally, Section 5.4 summaries the main findings of this chapter.

5.1 Finite element analysis of retractor deployment

Finite element analysis in this section aims to find out how SESR interact with brain tissue phantom during deployment. C5A2 and C10A2 SESRs with uniform radial pressure are first deployed and their geometries analysed. Then SESRs with varying radial pressure are deployed to further explore the possible final shape of SESR. BrainPath retractor insertion and thin rigid retractor expansion are analysed again using the same brain tissue phantom so that they can be compared with SESRs.

5.1.1 Deployment of SESR with uniform radial pressure

Two SESRs with uniform radial pressure along the longitudinal direction, A C5A2 SESR with 0.32-mm stent wire diameter and A C10A2 SESR with 0.35-mm stent wire diameter, are deployed in brain tissue phantom, with dimension of 60 x 60 x 80 mm and a hole 32 mm in length and 8mm in diameter in the centre of the phantom. The purpose of the hole is to provide space for SESR to deploy and thus omit the penetration step. The material, mesh and boundary conditions of the brain tissue phantom are all the same as that in Chapter 3. The SESR deployment is the same as radial compression and vertical deployment simulation in Section 4.4.3. Settings not specifically mentioned here are the same as previous chapters. There are a total number of 278962 elements in the whole model including stents, Dacron fabric, crimp tool and brain tissue phantom. At the beginning of the simulation, the SESR are coaxially aligned with the hole in the brain tissue phantom. In the compression step, SESR is compressed so that it fits inside the hole. Only interactions between SESR and crimp tool is active. Then in the deployment step, the interaction between brain tissue and SESR are activated. Field output and history output requests are also the same as previous chapters. Simulations are performed in

Abaqus/Explicit. Figure 5.1 uses the C10A2 SESR as an example to illustrate the deployment process. Only the vertical release part of the simulation is shown. The crimp tool moves upward and fully deploys the SESR. Then as the SESR settles, brain tissue relaxes and stress level decreases. The lengths of C5A2 and C10A2 SESRs are compared in Fig. 5.2. Results agree with vertical deployment in the last chapter with C5A2 SESR having a final deployed length 1.12 mm shorter than C10A2 SESR.

As for radial expansion, deployment diameters of these two SESRs are compared in Fig. 5.3. The compression and deployment diameters of individual stents are plotted. Although both SESR's have radial pressure larger than the average 2.085 kPa required for 16 mm diameter expansion (2.13 kPa for C5A2 and 2.15 kPa for C10A2), as analysed in the last chapter, they both expand to less than 16 mm diameter in brain tissue due to loss of strain energy during deployment. Furthermore, uniform radial pressure SESR has a non-uniform deployed shape because, as explained earlier, at different depths inside the brain, different radial pressures are required. From top to bottom, at middle nodes of each stent, C5A2 SESR has deployed diameter of 14.73 mm, 15.01 mm and 15.63 mm, while C10A2 SESR has deployed diameter of 14.71 mm, 15.07 mm, and 15.61 mm, respectively. The deployed sizes are almost identical for these two SESR, both exhibiting a slight funnel shape with smaller diameter on top. The SESR is very flexible in the radial direction anyway, and a very gentle press with forceps or other surgical tools can easily enlarge the diameter. However, if an absolute tubular shape is desired, we need to explore more SESR design options by varying the radial pressure along the longitudinal direction.

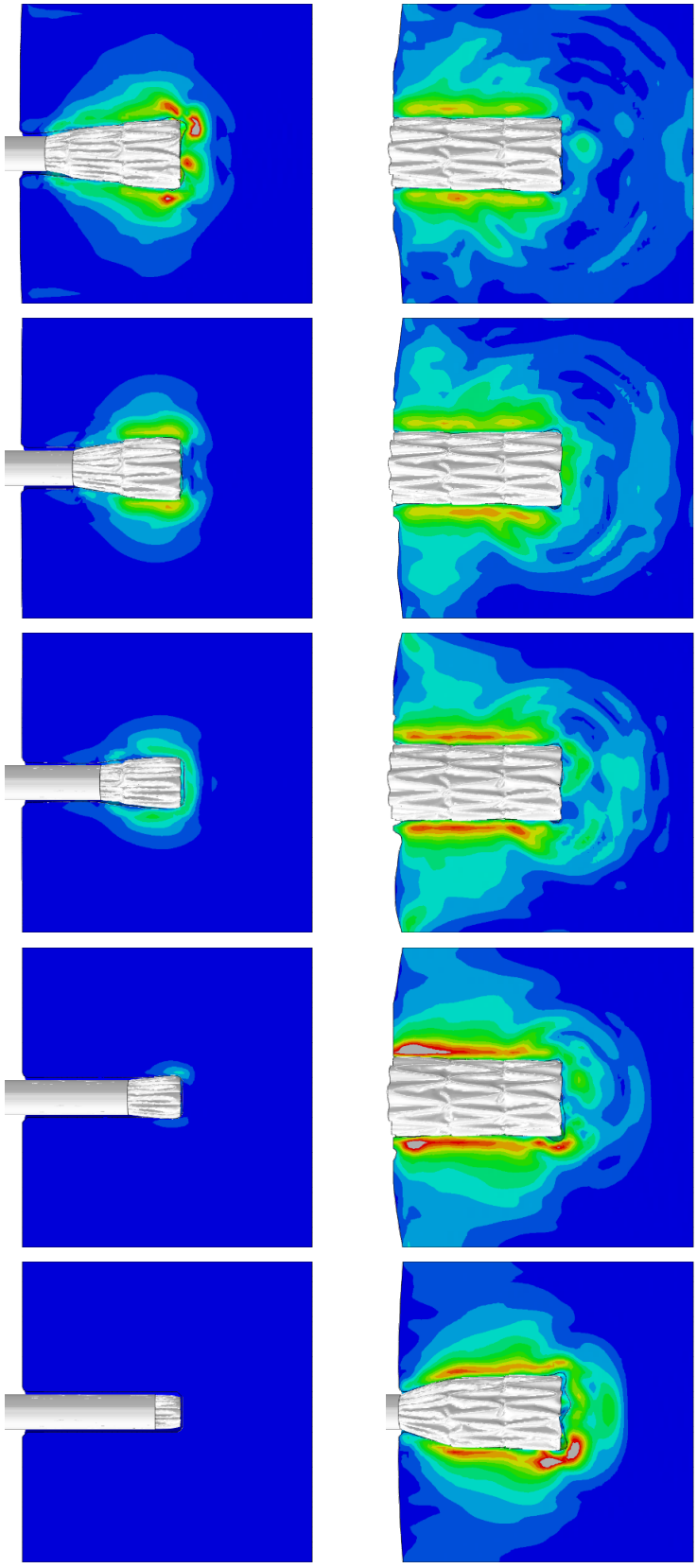

Figure 5.1 – Deployment of a C10A2 SESR with uniform radial pressure in brain tissue phantom.

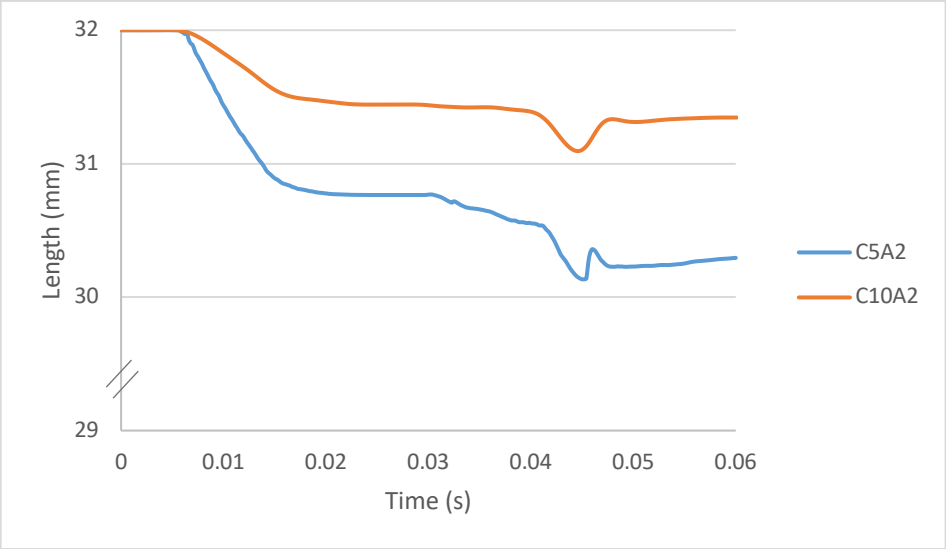

Figure 5.2 – Comparison of deployment length of C5A2 and C10A2 SESR's.

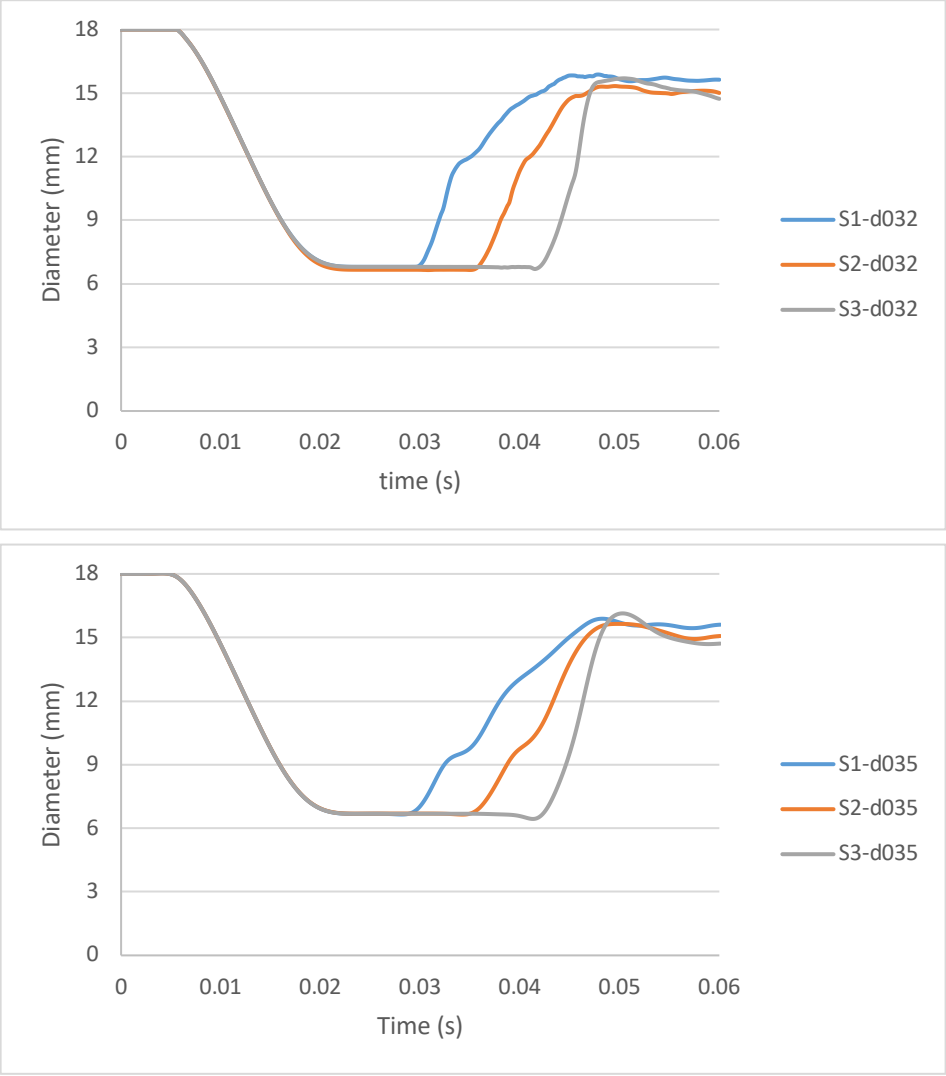

Figure 5.3 – Comparison of deployment diameters of (A) C5A2 and (B) C10A2 SESR.

5.1.2 Deployment of SESR with varying radial pressure

A C10A2 SESR with varying radial pressure deployment attempt is then made. Due to smaller expansion for the top stent and larger expansion for the bottom stent, in order to achieve a true cylindrical shape, we change the stent wire diameters to 0.36 mm, 0.35mm, and 0.34 mm, from top to bottom, respectively. Hence it has an increasing radial pressure with respect to shallower depth inside the brain. This SESR is named C10A2 d036-d035-d034. On the other hand, the funnel shape deployment is explored further by using a C10A2 SESR with stent wire diameters 0.36 mm, 0.32mm, and 0.28 mm, from top to bottom, respectively. The intentional narrower opening deeper inside aims to reduce stress in brain tissue. This SESR is named C10A2 d036-d032-d028. Von Mises stresses in brain tissue at the end of deployment are compared in Fig 5.4. A reference stress of 2.66 kPa is used to better visualise the stress contour.

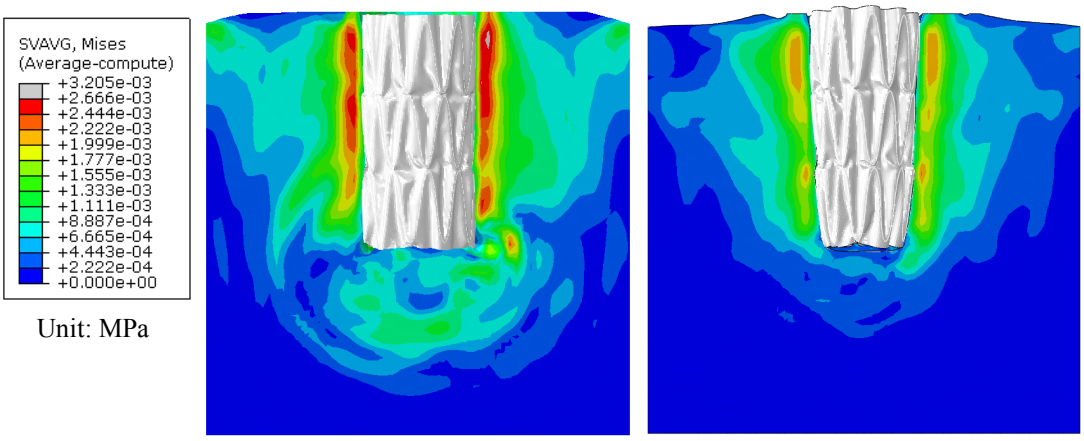

Figure 5.4 – Comparison of stress contour in brain tissue after SESR deployments of (A) straight tubular shape (B) funnel shape.

For the C10A2 d036-d035-d034 SESR, the maximum stress of 7.11 kPa occurs when the first ring of the stent is deployed from the crimp tool. As more portion of the SESR is deployed, the stress decreases because pressure is more evenly distributed on

surrounding tissue. At the instance when SESR is fully deployed, the maximum stress is 4.87 kPa. And finally, after the SESR settles and brain tissue relaxes, the maximum stress is 3.21 kPa. In the C10A2 d036-d032-d028 SESR case, maximum stresses during deployment, at full deployment, and at the end of simulation are 3.96 kPa, 3.74 kPa, and 2.55 kPa, respectively. Indeed, to create a bigger corridor, the C10A2 d036-d035-d034 SESR induced higher stresses in brain tissue than the C10A2 d036-d032-d028 SESR.

As for the SESRs, strains remaining in the stents at the end of deployments are compared in Fig. 5.5. LE means true strain. Maximum strains in stents are 0.479% and 0.624% for the first and second SESRs, respectively. The C10A2 d036-d035-d034 SESR has final expansion diameter of 15.62 mm, 15.61mm and 15.72 mm at the middle of stents from top to bottom. With the maximum difference in diameters less than 0.64%, we can say this SESR has achieved a straight tubular shape. For the C10A2 d036-d032-d028 SESR, since each stent ends up in a funnel shape, it is no longer sensible to look only at diameter in the middle of the stent. Diameter at top, middle and bottom nodes of the stents during compression and deployment are plotted in Fig. 5.6. At the end of deployment, the SESR has diameters of 15.48 mm, 15.25 mm, 14.85 mm, 14.89 mm, 14.17 mm, 13.21 mm, 13.72 mm, 12.90 mm and 11.86 mm from top to bottom.

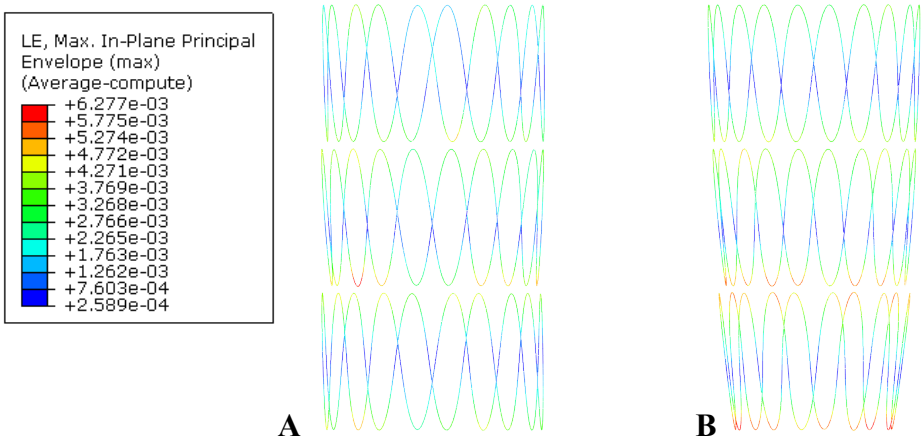

Figure 5.5 – Comparison of strain in stents and overall shape after deployments of (A) SESR C10A2 d036-d035-d034 and (B) SESR C10A2 d036-d032-d028.

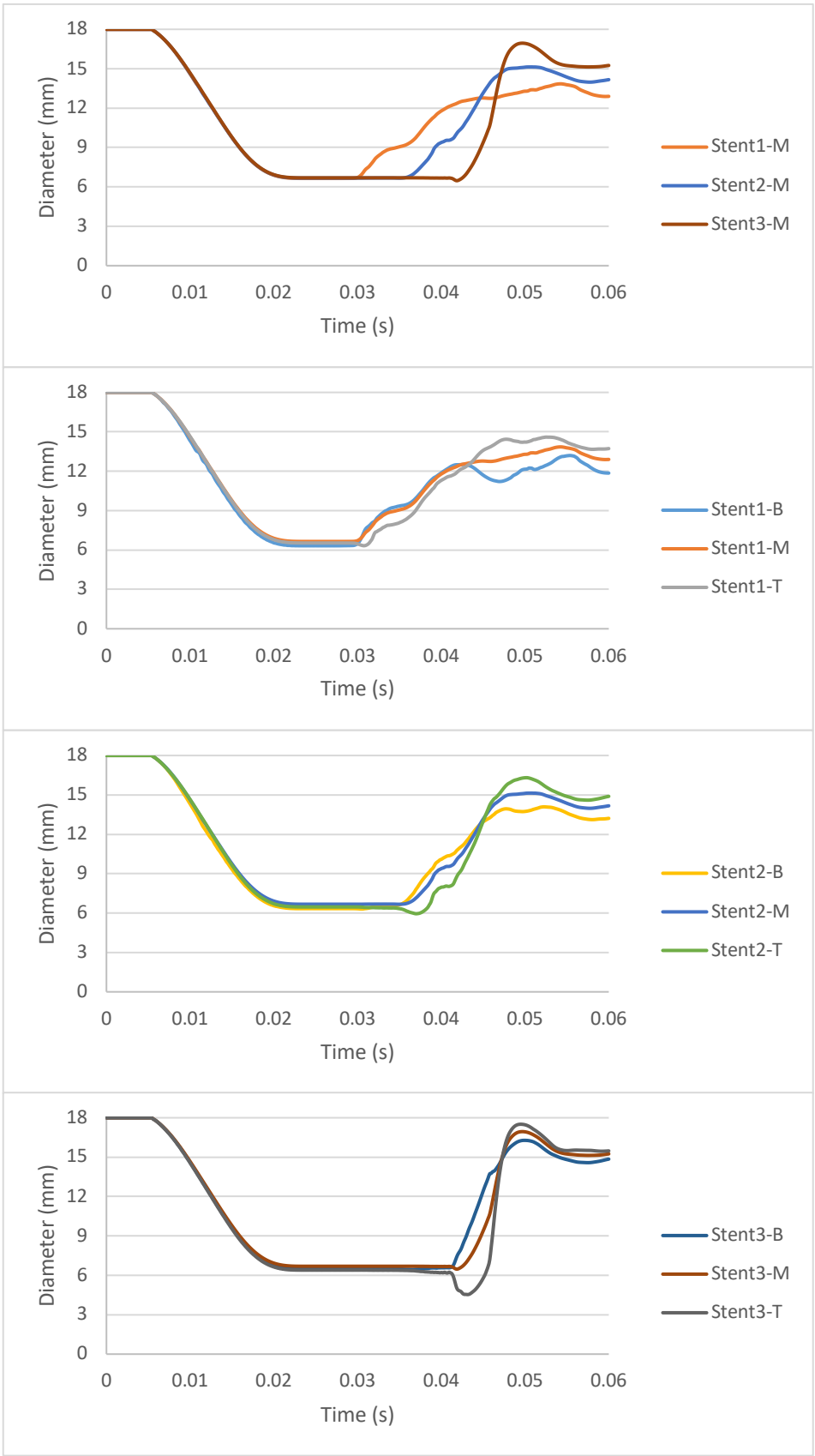

Figure 5.6 – Funnel shaped deployment with (A) SESR diameters in the middle of each stent and diameters at bottom, middle and top nodes of (B) Stent-1 (C) Stent-2 and (D) Stent-3.

5.1.3 Comparison with BrainPath and thin rigid retractor expansion

The stress induced in brain tissue phantom by SESRs is also compared with stress induced by rigid retractors. New simulations are needed because we need to control as many variables as possible. Hence, the BrainPath retractor insertion and thin rigid retractor expansion are performed in the same brain tissue phantom with a hole as in the last section. The time step for both cases is 0.06 second, which is the same as SESR deployment. Average computed von Mises stress contour plots at different frames are plotted in Fig. 5.7 and Fig. 5.8. Stress limit is set at 2.66 kPa. In the BrainPath retractor case, maximum stress during insertions is 4.72 kPa and the maximum stress remaining after brain tissue relaxes is 4.65 kPa. In the thin rigid retractor expansion case, maximum stress during expansion is 3.34 kPa and the maximum stress remaining after brain tissue relaxes is 3.30 kPa. The results are compared with stresses induced in SESR cases and summarised in Table 5.1.

Table 5.1 – Comparison of maximum stresses among four different access methods.

	Maximum stress during insertion/deployment	Maximum stress after insertion/deployment
BrainPath insertion	4.72 kPa	4.65 kPa
Rigid retractor expansion	3.34 kPa	3.30 kPa
C10A2 d036-d035-d034 deployment	4.87 kPa	3.21 kPa
C10A2 d036-d032-d028 deployment	3.74 kPa	2.55 kPa

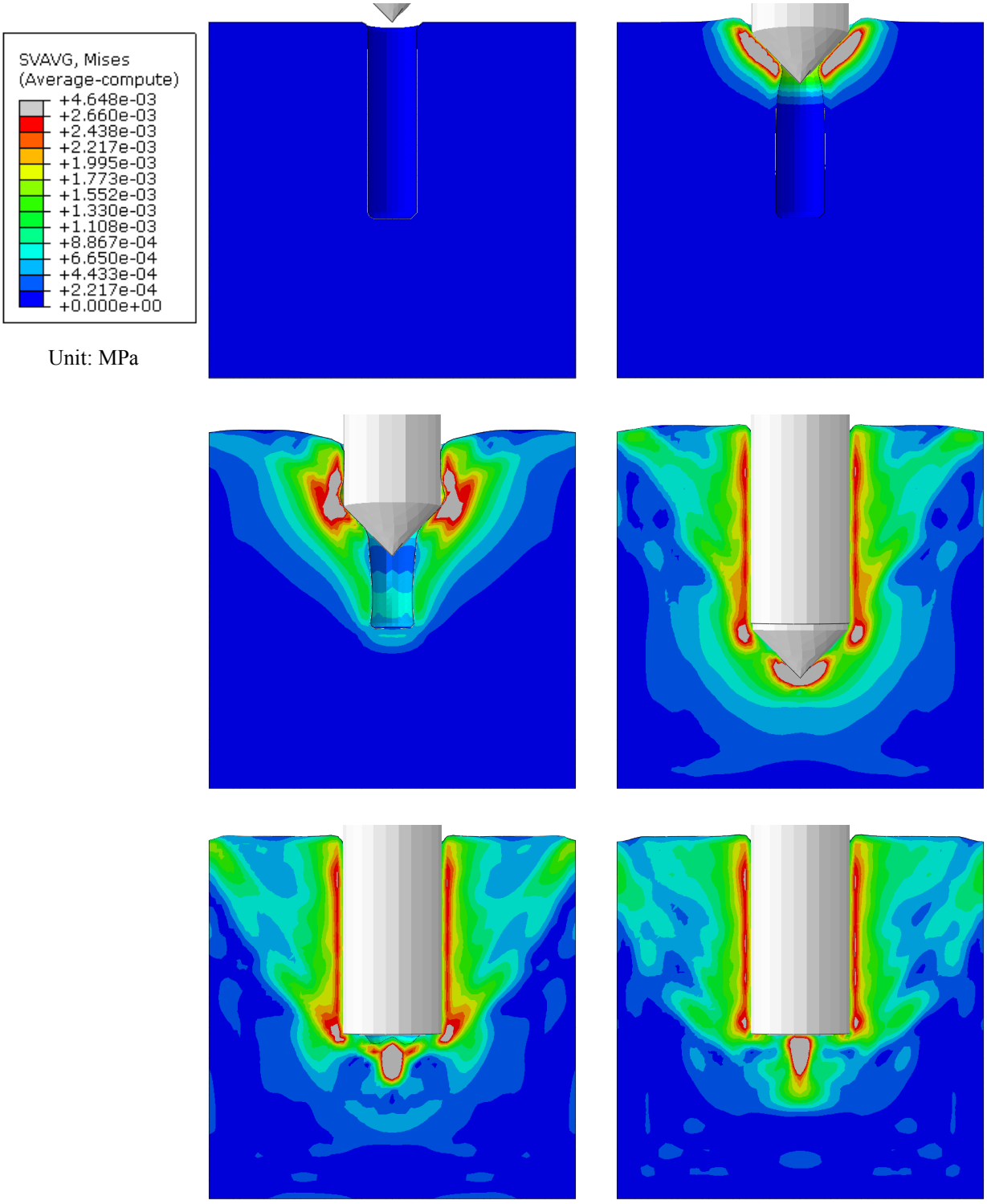

Figure 5.7 – Stress contour in brain tissue phantom after BrainPath insertion.

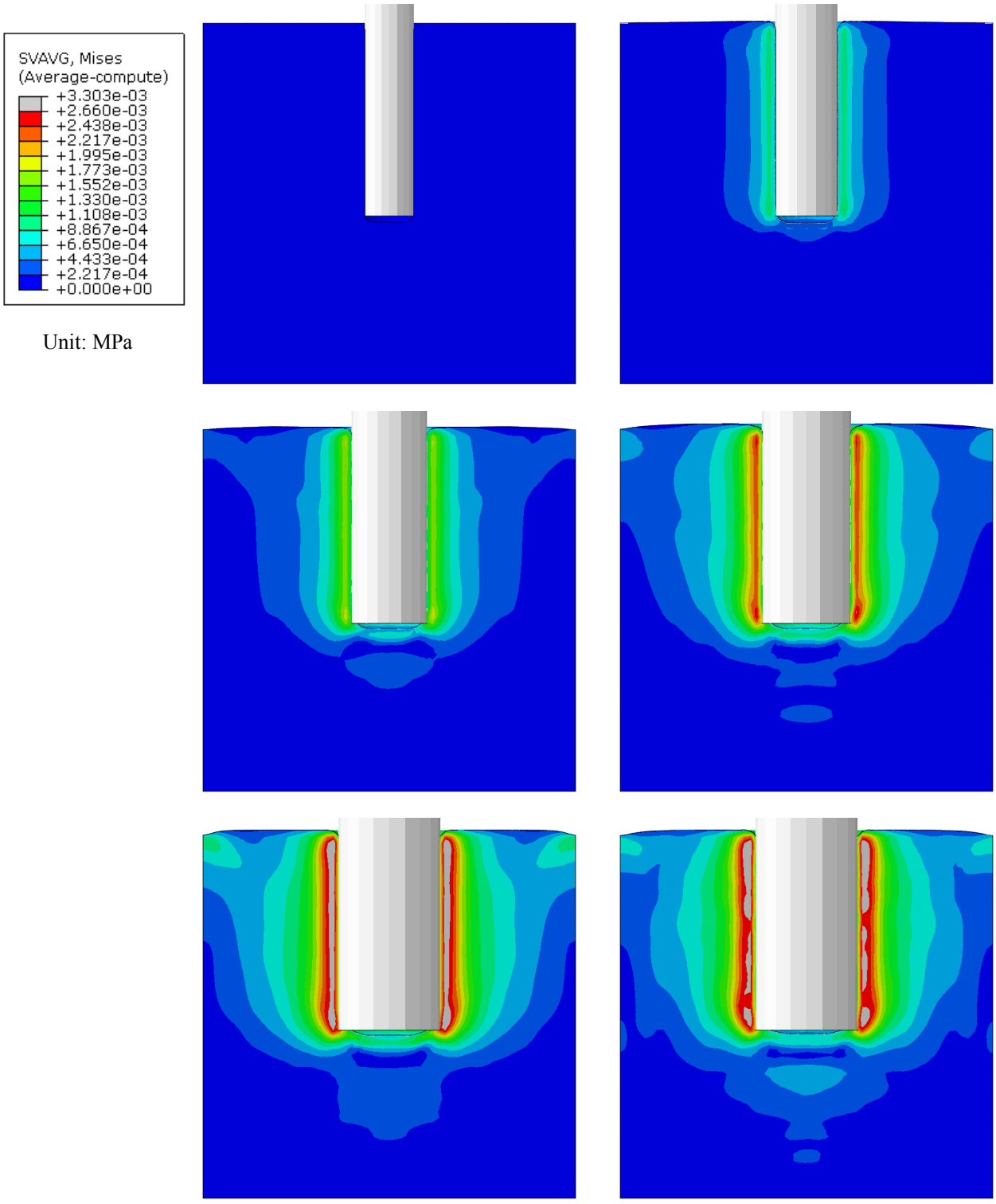

Figure 5.8 – Stress contour in brain tissue phantom after thin rigid retractor expansion.

5.2 Deployment experiments

5.2.1 Deployment in agarose gel

The deployment of SESR is first tested in agarose gel, which is a proven substitute of brain tissue. This is a proof of concept trial that intends to verify the functionality of prototypes as well as the overall conceptual design, before expanding to more complicate experiments involving real brain tissue. 0.6% (w/v) agarose-based hydrogel (Melford Laboratories Ltd., Suffolk, United Kingdom) was prepared by mixing and heating agarose powder in deionized water. Mixtures were then poured into a 100ml beaker and allowed to solidify at room temperature. After solidification, a thin layer of deionized water was maintained on top of the gel to prevent dehydration. A C5A2 SESR prototype of uniform radial pressure with a wire diameter of 0.32mm was then packaged into outer sheath together with dilator and stopper. Together they were slowly inserted into the agarose gel.

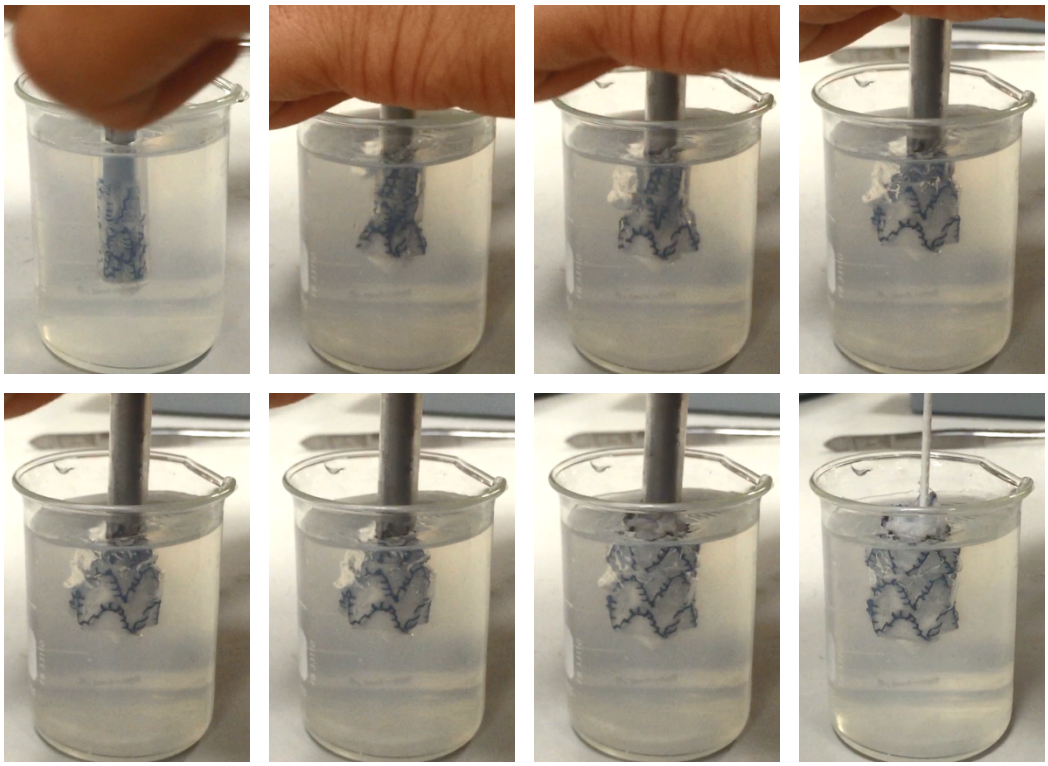

Figure 5.9 – Deployment of SESR in agarose gel.

Figure 5.9 shows the deployment process. With the stopper keeping the SESR in place, the outer sheath was slowly withdrawn and the SESR was deployed stent by stent. At the end of deployment, the SESR almost expanded to its original size, as shown in the top and side views in Fig. 5.10. The exact size of the deployed SESR was not studied because of the difficulty in measuring the diameter while submerged in agarose gel. Measurements from photos are not realistic because when looking from the side, the beaker and gel would the distort SESR's shape, though looking from the top the expansion size at the top is measurable.

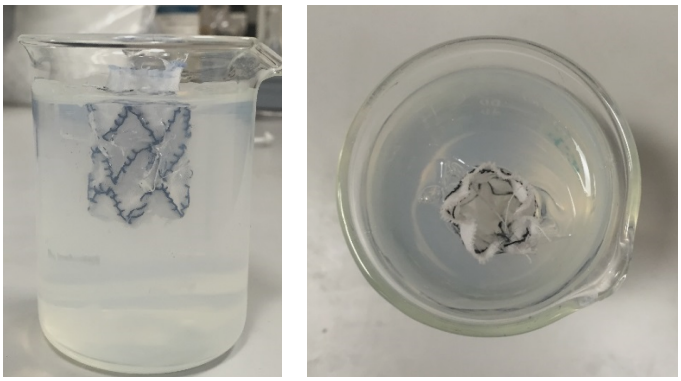

Figure 5.10 – Side and top view of deployed SESR.

However, this limitation does not matter after all because this experiment is a proof concept trial. Although agarose gel proves to be an excellent platform for study of *in vitro* brain, its disadvantage as a SESR deployment medium is obvious. For example, there are visible cracks in agarose gel during the insertion and deployment process, which are unlikely to happen if the medium were hyperelastic brain tissue. Furthermore, the concentration of gel greatly affects its elastic behaviour. Past studies have used concentrations ranging from 0.2% to 0.6% (w/v), but there is no conclusive evidence which concentration best mimics brain tissue mechanical behaviour (Pomfret et al. 2013). For this thesis, where the deployed size of SESR is very important, further experiments on real brain tissue are necessary.

5.2.2 Deployment in porcine brain *in vitro*

5.2.2.1 Deployment size

The deployment is thus conducted in the porcine brain *in vitro* to find the deployed size. The porcine brain was obtained from local butcher shop six hours post-mortem. It was placed in a rigid plastic container which has a diameter of 60mm and height of 80mm. The opening at the top of the container is 50mm in diameter. The wall thickness of the container is approximately 2.5mm. Although the dimension of the container does not perfectly match that of the brain tissue phantom in finite element analysis, their similar size ensured that in both cases the brain tissue was subjected to similar boundary conditions. A C5A2 SESR prototype of uniform radial pressure, with a wire diameter of 0.32mm, was then deployed in the same way as it was in the agarose gel experiment. After deployment, X-ray images were taken under Multix Select DR (Siemens, Berlin, Germany) from the side and top of the container, as shown in Fig. 5.11.

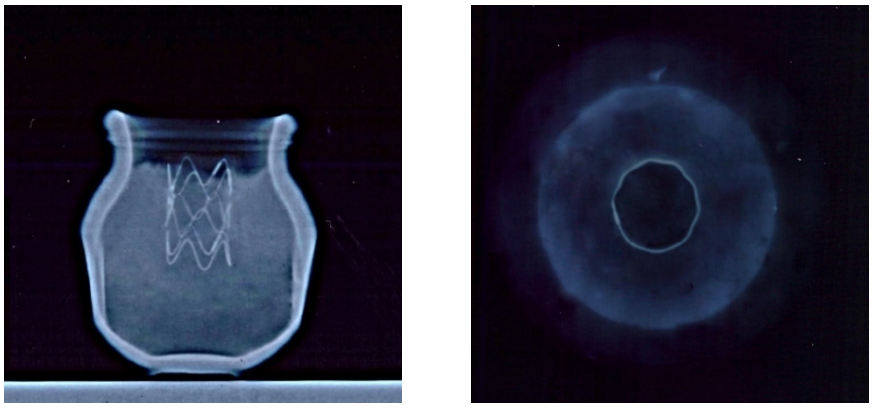

Figure 5.11 – Side and top view of deployed SESR in the porcine brain under X-ray.

The deployed SESR appears slightly tilted indicating the insertion was not perfectly vertical. The SESR length after deployment is thus hard to measure but since there is no overlap between stents, it is safe to say the length is more than 30 mm and therefore no

significant shortening occurred. The expansion appears to be uniform along the longitudinal direction with an average diameter of 15.3 mm. This result is somewhat different from finite element analysis of the same deployment, where expansion diameters from top to bottom are 14.73 mm, 15.01 mm and 15.63 mm. This is mainly due to the large opening of the plastic container, which does not provide as much confinement as the boundary conditions imposed in the finite element model. Furthermore, the complex geometric structure of the real porcine brain and interregional differences in material property might all affect the deployment results.

5.2.2.2 Wound closure after withdrawal

Another interesting observation in the porcine brain deployment experiment is how the wound closes after withdrawing the SESR (Fig. 5.12). Because the retractor is inserted through the folds of the brain, the wound closed to an oval shape at 2 minutes after withdrawal. At 5 minutes post-withdrawal, the wound was almost fully closed and at 20 minutes, the wound was no longer visible.

This inspired a further experiment to investigate the wound closure phenomenon. Instead of the plastic container, a petri dish with 10mm thickness was used to eliminate boundary conditions on the sides imposed by the plastic container wall. If the porcine brain were to be confined in such a tight space, the wound would more than likely close after withdrawal regardless of the retractor used. Porcine brains were again obtained from local butcher shop six hours post-mortem. Because of the height of porcine brains when placed on the petri dish, C5A2 SESR prototype of a shorter length (21 mm) was used; it consists of two stents. On the other hand, a plastic syringe tube of 16 mm diameter was

used as a rigid retractor for comparison. At the beginning of the experiment, they were both applied in porcine (Fig. 5.13 A1 and B1). They stayed in place for ten minutes before being withdrawn. Photos from top view were taken immediately and two minutes after withdrawal. The closure of wound in the SESR case is obvious at both time frame as shown in Fig. 5.13 A2 A3 and B2 B3.

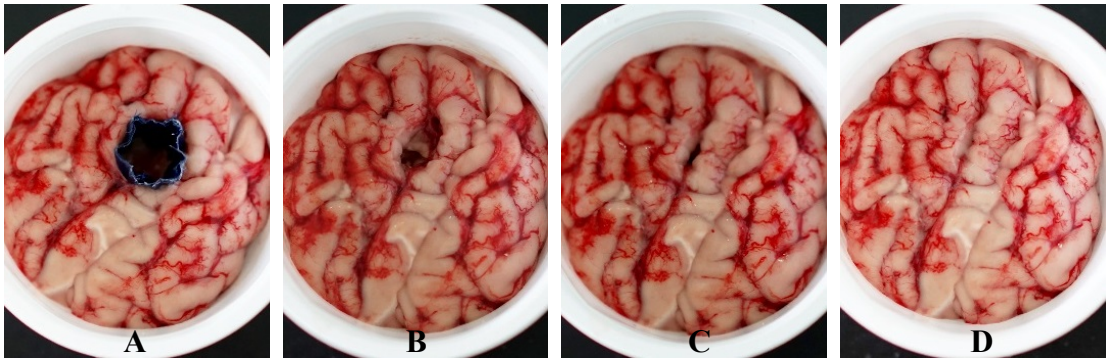

Figure 5.12 – Wound closure at (A) 0 minute (B) 2 minutes (C) 5 minutes and (D) 20 minutes after withdrawing SESR.

At two minutes after withdrawal, liquid nitrogen was slowly poured into the wound and over the brain. After the entire brain was fully frozen, cross-section cuts were made along the dash lines indicated in Fig. 5.14 A1 and B1. The cross sectional area of the wounds is outlined by black lines as shown in Fig. 5.14 A2 and B2. Wound size appears to be much smaller in the SESR case. A quantitative measure of the wound volume was not conducted because there are too many uncontrollable variables in this experiment. For example, it is impossible to obtain two identical porcine brains and have the rigid retractor and SESR deployed as the exact same location. The cross-section cut reveals very different structure inside brain tissue, i.e., white matter and grey matter composition, which could greatly affect the shape of wounds.

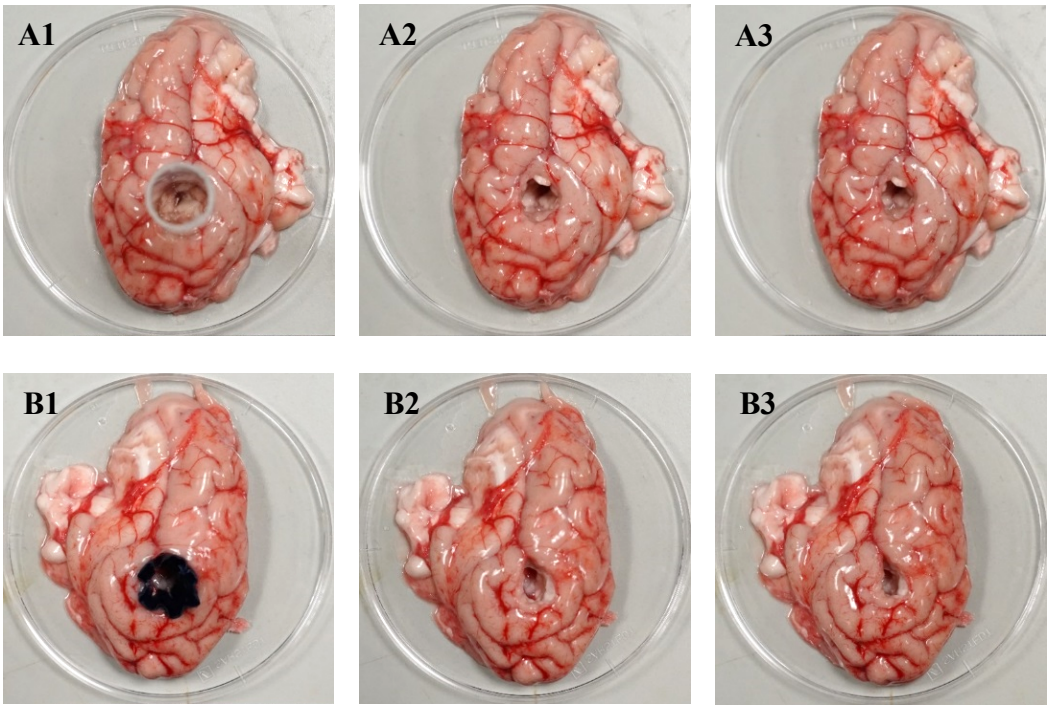

Figure 5.13 – Wound closure of (A) rigid retractor and (B) SESR immediately after and two minutes after withdrawals.

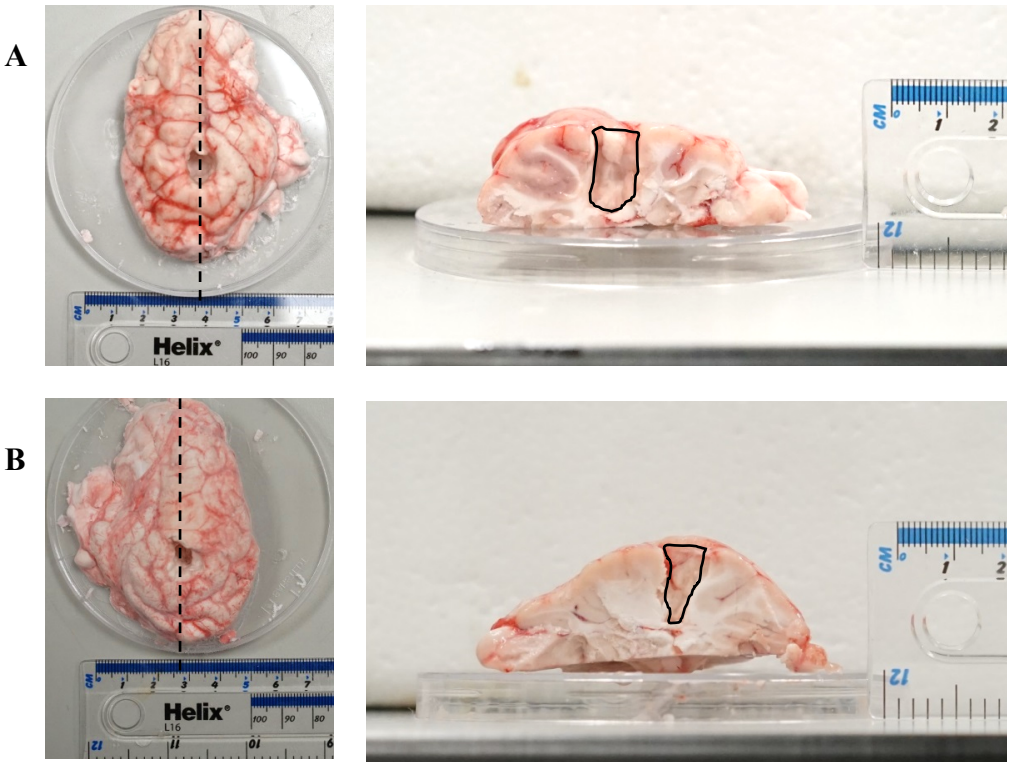

Figure 5.14 – Top and cross-section view of wounds two minutes after (A) rigid retractor and (B) SESR withdrawals.

5.3 Discussion

5.3.1 Deployed geometry of self-expanding stent retractors

Deployed SESR has a smaller diameter than predicted in Chapter 4 for two reasons. First, there is energy loss due to contact between brain tissue and SESR. Secondly, SESR radial pressure is loading path sensitive because of nitinol's superelasticity. In Chapter 4, unloading pressure is obtained from radial unloading simulation, while in deployment, SESR is vertically deployed. Given the bottom, middle and top nodes of the stent are deployed at different times, the strains in the stents will be slightly different to that in radial unloading, thus resulting in a slight change in radial pressure.

Uniform radial pressure SESR results in a slight funnel shape, with a smaller diameter at the top. To achieve absolute tubular shape, varying radial pressure SESR needs to be used. However, whether this absolute tubular shape is necessary is up to the surgeon and will be patient specific. Since the SESR is very flexible in the radial direction, a gentle push or pull with forceps will allow nearby surgeons to access nearby region. Moreover, the brain is a complex organ with interregional variations. Although the average expansion diameter of a C5A2 SESR (15.01 mm) predicted in finite element analysis differs from experimental results (15.3 mm) by only 4.6 %, the experimentally deployed SESR appear to have straight tubular shape. Prototype inaccuracy should be accounted for, but the structure of a real porcine brain might also be the reason for the final deployed shape.

In addition to achieving absolute tubular deployed shape, varying radial pressure SESR can create corridors of other shapes that best suit specific surgery. The funnel shape deployment with a larger opening at the top is just an example to demonstrate the

feasibility of such concept. Hourglass shape deployment is also possible if there are stiffer stents at top and bottom, with a softer stent in the middle of SESR. If the height of each stent is reduced, it will be possible to connect more stents in one SESR of fixed length, and thus enable more radial pressure variations along the longitudinal direction.

Lastly, we see no point in finding a SESR design that guarantees expansion more than 0.1 mm accuracy for the following three reasons. First, as discussed earlier, the SESR is very flexible and small adjustments can easily be made during surgery. Secondly, the neuroendoscopy procedure has many factors that are uncontrollable and situations that differ among patients. The presence of a tumour might change the surrounding tissue's elasticity, while a slightly larger or smaller hole opened in skull might change the boundary conditions. Thirdly, the brain tissue is a cubic phantom in our finite element model instead of real brain geometry. In a real brain, deployment size will be location sensitive and largely affected by structure complexity.

5.3.2 Comparison between stent retractors and rigid retractors

Self-expanding stent retractors compare favourably against rigid devices such as BrainPath retractor and thin rigid retractor expansion. In finite element analysis, the von Mises stress is used as a metric for comparison. To better visualise the stress contour, we used a reference stress limit of 2.66 kPa, or 20 mmHg, which is the value suggested by Rosenørn & Diemer (1982), at which focal ischemic damage can happen in brain tissue if retraction lasts longer than 30 minutes. At the end of deployment, it is possible to keep the stress in the brain tissue at less than 2.66 kPa in some SESR cases, whereas for rigid retractors the stresses are over this limit. If a varying radial pressure SESR is used to achieve funnel-shaped deployment, stress in brain tissue could be further reduced. The lower SESR-induced stresses agree in principle with results reported by García et al. (2012), who found that a variable radial force stent exerts less pressure on the artery wall than a constant force stent. Wound closure experiments also qualitatively support finite element results. In both cases, where the porcine brains are placed in plastic container or petri dish, the hole closes well after withdrawal of SESR.

The main limitations of the finite element model lie in the isotropic material assumption of brain tissue and simplification of the brain to a cubic phantom. Without failure criteria of brain tissue, the stress limit can be used for comparison purposes but not pinpointing injury risk at a specific region. Furthermore, Brain tissue-skull interaction, intracranial pressure and brain pulsation are not considered. The idealized geometry makes it possible to have a good approximation of the interaction between SESR and brain tissue, but a patient-specific geometry and deployment location would enable further SESR design improvements.

5.4 Summary

Self-expanding stent retractor deployments in brain tissue are studied in both finite element analysis and experiments. SESR with uniform radial pressure results in a slight funnel deployed shape with a smaller opening on top, due to different expansions required at different depths inside the brain. SESR with varying radial pressure can be used to achieve an absolute tubular deployed shape. More possible deployed shapes of SESR, i.e., funnel shape, are explored to show the design flexibility to suit surgical needs. Deployment experiments in agarose gel and porcine brain *in vitro* confirm the functionality of SESR and validate finite element analysis results. Furthermore, wound closure in porcine brain demonstrates that SESR induces less stress in brain tissue.

6. Conclusions

6.1 Summary of findings

Main findings of this thesis can be summarised in three parts. Firstly, for brain tissue, a finite element model suitable for neuroendoscopy has been built and validated. It predicted the reaction force and pressure on surgical tools to find out design requirement for the SESR. The predicted force required to insert a 7mm diameter dilator into the brain tissue for 45mm depth is 0.74N, which aligns well with data found in literature review. The pressure required to expand a hole from 7mm to 16mm in diameter in the brain tissue through rigid shell expansion is 2.089 kPa. Stress contour in brain tissue was used as a metric for comparison between surgical scenarios. The concept of expanding a thin retractor after insertion was thus verified as this method induces less stress on the brain tissue compared to that of a rigid retractor like the BrainPath. In addition, histology analysis of stab wound in mice brain was performed, which explored brain tissue injury that could not be found in finite element analysis.

Secondly, a complete roadmap of self-expanding stent retractor (SESR) design and analysis for neuroendoscopy was presented in this thesis. The SESR is to be used with three accessory components, the outer sheath, the dilator and the stopper. The SESR consists of three z shape stents and a layer of Dacron fabric. The stents are aligned peak-to-peak and there are no connections between them except for the fabric. The SESR has a length of 32mm and a diameter of 18mm. It is confined in an outer sheath of 7mm in diameter before insertion and aims to self-expand to 16mm in diameter after deployment. Z shape stents used in the SESRs have diameter of 18mm, height of 10mm, and 5 or 10

crowns. Radial pressure of a z shape stent is thoroughly understood through theoretical prediction, finite element analysis, and experimental measurements. The wire diameter of the stent is used as the variable that controls the radial pressure of the SESR. SESRs are then studied in finite element analysis to identify designs that provide adequate radial pressure for deployment in brain tissue. For the 5-crown stent SESRs and the 10-crown stent SESRs, wire diameters from 0.31mm to 0.33mm and wire diameters from 0.34mm to 0.36mm, respectively, are considered sufficient in providing radial pressure ranging from 1.473 kPa to 2.24 kPa at 16mm diameter. Moreover, after being vertically deployed from the outer sheath, the SESRs have a less than 2mm shortening in length. In addition, SESR and accessory components prototypes were made and deployment experiments were conducted to verify design concept.

Thirdly, deployment of the SESR in the brain tissue was studied. The finite element analysis of the SESR deployment is validated by comparing simulation results with experimental measurements. For a 5-crown stent SESR with wire diameter of 0.32mm deployment, the SESR has an average diameter of 15.12mm while in the in vitro experiment the prototype has an average diameter of 15.3mm. Further finite element analysis demonstrates that different deployed shapes of SESR can be achieved by adjusting the wire diameters of individual stents. To achieve a true cylindrical shape with a diameter of 15.6mm, a 10-crown stent SESR with wire diameters of 0.36mm, 0.35mm and 0.34mm can be used. To achieve a funnel shape with a 15.5mm diameter at top and 11.9mm diameter at bottom, a 10-crown stent SESR with wire diameter of 0.36mm, 0.32mm and 0.28mm can be used. Moreover, stress contour in brain tissue caused by SESR compares favourably with BrainPath and Rigid expansion, indicating that the SESR is less likely to induce brain tissue injury. Experimental results qualitatively

support finite element analysis results. Better wound closure indicates less damage to brain tissue in the SESR case.

There are, however, certain limitations in both the finite element analysis and the experiments discussed in this thesis. Concerning the brain tissue segment, the main limitation of the finite element model comes from the lack of failure criteria in material model. Without such criteria, the stress induced in the brain tissue can only be used as a metric for comparison among different surgical scenarios, instead of an indicator of brain tissue injury. The use of the Coupled Eulerian Lagrangian (CEL) method also affects the accuracy of the stress predicted by the finite element model. However, it is a trade-off this study had to accept in order to simulate the large deformation which usually happen during neuroendoscopy. Furthermore, by simplifying the complicated brain geometry into a cubic phantom, this study relinquished its ability to predict stress or strain in a specific region of the brain, so it could only look at the response of brain tissue phantom as a whole. For the SESRs, the main limitation of the finite element model is the use of B31 element in stents. Although the B31 element is adequate in predicting force and pressure, it is inadequate at calculating stress and strain at a particular part of the stent comparing to continuum elements like C3D8I. However, fatigue life of the SESR is not of concern in this thesis and the strain in stents is far lower than nitinol's elastic limit of 8% among all designs. This is another trade-off this study was willing to accept in exchange for computational efficiency.

As for the experiments and prototypes, there are two main limitations. Firstly, all porcine brain tissue experiments were conducted ***in vitro*** due to both time and resource constraints on this project. This is relevant for it is well acknowledged in literature that brain tissue is slightly stiffer ***in vitro*** than ***in vivo*** and even post-mortem time influences

its stiffness to a certain extent (Goriely et al. 2015). Furthermore, the container used for brain tissue has dimensions similar to that of the phantom used in finite element analysis, but not of the exact same geometry. This slight discrepancy in boundary conditions might affect the final deployed shape and size of the SESR. Secondly, due to the time and resource constraints of this project, the SESR prototypes were made by hand. The heat treatment of nitinol and especially the stitching of Dacron fabric are complicated procedures, the repeated accuracies of which difficult to guarantee. Therefore, slight discrepancies among individual prototypes are inevitable and their quality thus by no means comparable to that of standard commercial medical devices.

6.2 Future work

This novel self-expanding stent retractor (SESR) is, necessarily, only an incremental step towards enhanced access technology in neurosurgery. Possible future works are discussed with respect to both research and commercialisation.

6.2.1 Research

Future research of this project can progress in two tranches: one focusing on the brain tissue and another on the SESR. For the brain tissue, the finite element model can be improved to better predict how surgical tools interact with the brain. For example, if a suitable set of injury criteria becomes available, it can be incorporated into the finite element model to this end. This way, finite element analysis results can not only serve as a metric for comparison between surgical tools, but also a prediction on brain tissue injury

during surgery. The complex geometry and structure of the brain, including respective lesion information, can also be incorporated to make the finite element model patient-specific. For example, if a patient has a tumour located 38mm deep in the intraparenchymal region of the brain, a patient-specific finite element model of the brain can be developed based on MRI scans. A patient-specific access strategy can then be developed and the SESR can be customised to meet the needs of this particular surgery. Furthermore, pulsation of the brain can also be incorporated into the finite element model to fully demonstrate SESR's advantage over rigid retractors.

Secondly, for the SESR, more z stent geometries can be explored to exploit the biased stiffness property of self-expanding stent made from nitinol, which would consequently further reduce SESR's pressure on brain tissue. Current SESR design focuses on guaranteeing a certain expansion diameter after deployment, instead of minimising the pressure exerted on the brain tissue. By exploring more z stent geometries, an optimal balance between expansion diameter and pressure exerted on the brain tissue can be achieved. Different alignment of stents and radial pressure of stents in SESR can also be explored, if other final deployed shapes are desired. For example, if certain surgery situation requires a large opening at the top and the bottom, but not so much space in the middle, the SESR can be designed to have an hourglass shape after deployment. Different delivery and deployment strategy also worth studying. For example, in a hypothetical surgical situation where it is more beneficial to cut a slit instead of drilling a hole in patient's brain, an outer sheath with oval cross-section might be better than a tubular outer sheath.

6.2.2 Commercialisation

The self-expanding stent retractor (SESR) has a potential to be commercialised. Locally, the John Radcliff Hospital, for instance, has estimated that the SESR could be used for approximately 100 cases per year. Globally, more than 1 million patients diagnosed with brain abnormalities have limited surgical options available to them. In addition to intraparenchymal and intraventricular surgery, the SESR can also be used for trans nasal surgery and cerebellopontine angle surgery in the posterior fossa. If commercialised, it can help neurosurgeons to access brain lesions in a novel way that reduces injury to healthy brain tissue.

Here are a few possible steps towards commercialising the SESR. To begin with, the prototyping technique and experimental evaluation of SESR should be improved and standardised so that batches of prototypes can be produced for animal experiment. Specialised equipment should be purchased to improve the heat treatment and fabric stitching process. Electrochemical polishing of the stents should be carried out to refine the prototype. Subsequently, *in vivo* animal experiment should be conducted to evaluate the SESR and compare it with existing rigid retractors. Porcine brain is the best medium to conduct experiment because of its relative large size. The pigs should be divided into two groups, one for SESR and one for rigid retractor like the BrainPath. During the *in vivo* experiment, cerebral blood flow, intracranial pressure and other measurements should be taken and compared between groups. If needed, the pigs can be sacrificed at some certain days after surgery and histology analysis can be conducted. Cellular death, cavity volumes and other metric can be used to further investigate the difference between the SESR group and the rigid retractor group. Finally, once advantages of the SESR are

confirmed in animal experiments, we can responsibly move on to clinical trials and use the SESR for the benefit of human patients.

References

Abràmoff, M.D. et al., 2004. Image Processing with ImageJ. *Biophotonics International*, 11(7), pp.36–42.

Akiyama, Y. et al., 2015. Rigid endoscopic resection of deep-seated or intraventricular brain tumors. *Neurological Research*, 37(3), pp.278–282.

ASTM, 2006. *Standard Test Method for Tension Testing of Nickel-Titanium Superelastic Materials*.

Auricchio, F. et al., 1997. Shape-Memory alloys: modelling and numerical simulations of the finite-strain superelastic behavior. *Computer methods in applied mechanics and engineering*, 143 (1997), pp.175-194.

Azaouzi, M., Makradi, a. & Belouettar, S., 2012. Deployment of a self-expanding stent inside an artery: A finite element analysis. *Materials and Design*, 41, pp.410–420.

Bain, A.C., Meaney, D.F. & Hall, H., 2000. Tissue-Level Thresholds for Axonal Damage in an Nervous System White Matter Injury. *Journal of Biomechanical Engineering*, 122(December), pp.615–622.

Bernardo, A. et al., 2015. A Percutaneous Transtubular Middle Fossa Approach for Intracanalicular Tumors. *World Neurosurgery*, 84(1), pp.132–146.

Bilston, L.E., 2011. Brain Tissue Mechanical Properties. In *Biomechanics of the Brain*. Springer, pp. 69–90.

Blockwise Engineering, Self-Expanding Stent Loaders. Available at: http://www.blockwise.com/stentloaders.htm#Zero-G^{TM}_Products [Accessed November 17, 2016].

De Bock, S. et al., 2013. Filling the void: A coalescent numerical and experimental technique to determine aortic stent graft mechanics. *Journal of Biomechanics*, 46(14), pp.2477–2482. Available at: http://dx.doi.org/10.1016/j.jbiomech.2013.07.010.

De Bock, S., Iannaccone, F., De Santis, G., De Beule, M., Mortier, P., et al., 2012. Our capricious vessels: The influence of stent design and vessel geometry on the mechanics of intracranial aneurysm stent deployment. *Journal of Biomechanics*, 45(8), pp.1353–1359.

De Bock, S., Iannaccone, F., De Santis, G., De Beule, M., Van Loo, D., et al., 2012. Virtual evaluation of stent graft deployment: A validated modeling and simulation study. *Journal of the Mechanical Behavior of Biomedical Materials*, 13, pp.129–139.

Boston Scientific, 2014. Carotid WALLSTENT.

Budday, S. et al., 2015. Mechanical properties of gray and white matter brain tissue by indentation. *Journal of the Mechanical Behavior of Biomedical Materials*, 46, pp.318–330.

Casanova, F., Carney, P.R. & Sarntinoranont, M., 2014a. Effect of needle insertion speed on tissue injury, stress, and backflow distribution for convection-enhanced delivery in the rat brain. *PLoS ONE*, 9(4).

Casanova, F., Carney, P.R. & Sarntinoranont, M., 2014b. In vivo evaluation of needle force and friction stress during insertion at varying insertion speed into the brain. *Journal of Neuroscience Methods*, 237, pp.79–89.

Castellano-Smith, A.D. et al., 2001. Constructing patient specific models for correcting intraoperative brain deformation. *Lecture Notes in Computer Science (including subseries Lecture Notes in Artificial Intelligence and Lecture Notes in Bioinformatics)*, 2208, pp.1091–1098.

Chen, C.-C. et al., 2005. A stainless steel sheath for endoscopic surgery and its application in surgical evacuation of putaminal haemorrhage. *Journal of clinical neuroscience : official journal of the Neurosurgical Society of Australasia*, 12(8), pp.937–40.

Clatz, O. et al., 2005. Realistic Simulation of the 3D Growth of Brain Tumors in MR Images Coupling Diffusion with Biomechanical Deformation. *IEEE Trans Med Imaging*, October(24(10)), pp.1334–1346.

Conti, M., 2007. *Finite Element Analysis of self-expanding braided wirestent*.

Cook Medical, 2001. *Cook Medical Launches Balloon-Expandable Renal Stent at SCAI 2011 Scientific Sessions*.

Dassault Systèmes Simulia Corp., 2013. ABAQUS Documentation.

Dassault Systèmes Simulia Corp., 2011. *Best Practices for Stent Analysis with Abaqus*.

Dassault Systèmes Simulia Corp., 2009. Earth Penetration Simulation using Coupled Eulerian-Lagrangian Analysis. In *Abaqus Technology Brief*. pp. 1–4.

Dassault Systèmes Simulia Corp., 2010. Installation and Extraction of Spudcans using Abaqus/Explicit. In *Abaqus Technology Brief*. pp. 8–11.

Dassault Systèmes Simulia Corp., 2004. *VUMAT for Superelasticity and Plasticity of Shape Memory Alloys*,

De, S. et al., 2007. Assessment of Tissue Damage due to Mechanical Stresses. *The International Journal of Robotics Research*, 26(11–12), pp.1159–1171.

Demanget, N., Avril, S., et al., 2012. Computational comparison of the bending behavior of aortic stent-grafts. *Journal of the mechanical behavior of biomedical materials*, 5(1), pp.272–82.

Demanget, N. et al., 2013. Finite element analysis of the mechanical performances of 8 marketed aortic stent-grafts. *Journal of endovascular therapy : an official journal of the International Society of Endovascular Specialists*, 20(4), pp.523–35.

Demanget, N., Latil, P., et al., 2012. Severe Bending of Two Aortic Stent-Grafts: An Experimental and Numerical Mechanical Analysis. *Annals of Biomedical Engineering*, 40(12), pp.1–13.

Ding, D. et al., 2015. A minimally invasive anterior skull base approach for evacuation of a basal ganglia hemorrhage. *Journal of Clinical Neuroscience*, pp.5–8.

Dommelen, J.A.W. Van et al., 2010. Mechanical properties of brain tissue by indentation :

Interregional variation. *Journal of the Mechanical Behavior of Biomedical Materials*, 3, pp.158–166.

van Dommelen, J. a W., Hrapko, M. & Peters, G.W.M., 2009. Mechanical Properties of Brain Tissue: Characterisation and Constitutive Modelling. In *Mechanosensitivity of the Nervous System*. Springer, pp. 249–281.

Drexel, M., Selvaduray, G. & Pelton, a, 2006. The effects of cold work and heat treatment on the properties of nitinol wire. *Proceedings of the international conference on shape memory and superelastic technologies*, pp.447–454.

Duerig, T.W., Tolomeo, D.E. & Wholey, M., 2000. An overview of superelastic stent design. *Minimally invasive therapy & allied technologies : MITAT : official journal of the Society for Minimally Invasive Therapy*, 9(3–4), pp.235–46.

Feinsod, M., 2010. De Motu Cerebri : The History of the Study of Brain Pulsations. *The Open Neurosurgery Journal*, 3, pp.10–16.

Fischl, B. & Dale, A.M., 2000. Measuring the thickness of the human cerebral cortex from magnetic resonance images. *Proceedings of the National Academy of Sciences*, 97(20), pp.11050–11055.

Gao, C., 2007. Finite element modelling of the human brain and application in neurosurgical procedures. *National University of Singapore.*

Gao, C., Tay, F.E.H. & Nowinski, W.L., 2005. A Finite Element Method Based Deformable Brain Atlas Suited for Surgery Simulation. In *Proceedings of the 2005 IEEE Engineering in Medicine and Biologu 27th Annual Conference*. pp. 4337–4340.

García, a., Peña, E. & Martínez, M. a., 2012. Influence of geometrical parameters on radial force during self-expanding stent deployment. Application for a variable radial stiffness stent. *Journal of the Mechanical Behavior of Biomedical Materials*, 10, pp.166–175.

Goriely, A. et al., 2015. Mechanics of the brain: perspectives, challenges, and

opportunities. *Biomechanics and Modeling in Mechanobiology*.

Grunert, P., 2013. From the idea to its realization: The evolution of minimally invasive techniques in neurosurgery. *Minimally Invasive Surgery*, 2013.

Gütz, P., Abdel-Rahman, K. & Achmus, M., 2013. Numerical Modeling of Spudcan Footing Penetration in Sand. In *2013 SIMULIA Customer Conference*. pp. 1–14.

Hall, G.J. & Kasper, E.P., 2006. Comparison of element technologies for modeling stent expansion. *Journal of biomechanical engineering*, 128(5), pp.751–756.

Hamzavi, N., Tsang, W.M. & Shim, V.P.W., 2013. Nonlinear elastic brain tissue model for neural probe-tissue mechanical interaction. *International IEEE/EMBS Conference on Neural Engineering, NER*, pp.1119–1122.

Henderson, E., Nash, D.H. & Dempster, W.M., 2011. On the experimental testing of fine Nitinol wires for medical devices. *Journal of the Mechanical Behavior of Biomedical Materials*, 4(3), pp.261–268.

Herrera, S.R. et al., 2010. Use of transparent plastic tubular retractor in surgery for deep brain lesions: a case series. *Surgical technology international*, 19, pp.47–50.

Howard, M.A. et al., 1999. Measurement of the Force Required to Move a Neurosurgical Probe Through in vivo Human Brain Tissue. *IEEE Transactions on Biomedical Engineering*, 46(7), pp.891–894.

Hrapko, M. et al., 2006. The mechanical behaviour of brain tissue : Large strain response and constitutive modelling. *Biorheology*, 43, pp.623–636.

Di Ieva, A. et al., 2014. A Journey into the Technical Evolution of Neuroendoscopy. *World Neurosurgery*, 82(6), pp.e777–e789.

Jamshidi, P., Mahmoody, K. & Erne, P., 2008. Covered stents: a review. *International journal of cardiology*, 130(3), pp.310–8.

Jensen, W., Yoshida, K. & Hofmann, U.G., 2007. In vivo implant mechanics of single-shaft microeletrodes in peripheral nervous tissue. In *Proceedings of the 3rd*

International IEEE EMBS Conference on Neural Engineering. pp. 20–23.

Johe, R., 2009. Tensile testing of nitinol tubes and wires with higher strain rates. *Journal of Materials Engineering and Performance*, 18(5–6), pp.836–842.

Kassam, A.B. et al., 2009. Completely endoscopic resection of intraparenchymal brain tumors. *Journal of neurosurgery*, 110(1), pp.116–23.

Kataoka, H. et al., 2008. Simulations of Needle Insertion by Using a Eulerian Hydrocode FEM and the Experimental Validations. *Med Image Comput Comput Assist Interv*, 11(Pt 2), pp.560–568.

Kawano, H. et al., 2012. Role of the lesion scar in the response to damage and repair of the central nervous system. *Cell and tissue research*, 349(1), pp.169–80.

Kelly, P.J., Goerss, S.J. & Kall, B. a, 1988. The stereotaxic retractor in computer-assisted stereotaxic microsurgery. Technical note. *Journal of neurosurgery*, 69(2), pp.301–6.

Kerl, J. et al., 2012. Tissue deformation analysis using a laser based digital image correlation technique. *Journal of the mechanical behavior of biomedical materials*, 6, pp.159–65.

Kirkpatrick, D.B., 1984. The first primary brain-tumor operation. *Journal of neurosurgery*, 61(5), pp.809–13.

Kleinstreuer, C. et al., 2008. Computational mechanics of Nitinol stent grafts. *Journal of Biomechanics*, 41, pp.2370–2378.

Lally, C., Kelly, D.J. & Prendergast, P.J., 2006. Stents. *Wiley Encyclopedia of Biomedical Engineering*, pp.1–10.

Lehocky, C.A., Shi, Y. & Riviere, C.N., 2014. Hyper- and viscoelastic modeling of needle and brain tissue interaction. *2014 36th Annual International Conference of the IEEE Engineering in Medicine and Biology Society, EMBC 2014*, pp.6530–6533.

Ma, J. et al., 2010. Evaluation of accuracy of non-linear finite element computations for

surgical simulation: study using brain phantom. *Computer methods in biomechanics and biomedical engineering*, 13(6), pp.783–94.

Mao, H. et al., 2010. Finite element analysis of controlled cortical impact-induced cell loss. *Journal of Neurotrauma*, 27(May), pp.877–888.

Materials, S., 2011. Standard Guide for Finite Element Analysis (FEA) of Metallic Vascular Stents Subjected to Uniform Radial Loading 1. *Current*, (C), pp.2–9.

Mazumder, M.M.G. et al., 2013. Mechanical properties of the brain-skull interface. *Acta of Bioengineering and Biomechanics*, 15(2), pp.3–11.

Mendizabal, a., Aguinaga, I. & Sánchez, E., 2015. Characterisation and modelling of brain tissue for surgical simulation. *Journal of the Mechanical Behavior of Biomedical Materials*, 45, pp.1–10.

Mihai, L.A. et al., 2015. A comparison of hyperelastic constitutive models applicable to brain and fat tissues. *Journal of the Royal Society, Interface / the Royal Society*, 12(110), p.486.

Miller, K., 1999. Constitutive model of brain tissue suitable for finite element analysis of surgical procedures. *Journal of Biomechanics*, 32, pp.531–537.

Miller, K. et al., 2000. Mechanical properties of brain tissue in-vivo : experiment and computer simulation. *Journal of Biomechanics*, 33, pp.1369–1376.

Miller, K. & Chinzei, K., 2002. Mechanical properties of brain tissue in tension. *Journal of Biomechanics*, 35, pp.483–490.

Miller, K., Wittek, A. & Joldes, G., 2010. Biomechanics of the brain for computer-integrated surgery. *Acta of Bioengineering and Biomechanics*, 12(2), pp.25–37.

Molloy, J.A. et al., 1990. Experimental Determination of the Force Required for Insertion of a Thermoseed Into Deep Brain Tissue. *Annals of Biomedical Engineering*, 18, pp.299–313.

Nematzadeh, F. & Sadrnezhaad, S.K., 2013. Effects of crimping on mechanical

performance of nitinol stent designed for femoral artery: Finite element analysis. *Journal of Materials Engineering and Performance*, 22(11), pp.3228–3236.

NICO Corporation, 2014. NICO BrainPath Product Guide.

Nishihara, T. et al., 2000. A transparent sheath for endoscopic surgery and its application in surgical evacuation of spontaneous intracerebral hematomas. Technical note. *Journal of neurosurgery*, 92(6), pp.1053–5.

Ogura, K. et al., 2006. New microsurgical technique for intraparenchymal lesions of the brain: transcylinder approach. *Acta neurochirurgica*, 148(7), p.779–85; discussion 785.

Oldfield, M. et al., 2013. Detailed finite element modelling of deep needle insertions into a soft tissue phantom using a cohesive approach. *Computer methods in biomechanics and biomedical engineering*, 16(5), pp.530–43.

Plaha, P. et al., 2014. Minimally invasive endoscopic resection of intraparenchymal brain tumors. *World Neurosurgery*, 82(6), pp.1198–1208.

Pomfret, R., Miranpuri, G. & Sillay, K., 2013. The substitute brain and the potential of the gel model. *Annals of Neurosciences*, 20(3), pp.118–122.

Preul, M.C., 2005. History of brain tumor surgery. *Neurosurgical FOCUS*, 18(4), pp.1–1. Available at: http://thejns.org/doi/abs/10.3171/foc.2005.18.4.1.

Qiu, G., Henke, S. & Grabe, J., 2009. Applications of Coupled Eulerian-Lagrangian Method to Geotechnical Problems with Large Deformations. In *2009 SIMULIA Customer Conference*. pp. 1–16.

Ritter, R.C. et al., 1998. Measurement of Friction on Straight Catheters in in vitro Brain and Phantom Material. *IEEE Transactions on Biomedical Engineering*, 45(4), pp.476–485.

Roguin, A., 2011. Stent: the man and word behind the coronary metal prosthesis. *Circulation. Cardiovascular interventions*, 4(2), pp.206–9.

Rosenørn, J. & Diemer, N., 1982. Reduction of regional cerebral blood flow during brain retraction pressure in the rat. *Journal of neurosurgery*, 56(6), pp.826–829.

Rymarczuk, G.N. et al., 2015. Use of a Minimally Invasive Retractor System for Retrieval of Intracranial Fragments in Wartime Trauma. *World Neurosurgery*, pp.1–7.

Sgouros, S., 2014. *Neuroendoscopy - Current Status and Future Trends*, Springer.

Sharp, A.A. et al., 2009. In Vivo Penetration Mechanics and Mechanical Properties of Mouse Brain Tissue at Micrometer Scales. *IEEE Transactions on Biomedical Engineering*, 56(1), pp.45–53.

Shoakazemi, A. et al., 2015. A 3D endoscopic transtubular transcallosal approach to the third ventricle. *Journal of neurosurgery*, 122(March), pp.564–573.

Shreiber, D.I., Bain, A.C. & Meaney, D.F., 1997. In Vivo Threshlolds for Mechanical Injury to the Blood-Brain Barrier. *SAE technical paper*, p.No. 973335.

Singh, L. & Agrawal, N., 2010. Stitch retractor-simple and easy technique to retract brain. *World Neurosurgery*, 73(2), pp.123–127.

Snowhill, P.B. et al., 2001. Characterization of radial forces in Z stents. *Investigative radiology*, 36(9), pp.521–30.

Standring, S., 2005. *Gray's Anatomy. The Anatomical Basis of Clinical Practice, 39th ed.*,

Stoeckel, D. et al., 2002. A survey of stent designs. *Minimally invasive therapy & allied technologies : MITAT : official journal of the Society for Minimally Invasive Therapy*, 11(4), pp.137–47.

Stoeckel, D., Pelton, A. & Duerig, T., 2004. Self-expanding Nitinol stents: Material and design considerations. *European Radiology*, 14(2), pp.292–301.

Sullivan, S. et al., 2014. White matter tract-oriented deformation predicts traumatic axonal brain injury and reveals rotational direction-specific vulnerabilities. *Biomechanics and Modeling in Mechanobiology*, 14(4), pp.877–896.

Wagshul, M.E., Eide, P.K. & Madsen, J.R., 2011. The pulsating brain: A review of experimental and clinical studies of intracranial pulsatility. *Fluids and barriers of the CNS*, 8(1), p.5. Available at: http://www.fluidsbarrierscns.com/content/8/1/5.

Wang, Y. et al., 2007. Smad3 null mice display more rapid wound closure and reduced scar formation after a stab wound to the cerebral cortex. *Experimental neurology*, 203(1), pp.168–84.

Waran, V. et al., 2009. A new expandable cannula system for endoscopic evacuation of intraparenchymal hemorrhages. *Journal of neurosurgery*, 111(6), pp.1127–30.

Weickenmeier, J. et al., 2016. The mechanics of decompressive craniectomy: Personalized simulations. *Journal of the Mechanics and Physics of Solids*, 96, pp.572–590.

Weldon, C. et al., 1966. A prosthetic stented aortic homograft for mitral valve replacement. *Journal of Surgical Research*, 6(12), pp.548–552.

Wittek, a. et al., 2008. Subject-specific non-linear biomechanical model of needle insertion into brain. *Computer Methods in Biomechanics and Biomedical Engineering*, 11(2), pp.135–146.

Wright, R.M. & Ramesh, K.T., 2012. An axonal strain injury criterion for traumatic brain injury. *Biomechanics and Modeling in Mechanobiology*, 11, pp.245–260.

Zhang, L., Yang, K.H. & King, A.I., 2001. Comparison of brain responses between frontal and lateral impacts by finite element modeling. *J Neurotrauma*, 18(1), pp.21–30.

Zhong, J. et al., 2003. Brain retraction injury. *Neurological research*, 25(8), pp.831–8.

Appendices

Appendix 1 – Calculation of rigid shells radial expansion force

Calculation is performed in Abaqus .odb. Reacting forces on each rigid shell in X and Y directions are saved as “FX-#” and “FY-#”, respectively, where “#” is the rigid shell number. Radial force is then calculated with the following script.

```
sqrt("FX-1"*"FX-1"+"FY-1"*"FY-1") + sqrt("FX-2"*"FX-2"+"FY-2"*"FY-2") +
sqrt("FX-3"*"FX-3"+"FY-3"*"FY-3") + sqrt("FX-4"*"FX-4"+"FY-4"*"FY-4") +
sqrt("FX-5"*"FX-5"+"FY-5"*"FY-5") + sqrt("FX-6"*"FX-6"+"FY-6"*"FY-6") +
sqrt("FX-7"*"FX-7"+"FY-7"*"FY-7") + sqrt("FX-8"*"FX-8"+"FY-8"*"FY-8") +
sqrt("FX-9"*"FX-9"+"FY-9"*"FY-9") + sqrt("FX-10"*"FX-10"+"FY-10"*"FY-10") +
sqrt("FX-11"*"FX-11"+"FY-11"*"FY-11") + sqrt("FX-12"*"FX-12"+"FY-12"*"FY-12") +
sqrt("FX-13"*"FX-13"+"FY-13"*"FY-13") + sqrt("FX-14"*"FX-14"+"FY-14"*"FY-14") +
sqrt("FX-15"*"FX-15"+"FY-15"*"FY-15") + sqrt("FX-16"*"FX-16"+"FY-16"*"FY-16")
```

Appendix 2 – Calculation of deformable surface radial expansion force

Calculation is performed by exporting data from Abaqus .odb and running a scrip in MATLAB. Reaction force on all deformable surface nodes are exported as a .rpt file with all data in a single table. Number of significant digits is 6. The .rpt file is then used to import into MATLAB as a matrix. The scalar radial force for each line of nodes is calculated with the following script.

```
function RF = combineDirection (F)
% This code combines nodal forces in X and Y direction and outputs a
scalar radial force.
% F is a matrix imported from ABAQUS history output.
% RF is combined force matrix.
% m is time steps, n is number of data per X or Y direction

[m n] = size(F);

X = F(:,1:n/2);
Y = F(:,n/2+1:n);

FX = zeros(m, n/2);
RF = zeros(m,1);

for i = 1:m
    for j = 1:n/2
        FX(i,j) = sqrt((X(i,j))^2+(Y(i,j))^2);
        RF(i)= sum(FX(i,:));
    end
end

plot((1:m),RF);

end
```

Appendix 3 – Calculation of SESR geometry during deployment

Calculation is performed in Abaqus .odb using displacements of “Top”, “Middle” and “Bottom” nodes in X, Y and Z directions. Take the SESR of C10 stents as an example. There are 10 “Top” nodes, 20 “Middle” nodes and 10 “Bottom” nodes. The displacement in longitudinal direction for “Top” nodes of the first stent and “Bottom” nodes of the third stent are used to calculate SESR length with the following script.

```
32-(abs("U3-Stent1Top-1"+"U3-Stent1Top-2"+"U3-Stent1Top-3"+"U3-Stent1Top-4"+"U3-
Stent1Top-5"+"U3-Stent1Top-6"+"U3-Stent1Top-7"+"U3-Stent1Top-8"+"U3-Stent1Top-
9"+"U3-Stent1Top-10")/10+abs("U3-Stent3Bottom-1"+"U3-Stent3Bottom-2"+"U3-
Stent3Bottom-3"+"U3-Stent3Bottom-4"+"U3-Stent3Bottom-5"+"U3-Stent3Bottom-6"+"U3-
Stent3Bottom-7"+"U3-Stent3Bottom-8"+"U3-Stent3Bottom-9"+"U3-Stent3Bottom-10")/10)
```

For each stent, for all “Middle” nodes, the displacements in X and Y direction are save as “U1” and “U2”, respectively. The average stent diameter is then calculated with the following script.

```
18-2*(sqrt("U1-1"*"U1-1"+"U2-1"*"U2-1") + sqrt("U1-2"*"U1-2"+"U2-2"*"U2-2") +
sqrt("U1-3"*"U1-3"+"U2-3"*"U2-3") + sqrt("U1-4"*"U1-4"+"U2-4"*"U2-4") +
sqrt("U1-5"*"U1-5"+"U2-5"*"U2-5") + sqrt("U1-6"*"U1-6"+"U2-6"*"U2-6") +
sqrt("U1-7"*"U1-7"+"U2-7"*"U2-7") + sqrt("U1-8"*"U1-8"+"U2-8"*"U2-8") +
sqrt("U1-9"*"U1-9"+"U2-9"*"U2-9") + sqrt("U1-10"*"U1-10"+"U2-10"*"U2-10") +
sqrt("U1-11"*"U1-11"+"U2-11"*"U2-11") + sqrt("U1-12"*"U1-12"+"U2-12"*"U2-12") +
sqrt("U1-13"*"U1-13"+"U2-13"*"U2-13") + sqrt("U1-14"*"U1-14"+"U2-14"*"U2-14") +
sqrt("U1-15"*"U1-15"+"U2-15"*"U2-15") + sqrt("U1-16"*"U1-16"+"U2-16"*"U2-16") +
sqrt("U1-17"*"U1-17"+"U2-17"*"U2-17") + sqrt("U1-18"*"U1-18"+"U2-18"*"U2-18") +
sqrt("U1-19"*"U1-19"+"U2-19"*"U2-19") + sqrt("U1-20"*"U1-20"+"U2-20"*"U2-20"))/20
```